INVESTIGATION OF AIR POLLUTANTS NEAR THE GREAT LAKES IN ONTARIO AND ALONG THE COAST OF CALIFORNIA

IBRAHEEM M. NUAAMAN

A DISSERTATION SUBMITTED TO
THE FACULTY OF GRADUATE STUDIES
IN PARTIAL FULFILLMENT OF THE REQUIREMENTS
FOR THR DEGREE OF
DOCTOR OF PHILOSOPHY

GRADUATE PROGRAM IN CHEMISTRY
YORK UNIVERSITY
TORONTO, ONTARIO

April 2015

Abstract

This dissertation is of two parts. In the first part, carbonyls were measured in Ridgetown, Ontario using an automated HPLC-DNPH system during the BAQS-Met study in 2007. Median concentrations for formaldehyde, acetaldehyde, acetone, propanal, MEK and butanal were observed to be 1.5, 0.67, 1.9, 0.072, 0.22 and 0.041 ppb respectively. The highest carbonyl concentrations were observed with trans-boundary transport associated with airmasses that passed over Michigan and Illinois and could have originated from the Ohio Valley. Local ozone sensitivity was established using the $HCHO/NO_2$ ratio and this area was found to be sensitive to both VOCs and NO_x. Carbonyls accounted for 35% of O_3 formation estimated using the MIR scale. Lake breeze events had no significant impact on carbonyl concentrations in this location.

In the second part of this dissertation, aerosol concentrations and composition were obtained along the coast of California using a High-Resolution Time-of-Flight aerosol mass spectrometer (HR-AMS) onboard *RV Atlantis* during CalNex in 2010. Measured submicron aerosols were dominated by particulate sulfate and particulate organic matter (pOM), which accounted for 86% of all measured submicron aerosol mass. High aerosol concentrations were associated with land breezes from polluted cities while low concentrations were observed with sea breezes.

For the first time, a method is proposed to establish non-refractory particulate chloride (NR p-Cl) in ambient air that is enriched with sea salt chloride. This method involves the subtraction of refractory chloride signal (RF H_xCl^+), which was estimated using the H_xCl^+ (total chloride signal) to $Na^{35}Cl^+$ ratio in artificially generated sea

spray aerosols. Also for the first time, a method is proposed to determine percentage chloride depletion in ambient aerosols using HR-AMS measurements of Na^+ and $Na^{35}Cl^+$. Using this proposed method, study-wide median chloride depletion in submicron aerosols was determined to be 78%. For NR p-Cl, an increasing trend with increasing RH and pH and decreasing temperature was observed. Finally, pOM in sea spray aerosols was observed to be dominated by hydrocarbons (55%) and oxygenated hydrocarbon classes (37%); this pOM was found to be positively correlated with seawater DMS.

I dedicate this dissertation to my wife Dawsar, my son Adam and our soon-to-born baby.

Acknowledgements

First and foremost, I would like to acknowledge my supervisor and mentor Dr. Robert McLaren. It was a pleasure working with you, thank you for sharing your valuable ideas with me and allowing me to pursue my own ideas freely. You have often directed me towards the correct path and made sure that all science ideas and approaches are well-thought-of and clearly communicated. I would also like to acknowledge my supervising committee Dr. Jochen Rudolph and Dr. Shao-Meng Li who made sure I stay focus on my research goals and not deviate into many side points. Dr. Jochen was always available with answers if I ever had any research-related questions. Dr. Shao-Meng, it was a great privilege to work with you at Environment Canada in a superb research environment.

From BAQS-Met, I want to thank Anna Kornilova, Corrine Schiller and Andy Ng for sharing their measurements. From CalNex, I thank the scientists and crew of *RV Atlantis*, especially Katherine Hayden, Tim Onasch, Paola Massoli and Donna Sueper for their help with the HR-AMS and data analysis. I thank Tim Bates and Patricia Quinn for the sea sweep experiments and filter measurement data. I thank Eric Williams, Brian Lerner, Jerome Brioude, Joel Thornton and Theran Riedel For facilitating and sharing measurements and analysis during CalNex. I also want to thank my previous group members Jamie Halla and Patryk Wojtal for the exchange of scientific ideas. Jamie is a friend, we worked, talked and had fun at York University. I want to thank Dr. Mark Gordon and Dr. Haider A. Khwaja for agreeing to be a part my examining committee and for reading my lengthy thesis.

A huge thank you and shokran to my family for their endless love and support.

Thank you to my beautiful wife Dawsar for her support, believing in me, pushing me to greatness and giving me Adam. Thank you to my beautiful baby boy Adam a.k.a Dudee (with the big beautiful eyes) who has brought so much joy and meaning to my life. Thank you to the new baby on the way, I haven't met you yet but I love you already. Thank you to my wonderful parents Dr. Mohammed and Dr. Hayfa for taking us out of a war-torn poverty-stricken country in 1997 and moving us to a land of freedom and opportunity. Thank you to my sisters and nephew Saba, Mais and Yaseen for being there for me.

Table of Contents

List of Tables

List of Figures

Abbreviations

ACN: Acetonitrile

AMS: Aerodyne Aerosol Mass Spectrometer

AT-DNPH-HPLC: Automated HPLC system with DNPH derivitization

BAQS-Met: Border Air Quality and METerology Study

BLH: Boundary layer height

C-ToF-AMS: Compact Time-of-Flight AMS

CalNex: The research at the nexus of air quality and climate change

CE: Collection Efficiency

CEC: Chloride Equivalent Concentration

CL: ChemiLuminescence NO_2 monitors

DMS: Dimethyl sulfide

DNPH: 2,4-dinitrophenylhydrazine

DOAS: Differential Optical Absorption Spectroscopy

GC-FID: Gas Chromatography with Flame Ionization Detector (GC-FID)

GC-MSD: GC with Mass Selective Detector

GHGs: Greenhouse gases

HPLC: High Performance Liquid Chromatography

HR-AMS: High-Resolution Time-of-Flight AMS

H_xCl^+: Ion group of $^{35}Cl^+$, $H^{35}Cl^+$, $^{37}Cl^+$, $H^{37}Cl^+$

L.A.: Los Angeles

MEK: Methyl ethyl ketone

MFC: Mass flow controller

MIR: Maximum incremental reactivity

NEC: Nitrate Equivalent Concentration

NMHC: Non-Methane HydroCarbons

NR: Non-Refractory

OAK: Oakland

p-NH_4: Particulate ammonium

p-NO_3: Particulate nitrate

p-SO_4: Particulate sulfate

p-Cl: Particulate chloride

PANs: Peroxy acetyl nitrates

pOM: Particulate organic matter

Q-AMS: Quadrupole AMS

RF: Refractory

RH: Relative Humidity

RSF: Response Factor

RU: Rural location

RV: Research Vessel

S.F. : San Francisco

SAC.: Sacramento

SGGS: Standard Gas Generation System

SMB: Santa Monica Bay

SMPS: Scanning Mobility Particle Sizer

SOA: Secondary Organic Aerosol

ss p-Cl: sea salt p-Cl

SUB: Suburban

UR: Urban

VOC: Volatile Organic Compounds

1 Introduction

1.1 The effect of air pollution on human health and climate

Air pollution is the contamination of the natural atmosphere by chemical, physical and biological agents (Environment Canada, 2015; WHO, 2015). Environment Canada (2015) segregates air pollutants into four categories, which are: criteria air pollutants, persistent organic compounds, heavy metals and toxics. Criteria air pollutants include aerosols, volatile organic compounds (VOCs), ozone (O_3), nitrogen oxides (NO_x), sulfur dioxide (SO_2), carbon monoxide (CO), among others. Persistent organic compounds refer to organic compounds that have long lifetimes in the atmosphere and can be transported across long distances; these include furans and dioxins. Heavy metals refer to harmful metals such as lead and mercury. Finally, toxics are a group of substances that are harmful to human health and the environment due to their toxicity.

The main sources of air pollution include motor vehicles, electrical power generation plants, oil extraction and processing, mining, agriculture, wood industry and other industrial facilities. Pollution sources also include volcanoes, lightning, biomass burning and indoor sources such as building material, household combustion devices and

household cleaning products. Given these sources, the contamination of air by pollutants is prevalent in indoor and outdoor environments (Environment Canada, 2014; EPA, 2015; WHO, 2015). Sources of air pollutants are both primary and secondary in nature, where primary pollutants are emitted directly into the atmosphere (SO_2, NO, NO_2, CO, CO_2, black carbon aerosols) and secondary sources involve the formation of the pollutant from chemical reactions in the atmosphere (O_3, peroxy acetyl nitrates, carbonyls, secondary organic aerosols).

Air pollution has adverse effects on human health, climate and eco-systems. The World Health Organization (WHO, 2015) estimates that 3.7 million people died prematurely in 2012 due to ambient air pollution (WHO, 2015). These cases were predominantly in low and middle income countries in South-East Asia and Western Pacific, which accounted for $\sim$ 3.3 million premature deaths. Premature deaths from air pollution are typically associated with ischaemic heart disease (restricted blood supply to the heart) and strokes, which accounted for $\sim$ 3.0 million. Another 0.52 million are associated with chronic obstructive pulmonary disease (chronically poor air flow due to obstruction of the lungs) or acute lower respiratory infections. The rest of cases equal to 0.22 million were reported to result from lung cancer (WHO, 2015).

Indoor air pollution is also known to negatively impact human health. The biggest concern of indoor pollution comes from smoke inhalation due to coal and biomass fuel burning for the purposes of domestic heating and cooking (WHO, 2015).

Air pollutants are also known to affect our climate system, which affects the well-being of the human population and the ecosystem. Earths surface and climate is affected

by the absorption of solar radiation at the Earths surface and trapping of outgoing radiation by greenhouse gases (GHGs) in a phenomena known as the natural greenhouse effect. Solar radiation absorbed by the surface of the earth is re-emitted into the atmosphere and a fraction is absorbed by the atmosphere with the rest escaping into outer space. The absorption of terrestrial radiation by atmospheric GHGs is a major process in this warming effect. These GHGs include carbon dioxide (CO_2), nitrous oxide (N_2O), methane (CH_4) and ozone (O_3). In contrast to GHGs, aerosols are known to reflect solar radiation and result in a "net cooling effect", although some aerosol components (such as black carbon) are known to absorb solar radition similar to GHGs (IPCC, 2013, 2014). Aerosols can also brighten clouds, which alters the albedo of said clouds; further discussion of how aerosols impact climate will follow in a later section. It is this balance between the absorbed, re-emitted and reflected radiation that ultimately determine the temperature of the Earth (Finalyson-Pitts and Pitts, 1999; Seinfeld and Pandis, 2006).

In the atmosphere, the ambient concentrations of GHGs are at record levels that have not been reached in 800,000 years or more. The observed increase in GHGs lead to an increase in energy uptake by the climate system. Subsequently, there are clear indications of climate warming including an increase in surface and ocean temperatures, a decrease in ice and snow cover and an increase in global sea levels. For the period from 1880 to 2012, the increase in combined global surface and ocean temperatures ranged from 0.65 to 1.05 °C with an average of 0.85 °C. A decrease in the annual mean ice-snow extent of the Arctic and Antarctic was observed to be 3.5-4.1% and 1.2-1.8%

per decade for the period from 1979-2012 respectively. In addition, a decrease in the mass of ice sheets in Greenland and the Antartic has been reported in the period from 1992 to 2011. Glaciers have also decreased in size almost worldwide (IPCC, 2014).

Global sea levels saw an increase of 0.19 m (0.17-0.21 m) for the period from 1901 to 2012. From the mid 19^{th} century, the rate of increase observed for the global sea level was larger than the two last millennia. Finally, the increase in CO_2 concentrations lead to an increase in CO_2 ocean uptake. As a result of the uptake of CO_2, the ocean acidity increased as indicated by a 0.1 decrease in pH of the ocean surface water. This corresponds to a 26% increase in the acidity of the ocean surface water (IPCC, 2014).

The influence of anthropogenic activities on our climate system is evident. The increased emissions of GHGs from these activities contributed more than half to the increase in global surface temperatures from 1951 to 2010. Human influences have contributed to an increase in the heat content of the global upper ocean since the 1970s, a decrease in Arctic snow-ice mass since 1979, a shrinkage in glaciers since the 1960s, an alteration of the global water cycle since the 1960s and a rise in the global mean sea level since the 1970s (IPCC, 2014).

On a global scale, climate warming lead to an increase in heat waves and heavy precipitation on land. This precipitation has affected the global hydrological systems, which directly affects the quantity and quality of the water resources. The changes in hydrological systems have also resulted in droughts, cyclones and wildfires (IPCC, 2014). Crop yields have had a net loss due to climate warming, which lead to higher food prices. Finally climate warming forced animal and plant species (on land, in freshwater

and in marine environments), to shift their natural geographical inhabitance, seasonal activities, interactions with other species, migration patterns and even their numbers. Marine and freshwater species are especially at risk given the acidification of oceans surface and the rise in sea level (IPCC, 2014).

Effective strategies to curb air pollution are important given the adverse effects that air pollution has on human health, climate and the ecosystem. A reduction in air pollution leads to improved cardiovascular and respiratory health for the human population (WHO, 2015). This reduction would help lower the risks associated with climate variability (IPCC, 2014). Some measures to reduce air pollution include: cleaner sources of fuel for power generation, better technologies to reduce emissions associated with transport, strategies to curb emissions from industries, improved waster management, reduce agricultural biomass burning practices, among others (see for example: EPA, 2015; WHO, 2015).

In order to propose effective local and regional control strategies for air pollutants, it is important to establish the sources and the removal mechanisms of these pollutants. In the case of primary sources, it is important to establish which sources are giving rise to the highest emissions. For the secondary sources, reduction strategies requires knowledge of the pollutant formation mechanisms, atmospheric removal processes and the emission sources of the pollutant precursors.

1.2 Oxidants in the troposphere

In the atmosphere, oxidants are a pinnacle of the formation of gas and particle phase secondary pollutants including those discussed in this study, namely gaseous carbonyls and organic and inorganic aerosols. The most important oxidants in the troposphere are ozone, hydroxyl radical, nitrate radical and atomic chlorine (see for example Finalyson-Pitts and Pitts, 1999).

1.2.1 Ozone

Ozone formation in the troposphere proceeds via the photolysis of nitrogen dioxide (NO_2), a primary pollutant emitted primarily from combustion sources (vehicle exhausts, electrical power generation, petrochemical sources and other industries) and natural sources (lightning and biomass burning) to a lesser extent (Finalyson-Pitts and Pitts, 1999; OME, 2006) . The photolysis of NO_2 yields ground state atomic oxygen ($O(^3P)$) (R 1.1). In the presence of an air molecule M, $O(^3P)$ reacts with molecular oxygen to form ozone (R 1.2).

$$NO_2 + h\nu \ (\lambda < 424\,\text{nm}) \longrightarrow NO + O(^3P) \qquad \text{(R 1.1)}$$

$$O(^3P) + O_2 + M \longrightarrow O_3 + M \qquad \text{(R 1.2)}$$

$$NO + O_3 \longrightarrow NO_2 + O_2 \qquad \text{(R 1.3)}$$

Ozone reacts rapidly with nitric oxide (NO) to form NO_2 in what is known as the ozone titration reaction (R 1.3). Nitric oxide has the same primary sources discussed

above for NO_2. The term NO_x is typically used to refer to NO + NO_2. Emissions of NO_x from vehicle exhaust are primarily in the form of NO, which accounts for 70 - 98% of NO_x emitted from vehicles (see Yao et al., 2005, and the references therein).

Organic radicals enhance O_3 formation through a conversion of NO to NO_2. Alkyl radicals are formed from the oxidation and photolysis of VOCs that form peroxy radicals RO_2 and HO_2 upon reactions with molecular oxygen. These peroxy radical react with NO to form NO_2 as follows:

$$RO_2 + NO \longrightarrow NO_2 \qquad \text{(R 1.4)}$$

1.2.2 Hydroxyl Radical

Hydroxyl radical (OH) is the most important and most dominant daytime radical in the troposphere and is largely responsible for the removal of trace gases in the troposphere (Stone et al., 2012). The formation mechanism of OH in the troposphere is driven primarily by the photo-dissociation of O_3 thus forming the excited state atomic oxygen ($O(^1D)$ (R 1.5). Hydroxyl radical is then formed via a reaction of water vapour and $O(^1D)$(R 1.6) (Atkinson, 2000; Stone et al., 2012).

$$O_3 + h\nu\ (\lambda < 319\,\text{nm}) \longrightarrow O_2 + O(^1D) \qquad \text{(R 1.5)}$$

$$O(^1D) + H_2O \longrightarrow 2\,OH \qquad \text{(R 1.6)}$$

Another reaction pathway for $O(^1D$ is its collision deactivation with N_2 and O_2 (R 1.7) (Atkinson, 2000).

$$O(^1D) + M \longrightarrow O(^3P) + M \qquad \text{(R 1.7)}$$

where M in R 1.7 refers to N_2 or O_2. Atkinson (2000) argues that 0.2 OH radicals are formed per O^1D atom formed from O_3 photolysis, which is due to the competitive deactivation through reaction R 1.7.

Another source of OH radicals in the troposphere is the photolysis of aldehydes. The mechanism of formaldehyde (HCHO) photolysis is as follows (Sumner et al., 2001):

$$HCHO + h\nu \longrightarrow CHO + H \quad \text{(R 1.8a)}$$

$$\longrightarrow CO + H_2 \quad \text{(R 1.8b)}$$

$$H + O_2 \longrightarrow HO_2 \quad \text{(R 1.9)}$$

$$CHO + O_2 \longrightarrow HO_2 + CO \quad \text{(R 1.10)}$$

$$HO_2 + NO \longrightarrow OH + NO_2 \quad \text{(R 1.11)}$$

Note that reactionR 1.11 proceeds in NO_x-rich environments (Sumner et al., 2001). This translates into all locations except in remote areas where NO_x is too low (Finalyson-Pitts and Pitts, 1999).

Hydroxyl radical can also be formed from the photolysis of nitrous acid (HONO) and the dark reaction of O_3 with alkenes. These formation mechanisms are less significant and are a function of location and time-of-day (Atkinson, 2000). The mean daytime concentration range for OH radical is approximately 0.5-5 molec cm^{-3} (Hewitt and Harrison, 1985).

1.2.3 Nitrate radical

Nitrate radical is formed from the reaction of NO_2 with O_3. This reaction is as follows (Atkison, 2000; McLaren et al., 2010):

$$NO_2 + O_3 \longrightarrow NO_3 + O_2 \qquad \text{(R 1.12)}$$

Nitrate radical photolyzes rapidly within seconds and is typically low during daytime (Atkinson, 2000). The reactivity of NO_3 towards VOCs is lower than that of OH (McLaren et al., 2010). At night, NO_3 concentrations increase and play significant role in the chemistry of the troposphere. In polluted regions, NO_3 is expected to be the dominant radical at night (McLaren et al., 2010).

1.2.4 Chlorine radical

Chlorine atoms (Cl) can play a significant role in tropospheric chemistry especially in marine areas (Spicer et al.,1998; Tanaka et al., 2000; Osthoff et al, 2008; Roberts et al., 2008; Thornton et al., 2010). Although Cl atoms exists at much lower concentrations than OH radical, the reaction of alkanes with Cl is faster (by up to two orders of magnitude) than that with OH (Tanaka et al., 2000). Some formation mechanisms of Cl include sodium chloride (NaCl). In marine areas, wind-induced bubble bursting at the ocean surface generates droplets of sea water, which upon drying form solid particle suspension. These particles are composed mainly of NaCl and could produce Cl atoms through the following reaction pathways (Finalyson-Pitts and Pitts, 1999; McLaren et

al., 2010; Riedel et al., 2012, and references therein):

$$NO_3 + NO_2 \overset{M}{\rightleftharpoons} N_2O_5 \qquad \text{(R 1.13)}$$

$$N_2O_5 + Cl^-(s, aq) \longrightarrow ClNO_2(g, aq) + {NO_3}^-(s, aq) \qquad \text{(R 1.14)}$$

$$ClNO_2 + h\nu \longrightarrow Cl + NO_2 \qquad \text{(R 1.15)}$$

$$ClNO_2 + H^+(aq) + Cl^-(aq) \longrightarrow Cl_2 + HONO \qquad \text{(R 1.16)}$$

$$Cl_2 + h\nu \longrightarrow 2\,Cl \qquad \text{(R 1.17)}$$

Tropospheric nitryl chloride ($ClNO_2$) gas was first measured in Houston (Osthoff et al., 2008) and reported concentrations were observed to exceed 1 ppb. Along the coast of California during the CalNex study, $ClNO_2$ concentrations were reported to be higher than 2 ppb (Reidel et al, 2012). Nitryl chloride was observed to be a significant source of Cl atoms in these studies.

Further to reactions R 1.16, chlorine gas can also be emitted directly into the atmosphere from various industrial sources. Tanaka et al. (2000) reports emissions from water treatment plants, chemical production facilities, smelter and paper production operations. Another source of Cl_2 is expected to be the autocatyltic halogen activation mechanism (Vogt et al., 1996; Platt and Hönninger, 2003; Riedel et al., 2012):

$$Cl + O_3 \longrightarrow ClO + O_2 \qquad \text{(R 1.18)}$$

$$ClO + NO \longrightarrow Cl + NO_2 \qquad \text{(R 1.19)}$$

$$ClO + HO_2 \longrightarrow HOCl + O_2 \qquad \text{(R 1.20)}$$

$$ClO + NO_2 + M \longrightarrow ClONO_2 + M \quad \text{(R 1.21)}$$

$$HOCl + Cl^-(aq) + H^+(aq) \longrightarrow Cl_2 + H_2O \quad \text{(R 1.22)}$$

$$ClONO_2 + Cl^-(aq) + H^+(aq) \longrightarrow Cl_2 + HNO_3 \quad \text{(R 1.23)}$$

Chlorine gas levels have been observed to reach 150 ppt in New York (Spicer et al., 1998) and 200 ppt along the coast of California (Riedel et al., 2012).

1.3 Carbonyls

Carbonyls are organic compounds that contains the functional group C=O. Carbonyls are further categorized into aldehydes (R-CHO) and ketones (R_1-CO-R_2), which comprise the simplest carbonyls. Other organic compounds that are also classified as carbonyls include: carboxylic acids (R-COOH), acid chlorides (R-CO-Cl), esters (R1-CO-OR) and amides R-CO-NH_2) (Wade, 2002). In the context of this work, the term carbonyl compounds will henceforth only refer to aldehydes and ketones.

Carbonyls are ubiquitous in the atmosphere and are an important part of the oxygenated volatile organic compounds (OVOCs) and total volatile organic budget (Singh et al., 1994,1995; Khwaja and Narang, 2008 Aiello and McLaren, 2009; Sommariva et al., 2011). Carbonyls contribute to the organic carbon budget and in some cases their contribution is a factor of 2-5 higher than all the other non-methane hydrocarbons (Singh et al., 2001).

Carbonyl concentrations in the atmosphere are variable and are a function of location, time and season (Carlier et al., 1986). In the atmosphere, the three most

abundant carbonyls are typically formaldehyde, acetaldehyde and acetone (see Chapter 3). Formaldehyde can range from 0.1-150 ppb (Carlier et al., 1986) while the range for acetaldehyde can be from 0.2-17 ppb (Possanzini et al., 1996; Khwaja and Narang, 2008) and that of acetone can be from 0.1-13 (Singh et al., 1994; Grosjean et al 1998).

Carbonyl compounds play a significant role in the chemistry of the atmosphere. They are an important source of free radicals in tropospheric chemistry, especially in moderately and highly polluted regions of the atmosphere (P. Carlier et al, 1986; Singh et al., 1995; Possanzini et al., 2002; Khwaja and Naranj, 2008). Aldehydes are known to contribute to OH formation as was discussed in Section 1.2.2, as well as other free radicals such as HO_2, RO and RO_2 (Khwaja and Naranj, 2008). Carlier et al (1986) argues that carbonyls are the most important source of tropospheric free radicals in moderate and strongly polluted areas. Through its formation of the free radicals, carbonyls enhance the formation of tropospheric ozone (Carter, 2010) as will be discussed in detail in Section 3.11. Carbonyls are precursors to important pollutants such as ozone, CO, CO_2, peroxyacetylnitrates (PANs) and carboxylic acids (see for example Carlier et al., 1986; Khwaja and Naranj, 2008) and are known to contribute to the formation of secondary organic aerosols (SOAs) (Liggio et al., 2005).

Increased levels of carbonyls, particularly aldehydes, have adverse effects on human health due to their toxicity (WHO, 2000). Exposure to formaldehyde causes irritation of the throat, nose and eyes. Increased discomfort, coughing, sneezing, lachrymation and even death can result from exposure to high concentrations of HCHO. More severe synergetic effects are expected when the exposure includes other respiraotory toxins such

as acetaldehyde and acrolein (WHO, 2000). Acrolein is a cytotoxic aldehyde, which has been linked, in animal testing, to inflammation, exfoliation, vascular congestion, haemorrhagic necrosis and oedema in the bronchi and trachea (WHO, 2002). Some studies suggest that adehydes are potential carciogenic and mutagenic agents (Carlier et al., 1986; WHO, 2000; Possanzini et al., 2002, and references therein). Occupational exposure to high levels of HCHO has been linked to nasopharyngeal and sinonasal cancers in epidemiological studies (WHO, 2000). Finally, secondary compounds generated from carbonyls such as PANs and SOAs also have adverse human health effects. Peroxyacetylnitrates are reportedly more toxic than carbonyls (Carlier et al., 1986).

1.3.1 Sources and sinks of Carbonyl compounds

Carbonyl compounds are emitted directly into the atmosphere by primary sources and formed through the photo-oxidation of VOC precursors, which constitute secondary sources of carbonyls. Primary sources include anthropogenic and biogenic emissions, where anthropogenic emissions include light and heavy-duty vehicles (Grosjean et al., 2001), fossil fuel combustion, petrochemical refining, coal chemistry, sewage treatment, garbage incineration, plastics and paint and varnish (Carlier et al,. 1986). Biogenic sources include deciduous and coniferous trees (Martin et al., 1999; Villanueva-Fierro et al., 2004), biomass burning (Singh et al., 1994), animal excretions, forest fires and certain insects (P. Carlier et al, 1986). Vehicle emissions of carbonyls were investigated in a tunnel study in California by Harley and Kean (2004). In this study, the measured carbonyls accounted for 4% by weight of non-methane organic compounds. The highest

contributions were from formaldehyde, acetaldehyde, benzaldehyde, acetone and m-tolualdehyde which accounted for 1.8%, 0.5%, 0.3%, 0.2% and 0.2% respectively.

The photochemical oxidation of VOCs is a significant secondary source of carbonyls in the troposphere. The main carbonyl formation mechanisms during the day involve the oxidation of hydrocarbons by OH and HO_2 radicals, as well as ozone (Grosjean, 1982; Carlier et al., 1986; Shepson et al., 1991; Altshuller, 1993). At night, oxidation of hydrocarbons by ozone and nitrate radicals are the main carbonyl formation mechanisms (Carlier et al., 1986; Alshuller, 1993). The oxidation of alkanes by OH is initiated by hydrogen abstraction, which forms an alkyl radical:

$$CH_2R_1R_2 + OH^{\cdot} \longrightarrow CHR_1R_2^{\cdot} + H_2O \qquad \text{(R 1.24)}$$

The alkyl radical then reacts with molecular oxygen forming a alkylperoxy radical.

$$CHR_1R_2^{\cdot} + O_2 \longrightarrow CHR_1R_2O_2^{\cdot} \qquad \text{(R 1.25)}$$

The alkylperoxy radical rapidly reacts with nitric oxide forming an alkoxy radical and NO_2:

$$CHR_1R_2O_2^{\cdot} + NO \longrightarrow CHR_1R_2O^{\cdot} + NO_2 \qquad \text{(R 1.26)}$$

A less significant pathway for reaction R 1.25 is the addition of NO to the alkyl radical. This pathway can form alkyl nitrates upon isomerization. The formation of alkyl nitrates is dependant on pressure, temperature and size of the radical. This addition reaction to form alkyl nitrates is more important for larger radicals. For octyl radical, more than 30% is reported to react by the addition pathway (Finalyson-Pitts and Pitts, 1999). The alkoxy radical formed in reaction R 1.25 then reacts with

molecular oxygen to form carbonyls and HO_2:

$$CHR_1R_2O^{\cdot} + O_2 \longrightarrow R_1(CO)R_2 + HO_2^{\cdot} \quad \text{(R 1.27)}$$

Carbonyls are also formed from the oxidation of alkenes by hydroxyl radical and ozone. The oxidation by OH is initiated by addition across the carbon-carbon double bond. In the following mechanism, we use propene oxidation by OH as an example (Finalyson-Pitts and Pitts, 1999):

$$CH_3HC{=}CH_2 + {}^{\cdot}OH \longrightarrow CH_3HC^{\cdot}{-}CH_2OH \quad \text{(R 1.28)}$$

This reaction forms a β-hydroxyalkyl radical, which reacts with O_2 to form β-hydroxyalkylperoxy radical. The β-hydroxyalkylperoxy radical then reacts with NO to form a β-hydroxyalkoxy radical and NO_2:

$$CH_3HC^{\cdot}{-}CH_2OH + O_2 \longrightarrow CH_3CHO_2^{\cdot}{-}CH_2OH \quad \text{(R 1.29)}$$

$$CH_3CHO_2^{\cdot}{-}CH_2OH + NO \longrightarrow CH_3CHO^{\cdot}{-}CH_2OH + NO_2 \quad \text{(R 1.30)}$$

Reaction R 1.30 can also proceed via NO addition to form alkyl nitrates as discussed previously. The yield for the addition of NO is only estimated to be $\sim$ 2-6 % (Finalyson-Pitts and Pitts, 1999). From reaction R 1.30, the β-hydroxyalkoxyl radical decomposes to form a carbonyl (acetaldehyde in this case) and an α-hydroxy radical:

$$CH_3CHO^{\cdot}{-}CH_2OH \longrightarrow CH_3CHO + {}^{\cdot}CH_2OH \quad \text{(R 1.31)}$$

The α-hydroxy radical further reacts with O_2 to form another carbonyl (formaldehyde in this case) and HO_2:

$${}^{\cdot}CH_2OH + O_2 \longrightarrow CH_2O + HO_2 \quad \text{(R 1.32)}$$

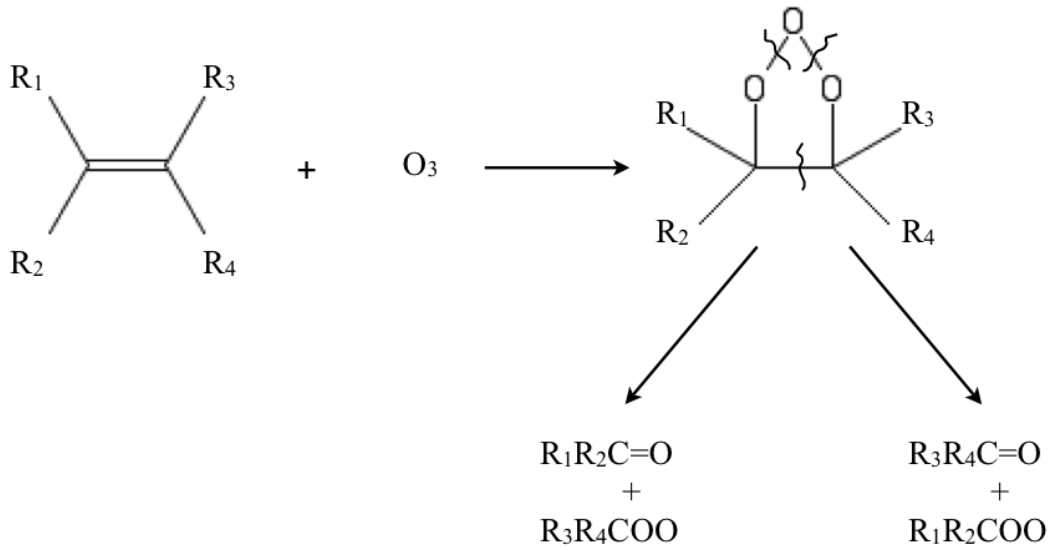

Figure 1.1: Carbonyl formation mechanism from the oxidation of alkenes by ozone.

.

Figure 1.1 shows the carbonyl formation mechanism from the oxidation of alkenes by ozone. The initiation reaction occurs with the addition of ozone across the carbon-carbon double bond to form an unstable primary ozonide or molozonide. After the formation of the molozonide, simultaneous cleavage occurs for the C-C bond and one of the O-O peroxy bonds. This cleavage yields an aldehyde or a ketone and a Criegee intermediate (Carlier et al., 1986; Grosjean et al., 1996a).

The removal of carbonyls from the atmosphere is driven by photolysis and hydroxyl radical oxidation (Grosjean, 1982; Carlier et al., 1986; Khwaja and Narang, 2008). Other removal processes include wet and/or dry deposition (Grosjean and Wright, 1983; Kawamura et al., 2001). The photolysis of carbonyls follow the following pathway

(Carlier et al., 1986):

$$R_1{-}CO{-}R_2 + h\nu \longrightarrow R_1{-}CO + R_2 \quad \text{(R 1.33a)}$$

$$\longrightarrow R_2{-}CO + R_1 \quad \text{(R 1.33b)}$$

$$R_1{-}CO{-}CH_2{-}CH_2{-}CH_2{-}R_2 + h\nu \longrightarrow R_1{-}CO + CH_3 + CH_2{=}CH{-}R_2 \quad \text{(R 1.34)}$$

$$R_1{-}CO{-}CH_2{-}CH_2{-}R_2 + h\nu \longrightarrow R_1{-}CHO + CH_2{=}CH{-}R_2 \quad \text{(R 1.35)}$$

$$R{-}CHO + h\nu \longrightarrow RH + CO \quad \text{(R 1.36)}$$

Reactions R 1.33a and R 1.33b are important pathways for radical formation (Carlier et al., 1986). This is similar to OH formation mechanism from the photolysis of HCHO, given above in section 1.2.2 R 1.8a through R 1.11.

The oxidation of carbonyls by hydroxyl radical is another removal mechanism that could lead to the formation of PANs. The mechanism for OH oxidation of an aldehyde to form PANs is initiated by abstraction of the aldehydic hydrogen and is as follows (Carlier et al., 1986):

$$R{-}CHO + OH \longrightarrow RCO + H_2O \quad \text{(R 1.37)}$$

$$R{-}CO + O_2 \longrightarrow RCO{-}O_2 \quad \text{(R 1.38)}$$

The RCO-O_2 radical can then react with NO and/or NO_2, the reaction with NO is typically followed by decomposition, shown below:

$$R{-}CO{-}O_2 + NO \longrightarrow RCO{-}O + NO_2 \quad \text{(R 1.39)}$$

$$\mathrm{R{-}CO{-}O} \longrightarrow \mathrm{R} + \mathrm{CO{-}O} \qquad (\mathrm{R}\,1.40)$$

The addition of NO_2 to the RCO-O_2 radical leads to the formation of PANs and is as follows:

$$\mathrm{R{-}CO{-}O_2} + \mathrm{NO_2} \longrightarrow \mathrm{RCO{-}O_2{-}NO_2} + \mathrm{NO_2} \qquad (\mathrm{R}\,1.41)$$

1.4 Particles in the atmosphere

Particles are ubiquitous in the atmosphere regardless of location and time. The term aerosol is technically defined as stable suspensions of solid or liquid particles in a gas but is commonly used to refer only to the particles (Finalyson-Pitts and Pitts, 1999; Seinfeld and Pandis, 2006). These two terms will be used interchangeable throughout this dissertation. Primary particles are emitted directly from natural sources including windborne dust, sea spray and volcanoes (Seinfeld and Pandis, 2006). In addition to these natural sources, anthropogenic activities such as fuel combustion and biomass burning, are known to directly emit particulates. Another source of atmospheric particles is their secondary formation as byproducts of chemical reactions. This secondary formation typically involves gas to particle conversion, whereby gaseous pollutants react to form particulate matter. Examples of particle formation from precursor gaseous species include the formation of ammonium chloride (NH_4Cl) from the reaction of ammonia (NH_3) and hydrochloric acid (HCl) (Wexler and Seinfeld, 1990). Another example is the oxidation of organics to form secondary organic aerosols (SOAs), where formation mechanisms are seldom well understood (Kroll and Seinfeld, 2008). Particles

can also form from condensation of volatile chemicals (hot vapours) upon encountering cold air (Canagaratna et al., 2007) and through the nucleation process, which leads to the formation of new particles (Seinfeld and Pandis, 2006).

In the atmosphere, the removal processes of atmospheric particulate matter are via dry and wet deposition. Dry deposition refers to particle deposition onto the Earth's surface while wet deposition refers to the scavenging of particles into fog, rain, snow and cloud droplets. Particle residence time is variable and is dependant on the size of the particle. Coarse particles have shorter residence times in the atmosphere ranging from minutes to days, while for fine particles the residence time is higher and is in the order of days to weeks (Seinfeld and Pandis, 2006).

Particles are typically characterized by their size, mass, surface, and volume distributions, as well as, their chemical composition. The size of particulate matter (PM) in the atmosphere ranges from 0.002 to 100 μm in diameter, however particles in the 0.002 to 10 μm are the most important due to their longer lifetime and subsequent health impacts. Based on their size, PM is divided into fine and coarse modes, where the former refers to PM less than 2.5 μm (defined as $PM_{2.5}$) and the latter refers to PM with diameters greater than 2.5 μm. Coarse and fine PM have different sources, formation and transformation mechanisms, optical properties, chemical composition, removal rates and deposition in human respiratory tract and other surfaces (Seinfeld and Pandis, 2006).

The fine particle mode can be further be divided into the nucleation, Aitken and accumulation modes. Particles in the nucleation mode have diameters up to 0.01 μm,

while those in the Aitken mode have a diameter range from 0.01 to 0.1 μm. Finally, the accumulation mode contains particles with diameters from 0.1 to 2.5 μm (Seinfeld and Pandis, 2006). Particles in the nucleation and Aitken mode dominate particle numbers in the atmosphere but account only for a few percent of particle mass due to their size. In the nucleation mode, particles are formed from condensation of volatile species as discussed above (Seinfeld and Pandis, 2006). Within the nucleation and Aitken modes, particles in the 0.005 - 0.035 μm are emitted from combustion sources, which includes vehicles and trucks, incineration processes and oil-fired boilers (see Finalyson-Pitts and Pitts, 1999, and references therein). For the range from 0.01 - 0.08 μm, the source of particles include gas to particle conversion, as well as the condensation of vapours emitted from combustion processes (Finalyson-Pitts and Pitts, 1999). Particles in the nucleation and Aitken modes are lost due to coagulation, which forms accumaltion mode particles (Seinfeld and Pandis, 2006).

The accumulation mode dominates the particle surface area and contributes significantly to the total particle mass. Particles in the accumulation range are formed from the coagulation of smaller size aerosol in the Aitken and nucleation modes (Seinfeld and Pandis, 2006). In addition, accumulation mode particles are formed from the growth of Aitken and nuclei mode particles due to nucleation of gases with low vapour pressure.

Aerosol chemical composition is complex and is a function of a wide variety of parameters including source, age, location, water content, temperature, emissions among others (Liggio, 2004). Finalyson-Pitts and Pitts (1999) reviewed the chemical composition in few categorized areas, some of which are given here. In continental areas, the

chemical composition of the fine aerosols include sulfates, ammonium, nitrate, chloride, organic and elemental carbon, while the larger aerosols in the coarse mode includes crustal elements such as Fe and Si. In the deserts, the aerosols contain Si, Al, Fe and Ca. In marine areas, the aerosols are composed of Na, Cl, Mg, Ca, SO_4, NO_3 and other sea salt aerosol components.

Some typical mass concentrations in the troposphere were summarised by Seinfeld and Pandis (2006). The average mass concentrations of fine particles observed were 4.8, 15 and 32 μg m^{-3} in remote areas, non-urban continental areas and urban areas respectively. Aerosol number concentrations are also variable, they range from few tens in the free troposphere and polar regions to $\sim 10^5$ in urban areas. This number is estimated to be $\sim 10^3$ and $\sim 10^4$ in non-urban continental and remote continental regions respectively (Finalyson-Pitts and Pitts 1999).

1.4.1 Importance of aerosols

Aerosols in the atmosphere have an adverse effect on human health as exposure to aerosol mass concentrations of 10 to 20 μg m^{-3} have been linked to increased mortality from cardiovascular and respiratory diseases (Canagaratna et al., 2007; Dockery et al., 1993; Pope et al., 2002; WHO, 2006). The composition of aerosols can also have a significant role as the number of ill people has been found to increase with elevated levels of $PM_{2.5}$ and $PM_{2.5}$ ${SO_4}^{2-}$ (Davidson et al., 2005; Dockery et al., 1993). Aerosols also impact the climate system through direct and indirect effects on Earths radiative balance; this impact is largely from fine particulate matter (IPCC, 2013).

The direct effects of aerosols on climate refers to aerosol-radiation interaction, where aerosols scatter or absorb shortwave and longwave radiation. The scattering or absorption is dependent on the composition of aerosols, which is a function of the parameters listed previously. The primary aerosol-radiation interaction is scattering of the solar radiation by aerosols, however, few components absorb solar radiation with black carbon (BC) being the strongest absorber. The indirect effects of aerosol on Earths radiative balance are often associated with the alteration of cloud and snow albedos. Aerosols can alter cloud albedo through the formation of cloud condensation nuclei (CCN) upon which small cloud droplets can form. An increase in the concentration of these small liquid droplets leads to brighter clouds and an increased cloud albedo. In the case of snow albedo, the deposition of BC aerosols on snow tends to decrease snows albedo as BC absorbs solar radiation (IPCC, 2013).

Radiative forcing (RF) refers to the net change in irradiance at the tropopause evaluated at constant temperatures and state for the surface and troposphere. Stratospheric temperatures is allowed to vary so as to achieve radiative equilibrium. The effect of aerosols on radiative forcing is highly variable and is dependent on aerosol composition, but a net cooling effect that offsets the warming effect of green house gases is widely accepted (IPCC, 2013). Figure 1.2[1] shows the radiative forcing values of different components including aerosols. The variability of aerosol RF values for different aerosol components is apparent from Figure 1.2 and is the single major factor in the

[1]The reproduction and reuse of Figure 1.2 is granted without the need for a written permission from the copyright holders (https : //www.ipcc.ch, accessed January 22, 2015).

uncertainty that relates to the total anthropogenic driving of climate change (IPCC, 2013).

Other adverse effects of aerosols include the enhancement of the deposition of pollutants onto ecosystems and significant reduction of visibility with high aerosol loading (Watson, 2002; Aiken et al., 2007; Canagaratna et al., 2007). For atmospheric scientists, the quantification of aerosol mass concentrations, composition and sizing are vital to understanding the chemical processes that take place in the atmosphere. These processed include the formation of PM from gaseous precursors and aerosol degradation by chemical reactions and UV to form radicals and organic compounds respectively. It then follows that the interaction of PM with gases in the atmosphere greatly impacts the composition of gases and PM in the atmosphere (Canagaratna et al., 2007; Kroll and Seinfeld, 2008). In the past couple of decades, significant research has been done on aerosol formation and transformation processes, however numerous processes remain poorly understood (Kroll and Seinfeld, 2008). In the following sections, we will discuss the formation mechanisms of particulate chloride (p-Cl), particulate sulfate (p-SO_4), particulate nitrate (p-NO_3) and particulate organics (pOM).

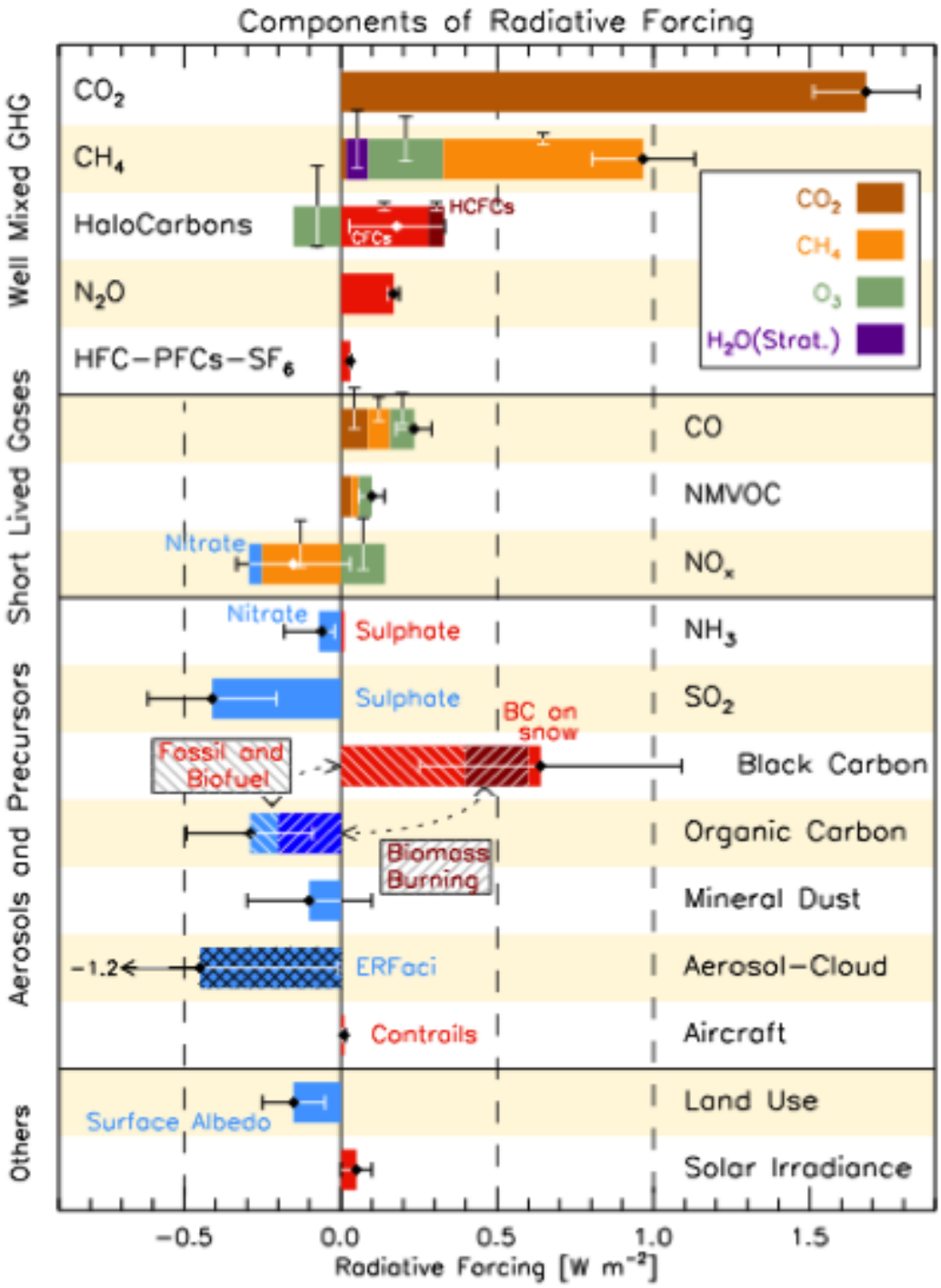

Figure 1.2: Radiative forcing of aerosols, greenhouse gases and other components. Variability of radiative forcing values among various aerosol components is apparent. Adapted from IPCC report, 2013.

1.4.2 Particulate chloride

[2]Particulate chloride (p-Cl) can be a major component in coastal and marine aerosols (Moya et al., 2002, and references therein). Sources of p-Cl are both primary and secondary in nature. Wind-induced bubble bursting at the ocean surface, which generates sea salt aerosols, is the most significant source of p-Cl on a global scale (Keene et al., 1999). Other primary sources of inorganic chloride, from crustal dust, refuse burning and biomass burning are insignificant by comparison (Keene et al., 1999). Secondary particulate chloride can arise from the reversible formation of ammonium chloride (NH_4Cl) in the solid (s) and aqueous (aq) phases. The following reaction shows the equilibrium of of NH_4Cl (s, aq) with its gaseous precursors hydrochloric acid (HCl) and ammonia (NH_3):

$$HCl(g) + NH_3(g) \rightleftharpoons NH_4Cl(s, aq) \qquad (R\,1.42)$$

Ammonia is the only significant base in the troposphere and typically neutralizes atmospheric acids (Finalyson-Pitts and Pitts, 1999). Sources of ammonia include livestock waste and fertilizer. Lower emissions are expected from industrial sources, burning of agricultural waste and natural processes in the soil (see Finalyson-Pitts and Pitts, 1999, and references therein). In California, where our aerosol formation study took

[2]Disclaimer: This section was published as part of a journal article entitled "Separating refractory and non-refractory particulate chloride and estimating chloride depletion by aerosol mass spectrometry in a marine environment" authored by Ibraheem Nuaaman et al (2015). This journal article was published in Atmospheric Chemistry and Physics Discussions Journal in January of 2015. Copernicus Publications is the publisher of this work, which is licensed under the Creative Commons Attribution 3.0 License. Under this license, an explicit permission from Copernicus Publications to reproduce, reuse and reprint this published work is not required. For more details, the reader can visit the publisher's copyright webpage at http : //www.atmospheric − chemistry − and − physics.net, accessed on January 23rd, 2015.

place, the regional sources of NH_3 arise mainly from dairy farms and automobiles that are equipped with three-way catalytic converters (Neuman, 2003; Docherty et al., 2008; Livingston et al., 2009; Nowak et al., 2012; Hersey et al., 2013).

HCl is emitted directly in the atmosphere from biomass burning, coal combustion and waste incineration (Andreae et al., 1996; McCulloch et al., 1999; Ianniello et al., 2011). Significant amounts of gaseous HCl are also produced from acid displacement of chloride from sea salt aerosols. This acid displacement is driven by nitric acid, sulfuric acid (Finalyson-Pitts and Pitts, 1999; Keene et al., 1999), nitric acid anhydride, N_2O_5 (McLaren et al., 2004) and organic acids (Laskin et al., 2012). The displacement by HNO_3 and H_2SO_4 is particularly important during the daytime, since they are formed from the photo-oxidation of nitrogen and sulfur oxides respectively (see sections 1.4.3 and 1.4.4). At night, however, N_2O_5, can contribute significantly to acid displacement and subsequent formation of HCl. Some of the HCl can repartition into the aerosol through reaction with ammonia and/or dissolve in hygroscopic aerosols directly in environments with high relative humidity, such as marine environments, especially if the aerosols are non-acidic in nature (Keene et al., 1999; Kim et al., 2008).

In reaction R 1.42, the formation of particle phase NH_4Cl is dependent on temperature, relative humidity (RH), aerosol chemical composition, and the partial pressures of both HCl and NH_3. The formation of NH_4Cl(s,aq) is favourable under conditions of low temperatures and high RH (Pio and Harrison, 1987; Wexler and Seinfeld, 1990; Matsumoto and Tanaka, 1996; Trebs et al., 2005; Ianniello et al., 2011). Furthermore, the partitioning of NH_4Cl to the aerosol phase is reported to be dependent on the avail-

ability of excess NH_3 after the neutralization of H_2SO_4 to form $(NH_4)_2SO_4$, since the affinity of NH_3 for H_2SO_4 is higher than its affinity for HCl (Trebs et al., 2005; Ianniello et al., 2011).

The HCl released during acid displacement (see Finlayson-Pitts and Pitts, 1999, and references therein) is a significant sink of sea salt chloride (ss p-Cl) (Keene et al., 1999). The released HCl can lead to halogen activation since HCl can react with OH, to form chlorine atoms in the gas phase, as follows:

$$HCl + OH \longrightarrow Cl + H_2O \qquad (R\,1.43)$$

Other secondary sources of HCl include the reaction of chlorine atoms with methane and other VOCs (Kim et al., 2008; Mielke et al., 2011). Recall from section 1.2.4 that chlorine atoms are formed from the photolysis of nitryl chloride and molecular chlorine (Osthoff et al., 2008; Roberts et al., 2008; Riedel et al., 2012).

1.4.3 Particulate sulfate

Sulfate (p-SO_4) is a major component of particulate matter in the troposphere. Natural sources of sulfate include volcanic emissions, mineral dust and oceans, where dimethyl sulfide (DMS) is produced by marine phytoplankton and is a source of SO_4. The anthropogenic sources include fossil fuel combustion, biomass burning and the oxidation of sulfur dioxide. The latter is primarily emitted by oil and coal combustion (Chin and Jacob, 1996; Seinfeld and Pandis, 2006; Ianniello et al., 2011).

The secondary formation of particulate sulfate typically involves the formation of

sulfuric acid from the gas phase oxdiation of SO_2. Sulfuric acid is produced via SO_2 oxidation by OH radical and subsequent reactions with O_2 and H_2O (Seinfeld and Pandis, 2006; Ianniello et al., 2011):

$$SO_2 + OH + M \longrightarrow HOSO_2 + M \quad \text{(R 1.44)}$$

$$HOSO_2 + O_2 \longrightarrow SO_3 + HO_2 \quad \text{(R 1.45)}$$

$$SO_3 + H_2O + M \longrightarrow H_2SO_4 + M \quad \text{(R 1.46)}$$

Particulate sulfate is formed from the binary homogeneous nucleation of sulfuric acid and water (see Finalyson-Pitts and Pitts, 1999, and the references therein). In the presence of NH_3, p-SO_4 is produced via the following reactions (see for example Seinfeld and Pandis; Ianniello et al., 2011):

$$H_2SO_4(g) + NH_3(g) \rightleftharpoons NH_4HSO_4(s) \quad \text{(R 1.47)}$$

$$NH_4HSO_4 + NH_3(g) \rightleftharpoons (NH_4)_2SO_4(s) \quad \text{(R 1.48)}$$

Another solid phase compound ($(NH_4)_3H(SO_4)_2$) is also known to be formed from the reactions of H_2SO_4 and NH_3. The relative formation of solid phase NH_4HSO_4, ($(NH_4)_3H(SO_4)_2$) and $(NH_4)_2SO_4$ is dependant on the availability of NH_3 in ambient air (Seinfled and Pandis, 2006).

Further to the mechanism above, aqueous processing of SO_2 leads to the formation of sulfates. This mechanism is as follows (Finalyson-Pitts and Pitts, 1999; Seinfeld and Pandis, 2006; Ianniello et al., 2011):

$$SO_2(g) + H_2O \leftrightarrow SO_2 \cdot H_2O(aq) \quad \text{(R 1.49)}$$

$$SO_2 \cdot H_2O(aq) \leftrightarrow HSO_3^-(aq) + H^+(aq) \quad \text{(R 1.50)}$$

$$HSO_3^-(aq) \leftrightarrow SO_3^{2-}(aq) + H^+(aq) \quad \text{(R 1.51)}$$

$$SO_3^{2-}(aq) + O_3 \longrightarrow \text{sulfates} \quad \text{(R 1.52)}$$

In reaction R 1.52 the oxidation of SO_3 can also occur through reactions with hydrogen peroxide, iron and manganese.

An important formation mechanism for H_2SO_4 is the oxidation of dimethyl sulfide (DMS), the dominant formation mechanism is as follows (Seinfeld and Pandis, 2006):

$$CH_3SCH_3 + OH \longrightarrow CH_3SCH_2 + H_2O \quad \text{(R 1.53)}$$

$$CH_3SCH_2 + O_2 + M \longrightarrow CH_3SCH_2O_2 + M \quad \text{(R 1.54)}$$

$$CH_3SCH_2O_2 + NO \longrightarrow CH_3SCH_2O + NO_2 \quad \text{(R 1.55)}$$

$$CH_3SCH_2O \longrightarrow CH_3S + HCHO \quad \text{(R 1.56)}$$

In environments with significant NO_x levels, CH_3S radical react with O_2 but also may react with NO_2 and O_3:

$$CH_3S + O_2 + M \longrightarrow CH_3SO_2 + M \quad \text{(R 1.57)}$$

$$CH_3SO_2 \longrightarrow CH_3 + SO_2 \quad \text{(R 1.58)}$$

Sulfur dioxide can then form H_2SO_4 and p-SO_4 from reactions R 1.44 through R 1.48 above.

1.4.4 Particulate nitrate

Particulate nitrate (p-NO_3) is formed directly from natural and anthropogenic sources. Natural sources of nitrate are soil and lightning, while anthropogenic sources include the combustion of fossil fuels, biomass burning and gas to particle conversion (Ianniello et al., 2011). The secondary formation of $p-NO_3$ involves nitric acid and ammonia, this equilibrium reaction is as follows:

$$HNO_3(g) + NH_3(g) \rightleftharpoons NH_4NO_3(s, aq) \quad \text{(R 1.59)}$$

Similar to NH_4Cl, the formation of NH_4NO_3 is favourable under condition of low temperatures and high relative humdity (Pio and Harrison, 1987; Wexler and Seinfeld, 1990; Matsumoto and Tanaka, 1996; Trebs et al., 2005; Ianniello et al., 2011).

Nitric acid is primarily formed from the oxidation of NO_2 by hydroxyl radical:

$$NO_2 + OH + M \longrightarrow HNO_3 + M \quad \text{(R 1.60)}$$

Another reaction pathway that forms HNO_3 involves a surface reaction of NO_2 with H_2O (Finalyson-Pitts and Pitts, 1999). This reaction is as follows:

$$2\,NO_2 + H_2O \leftrightarrow HONO + HNO_3 \quad \text{(R 1.61)}$$

:

At night, the formation of HNO_3 can proceed via the oxidation of VOCs by nitrate radical, as well as the hydrolysis of NO_3 and N_2O_5 to form HNO_3. these reactions are as follows:

$$NO_3(g) + RH \longrightarrow HNO_3(g) + R^{\cdot} \quad \text{(R 1.62)}$$

$$NO_3(aq) + H_2O(l) \longrightarrow HNO_3(aq) + OH(aq) \quad \text{(R 1.63)}$$

$$N_2O_5(g) + H_2O(g, l) \longrightarrow 2\,HNO_3(g, aq) \quad \text{(R 1.64)}$$

1.4.5 Particulate organics

Particulate organic matter (pOM) consitutes a significant fraction of the total particulate mass in the atmosphere. In mid-continental altitudes this fraction is $\sim$ 25 - 50 % and could reach 90% in tropical forested areas (see Kanakidou et al., 2005, and references therein). There are two classifications for pOM in the atmosphere, elemental carbon (also called graphitic, black carbon and free carbon) and organic carbon (Seinfeld and Pandis, 2006). Elemental carbon is emitted solely from combustion processes and therefore only has primary sources. Organic carbon is formed from primary and secondary sources, which will be covered in this section.

Primary sources of pOM constitute fossil fuel burning (associated with power generation and transportation sectors), domestic heating and cooking and biomass burning (Kanakidou et al., 2005). In marine areas, wind-induced bubble bursting can be a significant source of pOM especially in the fine particle mode (O'Dowd et al, 2004; Faccini et al, 2008; Ovadnevaite et al, 2011; Quinn et al 2014). Other primary sources of organic aerosol include plant debris, fungi, viruses and bacteria.

Secondary organic aerosol (SOA) is primarily produced from the oxidation of precursor VOCs by OH, O_3, NO_3 and Cl radicals (Kanakidou et al., 2005; Seinfeld and Pandis, 2006; Kroll and Seinfeld, 2008). This pathway can decrease the product's

volatility by adding functional groups. A compound with sufficiently low saturation vapour pressure can then condense forming SOAs. This oxidation can also increase the volatility of VOCs through carbon-carbon bond cleavage to form carbon monoxide, low molecular weight aldehydes, ketones, and carboxylic acids (Kroll and Seinfeld, 2008). A non-oxidative pathway for the formation of SOAs in the atmosphere has also been reported. This pathway proceeds through polymeric or oligiomeric association in what is known as an accretion reaction (Kroll and Seinfeld, 2008). An addition of two carbons lowers the compound's volatility by an order of magnitude and so these accretion reaction are a significant formation mechanism for the production of SOAs (Liggio et al., 2004; 2005; Kroll and Seinfeld, 2008).

Finally in the particle phase, the volatility and chemical composition of pOM can change due to oxidative "aging" reactions and other condensed phased reactions such as oligomeric formation (Liggio et al., 2005). Similar to gas phase oxidation, the oxidation is by atmospheric radicals (OH, O_3 and NO_3) and can lead to increased or decreased volatility due to the addition of functional group or carbon-carbon bond cleavage respectively (Kroll and Seinfeld, 2008).

1.4.6 Seawater particulate organics

Sea salt aerosols are composed of inorganic, organic and biological components (Ovadnevaite et al, 2011). This complex composition includes inorganic sea salt and non sea salt sulfate, as well as mixtures of water-soluble and water-insoluble organic compounds (Ovadnevaite et al, 2011; Quinn et al., 2014). Sampling North Atlantic sea-

water during periods of high biological activity (phytoplankton blooms), Faccini et al (2008) reported an organic fraction that increases from 3±0.4% to 77±5% with decreasing diameter from 8 to 0.125 μm respectively and ranges from 3±0.4% reaching 77±5% of the primary submicron marine aerosols measured in laboratory and field measurements. This organic fraction was dominated by water-insoluble OC, which accounted for 94 ± 4% of sea spray aerosols on average.

Investigating air masses originating from the North Atlantic during periods of high biological activity, O'Dowd et al (2004) reported a dominance of total organic compounds in marine aerosol in the 0.06 - 0.5 μm size range. This dominance was size dependent increasing with decreasing aerosol size and reaching 83% for the fine mode with size range of 0.06 - 0.125 μm. A study by Quinn et al (2014) reported a $\sim$ 50% average mass fraction for organic compounds in nascent sea spray aerosols < 0.18 μm from the North Atlantis. The average organic mass fraction was consistent in regions with high and low biological activity. Note that chlorophyll a was used as a proxy for biological activity.

Marine aerosols are injected into the atmosphere as a result of wave action on the ocean surface. This wind-driven wave action entrains air, which leads to bubble formation. The bubbles then rise to the ocean surface and burst into small droplets, which end up as aerosols in the air (Finalyson-Pitts & Pitts, 1999; Bates et al., 2012). Furthermore. dissolved organics can adsorb on the bubbles upon rising to the ocean surface.

There are two types of droplets that are injected into the air, namely jet drops and

film drops. Jet drops are formed from the jet of water, which rises from the bottom of the bursting bubble. Film drops, however, are produced from the breaking of the liquid film encapsulating the bubble (see Finalyson-Pitts & Pitts, 1999 and the references therein).

1.5 Effect of land-sea/lake circulation on pollutant concentrations

The air circulation between land and a large body of water has a significant effect on the pollutant levels in areas adjacent to an ocean or a lake. This effect was observed in Toronto (Hastie et al., 1999; Wentworth et al., 2015), Hastings (Hastie et al., 1999), southwestern Ontario (Makar et al., 2010; Levy et al., 2010; Sills et al., 2011), soutwestern British Columbia (Brook et al., 2004), Los Angeles (Blumenthal et al., 1978), Athens (Kambezidis et al., 1998), Taiwan (Cheng, 2002), Portugal (Evtyugina et al., 2006), Mexico (Baumgardner et al, 2006 a, b).

Figure 1.3 shows an idealized circulation of sea or lake breeze, as well as land breezes. The sea/lake-land breeze results from a temperature differential between the water body and adjacent coastal lands that is caused by the larger heat capacity of water. As a result of this thermal contrast, the air temperature above the land is higher than water during the day and that above the water is higher than land during the night. It then follows that the air pressure far above the surface of the land will be higher during the day and the flow of air (above the surface) will be from the land to the lake/sea. This

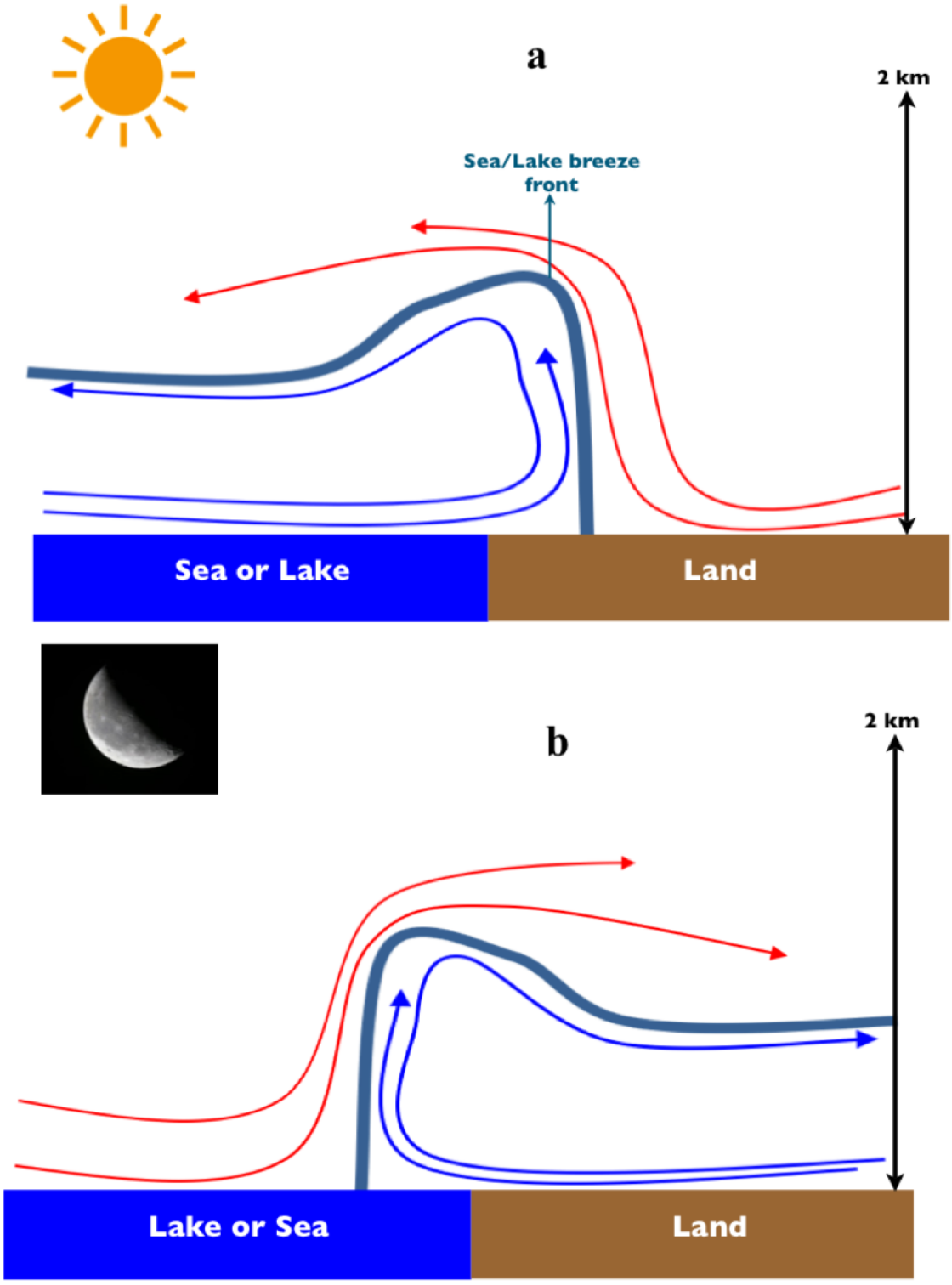

Figure 1.3: Vertical cross section of a) sea or lake breeze circulation and b) land breeze circulation.

flow decreases the mass of the air column over the land and the pressure of the air over the lake will be higher at the surface, which causes the air to flow from the lake/sea to the land (lake/sea breeze). During the night time, the land is cooler than the lake and the reverse circulation is observed (land breeze). The air over the lake is confined to a shallow inflow layer at the surface with a height of 500 m or less, which is a result of the denser air over the lake than over land. At the edge of the denser air is a convergence, which forms as a result of the higher wind speed in the inflow layer when compared to rate of lake breeze inland penetration. This convergence causes a compression of temperature, moisture and wind gradients, which form a lake/sea breeze front. Lake breeze inland penetration is typically few tens of kilometres but was reported to exceed 200 km in southwestern Ontario in select cases. The stability of the lake breeze front is a function of air temperature (Hastie et al., 1999; Sills et al, 2011; Wentworth et al., 2015).

Ozone concentrations were observed to increase by 20-30 ppb with the passage of lake breeze fronts in Hastings and at York University in Toronto in the summers of 1992-1994 (Hastie et al., 1999). More recently, Wentworth et al (2015) reported an increase of $\sim$20 ppb in Toronto on lake breeze days when compared to non-lake breeze days in May-September of 2010-2012. Ozone formation was reported to be higher over the Great lakes when compared to adjacent lands in southwester Ontario during the BAQS-Met study (Makar et al., 2010; Levy et al., 2010). In southwestern Ontario during the BAQS-Met study, Hayden et al (2011) reported an enhancement in the formation rates of particulate sulfate and secondary organic aerosols with lake breeze

circulation. In Los Angeles, the highest ozone concentrations were observed ahead a sea breeze front (Blumenthal et al., 1978)

Studying the Great Lakes in southwestern Ontario during the Border Air Quality and Meterology Study (BAQS-Met), Brook et al (2013) summarised three processes where the lakes enhanced the contribution of local emissions to O_3 formation. All three processes involve the entrapment of pollutants in a smaller volume above the lake. In the first process, O_3 and its precursors are confined within a shallow layer above the cool lake. This allows for the enhancement of O_3 secondary formation and a decrease of its sinks due to dry deposition and NO titration over the lake when compared to its land counterparts.

The horizontal and vertical entrapment of O_3 and its precursors constitute the second and third process respectively (Brook et al., 2013). These two processes involve a horizontal or vertical convergence zone that is close to an anthropogenic emission source. Horizontal convergence can occur when lake breezes encounter each other or the synoptic flow. The entrapment will lead to an enhanced O_3 formation and can transport O_3 and its precursors horizontally and/or vertically based the position of the convergence zone or lake breeze fronts.

The carbonyl and aerosol measurements and analysis presented here are from the BAQS-Met (Brook et al., 2013) and CalNex (The research at the nexus of air quality and climate change; Ryerson et al., 2013) studies. Carbonyls were measured in southwestern Ontario during the BAQS-Met study while aerosol measurements took place along the coast of California during the CalNex study. In both studies, frequent occurrences of

lake/sea breezes and land breezes took place. The effect of lake breeze on carbonyls during BAQS-Met and land breeze (continental outflow) on aerosols during CalNex constitute one the main objectives of this study; this effect was investigated and will be discussed.

1.6 Thesis objectives

This dissertation is of two parts, the first is an investigation of gaseous carbonyl measured using an automated high performance liquid chromatography system (AT-DNPH-HPLC) during the BAQS-Met study in 2007. The AT-DNPH-HPLC will be covered in Chapter 2, whereas the results obtained and a discussion of the results will be covered in Chapter 3. In the second part of this dissertation, we will discuss submicron aerosol concentrations and composition measured using a high-resolution time-of-flight aerosol mass spectrometer (HR-AMS) during the CalNex study measurements along the coast of California. A detailed description of the HR-AMS will be covered in Chapter 4. The results from the CalNex study will be presented and discussed in Chapter 5.

The motivation of this study is to the investigate the effect of air-sea/lake circulation (Section 1.5) on carbonyl and particle concentrations, as well as particle composition. More specifically, the objectives for the BAQS-Met carbonyl study are as follows:

1. Establish the effects of trans-boundary transport (Section 3.9) and lake breeze events on carbonyl concentrations (Section 3.12)

2. Determine the sources and sinks of carbonyls in southwestern Ontario (Sections

3.4 through 3.6)

3. Investigate the contribution of anthropogenic and biogenic precursors to carbonyl formation (Section 3.8)

4. Establish local ozone sensitivity (Section 3.10) and the contribution of carbonyls towards tropospheric ozone formation (Section 3.11)

The objectives for the CalNex submicron aerosol study were as follows:

1. Establish the effects of sea breeze and land breeze circulations on the concentrations and composition of submicron aerosols (Section 5.5)

2. Determine the effects of sampling sea salt chloride on the chloride signal measured by the HR-AMS (Sections 5.6 and 5.7)

3. Establish a method to deconvolve the chloride signal into its sea salt and non-sea salt components (Section 5.8)

4. Determine the effects of pH, temperature and RH on non refractory chloride measured by the HR-AMS (Sections 5.12 and 5.13)

5. Characterize the organic pOM signal in sea spray aerosols (Section 5.14)

In addition to the objectives outlined above, this dissertation will cover the relative contribution of carbonyls to the to non-methane hydrocarbon distribution and to the reactivity of the air mass (Section 3.3) during the. This dissertation will cover methods proposed to estimate non-refractory chloride (Section 5.8), sea salt chloride (Section

5.9), total chloride (Section 5.9) and total sea salt (Section 5.10) in submicron aerosols using AMS measurements. Finally this dissertation will cover a method to establish chloride depletion strictly using AMS measurements (Section 5.11).

2 An automated High Performance Liquid Chromatography System (AT-DNPH-HPLC) for the measurement of gaseous carbonyls

Several analytical measurement techniques are utilized for the measurement of atmospheric gaseous carbonyls. These include differential optical absorption spectroscopy for HCHO and glyoxal (MacDonald et al., 2012), laser induced fluorescence (Hottle et al., 2009), Fourier transform infrared spectroscopy (Tuazon et al., 1978), Tunable Diode Laser spectroscopy (Harris et al., 1989) and the Hantzsch method (Nash, 1953; Kelly et al., 1994) for the measurement of HCHO. Formaldehyde and acetone+methyl vinyl ketone are measured using the proton-transfer-reaction mass spectrometry (PTR-MS) method (Lindinger et al., 1998; Vlasenko et al., 2010). Column densities of HCHO and glyoxal have been measured using the Scanning Imaging Absorption Spectrometer for Atmospheric Cartography (SCIAMACHY) satellite instrument (Wittrock et al., 2006).

A widely used analytical method is the use of packed cartridges coated with a derivatizing agent that is 2,4-dinitrophenylhydrazine (DNPH), which is typically coupled with a High Performance Liquid Chromatography (HPLC) instrument (D. Grosjean, 1982;

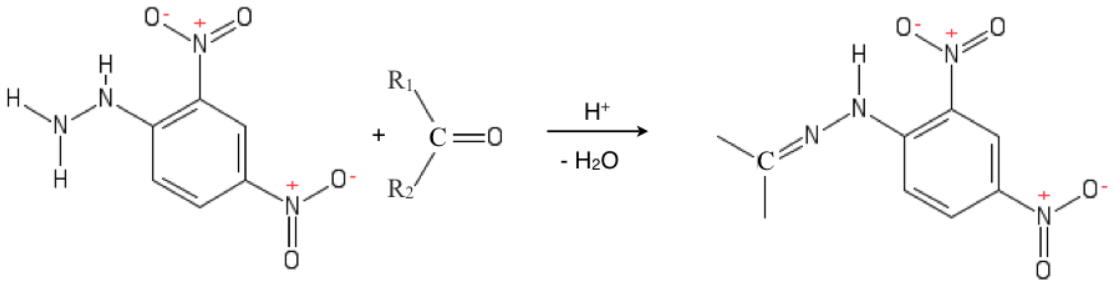

Figure 2.1: Reaction mechanism of carbonyls and 2,4-dinitrophenylhydrazine for the formation of a carbonyl hydrazone.

.

Shepson et al., 1991; E. Grosjean et al., 1999; Christensen et al., 2000; Possanzini et al., 2000, 2002, 2007; D. Grosjean et al., 2001; Aiello, 2003; Héllen, 2007; Wang, 2007; Aiello and McLaren, 2009). The reaction of a R_1-CO-R_2 carbonyl derivatization with acidified DNPH is shown in Figure 2.1. This is a nucleophilic addition-elimination reaction, where NH_2 adds to the C=O group and a H_2O molecule is removed. This reaction is also a condensation reaction, with the joining of two molecules and a loss of a small molecule that is H_2O. This reaction is universal for all carbonyls (Wade, 2002) and specific for carbonyl compounds (Uchiyama et al., 2011); i.e DNPH does not react with carboxylic acids, esters and amides. The carbonyl-DNPH hydrazone formed (in Figure 2.1) is strongly absorbent in the UV region of the spectrum from 292-473 nm (Aiello and McLaren, 2009). In this study we utilized an automated HPLC system (AT-DNPH-HPLC), where an HPLC was coupled to an automated DNPH derivitization system. This system was developed and published previously (Aiello, 2003; Wang, 2007; Aiello and McLaren, 2009).

2.1 Principle of operation

Figure 2.2 is a schematic of the AT-DNPH-HPLC system, which was used to measure six C_1-C_4 aliphatic gaseous carbonyls in ambient air and laboratory studies. This system consists of an HPLC, silica packed stainless steel cartridge, three valves (A, B and C), three reservoirs and a helium tank. The system is connected to a vacuum pump and a 500 SCCM calibrated mass flow controller (MFC). The HPLC is a commercial Agilent HP1100 which consists of a vacuum degasser, a dual high pressure pump, a column thermal compartment and a variable wavelength detector (VWD). The detector was set on 360 nm wavelength for the quantification of formaldehyde, acetaldehyde, acetone, propanal, methyl ethyl ketone and butanal. The use of the 360 nm wavelength for the aliphatic carbonyls is consistent with multiple other studies (Grosjean, 1982; E. Grosjean, 1999; Christensen et al., 2000; Possanzini et al., 2000; 2002; Pal and Kim, 2007; Uchiyama et al., 2011). The chromatographic column used is Discovery HS C18 that is 15 cm long with a 2.1 mm internal diameter and is packed with 3 μm sized particles. A guard column and an inlet filter (0.5 μm frit that is 2.11 mm long) were installed upstream of the chromatograhic column to removal particulate impurities. The mobile phase used composed of HPLC grade acetonitrile (ACN) and HPLC grade water. The mobile phase used was 65% ACN/35% H_2O from 0-20 min followed by a linear increase to 100% ACN from 20-45 min and then 100% ACN from 45-49 min. In order to ensure the complete removal of all analytes from run to run, the chromatographic column was continuously flushed with 100% ACN during the air sampling time from 49-120 min;

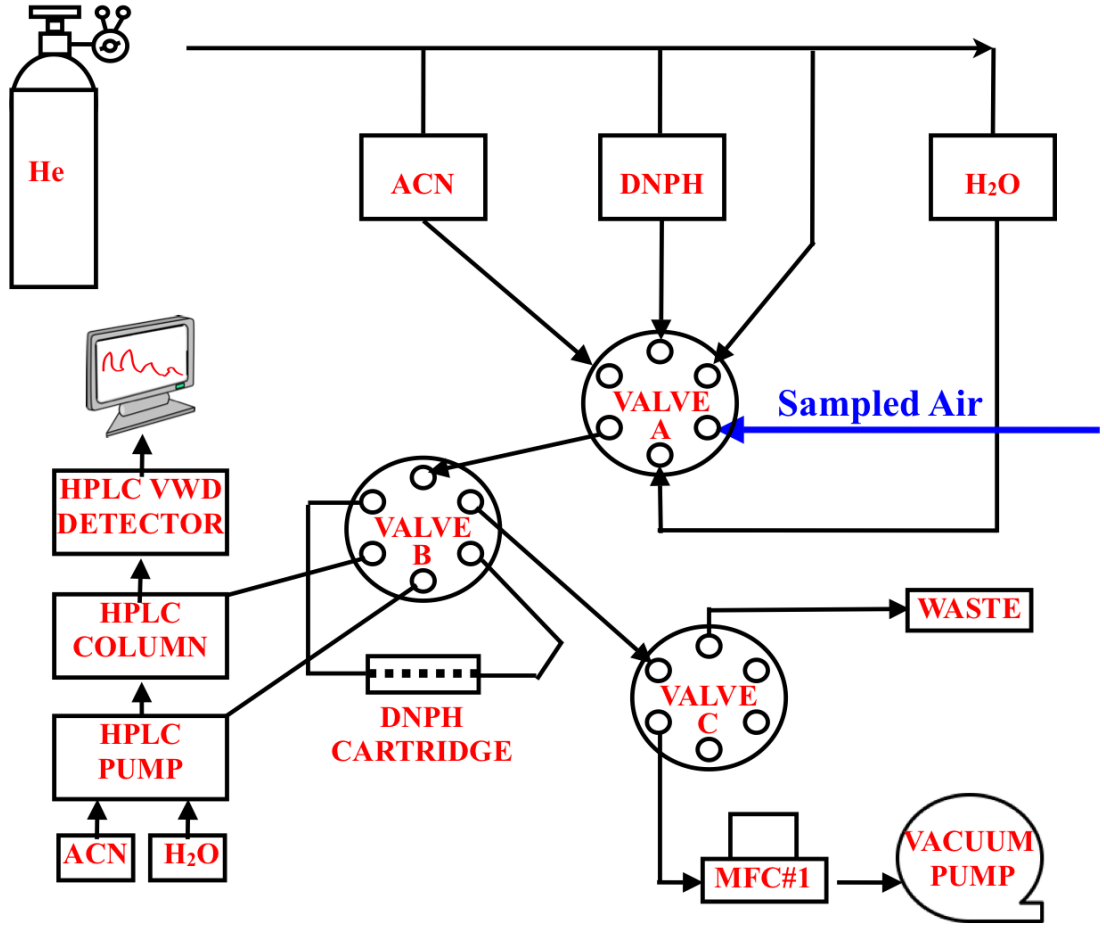

Figure 2.2: Schematic of the AT-DNPH-HPLC system used for measurements of gaseous carbonyls.

.

details of the sampling time will follow. A commercial potassium iodide (KI) ozone trap was placed upstream of the AT-DNPH-HPLC system to eliminate ozone from ambient air. Ozone causes a degradation of DNPH and carbonyl-DNPH hydrozones. This degradation results in the underestimation of carbonyl concentrations (Herrington and Hays, 2012; Ho et al., 2013).

The AT-DNPH-HPLC system (Figure 2.2) is equipped with a stainless steel car-

tridge that is 25 mm long with 3.5 mm i.d. and a total volume of 240 μL. This cartridge is packed with 250-381 μm irregular-shaped porous silica and contains two stainless steel screens and two teflon gaskets to hold the silica packing material in place. This system has three sampling valves (VICI® Valco Instruments); valve A is a 1/16" 6-port multi-position valve while valves B and C are 1/16" 6-port two-position valves. The three reservoirs hold HPLC-grade acetonitrile (ACN; Caledon Laboratories), HPLC grade H_2O (Fisher Scientific) and acidified DNPH solution. The crude DNPH (Sigma-Aldrich) is thrice recystallized from ACN under sealed condition and acidified to a pH of 3 with H_2SO_4; the final concentration of the DNPH solution used was 0.02 M. Helium gas was used as the driving pressurized force to flow the solutions through the cartridge as we will discuss shortly; and provided a blanket for the DNPH system to prevent contamination from ambient air.

The AT-DNPH-HPLC system uses a serial valve interface device (SVI) to control the position of the valves. The SVI device changes the position of the valves such that the cartridge goes through the following steps (Figure 2.3). The duration for each step is shown in brackets:

1. Cartridge cleaning (7 s): Cartridge is cleaned with ACN to ensure the complete removal of DNPH and carbonyl-hydrazones from previous runs

2. DNPH loading (5 s): Fresh 0.02 M DNPH is loaded for subsequent derivatization of carbonyls

3. Helium drying (30 s): Helium is passed through the cartridge to ensure no liquid

DNPH is left on the cartridge as only the DNPH coating is desired

4. Air sampling (70 min): Sampled air is passed through the cartridge at 300 SCCM

5. Cartridge filling (2 s): Cartridge is filled with H_2O to ensure that no gases get into the HPLC system, which could damage the column, hinder the separation and introduce noise into the chromatogram

6. Elution & analysis (49 min): HPLC mobile phase goes through the cartridge, enabling it to back flush all the carbonyl hydrazones and injecting them into the HPLC for separation

In these 6 steps, cartridge loading was controlled by applying constant helium pressure (30 psi) for a very specific amount of time. The AT-DNPH-HPLC system allows for online continuous measurements with minimum user input. In this study, the time resolution was 120 minutes, 70 minutes of which were for the sampling and 49 minutes for analysis. One minute was for cartridge cleaning, DNPH loading, He drying and cartridge filling, as well as a short wait time of 18 seconds at the end of each run after step 6

In the analysis step, the sample is delivered to the C18 chromatographic column for separation and unto the VWD detector which measures the absorbance of the seperated analytes. The VWD is composed of a deuterium lamp, a flow cell and a built-in holmium oxide optical filter. The deuterium lamp operates with high intensity and low detection limit in the 190-600 nm wavelength range, which covers our wavelength of choice at 360 nm. The dimensions of the flow cell used in the detector are 10 mm for length

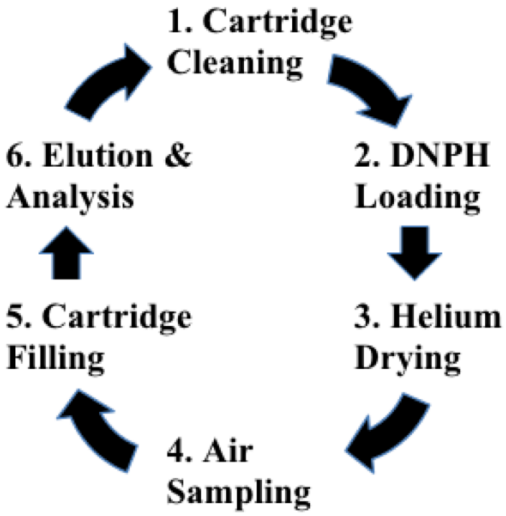

Figure 2.3: Sample chromatogram obtained using the AT-DNPH-HPLC system.

.

and 14 μl for volume. The holmium oxide filter allows for rapid verification of the wavelength accuracy. The detector measures the attenuation of the light intensity due to the absorption of light by the analytes. The relationship between absorbance (A), the light intensity entering the flow cell (I_0 and the light exiting the cell (I) is governed by the Beer-Lambert law:

$$A = -log_{10}\frac{I_0}{I} = \varepsilon cl \tag{2.1}$$

The absorbance signal is then plotted as a function of time in a chromatogram. Figure 2.4 shows a sample chromatogram obtained using the AT-DNPH-HPLC system. The largest peak in the chromatogram is that of leftover DNPH. Peak identification and mixing ratio determination for the six quantified carbonyls will be covered in the following sections.

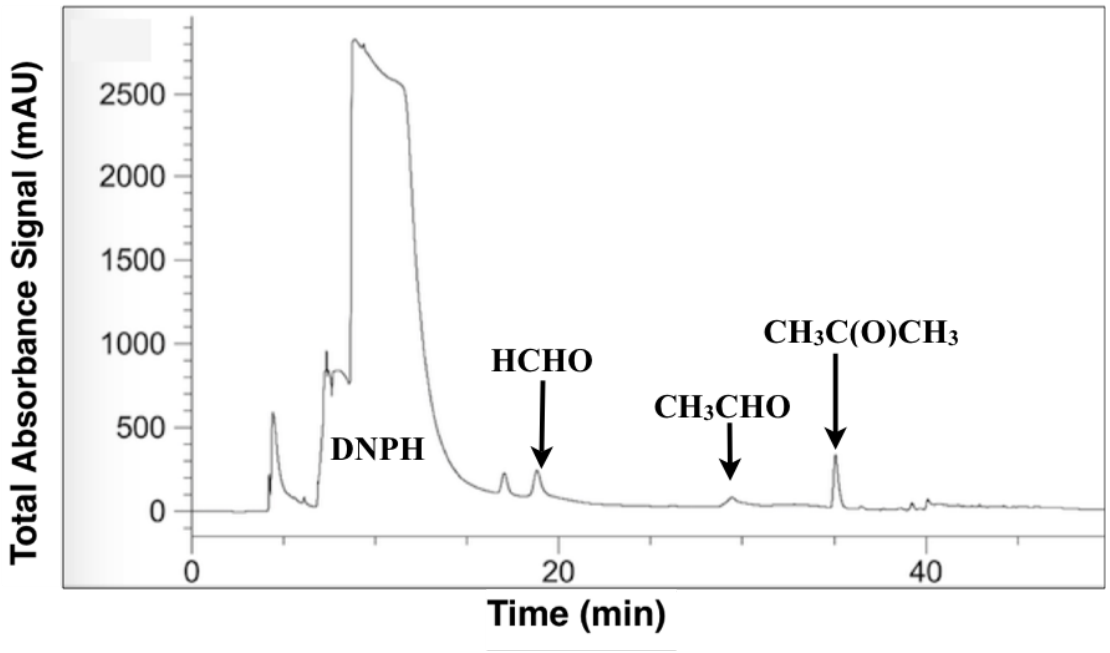

Figure 2.4: Sample chromatogram obtained using the AT-DNPH-HPLC system.

.

2.2 AT-DNPH-HPLC calibrations

Gas and liquid phase calibrations were performed to identify the different carbonyl peaks in the chromatograms, establish response factors (in peak area/nmol) for the carbonyl-DNPH hydrazones and determine the cartridge collection efficiency for all the carbonyl compounds. Peak identification, response factors and collection efficiencies are essential for the quantification of carbonyl concentrations. In his section, we will cover the procedure and results associated with these calibrations.

2.2.1 Gas Phase Calibrations

Gas phase calibration were performed for peak identification, which utilized characteristic chromatographic retention times of carbonyl-DNPH compounds. Gaseous carbonyls were generated using the standard gas generation system (SGGS). A schematic of the SGGS system is shown in Figure 2.5 (Wang, 2007). A syringe pump was used to inject known concentrations of liquid carbonyls into the mixing bulb at a steady predetermined rate. A high flow of AADCO zero air was used to rapidly and efficiently evaporate the carbonyl solution; and this flow was controlled with a with a 20000 SCCM MFC. Zero air was passed through a water bubbler to generate humid air (RH was 40-50%) and create ambient-like conditions before evaporating the carbonyl solution. The SGGS was connected to the AT-DNPH-HPLC system, which was operated in the same exact way as described previously when sampling ambient air during this study.

Table 2.1 shows the retention times obtained from the gas phase calibrations using the SGGS system. Also shown are the relative retention times, which are the retention times relative to that of the well resolved acetone-DNPH. The retention times and relative retention times were used to identify the peaks in ambient chromtograms such as those shown in Figure 2.4. Both the retention times and the relative retention times show clear overlaps between gas phase calibrations and ambient data. The relative retention times are important parameters for peak identification especially in the case of a shift in carbonyl retention times between runs. The maximum shift in retention time was 30 seconds for ambient data analyzed in this study.

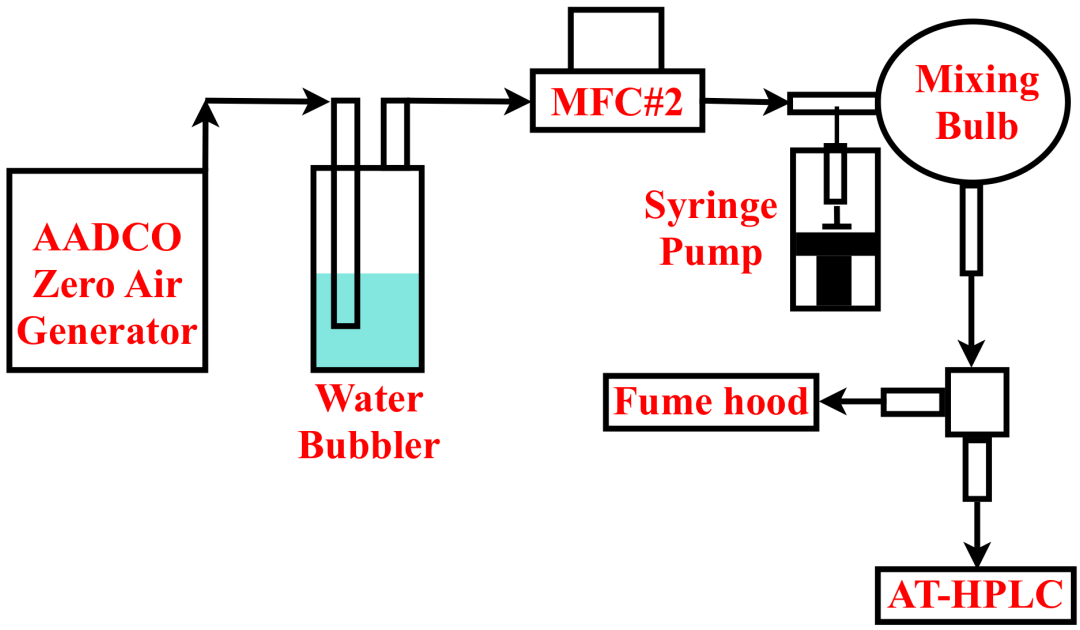

Figure 2.5: Schematic of the standard gas generation system used for peak identification.

.

Each carbonyl showed one peak except methyl ethyl ketone, which showed two distinct peaks (Table 2.1). Methyl ethyl ketone is an unsymetrrical ketone, which upon derivitization with DNPH forms syn and anti isomers as shown in Figure 2.6 (Grosjean et al., 1999). In Figure 2.6 the Y group refers to the (2,4-dinitrophenyl)amino substituent, which is -NH-$C_6H_3(NO_2)_2$. For unsymmetrical carbonyl derivatives, the syn and anti isomers could co-elute given their similar chromatographic properties or could give rise to two chromatographic peaks as is the case with MEK in this study.

Table 2.1: Retention times and relative retention times of carbonyl-DNPH derivatives established through gas phase calibrations[a]. The mobile phase used was 65% ACN/35% H_2O from 0-20 min followed by linear increase to 100% from 20-45 min and 100% ACN from 45-49 min.

Carbonyl	Retention Time (min)	Relative Retention Time[a]
Formaldehyde	18.0	0.520
Acetaldehyde	28.6	0.820
Acetone	35	1.00
Propanal	36.5	1.04
Methyl Ethyl Ketone 1	38.6	1.11
Methyl Ethyl Ketone 2	39.2	1.13
Butanal	39.7	1.14

[a]Retention time of a carbonyl-DNPH relative to that of acetone-DNPH

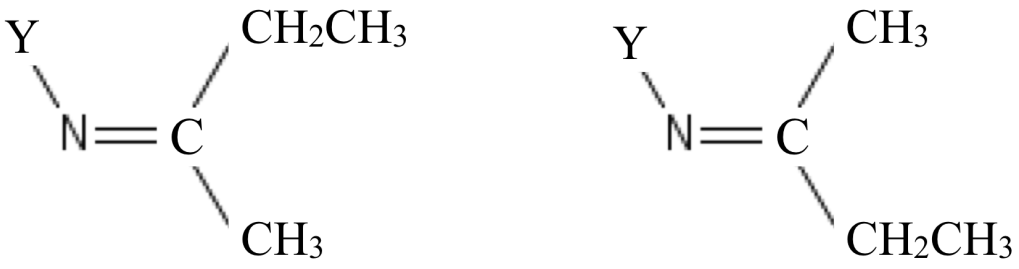

Figure 2.6: Isomers formed upon the derivitization of methyl ethyl ketone with DNPH.

.

2.2.2 Liquid phase calibrations

Liquid phase calibration were performed to establish response factors given as peak area/nmol. These factors are used to convert the chromatographic peak areas for each identified carbonyl into a number of moles. The amount of carbonyls will be used subsequently to determine carbonyl concentrations as will be discussed in the following section. For these calibrations pure carbonyl-DNPH hydrazones were dissolved in HPLC-grade ACN and this solution was diluted to varying concentrations. A 5 μL sample of the solutions were manually injected into the HPLC using A Rheodyne model 8125 micro-HPLC injection valve.

The carbonyl-DNPH hydrazones were synthesized in-lab using the following procedure: Twice recrystallized DNPH was dissolved in ACN with heating and stirring. The liquid pure carbonyl was then added in stoichiometric excess of the DNPH to ensure the complete removal of the DNPH. About 1 mL of water was added to the solution along with the carbonyl to be derivitized. Two drops of concentrated HCl was then added to catalyze the formation of the hydrazones. The solution was then cooled to allow for the crystallization of the derivitized hydrazone. The hydrazone was then filtered and washed with ACN then water to ensure the complete removal of liquid carbonyl. The purity of the hydrazones were tested with the HPLC and through melting point measurements. The absence of a DNPH peak in the chromtogram signifies a pure hydrazone with no DNPH traces. The melting point measurements were all within 2 °C of the literature value, which signifies high product purity. Table 2.2 shows the response

Table 2.2: Carbonyl-DNPH response factors (in peak area/nmol) established using liquid phase calibrations. The mobile phase used was 65% ACN/35% H_2O from 0-20 min followed by linear increase to 100% from 20-45 min and 100% ACN from 45-49 min.

Carbonyl-DNPH	Response Factor (peak area/nmol)	Number of measurements	Pearson's Correlation Coefficient (R^2)
Formaldehyde-DNPH	3.42×10^3	8	0.9992
Acetaldehyde-DNPH	3.36×10^3	5	0.9995
Acetone-DNPH	3.31×10^3	7	0.9998
Propanal-DNPH	4.12×10^3	9	0.9998
MEK-DNPH	3.54×10^3	5	0.9999
Butanal-DNPH	3.66×10^3	7	1.000

factors for the hydrazone DNPH derivatives of formaldehyde, acetaldehyde, acetone, propanal, MEK and butanal.

2.3 Determination of carbonyl mixing ratios

The carbonyl mixing ratio of a nominal carbonyl compound (CR_j can be established using the following equation:

$$mixing\ ratio\ (ppb)\ =\ \frac{peak\ area}{RSF\ \times CE\ \times V_S}\ \times\ \frac{N_A}{n_{air}} \tag{2.2}$$

where peak area is the integrated chromtographic peak(s) of a carbonyl hydrazone, RSF is the response factor of that hydrazone, CE is the cartridge collection efficieny for the hydrazone and V_S is the total sampling volume per run (equal to 2.1×10^4 cm^3). The terms N_A and n_{air} refer to Avogadro's number and the number density of air (2.46×10^{19} $molec/cm^3$ at a temperature of 25 °C and pressure of 1 atm).

The collection efficiency of the cartridge for all carbonyls were determined using gas-phase and liquid-phase calibrations outlined in the previous section. The CE for the carbonyl hydrazone can be determined using the following equations:

$$CE \;=\; \frac{moles\ of\ carbonyl-DNPH\ measured}{moles\ of carbonyl-DNPH\ sampled} \tag{2.3}$$

The carbonyl-DNPH measured is the ratio of the peak area (observed from the sample chromatogram) to the response factor of the carbonyl-DNPH measured as follows:

$$moles\ of\ carbonyl-DNPH\ measured \;=\; \frac{Peak\ Area\ of\ carbonyl-DNPH}{RSF\ of\ carbonyl-DNPH} \tag{2.4}$$

The carbonyl-DNPH sampled is determined using the following equation:

$$moles\ of\ carbonyl-DNPH\ Sampled \;=\; C\times\ f\times\ t\times\ \frac{F1}{F2} \tag{2.5}$$

where C is the concentration of the carbonyl-DNPH solution (in mol/L) and f is sample injector flow rate (in L/min) and t is the sampling time (in min). The terms F1 and F2 are the flow rates (in cm^3/min) of MFC#1 (Figure 2.2) and MFC#2 respectively (Figure 2.5). The carbonyl concentrations and mixing ratio equivalence used for these experiments are shown in Table 2.3.

Table 2.3: Average carbonyl concentrations and mixing ratio equivalence injected into cartridge during CE experiments.

Carbonyl	Concentration (mmol/L)	Mixing Ratio (ppb)
Formaldehyde	7.76	10.84
Acetaldehyde	5.93	8.30
Acetone	6.18	8.63
Propanal	5.45	7.63
MEK	3.86	5.39
Butanal	3.64	5.09

The collection efficiencies determined from these laboratory experiments are shown in Table 2.5. Also shown in Table 2.5 are the CEs determined by Wang (2007), which used the AT-DNPH-HPLC but with different specifications. In order to compare the two studies, it is important to highlight the differences in the system specifications and the operations of the AT-HPLC system; these differences are shown in Table 2.4. In this study, an increase in the particle size of the cartridge packing material allowed a higher sampled air flow rate and total sampling volume when compared to Wang (2007). For a given concentration, an increase in the sampling volume is desired as it results in a higher signal to noise ratio and lower detection limits.

Formaldehyde had the lowest collection efficiency, which was observed to be 67%. This was comparable to the 65% CE observed by Wang (2007). Using this system, Wang (2007) did a thorough analysis to explain this low CE and concluded that it

Table 2.4: AT-DNPH-HPLC system variation between this study and Wang (2007).

Specification	This Study	Wang (2007)
Cartridge packing(μm)	250-381	55-105
MFC#1 flow rate(SCCM)	300	150
Sampling volume(L)	21	9.2

was largely due to the manual skimming integration method employed; the reader is referred to the aforementioned publication for more details. Briefly This skimming technique could result in errors exceeding 50% for small peaks with poor resolution (Bicking, 2006). The resolution observed in this study between the DNPH peak and the formaldehyde peak is 1.5 and at this resolution and given the relative peak area of the formaldehyde peak to the DNPH peak, the error in peak area is estimated to be 32% (Bicking, 2006). In this study, the low collection efficiency is believed to result from the integration error associated with manual skimming integration utilized here. Note that for rider peak integration, the manual skimming technique is better than the valley and the drop integration techniques but worse than the gaussian skim technique (Bicking, 2006). This is since the manual skimming technique does not take into account the ride peak (HCHO in this case) incorporated into the large peak (DNPH). In this study, we used the ChemStation software (Agilent Technologies in Mississauaga, ON) where the gaussian skim is not an available technique. A better estimate of the measured formaldehyde peak could have resulted from the use of the gaussian skim integration technique.

Table 2.5: Cartridge collection efficiencies (CE$\pm\sigma$) for the six quantified carbonyls. These CEs are used for the determination of carbonyl mixing ratios.

Carbonyl	This Study	Wang (2007)	Saha et al (2007)	Pal and Kim (2008)
Formaldehyde	0.67±0.027	0.65±0.01	—	—
Acetaldehyde	1.0±0.33	1.0±0.035	0.92	0.73-1.1
Acetone	0.90±0.017	0.96±0.046	—	—
Propanal	0.79±0.061	1.1±0.036	0.53	0.57-0.75
MEK	0.72±0.08	—	—	
Butanal	0.69±0.09	0.91±0.045	0.55	0.65-1.0

The highest CEs were observed for acetaldehyde and acetone which were efficiently recovered at 100% and 90% respectively. These were comparable to the CEs reported by Wang (2007) which were observed to be 100% and 96% respectively. The CEs observed for propanal, methyl ethyl keone and butanal were determined to be 79%, 72% and 69% respectively. For propanal and butanal, the CEs determined here are lower than the ones reported by Wang (2007), higher than the ones reported by Saha et al (2007) and within the range reported by Pal and Kim (2008) (Table 2.5).

Similar to this study, Saha et al (2007) and Pal and Kim (2008) showed a lower gaseous CE for propanal and butanal when compared to acetaldehyde (Table 2.5). The determined collection efficiencies of all carbonyls is a function of the carbonyl reaction with the DNPH coated on the cartridge. This reaction is facilitated by absorption and adsorption of carbonyls by the DNPH coated cartridge (Saha et al., 2007). The initial

adsorption of heavier carbonyls is less efficient than the lighter ones (Pal and Kim,2008). This could explain the observed difference in CEs between propanal, methyl ethyl ketone and butanal versus acetaldehyde and acetone.

Using the AT-DNPH-HPLC, Wang (2007) achieved better CEs of 110% and 91% for propanal and butanal respectively. Recall from Table 2.4 that the cartridge was packed with smaller sized particles in the Wang (2007) study. Smaller particles typically have a greater surface area than larger particles (Finalyson-Pitts and Pitts, 1999; Seinfeld and Pandis, 2006). A higher internal surface area should enhance carbonyl adsorption onto the DNPH cartridge and is thus expected to result in a better derivitization efficiency. Gaseous diffusion losses are also expected to increase with bigger packing size. These reasons could be the reason that Wang (2007) achieved better collection efficiencies for propanal and butanal when compared to this study.

Measurement accuracy is a function of the error (standard deviation) that is associated with cartridge collection efficiency. The standard deviation of CE ranged from 2 to 33% (Table 2.5). The high standard deviation of 33% associated with acetaldehyde is unreasonably high in this study and is attributed to the evaporation of the highly volatile pure acetaldehyde solution. This error is not expected to be higher than 10%; Wang (2007) reported the error in acetaldehyde measurement to be 3.5%. Aiello (2003) performed multiple measurements of an acetone standard with a final mixing ratio of 4 ppb. The relative standard deviation determined from these measurements was 4.8% This relative standard deviation was reported to be an upper estimate of the precision for this measurement technique (Aiello, 2003).

2.4 Detection limits

Carbonyl detection limits were determined using blank runs, where the cartridge sampling step was bypassed (Figure 2.3). Subsequently the underivitized DNPH solution was back flushed into the HPLC. During this study, four blank runs were taken and their individual chromtograms analyzed. The baseline of each chromatogram was integrated in the sections where the carbonyl-DNPH peaks are typically eluted (Table 2.1)(Aiello and McLaren, 2009). The blank peak area can simply be converted to nmol using the RSF in peak area/nmol. The blank peak area can be converted into a blank mixing ratio using the following equation:

$$Blank\ mixing\ ratio\ (ppb)\ =\ \frac{peak\ area}{RSF\ \times V_S}\ \times\ \frac{N_A}{n_{air}} \tag{2.6}$$

The detection limits are then established using $3\sigma_{bl}$, where σ_{bl} is the standard deviation of all blank runs. Carbonyl detection limits are shown in Table 2.6. The detection limits of all carbonyls were less than 0.01 ppb except acetaldehyde and acetone. The detection limits of acetaldehyde and acetone were 0.269 and 0.126 ppb respectively. Acetaldehyde and acetone are blank limited and the observed detection limits reflect acetaldehyde-DNPH and acetone-DNPH traces in the DNPH solution. The impurities likely occured during the recrystallization of crude DNPH. Contamination during storage of the sealed DNPH solution during the study is also possible.

The detection limits were comparable to those reported by Aiello (2003) and Wang (2007) (Table 2.6). Aiello (2003) achieved better detection limits for the blank limited acetaldehyde and acetone. These detection limits are not intrinsic to the system and

Table 2.6: Carbonyl detection limits determined using the AT-DNPH-HPLC. Detection limits from the studies by Aiello (2003) and Wang (2007) are also shown for comparison.

Carbonyl	Blank Moles (nmoles)	Mixing Ratio (ppb)[a]	Aiello (2003)	Wang (2007)
Formaldehyde	<0.008	<0.010	0.089	0.014
Acetaldehyde	0.23	0.27	0.054	0.17
Acetone	0.13	0.15	0.054	0.21
Propanal	<0.008	<0.010	0.054	0.0069
MEK	<0.008	<0.010	—	—
Butanal	<0.008	<0.010	—	0.027

[a]At a flow rate of 300 SCCM and a sampling time of 70 min

can be lowered by further recrystallization of the crude DNPH and proper storage. For formaldehyde, the detection limit observed in this study is likely to be underestimated. The blank formaldehyde-DNPH peak could have been buried under the DNPH peak, which leads to an underestimation of formaldehyde's detection limit. Aiello (2003) reported a higher detection limit for formaldehyde-DNPH than acetaldehyde-DNPH and acetone-DNPH. Wang (2007) reported a detection limit of 0.0139 ppb but in her study, the formaldehyde-DNPH was also a rider peak on the DNPH peak as discussed previously. From the Aiello study (Table 2.6), the detection limit ratio of formaldehyde/acetaldhyde is 1.6 and is equal to the formaldehyde/acetone ratio. A crude assumption would be to assume that this ratio is the same as this study. If this was the case then the formaldehyde detection limit should be between 0.2-0.4 ppb.

3 Carbonyl concentrations in southwestern Ontario: The effects of local formation versus long range transport

3.1 Study overview

The Border Air Quality and Meteorology (BAQS-Met) Study took place in southwestern Ontario in the summer of 2007. Environment Canada led this study with participation from Ontario Ministry of the Environment and four universities including York University, which led the academic participation. The BAQS-Met study included a three week field intensive from Jun 20th to Jul 10th and an extended "mesonet" period (Jun to Sep) with enhanced meteorological and air quality measurements (Brook et al., 2013). The field intensive involved three supersites at Ridgetown, Harrow and Bear Creek (Figure 3.1), two buoys at lakes St. Clair and Erie and four mobile platforms. The mobile platforms consisted of a Twin Otter aircraft, a ferry equipped with monitoring instrumentation, as well as two vehicular ground-based mobile laboratories one for air quality measurements and another for meteorological measurements. These

Figure 3.1: Location of supersites at Ridgetown, Harrow and Bear Creek during the BAQS-Met field intensive. Also shown are populated urban areas in close proximity to the supersites.

.

measurement platforms are in addition to the existing ground provincial and federal monitoring stations (Brook et al., 2013).

The region probed by the BAQS-Met study suffers from the poorest air quality in Canada. Regional air quality is influenced by complex meteorology from the great lakes and trans-boundary pollution transport from populated U.S. cities. The objectives of this study was to investigate the influence of these factors on air quality and incorporate

the findings into weather forecasting and air quality forecasting models to better predict severe weather episodes and regional smog events (Brook et al., 2013).

We deployed the AT-DNPH-HPLC system to the Ridgetown site for the measurement of carbonyls during the intensive period of the BAQS-Met study. Ridgetown is a rural area that is located south-east of the Chatham-Kent municipality with an estimated population of 3500. The measurement location (42.45 N, 81.89 W and at 202 m above sea level) was in an agricultural field in the northern end of the University of Guelph (Ridgetown campus). This location was chosen to be away from the town center and the associated direct anthropogenic influences. In Ridgetown, local air quality is influenced by surrounding pollution sources. These sources include major provincial HWY 401 (4 km N), 2 Oil refineries and petrochemical industries in Sarnia (70 km NW). Ridgetown is close to the populated urban cities of London (E 90 km), Windsor and Detroit (N-NW 100 km), Cleveland (S 100), Toledo (SE 160 km) and the Golden Horseshoe of Toronto and Hamilton areas (NE 200 km). The Ohio valley region has numerous urban areas and coal-fired power stations is located 100 to 500 km from the measurement site in the SSW direction. Ridgetown is 10 km away from the northern shoreline of Lake Erie. Ridgetown's location is ideal to investigate the effects of lake breeze effects and long range transport on carbonyl concentrations given its proximity to Lake Erie and to the populated U.S. cities.

The AT-DNPH-HPLC system was located inside a trailer in the agricultural field. Air was sampled through a 10 cm manifold that brought excess air at 1 m^3 into the trailer. The manifold stood 4 m above the surface and air was brought through a 5

m sampling line. The AT-DNPH-HPLC system was connected to the sampling line through a 1.5 m 1/4" Teflon tubing. Although we participated for the full length of the intensive period, the data presented here are only for the period from July 5^{th} to July 10^{th}. This is due to an observed contamination of indoor trailer air for the rest of the samples from the 20^{th} of June to the 4^{th} of July. Given the 2 hr time resolution (Chapter 2), we measured 11 air samples and ran 1 blank run a day. For ambient measurements, we obtained a total of 63 valid data points for each of the 6 quantified carbonyls. Mixing ratios were established as covered in (Chapter 2). Blank limited acetaldehyde and acetone were corrected for the peak area arising from the blank. Note that the agricultural field is not expected to be a significant source of carbonyls measured in this study.

Other measurements that will be utilized throughout this Chapter include VOC measurements by the Rudolph group of York University. Evacuated 3 L SUMMA® canisters made from poslished stainless steel canister were used for grab sampling of VOCs four to five times daily and this process took about 1 min. The samples were then analyzed using gas chromatography with flame ionization detector (GC-FID). Fourty VOCs were measured and quantified using this method (Kornilova et al., unpublished report 2011).

A bigger set of VOCs were also measured at Wallaceburg (52 km away from Ridgetwon) by Environment Canada. Ambient air was sampled using 6 L or 3.2 L SUMMA® canisters utilizing whole air sampling. A GC-FID and GC/MSD (GC with mass selective detector) were used for the analysis of the samples at Environment Canada

(Environment Canada, 2013). During the study intensive, 24-hour integrated samples were collected and analyzed. Using this method, 111 different VOCs were measured and quantified. Ozone, NO_2 and meterological conditions (temperature, RH, wind direction and wind speed were measured at Ridgetown and reported by Andy Ng of Ontario Ministry of the Environment. Ozone and NO_2 concentrations were measured by a standard Ultraviolet Photometric Ambient O_3 Analyzer and Chemiluminescence monitors (equipped with molybdenum surface converters) respectively. Mixing ratios of NO_2 were also measured with a Differential Optical Absorption Spectroscopy (DOAS) (McLaren et al., 2010; Halla et al., 2011). A tunable diode laser was used to measure CO at Ridgetown and this measurement was done by Corrine Schiller from York University.

3.2 Overview of ambient carbonyl concentrations

Figure 3.2 shows the carbonyl mixing ratios observed at Ridgetown during BAQS-Met. The highest mixing ratios were observed during the regional smog episode in the period from July 8^{th} to July 10^{th} inclusive. Table 3.1 shows the 5^{th}, 25^{th}, 50^{th}, 75^{th} and 95^{th} percentiles for all the carbonyls measured. The highest carbonyl mixing ratios were observed for acetone followed by formaldehyde and acetaldhyde with study-wide median levels of 1.9, 1.5 and 0.67 ppb respectively (Figure 3.2 and Table 3.1). The observed mixing ratios for the other carbonyls were much lower with median levels of 0.22, 0.072 and 0.041 ppb for methyl ethyl ketone, propanal and butanal respectively. Formalde-

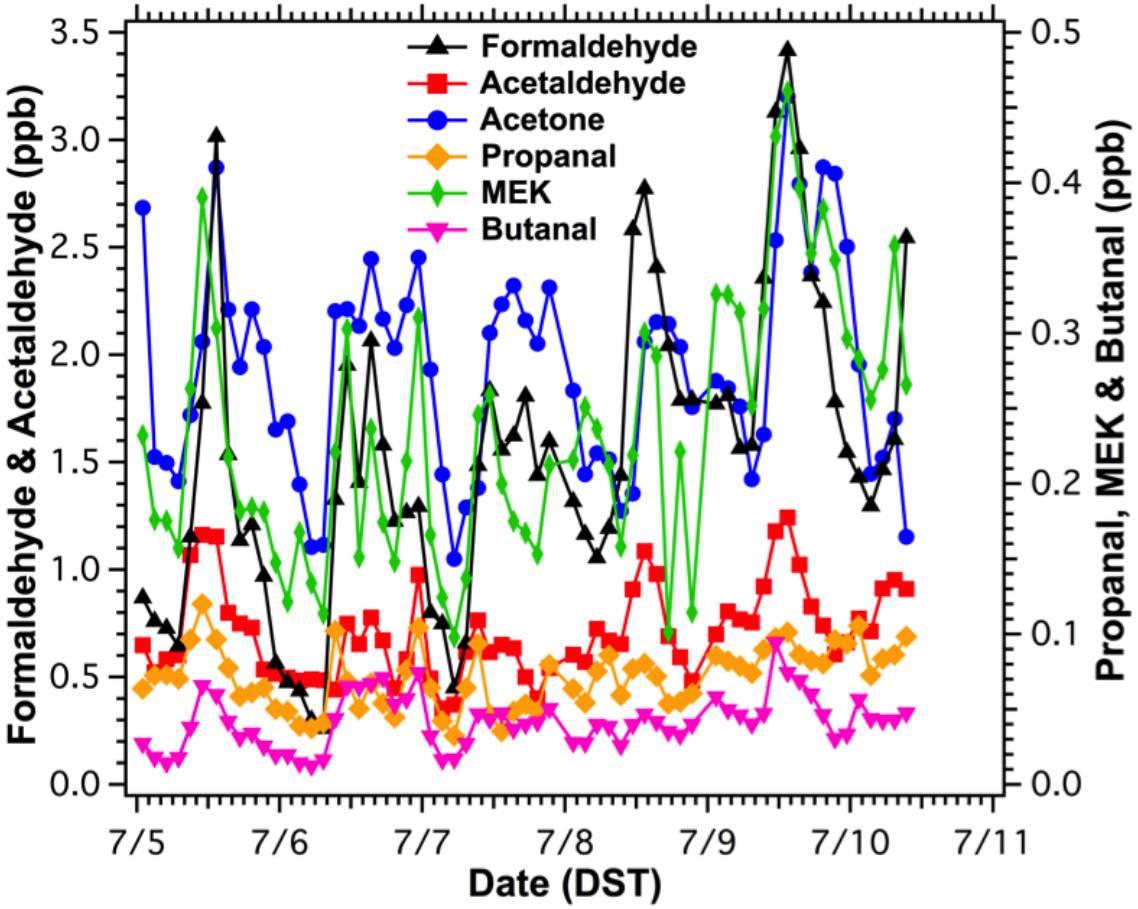

Figure 3.2: Carbonyl mixing ratios observed at Ridgetown during BAQS-Met.

.

hyde, acetaldehyde and acetone accounted for 90 - 96% (average = 92%) of the total carbonyls measured in this study. The 5^{th} and 95^{th} percentiles represent background and peak levels respectively. In this study, acetone had the highest background levels represented by the 5^{th} percentile, which could be due to the long lifetime of acetone, which is typically longer than 10 days (Singh et al., 1994). The highest peak levels were observed for formaldehyde, which has a stronger diurnal profile than acetone, given its shorter lifetime (few hours) and its primarily photochemical production (Possanzini et

Table 3.1: Frequency distribution of carbonyl mixing ratios in ppb.

Carbonyl	5^{th}	25^{th}	50^{th}	75^{th}	95^{th}
Formaldehyde	0.44	1.1	1.5	1.8	3.0
Acetaldehyde	0.41	0.54	0.67	0.81	1.16
Acetone	1.1	1.5	1.9	2.2	2.8
Propanal	0.037	0.054	0.072	0.086	0.10
MEK	0.11	0.16	0.22	0.30	0.40
Butanal	0.014	0.028	0.041	0.050	0.073

al., 2002).

Table 3.2 shows mixing ratios of formaldehyde, acetaldehyde and acetone observed in this study and other studies around the world. The levels observed in this study were compared to studies in rural (RU) and urban (UB) sites in Ontario at Simcoe (RU, Aiello 2003), Egbert and Dorset (RU, Shepson et al.,1991), as well as Toronto (UB, Wang, 2007) and Hamilton (UB, Aiello, 2003). Also shown in Table 3.2 are formaldehyde, acetladehyde and acetone levels measured in rural sites around the world, namely Whiteface Mountain in New York (Khwaja & Narang, 2008), Lille Valby in Denmark (Christensen et al., 2004), Hyytiälä in Finland (Héllen et al., 2004), Cabaneros National Park in Spain (Villanueva et al., 2014) and multiple locations summarised by Finalyson-Pitts & Pitts (1999). The mixing ratios of formaldehyde, acetaldehyde and acetone observed in this study are comparable to reported levels in rural sites in Ontario and around the world. The mixing ratios of formaldehyde, acetaldehyde and acetone observed were very close to the levels reported in Egbert, Dorset, Whiteface Mountain,

Lille Valby and Cabaneros National Park. When compared to Hyytiälä, the levels of formaldehyde, acetaldehyde and acetone are significantly higher in this study. This is since the area investigated in this study is frequently impacted by pollutant transport from populated cities (see Section 3.9 for an in depth discussion). Note that the average formaldehyde, acetladehyde and acetone mixing ratios observed in this study are within 6% of the median levels shown here, so a direct comparison can be made between the median mixing ratios observed here and the average mixing ratio reported in other studies.

Table 3.2: Comparison of formaldehyde, acetaldehyde and acetone mixing ratios (in ppb) observed in this study to rural (RU) and urban (UB) levels reported in other studies.

Location	Time	Statistic	HCHO	CH_3CHO	$(CH_3)_2CO$
Ridgetown, ON (RU)[a]	Jul 2007	Median	1.5	0.67	1.9
Hamilton, ON (UB)[b]	Jul 1999	Median	4.8	4.1	2.3
Simcoe, ON (RU)[b]	Jun-July 2000	Median	0.68	0.33	1.1
Toronto, ON (UB)[c]	Aug 2006	Average	2.31	1.38	3.6
Egbert, ON (RU)[d]	Jul-Aug 1988	Average	1.8	0.57	1.6
Dorset, ON (RU)[d]	Jul-Aug 1988	Average	2.2	0.46	1.8
Whiteface Mountain, NY (RU)[e]	Jul 1994	Average	1.16	0.49	1.6
Lille Valby, DK (RU)[f]	May-Jul 1995	Average	1.2	0.8	1.9

Continued on next page

Table 3.2 – *Continued from previous page*

Location	Time	Statistic	HCHO	CH_3CHO	$(CH_3)_2CO$
Cabaneros National Park, ES (RU)[g]	May-Aug 2011	Average	1.1	0.61	—
Hyytiälä, FI (RU)[h]	Mar-Apr 2003	Median	0.39	0.21	0.50
Multiple (RU-SUB)[ij]	Multiple	Range	0.1-10	0.1-4	0.2-8

[a] This study

[b] Aiello (2003)

[c] Wang (2007)

[d] Shepson et al. (1991)

[e] Khwaja & Narang (2008)

[f] Christensen et al. (2004)

[g] Villanueva et al (2014)

[h] Héllen et al. (2004)

[i] Finalyson-Pitts & Pitts (1999)

[j] Overview of carbonyl mixing ratios

Similar to our measurements, acetone was observed to be the most abundant carbonyl of the these three carbonyls in Simcoe, Whiteface Mountain, Lill Valby and Hyytiälä (Table 3.2). Biogenic sources of acetone is thought to give rise to this abundance in rural areas, which could explain the elevated levels in these areas (Singh et al., 1994; Goldstein and Schade, 2000; Possanzini et al., 2007). In remote areas, acetone levels have been reported to be in the range from 0.2 - 0.5 ppb (Singh et al., 1995; Khwaja and Narang, 2008). This range is lower than the 1.0 ppb background value observed in this study (5^{th} percentile in Table 3.1) and is much lower than the median level of 1.8 ppb.

Formaldehyde levels in remote areas are reported to be in the range of 0.1 - 0.4 ppb,

and results from the photooxidation of methane and lower hydrocarbons (see Khwaja and Narang, 2008). The higher end of this range is similar to the 0.44 ppb background observed in this study (5^{th} percentile in Table 3.1). The background and median levels of acetaldehyde study were 0.41 and 0.67 ppb respectively (Table 3.1), significantly higher than the background level range given in literature of 0.03 - 0.1 ppb (Singh et al., 1995; Khwaja and Narang, 2008).

Table 3.3 presents the mixing ratios of propanal, MEK and butanal observed in this study and other studies. Measurements of these three carbonyls are more scarce than measurements of formaldehyde, acetaldehyde and acetone (Table 3.2). The mixing ratios of propanal, MEK and butanal are significantly lower than the levels reported in rural Whiteface Mountain (for MEK) and suburban Montelibretti but higher than those reported in the rural location of Hyytiälä.

The difference in carbonyl levels between our study and these studies is likely to originate from local and regional emissions of the carbonyls and their precursors. As an example, higher propanal, MEK and butanal levels in Montelibretti is expected given its proximity to the centre of Rome as it lies 30 km to the North East (Possanzini, 2007). In comparison, Ridgetown is about 90 and 110 km from the urban cites of London and Windsor; both are smaller than Rome. For MEK, Goldan et al (1995) reported a higher mixing ratio of 0.31-0.49 in rural Kinterbish, Alabama and inferred a strong biogenic source for this carbonyl. Overall, the mixing ratios of the 6 carbonyls observed here are comparable to rural sites in Ontario and around the world.

Table 3.3: Comparison of propanal, MEK and butanal mixing ratios (in ppb) observed in this study to rural (RU), suburban (SUB) and urban (UB) levels reported in other studies.

Location	Time	Statistic	Propanal	MEK	Butanal
Ridgetown, ON (RU)[a]	Jul 2007	Median	0.058	0.16	0.029
Hamilton, ON (UB)[b]	Jul 1999	Median	0.13	—	—
Toronto, ON (UB)[c]	Aug 2006	Average	0.35	0.50	0.16
Whiteface Mountain, NY (RU)[d]	Jul 1994	Average	—	1.4	—
Montelibretti, IT (SUB)[e]	Jul-Aug 2005	Average	0.37	2.32	0.43
Hyytiälä, FI (RU)[f]	Mar-Apr 2003	Median	0.032	0.073	0.019
Langmuir, NM (RU)[g]	Jun-Aug 1997	Average	1.2	—	1.3
Vancouver, BC (SUB)[h]	Jul-Aug 1993	Range	—	0-2.4	—
Kinterbish, AL (RU)[i]	Jun-Jul 1990	Range	—	0.31-0.49	1.3
Multiple (RU-SUB)[j,k]	Multiple	Range	0.004-0.2	0.1-0.5	0.1-0.3

[a] This study

[b] Aiello (2003)

[c] Wang (2007)

[d] Khwaja & Narang (2008)

[e] Possanzini at al. (2007)

[f] Héllen et al. (2004)

[g] Villanueva-Fierro et al. (2004)

[h] O'Brien et al. (2004)

[i] Goldan et al. (1995)

[j] Finalyson-Pitts & Pitts (1999)

[k] Overview of carbonyl mixing ratios

3.3 The contribution of carbonyls to the NMHC carbon distribution and its relative reactivity towards OH radical

In this section we will evaluate the importance of carbonyl compounds as part of the non-methane hydrocarbon (NMHC) carbon distribution. The VOCs included in this analysis are 18 C3-C9 alkanes, 14 C_4-C_6 alkenes and 5 C_6-C_8 aromatics measured at Ridgetown, as well as ethane, ethene and propene which were measured at Wallaceburg. Figure 3.3 shows the median relative contribution of carbonyls to the NMHC ppbC distribution at Ridgetown. The ppbC of a hydrocarbon is the product of its mixing ratio and its number of carbons. The ppbC of a functional group (for example carbonyls) is the sum of all measured species that comprise said functional group (for example: ppbC HCHO + ppbC CH_3CHO +...). The median mixing ratios used for this analysis is shown in Table 3.4. The contribution of carbonyls to the NMHC carbon budget was observed to be 22% in this study. This is the second largest contribution after alkanes, which accounted for 47% of this budget. For carbonyls, the highest contributions were from acetone, formaldehyde and acetaldehyde at 9.8, 7.4 and 3.3% respectively. The cumulative contribution of propanal, MEK and butanal accounted for 1.7% of the carbon budget. For alkanes, 91% out of the 47% contribution were attributed to ethane, propane, butane, and isopentane.

Aromatics and alkenes accounted for 18% and 12% of the NMHC carbon distribution respectively. Toluene dominated the contribution of aromatics accounting for 13% of the total NMHC budget, while benzene accounted for 3%. For alkenes, isoprene and

Table 3.4: Median NMHC mixing ratios observed in this study and the associated rate constant for their reaction with OH radical, i.e. k_{OH}*.

Hydrocarbon	Median	10^{12}xk_{OH}	Hydrocarbon	Median	10^{12}xk_{OH}
Ethane	1.39	0.24	Propene	0.070	26
Propane	0.58	1.1	Butene	0.013	31
Butane	0.24	2.4	Isobutene	0.034	51
Isobutane	0.13	2.2	c-2-butene	0.0071	56
2-methylbutane	0.27	3.7	t-2-butene	0.0074	64
2,2-dimethylpropane	0.13	0.85	Pentene	0.017	31
Pentane	0.12	4.0	2-methyl-1-butene	0.0095	61
Cyclopentane	0.056	5.0	2-methyl-2-butene	0.0059	87
2,2-dimethylbutane	0.0099	2.3	c-2-pentene	0.0067	65
Methylcyclopentane	0.014	7.5	Isoprene	0.23	101
Cyclohexane	0.014	7.2	Hexene	0.0085	37
2,3-dimethylbutane	0.016	5.8	c-2-hexene	0.0041	62
2-methylpentane	0.051	5.3	t-2-hexene	0.0057	61
3-methylpentane	0.029	5.4	Benzene	0.089	1.2
Hexane	0.038	5.5	Toluene	0.30	6.0
Methylcyclohexane	0.0036	10	Ethylbenzene	0.13	7.1
Heptane	7	Average	p,m-xylene	0.10	19
Octane	0.0079	8.7	o-xylene	0.012	14
Nonane	0.0060	10	1,3-butadiene	0.0021	67
Ethene	0.23	8.5	t-2-pentene	0.0078	67
Formaldehyde	1.5	8.5	Acetaldehyde	0.67	15
Acetone	1.9	0.18	Propanal	0.058	20
MEK	0.16	1.2	Butanal	0.029	24

*Reaction rate constants obtained from Atkinson et al. (1997; 2006)

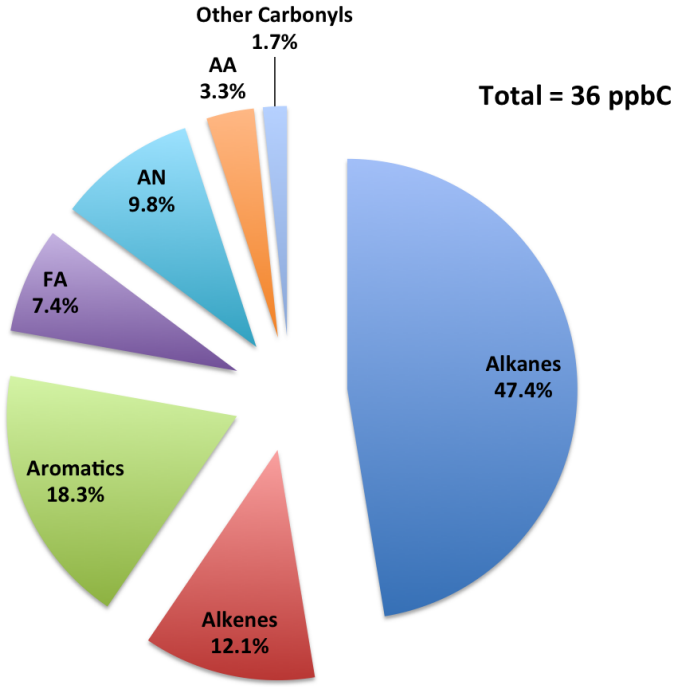

Figure 3.3: The relative contribution of carbonyls to the NMHC budget. Results presented as percentage ppbC.

.

ethene were dominant accounting for 7% and 3% respectively.

The carbon distribution outlined above does not take into the account the reactivity of the hydrocarbons considered. Another approach to evaluating the significance of carbonyls is to evaluate their reactivity towards OH radical, which is the most important daytime oxidant in the troposphere (Stone et al., 2012). For this analysis, NMHC ppbC was used along with the rate constant of the reaction of OH with HC_i, i.e. k_{OH,HC_i} shown in Table 3.4. Figure 3.4 shows the result of this analysis, where the values used in this plot are the product of ppbC and k_{OH,HC_i} for each hydrocarbon. The resulting product

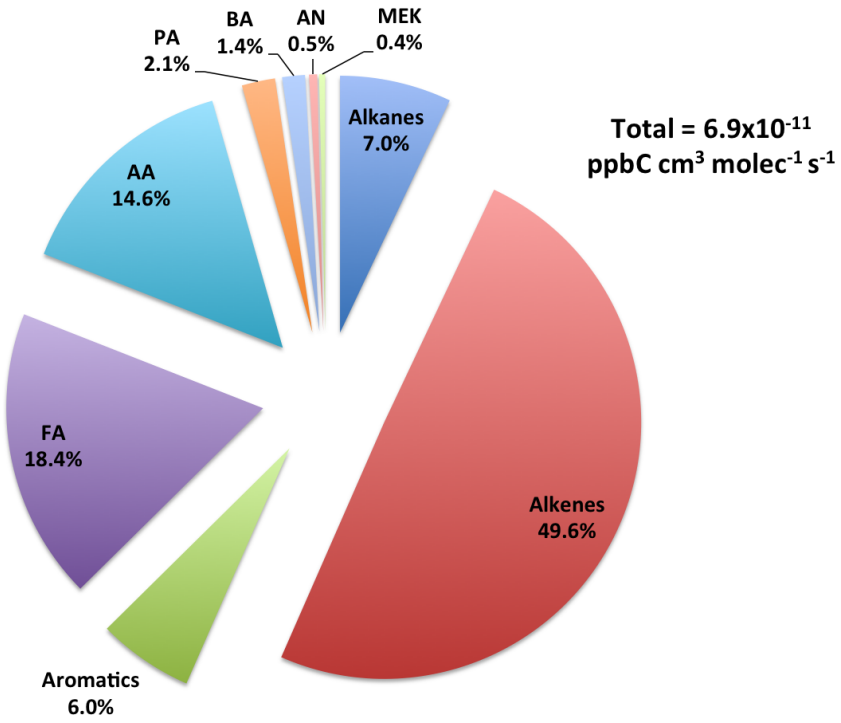

Figure 3.4: The relative contribution of carbonyls to the reactivity of NMHC towards OH radical. Results presented as percentage ppbC$\times k_{OH}$.

value is then grouped into the different functional groups that is presented into Figure 3.4. From Figure 3.4, the most reactive HC class observed was alkenes, which accounted for 50% of NMHC reactivity towards OH radical. This is in contrast to the 12% (lowest) contribution of alkenes to the NMHC distribution, which highlights the high reactivity of this class towards OH radical. For alkenes, isoprene and ethene accounted for 22% each of the total reactivity.

Aldehydes were the second largest contribution to NMHC reactivity accounting for 37% of the total reactivity. The contributions of formaldehyde, acetaldehyde, propanal and butanal were 18, 15, 2.0 and 1.4% respectively. Aldehyde contribution to the

NMHC budget was a much lower 17% (Figure 3.3), which highlights the high reactivity of aldehydes towards OH radical. This analysis does take account the contribution of carbonyls to reactivity of the airmass from aldehyde photolysis. Aldehyde photolysis further contribute to airmass reactivity through organic radical formation.

Alkanes, aromatics and ketones accounted for 7.0, 6.0 and 0.90% of the total NMHC reactivity respectively while their contribution to the NMHC distribution was 48, 12 and 4% respectively, which is significantly higher than their contribution to the total reactivity. This is reflective of the relative inertness of these classes towards OH radical.

We therefore conclude that aldehydes (especially formaldehyde and acetaldehyde) contribute significantly towards the NMHC carbon distribution and even more significantly to the total NMHC reactivity. Ketones (predominantly acetone), however, have a significant contribution to the NMHC carbon distribution but not to the NMHC reactivity.

3.4 Photochemical formation and sinks of formaldehyde

Photochemical oxidation of hydrocarbons is an important and significant source of carbonyls in the troposphere (Grosjean, 1982; Carlier et al., 1986; Shepson et al., 1991; Finalyson-Pitts and Pitts, 1999). The photo-oxidation of all organic compounds leads to the formation of carbonyl compounds (Carlier et al., 1986). In contrast, photochemical destruction by photolysis and reaction with OH radical are the main sinks of carbonyls (see for example Grosjean, 1982; Carlier et al., 1986; Finalyson-Pitts and Pitts, 1999;

Khwaja and Narang, 2008). The next three sections will assess the photochemical production and destruction of formaldehyde, acetaldehyde and acetone. These three carbonyls were chosen for this analysis because they constituted 92% of the carbonyls measured in this study (section 3.2).

The main source of formaldehyde in the summer is the oxidation of VOCs by hydroxyl radical and ozone. Possanzini et al (2002) estimated that this secondary formation of formaldehyde accounted for 80% of the formaldehyde measured in Rome. Satsumabayashi et al (1995) also reported that ratio to be as high as 60% in an area impacted by long range transport at Urawa in Central Japan. In this section we explore the daytime photochemical formation and removal of formaldehyde. At night, carbonyls are formed from the oxidation of hydrocarbons by O_3 (Altshuller, 1993). Carbonyls can be removed by nitrate radicals at night (Cantrell et al., 1985). These night time processes will not be covered in this section nor in Section 3.5 and Section 3.6.

The average daytime production of formaldehyde (P_{FA} in molec cm^{-3} s^{-1}) from its VOC precursors was estimated using the following equation:

$$P_{HCHO} = \sum_n k_{n,OH}[VOC_n][OH]\alpha_{n,OH} + \sum_n k_{n,O_3}[VOC_n][O_3]\alpha_{n,O_3} \quad (3.1)$$

Where $k_{n,OH}$ and k_{n,O_3} are the rate constants for the reaction of VOC_n with OH and O_3 respectively. $[VOC_n]$, [OH] and $[O_3]$ are the ambient concentrations of VOC, OH radical and ozone. Finally, $\alpha_{n,OH}$ and α_{n,O_3} are the fractional yields that lead to the

formation of formaldehyde from the oxidation of VOC_n with OH and O_3 respectively.

Study-wide average daytime (08:00 - 18:00) concentrations of VOCs were used to estimate P_{HCHO} using Eq 3.1. All VOC concentrations but four (ethane, ethene, propene and β-pinene) were measured in Ridgetown. Ethane, ethene, propene and β-pinene were estimated using the Wallaceburg VOC measurements. Methane was estimated to be 1880 ppb, using measurements in Egbert, Ontario in the summer of 2007 (EC CGGMP, 2013). Environment Canada utilized a GC-FID to obtain hourly CH_4 measurements, which were averaged into monthly data points used in this estimate. For this analysis, the daytime mean concentration of hydroxyl radical was assumed to be $5x10^6$ molec cm^{-3}. The concentration of OH can range from 0 to $2x10^7$ molec cm^{-3} based on several measurements in multiple locations (Hewitt and Harrison, 1985). A daytime mean range of 0.5-$5x10^6$ molec cm^{-3} was suggested by Hewitt and Harrison (1985) and the upper limit of that range was adopted for this analysis. In this location, the concentration of OH in daytime is expected to be variable and can be close to 0 and as high as 2 x 10^7 molec cm^{-3} right at night and at midday respectively. Ozone concentrations were obtained in Ridgetown and subsequently used for this analysis.

Table 3.5 shows $k_{n,OH}$ and $\alpha_{n,OH}$ for the reaction of selected VOCs with OH. Table 3.6 shows k_{n,O_3} and α_{n,O_3} for the reaction of O_3 with selected alkenes. The VOCs selected were based on the most prominent formaldehyde precursors as identified in the literature (Carlier et al., 1986; Alshuller, 1991b; Sumner et al., 2001). A significant fraction of the observed HCHO is expected to form from the oxidation of these selected VOCs. This is given the significant concentrations, reaction rate constants and reaction

yields for these selected VOCs. However, these VOCs are a subset of the total VOCs that can be oxidized to form HCHO. Adding more VOCs to this analysis will increase the total rate of formaldehyde formation. This is also true for the photochemical formation of acetaldehyde and acetone covered in Sections 3.5 and 3.6.

The fractional yields of formaldehyde from methane and acetaldhyde were estimated to be 1.0 (Table 3.5). This estimate is based on the oxidation mechanism of CH_4 and CH_3CHO by OH radical to form formaldehyde, which are as follows (Seinfeld and Pandis [Ch. 6], 2006; Holloway and Wayne [Ch. 8], 2010):

$$CH_4 + OH \longrightarrow CH_3 + H_2O \tag{R 3.1}$$

$$CH_3 + O_2 \longrightarrow CH_3O_2 + H_2O \tag{R 3.2}$$

$$CH_3O_2 + NO \xrightarrow{O2} HCHO + HO_2 + NO_2 \tag{R 3.3}$$

$$CH_3CHO + OH \xrightarrow{O2} CH_3CO \cdot O_2 + H_2O \tag{R 3.4}$$

$$CH_3CO \cdot O_2 + NO \longrightarrow CH_3CO \cdot O + NO_2 \tag{R 3.5}$$

$$CH_3CO \cdot O \longrightarrow CH_3 + CO_2 \tag{R 3.6}$$

Note that the methyl radical formed from reaction R 3.6 will form HCHO through reactions R 3.2 and R 3.3.

Figure 3.5 shows the study-wide relative contribution of precursor VOCs to the formation of formaldehyde, which was determined using Eq 3.1. The highest contributions to formaldehyde production were observed to be from the oxidation of isoprene,

Table 3.5: Reaction rate constants of OH with selected VOCs and associated yields of formaldehyde production.

Hydrocarbon	k_{OH}	Reference	Yield	Reference
Acetaldehyde	1.5×10^{-11}	Atkinson et al. (2006)	1.0	Estimate
Methane	6.4×10^{-15}	Atkinson et al. (2006)	1.0	Estimate
Ethene	9.0×10^{-12}	Atkinson et al. (2006)	1.6	Altshuller (1991b)
Propene	3.0×10^{-11}	Atkinson et al. (2006)	1.0	Altshuller (1991b)
Butene	3.1×10^{-11}	Atkinson et al. (1997)	1.0	Altshuller (1991b)
Isobutene	5.1×10^{-11}	Atkinson et al. (1997)	0.92	Tuazon et al. (1998)
Isoprene	1.1×10^{-10}	Atkinson et al. (2006)	0.62	Carter & Atkinson (1996)
Pentene	3.1×10^{-11}	Atkinson et al. (1997)	0.60	Atkinson et al. (1995a)
Hexene	3.7×10^{-11}	Grosjean & Williams (1992)	0.58	Atkinson et al. (1995a)
Toluene	6.0×10^{-12}	Atkinson (1990)	0.010	Andino et al. (1996)
p,m-Xylene	1.9×10^{-11}*	Atkinson (1990)	0.17	Andino et al. (1996)
β-Pinene	7.7×10^{-11}	Lee et al. (2006)	0.49	Lee et al. (2006)

* Average of the k_{OH} rate constants for m-Xylene and p-Xylene

Table 3.6: Reaction rate constants of O_3 with selected alkenes and associated yields of formaldehyde production.

Alkene	k_{O_3}	Reference	Yield	Reference
Ethene	1.6×10^{-18}	Atkinson et al. (1997)	1.1	Grosjean et al (1996a)
Propene	1.0×10^{-17}	Atkinson et al. (1997)	0.78	Grosjean et al (1996a)
Isobutene	1.1×10^{-17}	Atkinson et al. (1997)	0.95	Carter & Grosjean et al (1996a)
Butene	9.6×10^{-18}	Atkinson et al. (1997)	0.63	Grosjean et al (1996a)
Pentene	1.0×10^{-17}	Atkinson et al. (1997)	0.60	Atkinson et al. (1995b)
Isoprene	1.3×10^{-17}	Atkinson et al. (1997)	0.90	Atkinson et al. (1995b)
Hexene	1.1×10^{-17}*	Atkinson et al. (1997)	0.58	Atkinson et al. (1995b)

methane and acetaldehyde hydroxyl radical. The reaction of isoprene and OH radical accounted for 32% of HCHO production, while the reactions of CH_4 and acetaldehyde with OH accounted for 24% and 23% respectively. The high contribution of methane to HCHO formation is due to its high concentration of 1880 ppb. The contributions of of isoprene and acetaldehyde, however, are high due to their high reactivity towards OH radical as their concentrations only averaged 0.25 and 0.77 ppb respectively.

Lower contributions to HCHO production were observed from the reactions of ethene and propene with OH radical, which accounted for 8% and 5% respectively. All other reactions accounted for only 8% of HCHO production, 2% of which were from the reaction of O_3 with VOCs. Aiello (2003) also observed the highest contribution to be from isoprene, methane and acetaldehyde in the rural site of Simcoe, Ontario. The reaction of isoprene with OH accounted for 43% in Simcoe, which is similar to the 32%

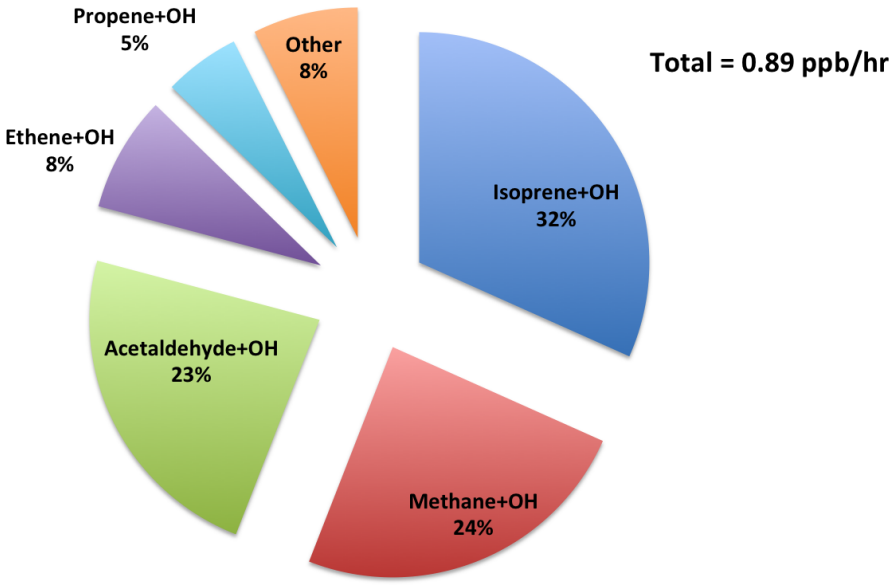

Figure 3.5: Relative contribution of hydrocarbon precursors to formaldehyde formation in Ridgetown.

.

observed in this study.

In the daytime, three processes are responsible for the removal of HCHO namely photolysis, reaction with OH and deposition. Here we offer a discussion of these sinks and their importance in Ridgetown during BAQS-Met. Wet deposition of carbonyls can be significant for carbonyls (Grosjean and Wright, 1983); this removal process was not considered in this study. At night, the oxidation of HCHO by nitrate radical is not expected to be a significant sink and will not be considered here. The lifetime of HCHO with respect to its reaction with NO_3 radical is estimated to be 146 days given a

reaction rate constant of 3.23x10^{-16} cm^3 molec^{-1} s^{-1} and a NO_3 mixing ratio of 10 ppt (Christensen et al., 2000; Wayne et al., 1991). This lifetime is much higher than the daytime removal processes, as will be discussed shortly. We first discuss the removal of HCHO through oxidation by OH radical. The rate constant for the reaction of OH with HCHO is 8.5 x 10^{-12} cm^3 molec^{-1} s^{-1} (Atkinson et al., 2006). OH concentration was estimated to be 5 x 10^6 molec cm^{-3} similar to the value used in formaldehyde production. The lifetime of HCHO with regards to OH oxidation was estimated to be 6.5 hour. Using the HCHO median mixing ratio of 1.5 ppb, HCHO removal rate due to OH oxidation is estimated to be 0.23 ppb/hr.

The next removal process of HCHO that we will consider is photolysis. Recall from Chapter 1 that HCHO photolyzes through the following pathways:

$$\mathrm{HCHO} + h\nu \longrightarrow \mathrm{HCO} + \mathrm{H} \qquad \text{(R 3.7)}$$

$$\mathrm{HCHO} + h\nu \longrightarrow \mathrm{CO} + \mathrm{H_2} \qquad \text{(R 3.8)}$$

The rate of HCHO photolysis can be estimated using the following equation (Jenkin et al., 1997.):

$$J = l(cos\ \chi)^m\ e^{-n\ sec\ \chi} \qquad (3.2)$$

where J is the photolysis rate constant, χ is the solar zenith angle at Ridgetown, estimated to be 27.6° (Solar position calculator available at http://solardat.uoregon.edu/cgi-bin/SolarPositionCalculator.cgi, acessed July 8th of 2014). l, m and n are parameters determined to be 4.866 x 10^{-5}, 0.781 and 0.349 respectively for reaction R 3.7 (Jenkin et al., 1997). For reaction R 3.8, the parameter l, m and n were determined to be 6.790

x 10^{-5}, 0.565 and 0.275 respectively. Using Eq 3.2, the rate of HCHO photolysis is estimated to be 7.6 x 10^{-5} s^{-1}. The lifetime of HCHO with regards to photolysis is estimated to be 3.6 hours, which corresponds to a removal rate of 0.42 ppb/hr for 1.5 ppb of HCHO.

The third removal process is the deposition of HCHO. The rate of deposition for formaldehyde is reported to be 0.45 cm/sec (see Christensen et al., 2000, and references therein). This rate is dependant on atmospheric turbulence and the surface type upon which deposition takes place. We consider three boundary layer heights (BLHs) for this analysis, 500 m, 1000 m and 1500 m. These three heights were chosen as the majority of meausred BLHs were in the 500-1500 m range in Ridgetown (Halla et al., 2011). The lifetime of HCHO with regards to deposition would be 31 hrs (0.048 ppb/hr) at 500 m, 62 hrs (0.024 ppb/hr) at 1000 m and 93 hrs (0.016 ppb/hr) at 1500 m, where the removal rate are calculated for 1.5 ppb.

Photolysis is the dominant removal process of the three discussed, accounting for 60-63% of the total HCHO removal depending on the boundary layer height. The second largest contribution to HCHO removal is oxidation by OH, which accounted for 33-35% at 500-1500 m respectively. Deposition had the lowest contribution to HCHO removal accounting for 2-7% for 1500-500 m boundary layer height. Considering these three process, the lifetime of HCHO at Ridgetown is 2 hours. Using the median mixing ratio of 1.5 ppb for formaldehyde, this removal rate is 0.75 ppb/hr. This lifetime is highly dependant on OH radical concentration, which can be above or below the estimated 5 x 10^6 molec cm^{-3}.

3.5 Photochemical formation and sinks of acetaldehyde

The photochemical formation of acetaldehyde from its VOC precursors is the dominant source for this carbonyl. This pathway was found to account for 90% of acetaldehyde measured in Rome (Possanzini et al., 2002) and up to 85% in Urawa in Central Japan (Satsumabayashi et al., 1995). In this section we assess the contribution of precursor VOCs to the daytime photochemical formation of acetaldehyde. The rate of acetaldehyde photochemical production was estimated using Eq 3.1 and daytime VOC concentrations in a similar approach to that discussed in Section 3.4. Propene was measured in Wallaceburg, while ethanol was estimated to be 0.4 ppb based on measurements in rural Borden, Ontario by Zhou and McLaren (1999). Ethanol levels could have increased since these measurements were taken in 1998 due to an increased use of ethanol based fuel in recent years. The concentration of t-2-pentene were estimated using the concentration of c-2-pentene and a ratio of 1.43. This ratio was estimated using VOC emissions from motor vehicles established by Harley and Kean (2004).

Table 3.7 shows $k_{n,OH}$ and $\alpha_{n,OH}$ for the reaction of VOC precursors with OH. The k_{n,O_3} and α_{n,O_3} for the reaction of O_3 with alkenes precursors is shown in Table 3.8. Acetaldehyde precursors were selected based on literature (Carlier et al., 1986; Alshuller, 1991b; Millet et al., 2010). The values in Tables 3.7 and 3.8 were obtained from the references indicated within the tables. For the reaction of c-2-butene, 2-methyl-2-butene and ethanol with OH radical, the yield of acetaldehyde formation is an average of the yields determined by Tuazon et al (1998) in which two measurement

techniques (GC-FID) and Fourier transform infrared (FT-IR) absorption spectroscopy) were used. The fractional yields of the reaction of 2-methyl-1-butene with OH and O_3 were not found in literature and were estimated to be equal to the yields of 2-methyl-2-butene with OH and O_3 respectively. The yields of c-2-pentene and c-2-hexene with OH radical and O_3 to form acetaldehyde were estimated to be the same yield as the reaction of OH and O_3 with c-2-butene. The yield of t-2-pentene with OH and O_3 was estimated to be the same as the of t-2-butene.

The study-wide relative contribution of VOC precursors to the formation of acetaldehyde is shown in Figure 3.6. The highest contribution observed was for the reaction of propene with OH radical which, accounted for 21% of acetaldehyde formation. The reactions of ethanol, t-2-butene and t-2-pentene with OH accounted for 10, 10 and 9% respectively. Alkene reactions (except propene, t-2-butene and t-2-pentene) with OH accounted for 26%. The high contributions (66%) of the reactions of propene and other alkenes with OH radical is due to the high reactivity of alkenes towards OH radical.

The reactions of total alkenes with ozone accounted for 15% of daytime acetaldehyde photochemical formation.The lowest contribution to daytime acetladehyde photochemical formation was the reaction of alkanes with hydroxyl radical, which accounted for 9% and was dominated by the reaction of OH with ethane (3%) and 2-methylbutane (3%).

At Simcoe, Ontario, Aiello (2003) showed that the reaction of alkenes with OH was the main source of acetaldehyde photochemical production accounting for 64% followed by reaction of alkanes with OH and O_3 which, accounted for 19% and 17% respectively.

Table 3.7: Reaction rate constants of OH with selected VOCs and associated yields of acetladehyde production.

VOC	k_{OH}	Reference	Yield	Reference
Ethane	2.5×10^{-13}	Atkinson et al. (1997)	0.99	Altshuller (1991a)
Butane	2.4×10^{-12}	Atkinson et al. (1997)	0.31	Altshuller (1991a)
Pentane	4.0×10^{-12}	Atkinson et al. (1997)	0.19	Altshuller (1991a)
Isopentane	3.7×10^{-12}	Atkinson et al. (1997)	0.28	Altshuller (1991a)
Propene	2.6×10^{-11}	Atkinson et al. (1997)	1.0	Altshuller (1991b)
c-2-butene	5.6×10^{-11}	Atkinson et al. (1997)	1.7*	Tuazon et al. (1998)
t-2-butene	6.4×10^{-11}	Atkinson et al. (1997)	1.8	Atkinson & Lloyd (1984)
2-methyl-2-butene	8.7×10^{-11}	Atkinson et al. (1997)	0.91*	Tuazon et al. (1998)
2-methyl-1-butene	6.1×10^{-11}	Atkinson et al. (1997)	0.91	Estimate
c-2-hexene	6.2×10^{-11}	Grosjean & Williams (1992)	1.7	Estimate
c-2-pentene	5.7×10^{-11}	Grosjean & Williams (1992)	1.7	Estimate
t-2-pentene	5.7×10^{-11}	Grosjean & Williams (1992)	1.8	Estimate
Ethanol	3.3×10^{-12}	Grosjean (1997)	0.92*	Millet et al. (2010)

* Average value used

Table 3.8: Reaction rate constants of O_3 with selected alkenes and associated yields of acetaldehyde production.

Alkene	k_{O_3}	Reference	Yield	Reference
Propene	1.0×10^{-17}	Atkinson et al. (1997)	0.52	Grosjean et al (1996a)
Butene	9.6×10^{-18}	Atkinson et al. (1997)	0.13	Grosjean et al (1996a)
t-2-butene	1.9×10^{-16}	Atkinson et al. (1997)	1.2	Grosjean et al (1996a)
c-2-butene	1.3×10^{-16}	Atkinson et al. (1997)	1.2	Grosjean et al (1996a)
2-methyl-2-butene	4.0×10^{-16}	Atkinson et al. (1997)	0.69	Grosjean et al (1996a)
2-methyl-1-butene	1.6×10^{-17}	Atkinson et al. (1997)	0.69	Estimate
c-2-pentene	1.3×10^{-16}	Avzianova & Ariya (2002)	1.2	Estimate
t-2-pentene	1.1×10^{-16}	Avzianova & Ariya (2002)	1.2	Estimate
c-2-hexene	1.62×10^{-16}	Avzianova & Ariya (2002)	1.2	Estimate

The findings of this study is therefore comparable to those reported by Aiello (2003).

We will now discuss the removal process of acetaldehyde during the daytime. Similar to formaldehyde, oxidation by hydroxyl radical and photolysis are the main removal processes of acetaldehyde. But unlike HCHO, deposition is not a significant loss process for acetaldehyde (Christensen et al., 2000). At night, NO_3 oxidation of CH_3CHO by nitrate radical (rate constant=1.2x10^{-15} cm^3 $molec^{-1}$ s^{-1}) is not expected to be a significant sink, given its long lifetime of 39 days based on 10 ppt NO_3 mixing ratio

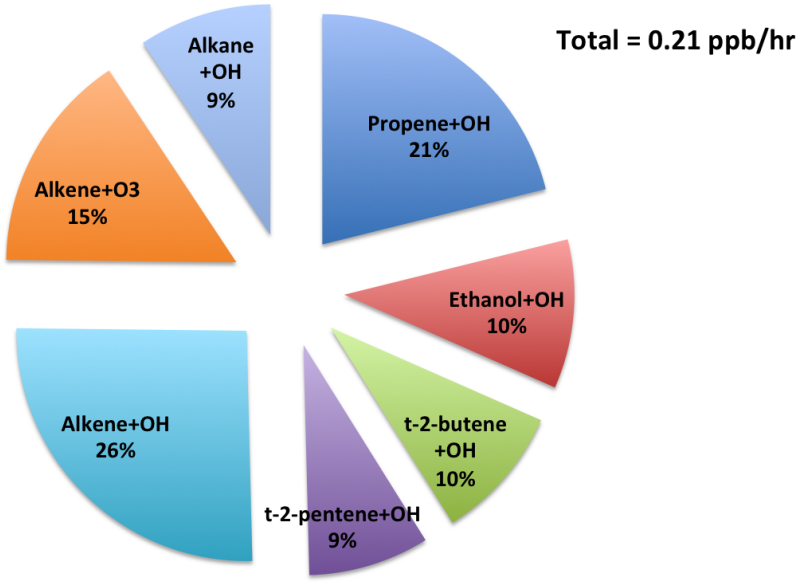

Figure 3.6: Contribution of hydrocarbon precursors to acetaldehyde formation in Ridgetown.

.

(Christensen et al., 2000; Wayne et al., 1991). This removal mechanism will not be considered here.

The removal of acetaldehyde through oxidation by OH radical can be estimated using the rate constant of the reaction of OH with acetaldehyde and an estimated OH concentration of 5 x 10^6 molec cm^{-3} (see section 3.4). The rate constant of the reaction of acetaldehyde with OH is reported to be 1.5 x 10^{-11} cm^3 $molec^{-1}$ s^{-1} (Atkinson et al., 2006). The lifetime of acetaldehyde with regards to its oxidation by hyrdoxyl radical is estimated to be 3.7 hrs, which corresponds to a removal rate of 0.18 ppb/hr when

using the study wide median of 0.67 ppb. Once again this rate of removal is highly dependant on the assumed OH concentration as was discussed in the previous section.

The photolysis rate of removal for acetaldehyde was estimated using the method proposed by Jenkins et al (1997) discussed in section 3.4. The photolysis reaction proceeds through the following pathway:

$$CH_3CHO + h\nu \longrightarrow HCO + CH_3 \qquad (R\,3.9)$$

Briefly, Eq 3.2 was used with parameters l, m and n determined to be 8.443 x 10^{-6}, 1.177 and 0.437 respectively (Jenkins et al., 1997). The rate of acetaldehyde photolysis was estimated to be 4.5×10^{-6} s^{-1}. It then follows that the lifetime of acetaldehyde with regards to photolysis is estimated to be 62 hours. Using the 0.67 ppb median level, the corresponding removal rate is estimated to be 0.011 ppb/hr. The oxidation by OH is largely responsible for acetaldehyde removal accounting for 94% of acetaldehyde loss. Photolysis, on the other hand was observed to be a minor loss process at only 6%. Recall that the dominant removal processes of HCHO was photolysis and so the removal processes of the two carbonyls are significantly different. Considering these two loss processes of CH_3CHO the lifetime of acetaldehyde was estimated to be 3.5 hrs, which corresponds to a removal rate of 0.19 ppb/hr (using 0.67 ppb).

3.6 Photochemical formation and sinks of acetone

The photo-oxidation of hydrocarbons is a significant source of acetone (Singh et al., 1994, Jacob et al., 2000). Singh et al (1994) argues that this is the largest source of

acetone in the atmosphere accounting for 50% of all sources. Similar to our approach in the last two sections, we estimate the contribution of precursor VOCs to the formation of acetone at Ridgetown. The daytime rate of acetone production was estimated using Eq 3.1 using daytime VOC concentrations measured at Ridgetown.

Table 3.9 shows $k_{n,OH}$ and $\alpha_{n,OH}$ for the reaction of VOC precursors with OH. Shown in Table 3.10 are the k_{n,O_3} and α_{n,O_3} for the reaction of O_3 with alkene precursors. The VOC precursors of acetone were selected from literature (Carlier et al., 1986; Alshuller, 1991b; Singh et al., 1994; Jacob et al., 2000).

Figure 3.7 shows the contributions of VOC precursors to the formation of acetone in Ridgetown. The highest contribution observed was from the reaction of isobutene with OH radical, which accounted for 42% of acetone formation. The reactions of propane, isopentane and 2-methyl-2-butene with OH accounted for 14, 13 and 13% respectively. The reactions of alkanes (except propane) with OH and the reactions of Alkenes with O_3 accounted for 12 and 6% of acetone formation respectively. The contributions of the reactions of isobutene and 2-methyl-2-butene (55%) with OH are high due to their reactivity towards OH radical which are higher than OH + alkane reactions (see Table 3.9).

Aiello (2003) estimated the contributions of VOC to acetone formation in Simcoe, Ontario. The highest contributions at Simcoe were from the reactions of isobutene and 2-methyl-2-butene which accounted for 64% of the total acetone production. This is similar to the findings of this study.

The main daytime removal processes for acetone are OH oxidation and photolysis.

Table 3.9: Reaction rate constants of OH with selected VOCs and associated yields of acetone production.

VOC	k_{OH}	Reference	Yield	Reference
Propane	2.1×10^{-12}	Atkinson et al. (1997)	0.66	Altshuller (1991a)
Isobutane	2.2×10^{-12}	Atkinson et al. (1997)	0.57	Altshuller (1991a)
Isopentane	3.7×10^{-12}	Atkinson et al. (1997)	0.42	Altshuller (1991a)
2,3-dimethylbutane	5.8×10^{-12}	Atkinson et al. (1997)	1.5	Cox et al. (1980)
Isobutene	5.1×10^{-11}	Atkinson et al. (1997)	0.84*	Tuazon et al. (1998)
2-methyl-2-butene	8.7×10^{-11}	Atkinson et al. (1997)	0.87*	Tuazon et al. (1998)

* Average value used

Table 3.10: Reaction rate constants of O_3 with selected alkenes and associated yields of acetone production.

Alkene	k_{O_3}	Reference	Yield	Reference
Isobutene	1.1×10^{-17}	Atkinson et al. (1997)	0.34	Grosjean et al (1996a)
2-methyl-2-butene	4.0×10^{-16}	Atkinson et al. (1997)	0.30	Grosjean et al (1996a)

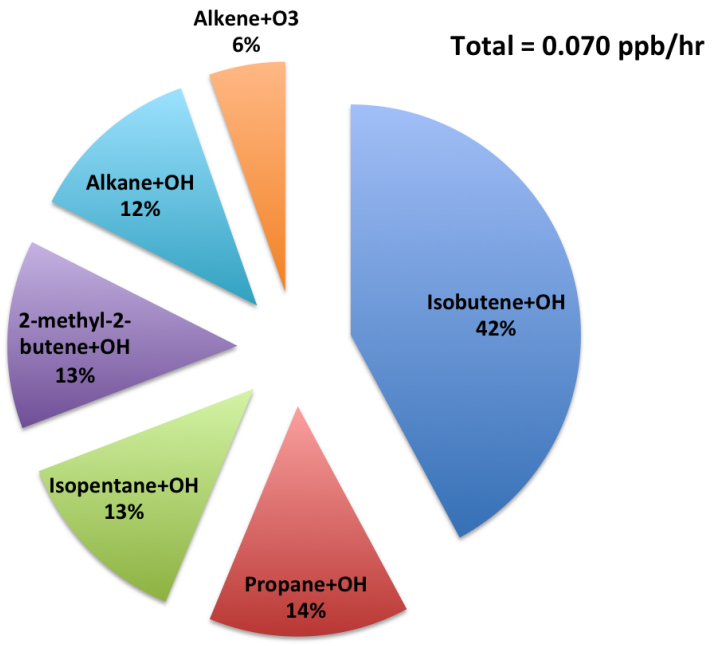

Figure 3.7: Contribution of hydrocarbon precursors to acetone formation in Ridgetown.

.

Similar to acetaldehyde, dry deposition is not expected to be a significant removal mechanism for acetone (Singh et al., 1994; Christensen et al., 2000). The removal of acetone by NO_3 at night is negligible with a reaction rate constant 8.5×10^{-18} cm^3 $molec^{-1}$ s^{-1} and an expected lifetime of 5.5×10^3 days when NO_3 is 10 ppt (Christensen et al., 2000; Wayne et al., 1991). This removal mechanism will not be considered here. The removal rate of acetone due to OH oxidation can be estimated using the reaction rate constant$k_{(CH_3)_2CO,\,OH}$, which is 1.8×10^{-13} (Atkinson et al., 2006). Using an estimated OH concentration of 5×10^6 molec cm^{-3} (see section 3.4), the lifetime of acetone with regards to OH oxidation is estimated to be 309 hrs. This corresponds to

a removal rate of 6.1 x 10^{-3} ppb/hr when using acetone's study-wide median mixing ratio of 1.9 ppb. This is much lower than the rates of removal of formaldehyde and acetaldehye at 0.23 and 0.18 ppb/hr respectively. The lower removal rate is due to a lower $k_{(CH_3)_2CO,\,OH}$ when compared to $k_{HCHO,\,OH}$ and $k_{CH_3CHO,\,OH}$.

The rate of acetone removal by photolysis was estimated using the method outlined in section 3.4 proposed by Jenkins et al (1997). The photolysis of acetone occurs via the following pathway:

$$CH_3C(O)CH_3 + h\nu \longrightarrow CH_3CO + CH_3 \qquad \text{(R 3.10)}$$

The paramters l,m and n used in Eq 3.2 to determine acetone photolysis are 9.269 x 10^{-7}, 1.563 and 0.301 respectively (Jenkins et al., 1997). The rate of acetone removal due to photolysis was estimated to be 5.5 $\times$ 10^{-7} s^{-1}. It then follows that the lifetime of acetone due to photolysis was 510 hours. Using a mixing ratio of 1.9 ppb for acetone, this lifetime corresponds to a removal rate of 3.7 x 10^{-3} ppb/hr. Considering the two removal mechanisms of acetone by OH oxidations and photolysis, the combined lifetime of acetone is estimated to be 190 hours. The OH oxidation accounts for 62% of acetone removal, while photolysis accounts for the remaining 38% at Ridgetown, Ontario. The total rate of removal is then estimated to be 0.010 ppb/hr when the acteone mixing ratio is 1.9 ppb. This rate of removal is a factor of 19 lower than that of acetaldehyde and a factor of 75 lower than that of formaldehyde.

3.7 Carbonyl diurnal profiles

The average diurnal profiles of aldehydes, ketones, ozone and CO are shown in Figure 3.8, where ozone is used as an indicator of secondary photochemical formation. Carbon monoxide can be used as a tracer for primary emissions as emission sources of CO in Ontario are primarily related to transportation which constituted 84% of all CO emission sources (OME, 2006). Study-wide average mixing ratios were used and plotted as a function of the time of the day. Sunrise and sunset at Ridgetown were at 06:00 and 21:00 respectively. The highest carbonyl and ozone concentrations were observed in the afternoon at 14:00. The similarity in the diurnal profile between carbonyls and ozone suggest a photochemical origin for the carbonyls (Christensen et al., 2000; Khwaja & Narang, 2008). The diurnal variability is less pronounced for ketones than aldehydes (Figure 3.8a), which is expected given the longer lifetimes of ketones when compared to aldehydes.

The diurnal profile of CO was significantly different than that of carbonyls and O_3. Peak CO mixing ratios were observed at 4:00, 10:00 and 12:00, which could be due to long range transport and the entrapment of CO in a shallow nocturnal inversion layer. A decrease in CO is observed after the breaking of this inversion layer at $\sim$ 10:00. The difference between the diurnal profiles of carbonyls and CO suggests that primary sources of carbonyls might not be significant contributors to their observed concentrations.

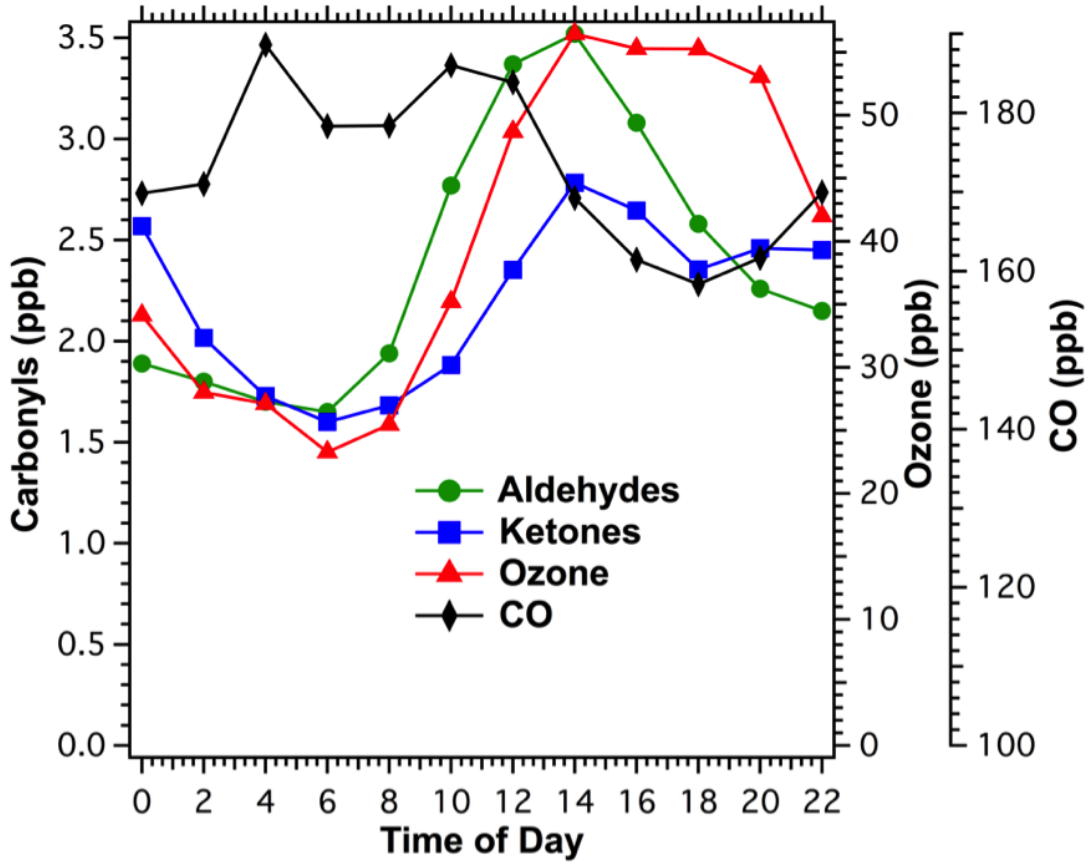

Figure 3.8: Average diurnal profile for measured aldehydes, ketones, ozone and CO.

.

3.8 Formaldehye to acetaldehyde ratio to measure the contribution of biogenic VOC to carbonyl formation

Shepson et al. (1991) proposed that the formaldehyde to acetaldehyde ratio can be used as an indicator on whether carbonyl precursors are anthropogenic or biogenic in nature. A higher $HCHO/CH_3CHO$ ratio indicates that the carbonyls are a result of the photo-oxidation of biogenic hydrocarbons, since biogenics, such as isoprene, form more formaldehyde than acetaldehyde upon photo-oxidation. In the study by Shep-

son et al (1991), model results show that the photo-oxidation of isoprene yields a $HCHO/CH_3CHO$ ratio of 10. In rural areas, this ratio ranges from 3 - 10 and in urban areas this value can range from 1 - 2 (Shepson et al., 1991; Cerón et al., 2007; Khwaja and Naranj, 2008). Grosjean (1992) showed that this ratio, while useful, can be very variable ranging from 0.29 - 14.3 in urban areas, which he attributed to variable fuels used and the use of catalytic converters. Nevertheless many studies have utilized this ratio to gain insight into carbonyl precursors (Possanzini et al., 1996, 2007; Aiello, 2003; Cerón et al., 2007; Khwaja and Naranj, 2008)

Figure 3.9 shows the HCHO to CH_3CHO ratio observed in this study. The 5^{th} - 95^{th} range observed was 0.713 - 3.60 with a median ratio of 2.16. The median ratio suggests that the photo-oxidation of anthropogenic VOCs was the main source for the photochemical formation of carbonyls. Specifically for this study, 41% of the points in Figure 3.9 are ≤ 2 and suggests anthropogenic precursors, while only 11% are ≥ 3 indicating biogenic contributions. It then follows that 48% of the points in Figure 3.9 are in the $2<HCHO/CH_3CHO<3$ range, and are believed to result from the photo-oxidation of both anthropogenic and biogenic VOCs. This last statement is in line with the conclusions from section 3.4, where isoprene accounts for 32% of formaldehyde photochemical formation.

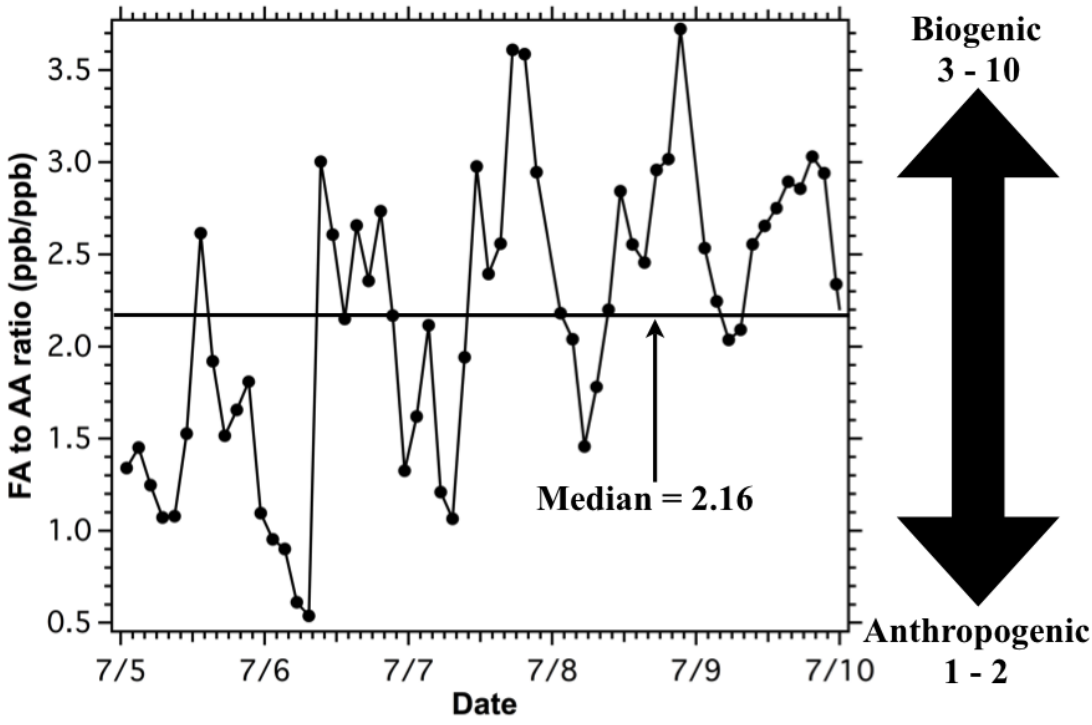

Figure 3.9: Formaldehyde to acetaldehyde ratio as an indication for biogenic influences in carbonyl formation.

.

3.9 Effect of trans-boundary transport on carbonyl concentrations

Air quality in Ontario is directly affected by local emissions and long range transport from the United States. The impact of this transport increases from the northeast to southwest of the province. During smog episodes, it is estimated that more than 50% of Ontarios O_3 and $PM_{2.5}$ levels is attributed to long range trans-boundary transport (OME, 2003). This contribution could be as much as 90% in border cities such as those in the extreme southwest, the northern shore of Lake Eire and the eastern shore of Lake

Huron (OME, 2003; Yap et al., 2005). In addition, the highest numbers of ozone and $PM_{2.5}$ exceedances were reported in areas closest to the border (OME, 2006).

Brankov et al (2003) studied the effect of trans-bounday transport on ozone levels in Toronto. In their study, Brankov et al (2003) observed the highest O_3 concentrations with air flow regimes that travelled over the United States. Owega et al. (2006) observed an increase in $PM_{2.5}$ mass concentrations in Toronto with southwestern winds, whereby the sampled air masses had passed over Michigan, the Ohio Valley and Southern Ontario.

In Ontario, the effect of long range transport on carbonyl concentrations has not been studied to our knowledge and will be covered in this section. The history of the airmass was probed in order to investigate the effects of trans-boundary pollution on carbonyl concentrations. This is similar to the studies of Brankov et al (2003) and Owega et al (2006) discussed above, although at a smaller scale for this study. Figure 3.10 is a time series of the mixing ratios of carbonyls, O_3 and CO. The mixing ratios of O_3 and CO are shown as indicators of photochemical activity and primary transportation emissions respectively. Three case studies of elevated carbonyl concentrations on the 5^{th}, 8^{th} and 9^{th} are highlighted and will be discussed below.

July 5^{th}

Elevated concentrations of carbonyls were observed in the afternoon, with the highest concentrations detected at 13:00. Peak concentrations of formaldehyde, acetaldehyde and acetone were 3.0, 1.15 and 2.9 ppb respectively. A concurrent increase in O_3 mixing ratio was also observed reaching 57 ppb at 14:00. In this time period, a

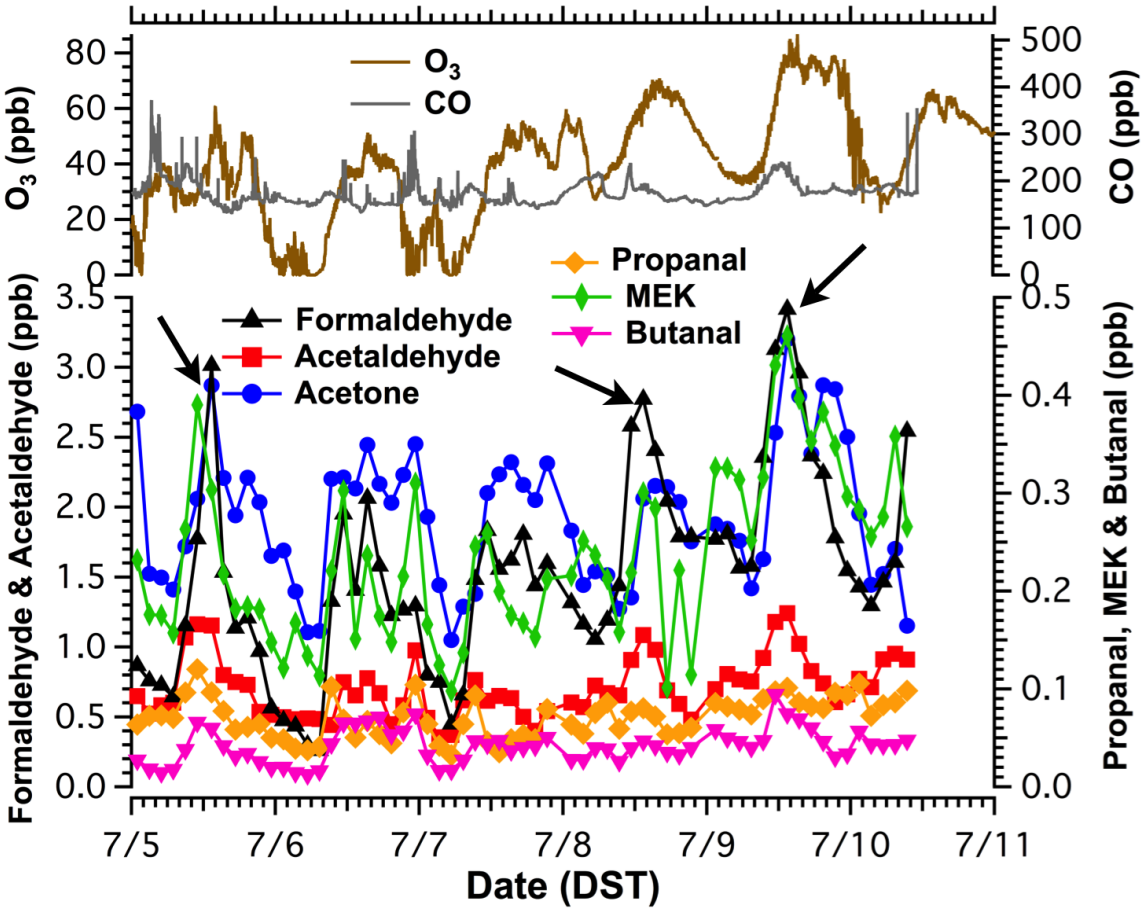

Figure 3.10: Case studies of elevated carbonyl concentrations are highlighted, which were observed during BAQS-Met.

.

decreasing trend of CO mixing ratio was observed. The increase in O_3 and decrease in CO suggest a secondary photochemical formation mechanism rather than primary transportation emission sources.

Figure 3.11 shows the 24 hr back trajectory of the airmass arriving Ridgetown on July 5^{th} at 13:00. This back trajectory was computed using the NOAA HYbrid Single-Particle Lagrangian Integrated Trajetory (HYSPLIT) (Draxler and Rolph, 2014; Rolph,

Figure 3.11: Airmass back trajectory (24 hr) arriving at Ridgetown at 13:00 on July 5^{th} computed using the NOAA HYSPLIT model. Heights computed: 200 m (Red), 500 m (blue), 1000 m (green).

.

2014). The airmass back trajectory was computed for three different heights arriving at Ridgetown, namely 200 m (red trace), 500 m (blue trace) and 1000 m (green trace). The back trajectory shows that the airmass passed over the state of Michigan, close to the cities of Saginaw and Flint and then shifted south-east north of Pontiac and Detroit (major city) and south of Port Huron and Sarnia. This back trajectory suggests that emissions from the U.S state of Michigan could have contributed to the enhancement of carbonyls and O_3 in Ridgetown, Ontario on the 5^{th} of July.

July 8^{th}

The mixing ratios of carbonyls were relatively high on the afternoon of this day.

This day was part of a regional smog episode that lasted from the 8^{th} to the 10^{th} of July. Carbonyls mixing ratios peaked at 13:00 reaching 2.8, 1.1 and 2.1 ppb for formaldehyde, acetaldehyde and acetone respectively. A wide O_3 peak was also observed in the afternoon reaching 70 ppb while CO levels stayed largely constant at $\sim$ 185 ppb. This is consistent with a photochemical formation mechanism similar to that of the 5^{th}.

Figure 3.12 shows the 24 hr HYSPLIT back trajectory of the airmass arriving at 13:00 on July 8^{th} at 200, 500 and 1000 m similar to Figure 3.11 above. The back trajectory shows the airmass passing over the states of Illinois and Michicgan, with all traces showing the airmass passing close to the major city of Detroit. Furthermore, The 500 m trace shows the airmass passing in close proximity to the major city of Chicago. Similar to the July 5^{th} case study, the enhancement of carbonyl and O_3 mixing ratios seems to be related to trans-boundary pollution, which in this case is from Illinois and Michigan.

July 9^{th}

During this study, the highest carbonyl and O_3 concentrations were observed on this day. The mixing ratios of formaldehyde, acetaldehyde and acetone peaked in the afternoon reaching 3.4, 1.2 and 3.2 ppb respectively. For O_3 and CO, elevated concentrations were observed peaking at 85 and 240 ppb respectively between 13:00-14:00. The increase in carbonyl and O_3 suggests photochemical formation. The increase of CO could be due to its secondary formation associated with ageing of the airmass although primary sources of CO can not be discounted. Secondary sources of CO include the degradation of formaldehyde by OH oxidation and photolysis.

Figure 3.12: Airmass back trajectory (24 hr) arriving at Ridgetown at 13:00 on July 8^{th} computed using the NOAA HYSPLIT model. Heights computed: 200 m (Red), 500 m (blue), 1000 m (green).

.

The wind direction on this day was from SW-W with average wind speeds of 11 m s^{-1}. Figure 3.13 shows the 24 hr HYSPLIT back trajectory for the airmass arriving Ridgetown at 13:00 and heights of 200, 500 and 1000 m similar to Figures 3.11 and 3.12 above. The airmass history of July 9^{th} is very similar to that of July 8^{th} discussed above. In both cases the airmass passes over Illinois and Michigan, with all traces showing the airmass passing in close proximity to Detroit and the 500 m trace shows the airmass passing close to the city of Chicago. The highest concentrations of carbonyls and O_3 observed in this study are coincident with an episode of trans-boundary transport. Finally, this study shows that carbonyl concentrations are enhanced with trans-boundary

Figure 3.13: Airmass back trajectory (24 hr) arriving at Ridgetown at 13:00 on July 9^{th} computed using the NOAA HYSPLIT model. Heights computed: 200 m (Red), 500 m (blue), 1000 m (green).

.

transport similar to O_3 and $PM_{2.5}$ reported in this study and by Brankov et al (2003) and Owega et al (2006) respectively.

3.10 Determination of ozone sensitivity in Ridgetown using the HCHO to NO_2 ratio

Tropospheric ozone is a major component of smog and has adverse health, climate and environmental effects (OME, 2006; WHO, 2006; IPCC, 2013). The formation of O_3 from VOCs and NO_x is non-linear in nature (Tonnesen and Dennis., 2000). The formation of O_3 is dependent on organic radical propagation, i.e. whether a peroxy

organic radical self-reacts in a NO_x limited regime or OH reacts with NO_2 to form HNO_3 in a VOC limited regime (Pugliese et al., 2014). Ozone sensitivity to its precursors is conditional, for example, O_3 will increase with increasing NO_x concentration in a NO_x limited regime, but O_3 might decrease with increasing NO_x in a VOC limited regime due to titration of O_3 by NO (Sillman et al., 1995). The determination of local and regional O_3 sensitivity to VOC and NO_x is important in the development of effective control strategies to limit O_3 formation.

Sillman et al (1995) proposed measurement ratios that are directly related to O_3 sensitivity towards VOC and NO_x. One such ratio is the $HCHO/NO_y$. The basis of this ratio is that HCHO reactivity is roughly equal to the reactivity sum of all reactive organic gases, while NO_y levels were significantly different for VOC versus NO_x limited regimes. In this study, HCHO measurements are available but NO_y measurements are lacking. Tonnesen and Dennis (2000) suggested that $HCHO/NO_2$ is more useful than $HCHO/NO_y$. They argue that the competition between NO_2 and VOC for reaction with OH is better approximated with the $HCHO/NO_2$ ratio than the $HCHO/NO_y$ ratio. In this section we will estimate local O_3 sensitivity at Ridgetown using the $HCHO/NO_2$ ratio proposed by Tonnesen and Dennis (2000), where $HCHO/NO_2<0.8$ indicates a VOC limited regime, $0.8\leq HCHO/NO_2\leq 1.8$ is either VOC limited or has equal sensitivity to VOC and NO_x and $HCHO/NO_2>1.8$ is NO_x limited. There are limitations to the use of this indicator, which were outlined by Tonnesen and Dennis (2000). The $HCHO/NO_2$ indicator performs poorly on cloudy days with low O_3 concentrations. This indicator and other proposed indicators, such as O_3-background/HNO_3, $H_2O_2/(O_3+NO_2)$,

H_2O_2/O_3 and O_3/NO_x, can clearly and easily distinguish between O_3 formation conditions that are strongly NO_x limited and those that are strongly VOC limited. All the aformentioned indicators, however, did not reliably distinguish between NO_x and VOC limited areas especially when the conditions are ideal for maximum O_3 formation.

For this analysis, HCHO and NO_2 afternoon (13:00 - 18:00) data were used. DOAS NO_2 data were not available for the 8^{th} and 9^{th} of July. For these days, NO_2 measurements with chemiluminescence (CL) monitors were used. With this measurement technique, NO_2 is reduced to NO and detected by chemiluminescence after reaction with O_3. The disadvantage of using the CL NO_2 measurement technique is that other oxidized species such as peroxyacetyl nitrate and nitric acid are also reduced to form NO. As such NO_2 is significantly overestimated using the CL technique (Steinbacher et al., 2007; Dunlea et al., 2007). In order to correct the CL NO_2 data from intemperances, the afternoon NO_2 data from both techniques were inter-compared for the entire BAQS-Met intensive from June 21^{st} to July 10^{th}(Figure 3.14). From the linear regression analysis in Figure 3.14, NO_2 measurements by CL NO_2 overestimated NO_2 mixing ratios by 27% during BAQS-Met.

In a study by Steinbacher et al. (2007) at two rural sites in Switzerland, measurements of NO_2 by CL were overestimated by 17 to 30 % at a non-elevated site and 24 to 57% at an elevated site. This overestimation was highest during the spring and summer months due to enhanced photochemistry (Steinbacher et al., 2007). Dunlea et al (2007) showed that CL monitors overestimated NO_2 mixing ratio by as much as 50% in Mexico City during afternoon hours. In this study, the observed 27% overestimation is in line

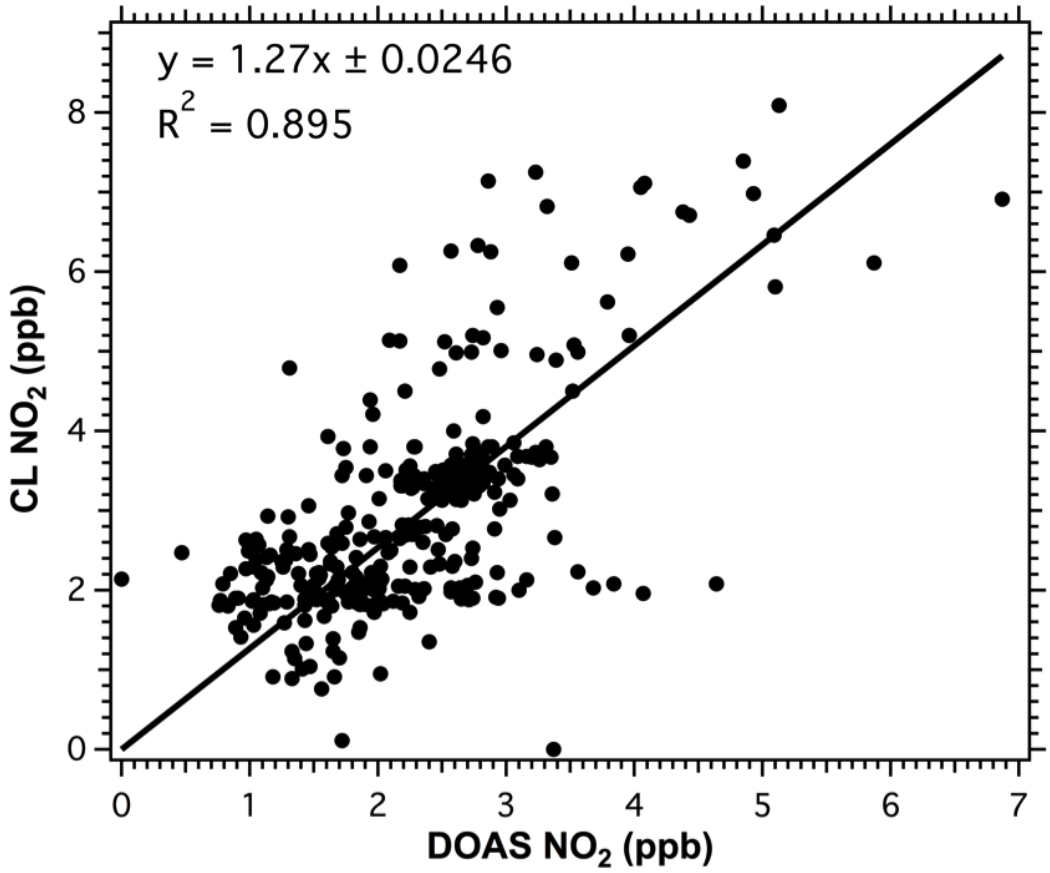

Figure 3.14: Inter-comparison between measurements of NO_2 by chemiluminescence and DOAS techniques.

.

with the studies by Steinbacher et al. (2007) and Dunlea et al (2007).

Given the observed overestimation (Figure 3.14), the "real" NO_2 mixing ratios for the 8^{th} and 9^{th} of July were established by dividing the CL NO_2 by a 1.27 factor. The HCHO/NO_2 ratios observed are shown in Figure 3.15. The ratio of HCHO to NO_2 ranged from 0.50 to 1.58 with a study-wide average of 1.00. This suggests that Ridgetown is either sensitive to VOCs or has equal sensitivity to VOC and NOx as

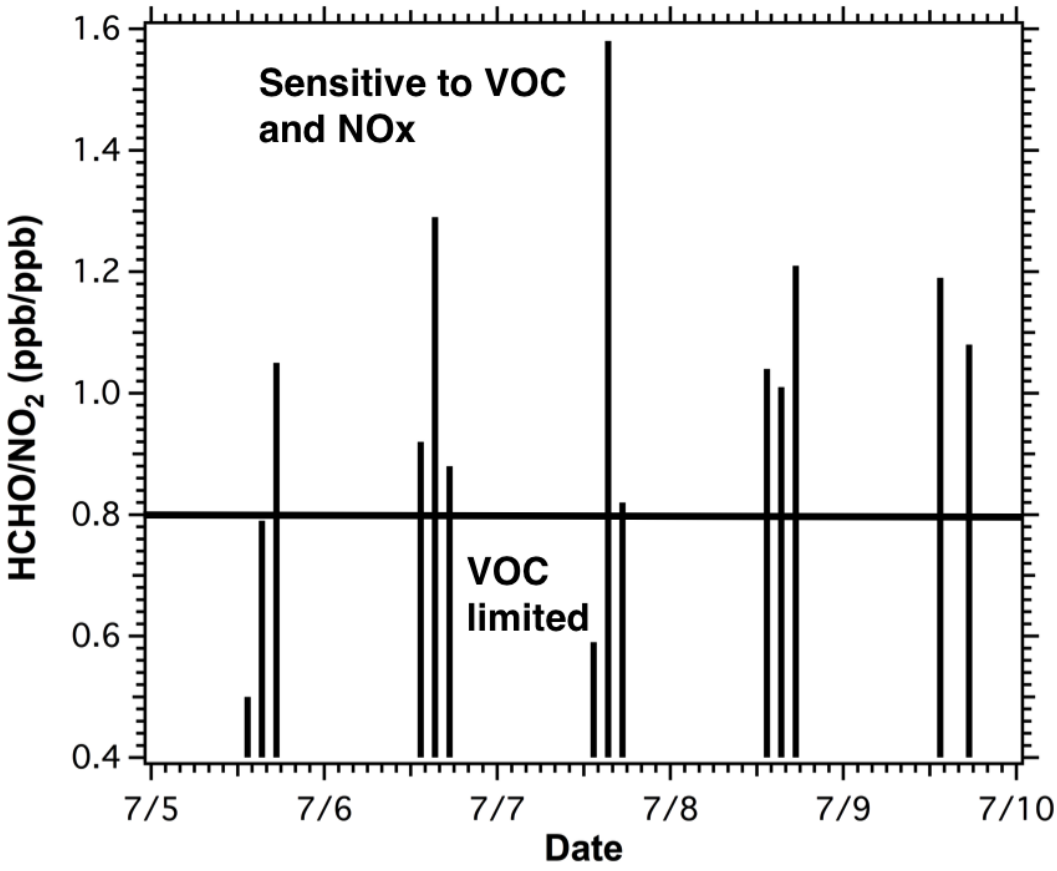

Figure 3.15: Formaldehyde to NO_2 ratio as a surrogate for ozone sensitivity.

.

discussed previously.

Rural areas are typically NO_x limited (Sillman et al., 1999) and the results of this study are, therefore, not typical of rural areas. When impacted by urban plumes, rural areas can exhibit VOC limited chemistry (see Sillman 1999, and references therein). Evidence of trans-boudary transport was discussed in section 3.9, and urban plumes were encountered on July 5^{th}, 8^{th} and 9^{th}, which is consistent with VOC sensitive regimes discussed by Sillman (1999). The 6^{th} and 7^{th} of July show similar VOC sensitivity to the

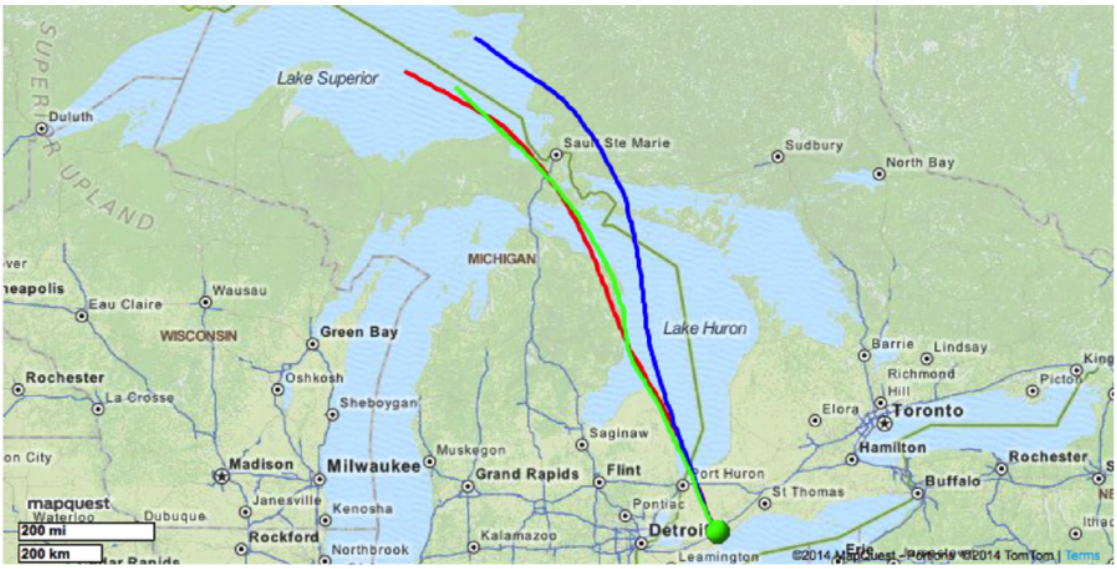

Figure 3.16: Airmass back trajectory arriving at Ridgetown at 13:00 on July 6^{th} computed using the NOAA HYSPLIT model. Heights computed: 200 m (Red), 500 m (blue), 1000 m (green).

.

5^{th}, 8^{th} and 9^{th} of July (Figure 3.15). These airmasses, however, were not investigated thus far and will be investigated here. Airmass HYSPLIT 24 hr back trajectories were computed for the 6^{th} and 7^{th} of July in a similar fashion to the analysis in section 3.9 (Figures 3.16 and 3.17). From Figure 3.16, the airmass passed close to the cities of Sault Ste. Marie, Port Huron and Sarnia, with the latter home to petrochemical refineries and other industries. For July 7^{th}, the airmass was close to the cities of Saginaw, Flint, Pontiac and Detroit. For these two days urban plumes could also give rise to the VOC sensitivity observed in Figure 3.15.

Finally, Makar et al (2010) investigated the sensitivity of O_3 towards VOC and NO_x in Ontario using an A Unified Regional Air-quality Modelling System (AURAMS). In

Figure 3.17: Airmass back trajectory arriving at Ridgetown at 13:00 on July 6^{th} computed using the NOAA HYSPLIT model. Heights computed: 200 m (Red), 500 m (blue), 1000 m (green).

.

their analysis, Makar et al (2010) examined the effect of 5% local emission perturbations of various VOCs and NO_x on O_3 formation. For the Ridgetown area, Makar et al (2010) showed high O_3 sensitivity towards VOCs, where an increase in VOCs leads to an increase in O_3. NO_x sensitivity for this area was also reported by Makar et al (2010) where an increase in NO_x leads to a decrease in O_3 due to the titration reaction of NO with O_3. We therefore conclude that for this area, ozone reduction is best achieved through a decrease in VOC and NO_x emissions locally and across the border.

3.11 Contribution of carbonyls and other VOCs to the formation of tropospheric ozone

In section 3.3 we explored the relative reactivity of carbonyls and NMHC towards OH radical, while in section 3.10 we explored the adverse effect of tropospheric ozone and the important role that VOCs play in the formation of ozone at Ridgetown. In this section we investigate how the reactivity of carbonyls and other VOCs lead to the formation of tropospheric ozone. For this analysis we use the maximum incremental reactivity (MIR) values proposed by Carter (2010), where the mass of ozone formed per mass of precursor VOC is calculated for various VOCs and under variable atmospheric conditions. This scale was developed using a one-day box model, where the NO_x emissions and initial concentrations was adjusted such that ozone was most sensitive to VOC emission variations. An increase in NO_x in this scenario would lead to a decrease in O_3 due to titration (Carter 1994; 2010).

For this analysis, the mixing ratios were converted to concentrations in μg m^{-3}, since the MIR values are grams of ozone formed per grams of precursor VOCs. All VOC measurements were discussed previously. Table 3.11 shows the average study-wide VOC concentrations used in this analysis. MIR values from Carter (2010) are also shown in Table 3.11. The product of VOC concentration and MIR gives us the amount of ozone formed from the precursor VOC (Table 3.11). Figure 3.18 and Table 3.11 show the relative contribution of carbonyls and other VOCs to tropospheric O_3 formation. The % Δ O_3 is calculated using the percentage ratio of O_3 formed from each

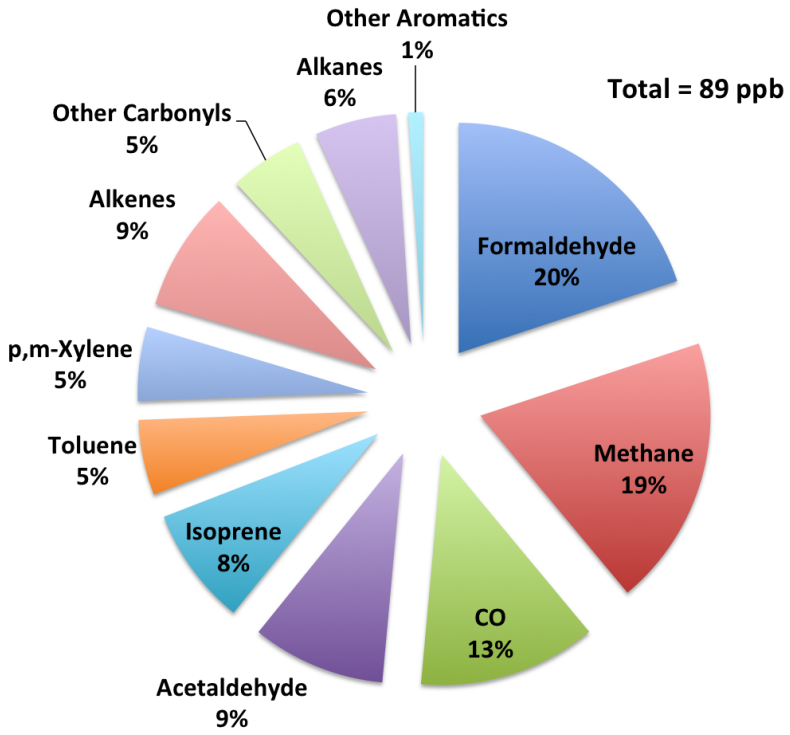

Figure 3.18: Relative contribution of carbonyls and other VOCs to the formation of tropospheric ozone.

.

VOC (HCHO for example) to the sum O_3 projected to form from all VOCs considered here.

From Table 3.11 and Figure 3.18, the highest contributions to ozone formation were formaldehyde and CH_4 at 20% and 19% respectively. Significant contributions were also observed for CO, acetaldehyde, isoprene, toluene and p,m-xylene at 13%, 9.4%,, 8.3%, 5.3 % and 5.2% respectively. Alkenes accounted for 8.5%, 5.2% of which were contributions from ethene (3.2%) and propene (2%). Alkanes (excluding methane), other carbonyls and aromatics accounted for 5.7%, 5.2% and 1.0% respectively. This analysis

Table 3.11: Carbonyl and VOC concentrations along with MIR values (Carter, 2010) used to estimate carbonyl and other VOC contributions to O_3 formation.

VOC	μg m^{-3} [a]	MIR	μg m^{-3} O_3	% Δ O_3
Formaldehyde	1.88	9.46	17.8	19.9
Methane	1176	0.0144	16.9	19.0
CO	199	0.0560	11.1	12.5
Acetaldehye	1.28	6.54	8.35	9.38
Isoprene	0.696	10.6	7.38	8.29
Toluene	1.18	4.00	4.71	5.29
p,m-Xylene	0.594	7.80[b]	4.63	5.20
Alkenes	0.809[c]	5.49 - 15.2	7.53	8.45
Alkanes	6.20[c]	0.28 - 1.5	5.10	5.73
Other Carbonyls	5.57[c]	0.360 - 7.08	4.60	5.17
Other Aromatics	0.438[c]	0.72 - 7.64	0.926	1.04

[a] Average concentration unless otherwise specified

[b] Average of p-xylene and m-xylene

[c] Sum of average concentrations

highlights the importance of carbonyl compounds as precursors for tropospheric ozone formation. In this study, the contributions of these six carbonyls to ozone formation was observed to be 34.5%. Using this analysis, an overlap in O_3 formation between different VOCs might be expected. For example, the formation of ozone from CH_4 can proceed through the formation of HCHO; both of which were used for this analysis.

3.12 The effect of lake breezes on pollutant concentrations

Three lake breeze events occurred during the study period on the 7^{th}, 8^{th} and 9^{th} of July (Figure 3.19). The lake breeze fronts were identified by an increase in RH, a decrease in temperature, a change in wind direction and an increase in wind speed; these lake breeze fronts are shown as lines in Figure 3.19. No significant changes in the concentrations of carbonyls, O_3 or CO were observed with the passage of the lake breeze. A typical diurnal profile was observed for carbonyls and O_3 and did not seem to be affected by lake breezes. One could argue that the time resolution of carbonyls is too low to observe a change but the one-min measurements of O_3 and CO confirm the findings presented here for these particular cases.

The lake breeze events on these days were identified as high deformation (HD) circulation (Sills et al., 2011). With HD events, the developement of lake breeze fronts in upwind and downwind shores are prevented due to the synoptic wind, however, a front can be observed parallel to the synoptic wind as the thermal contrast is maintained there. The HD circulation is typically characterized by high wind speeds (Sills et al.,

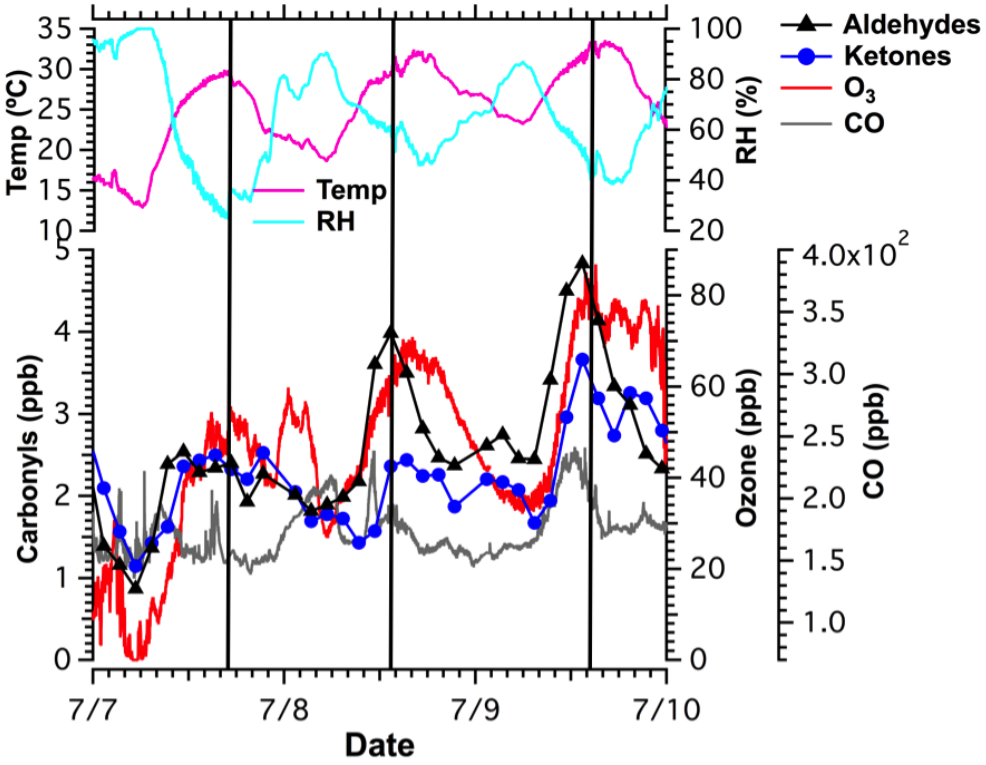

Figure 3.19: Lake breeze events and its effect on carbonyl, ozone and CO concentrations. Lake breeze fronts are shown as lines.

.

2011), which was consistent with our observation of increasing wind speed with the passage of the lake breeze front. The wind speed increased from 7 to 12 m s^{-1} on the 7^{th}, 9 to 15 m s^{-1} on the 8^{th} and 8 to 15 m s^{-1} on the 9^{th}.

Pollutant recirculation with HD deformation is reduced, which is due to an increase in the time required for the air parcel to move on-shore and into the lake breeze front and then back offshore. Moreover, the recirculation of pollutants does not occur on the upwind or downwind shores (Sills et al., 2011). This could explain the insignificant impact of lake breezes on pollutant concentrations observed here. This is since pollutant

enhancement is expected with the recirculation of air and the subsequent airmass ageing. Note that changes in O_3, CO and aerosol concentrations were observed during BAQS-MET with lake breezes outside this study period (Makar et al., 2010; Sills et al., 2011; Brook et al., 2013). The changes reported were more pronounced with lower wind speeds, which increases recirculation and/or differential photochemical developement on alternate sides of the front.

4 High-Resolution Time-of-Flight Aerosol Mass Spectrometer

The measurement and characterization of atmospheric particulate matter (PM) in real time is challenging. This is due to the fundamental complexity of the aerosols compounded with low mass concentrations and a wide size range of PM (Canagaratna et al., 2007). Traditional measurement methods involve the collection by filters and subsequent analysis to determine mass distribution and chemical composition. These methods typically suffer from low time resolution in the order of hours to days and have several sampling artifacts that compromise the accuracy of the measurements. Finalyson-Pitts and Pitts (1999) report some of these artifacts and suggest that particles on the filter or the filter medium itself can react with gaseous pollutants in the atmosphere. In addition and due to the hygroscopic nature of some filters they tend to adsorb water from humid air. Even when the filters are not hygroscopic the particles can adsorb or desorb water.

More recently, the Aerodyne aerosol mass spectrometer (AMS) offered measurements of submicron particle concentrations and composition in real time and as a func-

tion of particle size. The AMS can also provide valuable structural information about the sampled particles from collected mass spectra. This study utilized one type of an AMS, namely the high-resolution time-of-flight aerosol mass spectrometer (HR-AMS). The following sections include a detailed description of the instrumental operation, as well as, the methodology used to establish particulate concentrations and structural information.

4.1 Principle of operation

Decarlo et al (2006) gave a full description of the HR-AMS and this section provides a summary of that description. Figure 4.1 is a schematic of the HR-AMS [3]. Sampled air is introduced to the HR-AMS through a critical orifice into an aerodynamic lens that targets submicron particles in the range of 70 to 700 nm (50% cutoff) at 1 x 10^5 Pa (Liu et al., 2007). After the particles have been focused into a narrow beam, supersonic expansion at 10^{-5} Torr accelerates the particles into the particle time-of-flight sizing region and into the detection region. Particles are then thermally vaporized upon impact on a resistively heated surface at 600 °C. The temperature of the heated surface ensures most organic species, as well as, nitrate and sulfate salts (such as NH_4Cl, NH_4NO_3 and $(NH_4)_2SO_4$ are efficiently vaporized and ionized upon impact by an electron beam, with subsequent detection in the mass spectrometer. These species that evaporate at 600 °C are known as non-refractory (NR) and largely exclude refractory species (RF) such as

[3]Reprinted with permission from Decarlo et al (2006), Figure 4.1 was published as Figure 1 in Decarlo et al. (2006).

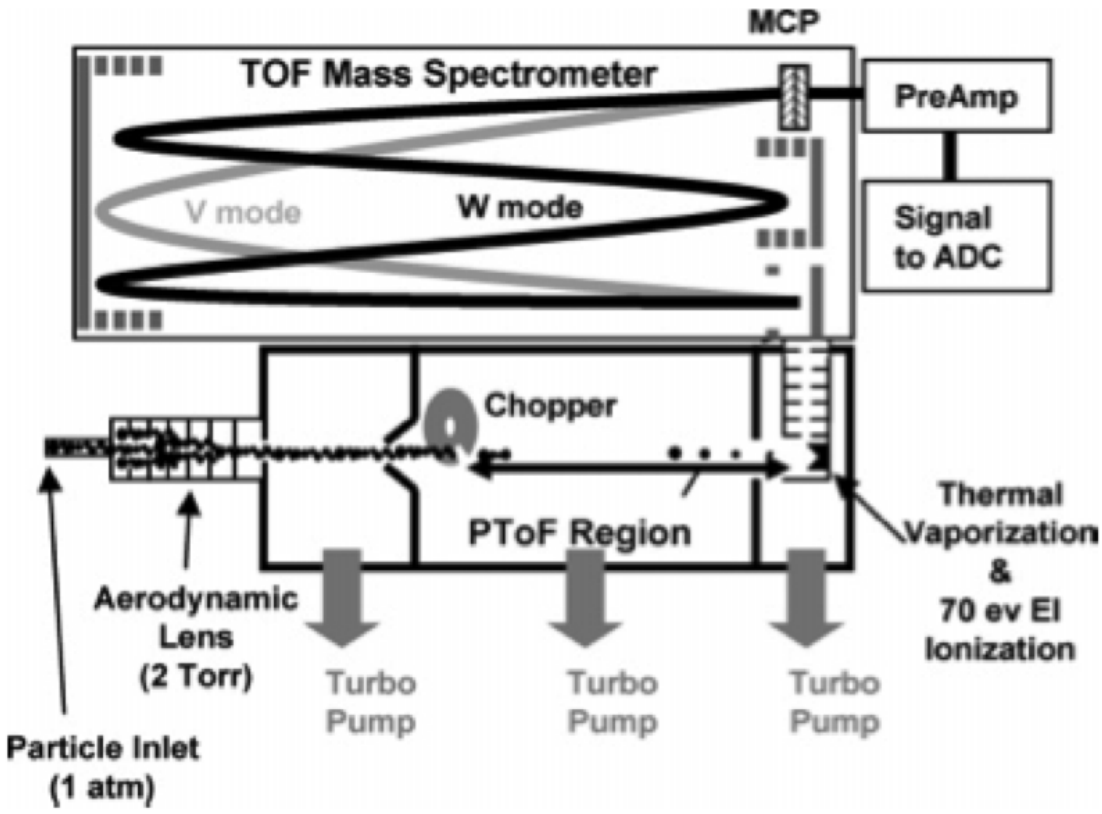

Figure 4.1: Schematic of a HR-AMS. Reprinted with permission from: Decarlo, P. F., Kimmel, J. R., Trimborn, A., Northway, M. J., Jayne, J. T., Aiken, A. C., Gonin, M., Fuhrer, K., Horvath, T., Docherty, K. S., Worsnop, D. R., and Jimenez, J. L. (2006), Field-Deployable, High-Resolution, Time-of-Flight Aerosol Mass Spectrometer, Analytical Chemistry, 78(24), 8281-8289, doi:10.1021/ac061249n. Copyright (2006) American Chemical Society.

sea salt, crustal material, black carbon and metal oxides. The vaporized particles are then ionized by electron impact ionization at 70eV.

After exiting the lens, a mechanical chopper is used to modulate the particle beam by assuming three positions: open, closed or chopped. In the open position the narrow

beam is fully transmitted into the detection region, while in the closed position the beam is completely blocked by the chopper. Placed in the chopped position, the chopper can determine the size of the particles by measuring the time it takes for the particle to travel a fixed distance, also known as time of flight.

Coupled with this system is a high resolution time of flight mass spectrometer, which operates in two modes referred to as V and W, as shown in Figure 4.1. In the V-mode, the ions travel from the extraction region and follow a traditional reflectron path ending up at the multi channel plate (MCP) detector. The effective path length in the V-mode is 1.3 m. In the W-mode, the ions make their way from the extraction region, into the reflectron and upon exiting reflect off a hard mirror that focuses the ions into the reflectron again before ending up in the MCP detector. The effective path length in the W-mode is more than double that of the V-mode at 2.9 m. Note that a longer path length, as in the case of W-mode, offers higher resolving power for the mass to charge ratios (m/z). A higher resolving power results in lower sensitivity (higher detection limits) since fewer ions make it to the detector due to lateral broadening.

The AMS typically operates in two modes known as the mass spectrum (MS) and particle time-of-flight (PTOF) respectively. In the MS mode the chopper alternates between the open and closed position every three seconds and a full spectrum of the sampled particles is obtained without particle size information. With the chopper in the open position, the signals obtained are those from particles and background gases in the detection region. In the closed position, however, the signal obtained is solely from the background gases. The particle signals are therefore obtained by subtracting

off the signals from the ions in the closed position. The data presented here are in MS V-mode only.

In the PTOF mode the particle beam is pulsed by the chopper, after exiting the aerodynamic lens. The chopper is equipped with a 2% slit opening and is rotated at 160 Hz. The opening of the slit mark time zero, while the mass spectroscopic detection marks the end of the flight path. After a delay of 200 μs, a number of mass spectra are acquired by the mass spectrometer. The spectra are separated by an extraction period that ranges from 30 to 50 μs and are recorded in the board memory. The mass spectra as a function of particle size can then be obtained by sorting the recorded spectra as a function of TOFMS extraction number from the time of the chopper opening.

4.2 Determination of aerosol chemical composition

The essence of aerosol chemical composition determination using a HR-AMS is assigning ionic fragments from the mass spectra to a family and/or species of interest. For example, an ionic fragment such as CO_2^+ at m/z 43.99, would be assigned to the organic species and to the $C_nH_mO_{w>1}$ family. The software used for the analysis, PIKA (D. Sueper, 2010), includes fits of expected ionic fragments that are automatically assigned to the species and family where applicable. One, however, must go through the spectra to ensure that the fitted ions do exist in the sampled aerosols and to include other ions that do exist in the mass spectrum but have not been fit. The identity of unfitted ions can be established by the use of their exact mass, which utilizes the various

mass defects of the ionic fragment. In addition, isotopic ratios can also be used, when applicable, to confirm the detection of the ionic fragment. Finally, some knowledge of the sampled air is required for the purposes of ionic fragment identification. Table 4.1 shows the major ion fragments used for the identification of the main species measured by the AMS; the respective m/z ratios for the ion fragments are also shown in Table 4.1. Note that H_xCl^+ group is typically depicted as a NR p-Cl when using the AMS. However, this group could include RF and NR p-Cl as will be discussed later and so this group of ions was denoted H_xCl^+ in this study.

The default ion fits were established primarily through laboratory studies, which use an AMS, and through a comparison of the obtained spectra to mass spectral databases. The laboratory studies show that a specific aerosol chemical component when measured with an AMS yields distinctive mass spectra (Canagaratna et al., 2007; Alfarra, 2004; Jimenez et al., 2003). In addition and given that the AMS utilizes a standard electron impact ionization at 70 eV, these spectra are often comparable to reported mass spectra in databases such as the National Institute of Standards and Technology (NIST) (Linstrom and Mallard, 2001). However the thermal vaporization utilized in the AMS could result in fragmentations patterns that are reproducible but significantly different than the NIST mass spectra. This difference is especially significant for species that thermally decompose and fragment upon impact with the vaporizer, such as some oxygenated organics. The mass spectra for these organics when measured by an AMS show preferentially higher intensities for small ionic fragments, such as CO_2^+ at m/z 44, when compared to their NIST counterparts. This bias in intensities is not observed if a

Table 4.1: Major ionic fragments (and their m/z ratio) used to identify the main species measured by the AMS.

Species	Parent Molecule	Major Ionic Fragments	m/z ratio
Hydrocarbon-like organics	C_nH_m	CH_3^+, $C_2H_2^+$, $C_2H_3^+$, $C_3H_3^+$, $C_3H_5^+$, $C_3H_7^+$, $C_4H_7^+$, $C_4H_9^+$	15.023, 26.016, 27.023, 39.023, 41.039, 43.055, 55.055, 57.070
Oxygenated organics	$C_nH_mO_w$	CHO^+, CH_2O^+, C_2HO^+, $C_2H_2O^+$, $C_2H_3O^+$, CO_2^+,	29.003, 30.011, 41.003, 42.011, 43.018, 43.990
Sulfate	H_2SO_4	S^+, SO^+, SO_2^+, SO_3^+, HSO_3^+	31.972, 47.967, 63.962, 79.957, 80.965
Nitrate	HNO_3	NO^+, NO_2^+, NO_3^+, HNO_3^+	29.998, 45.993, 61.988, 62.996
Ammonium	NH_4	NH^+, NH_2^+, NH_3^+, NH_4^+	15.011, 16.019, 17.027, 18.034
H_xCl^+	HCl	$^{35}Cl^+$, $H^{35}Cl^+$, $^{37}Cl^+$,$H^{37}Cl^+$	34.967, 35.977, 36.965, 37.973

species is resistant to the decomposition and fragmentation that is caused by thermal vaporization and the AMS mass spectra in this case would be very similar to the mass spectra in the NIST database (Canagaratna et al., 2007).

In the case of overlapping ionic fragments, PIKA generates a gaussian fit for each ionic fragment. However, if the ionic fragments overlap significantly and can not be distinguished by mathematical fitting then a user defined fragmentation table is utilized (Alfarra, 2004). This table can be used to deconvolve the ionic fragments using ratios of the ionic fragments obtained using the pure compounds in laboratory studies. As an example, in high resolution analysis the O_2^+ ion fragment from gaseous oxygen has significant overlap with S^+, which is an important sulfate fragment. In order to account for the S^+ fragment, the fragmentation table assigns a value to the S^+ signal that is determined through ratios of S^+ to SO_2^+, S^+ to SO^+ and S^+ to HSO_3^+. Furthermore, isotopic ratios (such as $^{37}Cl/^{35}Cl$) that utilize natural isotopic abundances are also used to deconvolve the overlap of a less abundant isotope fragment (^{37}Cl) with any other ionic fragments. When using a unit mass resolution spectrum, as is the case with the Q-AMS (Quadrupole AMS) and C-ToF-AMS (Compact Time-of-Flight AMS), this fragmentation table is a main characterization tool for establishing mass concentrations and chemical composition for the main species measured by the AMS. This table is still used with the HR-AMS but is less important due to the higher resolving power of this instrument, which in turn leads to a minimized overlap of ionic fragments.

4.3 Quantification of aerosol mass concentrations

The methodology of determining aerosol mass concentrations using an AMS was largely based on Jimenez et al (2003) and outlined by Canagaratna et al (2007). The following is a summary of the section in the Canagaratna et al (2007) study that deals with the determination of aerosol concentrations using the AMS. The AMS is capable of quantifying the mass concentrations of aerosol through a conversion of the detected ion rate I, which is obtained from the mass spectrometer at a specific m/z. A mass concentration can then be calculated by the following equation:

$$C = \frac{10^{12}\, MW}{IE\, Q\, N_A} \times I \tag{4.1}$$

Where MW is the molecular weight of the species in g mol^{-1}, Q is sampling flow rate in cm^3 s^{-1} and N_A is Avogadros number. IE is the ionization efficiency, a dimensionless quantity, which measures the ionization and detection efficiency and is defined as the ratio of the ions detected to the parent molecule vaporized. The ionization efficiency is established using monodispersed NH_4NO_3 and will be discussed further in Chapter 5. Since a species measured by the AMS fragments into multiple ions at different m/z, the total mass concentration of the species (X) can be calculated as follows:

$$C = \frac{10^{12}\, MW_X}{IE_x\, Q\, N_A} \sum_{all\ i} I_{x,i} \tag{4.2}$$

Where the summation in the above equation accounts for all the fragment ion rates of species X. In a complex aerosol sample, the two parameters that are not well constrained

in Equation 4.2 are the molecular weight and ionization efficiency. While it is feasible to establish the ionization efficiency for a small number of molecules through calibrations, it is impractical to calibrate hundreds of known inorganic and organic species. In order to overcome this complexity, a correction factor known as relative ionization efficiency (RIE) is utilized. Specifically, RIE is a ratio of the ionization efficiency of a species X to the ionization efficiency of nitrate (Alfarra, 2004). This RIE factor allows one to establish aerosol mass concentrations from the signal obtained by the AMS at a given m/z using the calibration performed for nitrate (from NH_4NO_3). The ionization efficiency of a species X can be established using the following equation:

$$\frac{IE_X}{MW_X} = RIE_X \times \frac{IE_{\mathrm{NO_3}}}{MW_{\mathrm{NO_3}}} \tag{4.3}$$

Equation 4.3 is valid given the following relationships that are based on the properties of electron impact ionization and were established by Jimenez et al (2003). The first is the linear relationship between the ionization cross section (σ) of a molecule with the number of electrons (N_e). Secondly, the ionization efficiency is proportional to σ and thirdly, for small atoms, such as S, H, C, N, O, the MW of a molecule is proportional to N_e. Given these relationships, the IE_X/MW_X ratio for a species X is proportional to σ/N_e. In addition, Jimenez et al (2003) proposes a linear relationship between IE and MW for the AMS. Canagaratna et al (2007) reports that laboratory studies observe this linear relationship. Although all species show a linear relationship, laboratory studies observed two distinct relationships for organic and inorganic species. Using Eq 4.3 and substituting it into Eq 4.2 gives us the following equation:

$$C = \frac{10^{12}\, MW_{\mathrm{NO_3}}}{RIE_x\, IE_{\mathrm{NO_3}}\, Q\, N_A} \sum_{all\ i} I_{x,i} \tag{4.4}$$

The RIE values used in this study are 1.1, 1.2, 1.3, 1.4 and 4 for nitrate, sulfate, chloride, organics and ammonium respectively based on the methodology by Jimenez et al (2003) and Alfarra et al (2004). The reason that the RIE for the nitrate signal is 1.1 and not 1 is that the ammonium nitrate calibration only uses the main nitrate ionic fragments of m/z 30 and 46. The total nitrate concentration, however, uses other ionic fragments that are not accounted for in the calibration of ammonium nitrate such as NO_3^+ and HNO_3^+ (Table 4.1). When the RIE of X is not known and/or not utilized in Eq 4.4, the value obtained is referred to as nitrate equivalent concentration (Jimenez et al., 2003; Canagaratna et al., 2007), which we denote to be NEC and is a proxy for signal intensity.

In this study, we introduce a parameter CEC, which we define to be chloride equivalent concentration. This is also a surrogate for signal intensity similar to NEC but utilizes an RIE of 1.3. This will be used for some ions with unknown RIE values such as Na^+ and $Na^{35}Cl^+$ in Chapter 5. We define an ion group H_xCl^+, which is the sum of ions typically used to establish the AMS chloride signal (Table 4.1). H_xCl^+ includes ion signals at m/z 34.97 ($^{35}Cl^+$), 35.98 ($H^{35}Cl^+$), 36.97 ($^{37}Cl^+$) and 37.98 ($H^{37}Cl^+$), where the contributions of $^{37}Cl^+$ and $H^{37}Cl^+$ are estimated using chlorine isotopic ratios (Allan et al., 2004).

Finally, drifting of the electron multiplier in the mass spectrometer results in degra-

dation of the signal magnitude per ion detected. This degradation is proportional for all ionic fragments and therefore can be detected by monitoring the ion fragments from abundant air molecules entering the mass spectrometer, such as N_2^+ and O_2^+ at m/z 28 and 32 respectively. These ions are measured continuously and are typically used to correct the data set for this signal degradation, in a correction known as an air beam correction (Allan et al., 2003).

The methodology outlined in this section and section 4.2 is incorporated in its entirety in software packages SQUIRREL (v1.51C) and PIKA (v1.10C) (Sueper, 2010) which were used for the data analysis in this study.

4.4 HR-AMS versus Q-AMS and C-ToF-AMS Models

This section will offer a comparison between the HR-AMS used in CalNex and other AMS models; namely the quadrupole AMS (Q-AMS) and compact time-of-flight AMS (C-ToF-AMS). The mass resolving power of the HR-AMS is much higher than the Q-AMS and C-ToF-AMS and Decarlo et al (2006) showed the following trend for the resolving power: W-mode > V-mode > C-ToF-AMS > Q-AMS. The authors of the aforementioned study quantified the resolving power using the ratio of the nominal m/z (m) to the full-width half-maximum (Δm). They report the maximum resolving power observed for the m/z range of 10 to 200, to be 4300 for the W-mode, 2100 for the V-mode, 800 for the C-ToF-AMS and 220 for the Q-AMS. It is because of this enhanced resolving power that the HR-AMS can separate different ions at the same nominal m/z

in real time, unlike the C-ToF-AMS and the Q-AMS, which are limited to unit mass resolution analysis.

The detection limits of HR-AMS, C-ToF-AMS and Q-AMS were also compared by Decarlo et al (2006); their results are shown in Table 4.2[4]. The values in Table 4.2 is for MS mode only, since this mode has the highest signal to noise ratio. From Table 4.2, The Q-AMS and W-mode are comparable and have the highest detection limits, which means that they are the least sensitive. The C-ToF-AMS is the most sensitive with the lowest detection limits. The time-of-flight models are more sensitive than the quadrupole-AMS because of the lower required averaging time for the TOF models. This is since, the time-of-flight mass spectrometer detects all m/z values simultaneously while the quadrupole model scans across m/z values. The difference in detection limits between the C-ToF-AMS and the V and W modes of the HR-AMS is caused by the difference in the ion throughput. DeCarlo et al. (2006) reported that there is an increase in the distance between the MCP and the extraction region for the HR-AMS when compared to the C-ToF-AMS. In addition and as was mentioned previously, the W-mode is less sensitive than the V-mode (and the C-ToF-AMS), which is caused by decreased ion throughput.

[4]The values in Table 4.2 was published in Table 2 by Decarlo et al (2006); used here with permisson.

Table 4.2: Inter-comparison of the detection limits (ng m^{-3}) of the HR-AMS deployed to CalNex and the HR-AMS, C-ToF-AMS and Q-AMS reported by Decarlo et al, 2006. Values adapted with permission from: Decarlo, P. F., Kimmel, J. R., Trimborn, A., Northway, M. J., Jayne, J. T., Aiken, A. C., Gonin, M., Fuhrer, K., Horvath, T., Docherty, K. S., Worsnop, D. R., and Jimenez, J. L. (2006), Field-Deployable, High-Resolution, Time-of-Flight Aerosol Mass Spectrometer, Analytical Chemistry, 78(24), 8281-8289, doi:10.1021/ac061249n. Copyright (2006) American Chemical Society.

Species	V-mode 70 s average[a]	V-mode 10 min average[a]	V-mode[b]	W-mode[b]	C-ToF-AMS[b]	Q-AMS[b]
Organics	51	19	22	360	19	470
Sulfate	43	16	5.2	110	2.2	160
Nitrate	14	5.2	2.9	32	1.2	32
Ammonium	59	22	38	150	16	350
H_xCl^+	21	8	12	53	4	32

[a]This study

[b]Decarlo et al. (2006)

4.5 CalNex Detection Limits

The detection limits of the five main species measured using the HR-AMS during CalNex is shown in Table 4.2. The detection limits are reported as 3σ, where σ is the standard deviation of the mass concentration of the species established using particle-free air that is charcoal and hepa filtered. This filtered air was sampled before every sea sweep experiment and was forced through the sampling mast and into the HR-AMS (Bates et al., 2012). Sea sweep experiments were utilized to generate artificial sea spray aerosols and will be covered in Section 5.4.

The detection limits are reported for 70 s sampled averages and the 10 min averages, since the latter was used for the analysis presented in the following sections. The detection limit of the 10 min averages was calculated using the 70 s detection limit and a 0.34 factor (square root of 70/600). The detection limits were higher than the ones reported by Decarlo et al. (2006) for all species, which could be due to poor instrument tuning during the study.

4.6 AMS limitations

The AMS is limited to measurements of non-refractory particle species in the sub-micron size region (70-700 nm), although this study and other recent studies have quantified refractory species such as chloride, total sea salt and lead (Ovadnevaite et al., 2012; Salcedo et al., 2010). Given the measurement size range, the AMS could show an enhancement of detectable organics over largely undetectable coarse sea salt

aerosols in the submicron region.

Another limitation of the AMS is particle bounce-off upon impact with the vaporizer, which is especially true for species with low volatility. A collection efficiency factor needs to be introduced to account for this particle bounce off effect, which introduces uncertainty in the quantification of particle concentrations. Applying a uniform collection efficiency for all species might lead to uncertainties when sampling externally mixed aerosols, where the collection efficiencies could vary for the different species. As a result of this variance, some species could be underestimated or overestimated.

In addition to particle bounce-off, Canagaratna et al (2006) suggested that the thermal vaporization method used by the AMS could result in the decomposition of labile species when flash heated. Finally, utilizing electron impact ionization in the AMS design makes the identification of parent molecules difficult, especially when analysing aerosols containing a mix of many species, which is often the case when analysing atmospheric aerosols.

5 Aerosol concentrations, composition and enhancement mechanisms off the coast of California: A focus on ambient chloride and seawater organics

5.1 Study overview

CalNex took place in California from May to July of 2010. It involved two ground sites in Pasadena and Bakersfield, several aircrafts and a Woods Hole Oceanic Institution research vessel called *Atlantis*. The broad objectives of this study were outlined by Ryerson et al. (2013) and are relevant to atmospheric pollution and climate change. These are as follows: (1) evaluate emission inventories (2) investigate atmospheric transport and dispersion (3) study atmospheric chemical processing (4) investigate aerosol-cloud interactions and aerosol radiative effects.

As part of an Environment Canada research group, I participated in the CalNex field study onboard the research vessel *Atlantis* from May 14$^{\text{th}}$ to Jun 8$^{\text{th}}$ of 2010. Figure 5.1 shows the ship track followed by *Atlantis* during CalNex. *Atlantis* departed from San Diego on May 14$^{\text{th}}$ and made its way northwest to Los Angeles, Santa Monica Bay

and Long Beach areas then further through Santa Barbara, Port Hueneme, Santa Cruz to San Francisco. *Atlantis* then headed east towards Sacramento and back into San Francisco where we docked on June 8th, 2010. Some objectives of the ship-borne study include:

1. Charcterize emissions from San Diego, Los Angeles, Long Beach Harbours, Port Hueneme, San Francisco, Sacramento and other populated regions
2. Characterize shipping emission
3. Investigate the effects of regional and long range transport
4. Study the chemical transformation mechanisms including night time chemistry
5. Determine aerosol concentration and composition in the atmosphere and ocean surface
6. Investigate aerosol- cloud chemistry and radiative forcing
7. Determine pollution levels aloft and entrainment into MBL
8. Study oceanic boundary conditions

Our objectives for this study were listed in Section 1.6. During CalNex we deployed an HR-AMS aboard *Atlantis* for the measurement of submicron particle concentrations and composition. A scanning mobility particle sizer and single particle soot photometer were also deployed but the measurements obtained from these instruments will not be discussed here as it does not pertain to this project.

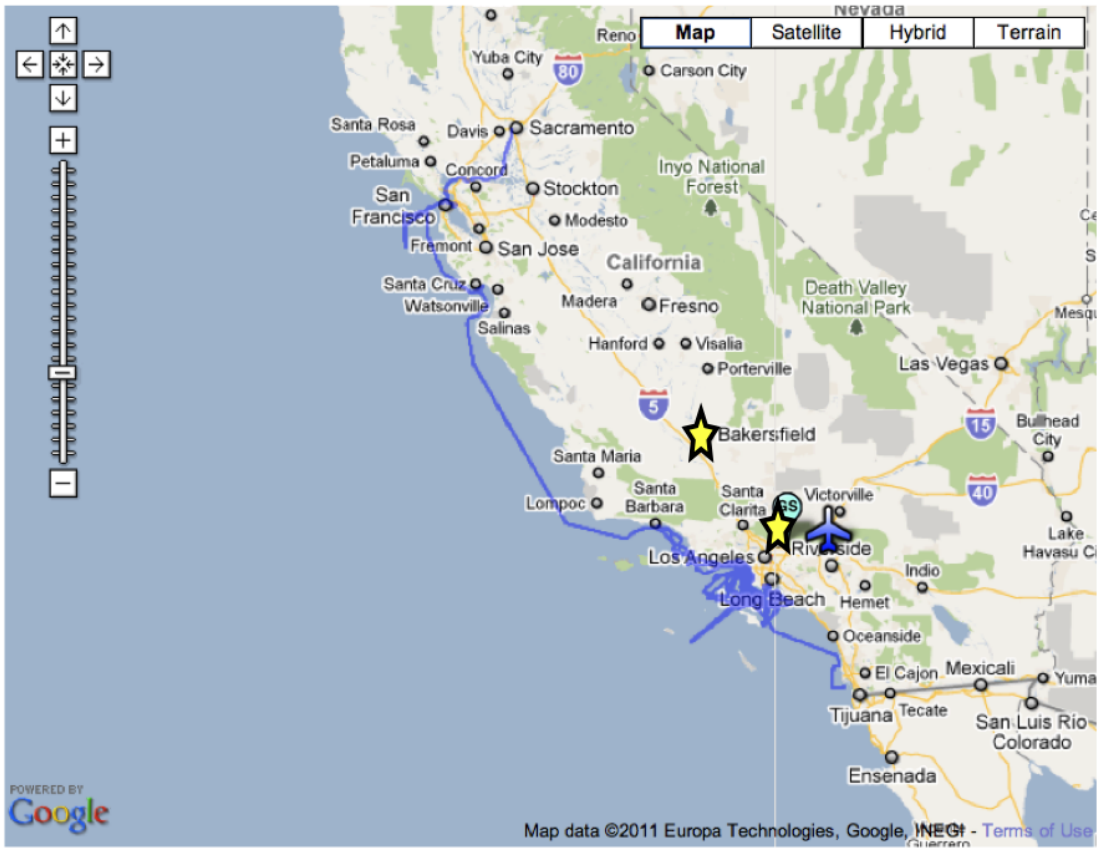

Figure 5.1: Track followed by RV *Atlantis* during CalNex from May 14$^{\text{th}}$ to Jun 8$^{\text{th}}$ 2010.

The HR-AMS was located in a container for the duration of the campaign. Figure 5.2 is a schematic of the the instrumentation setup in a container. Aerosols were sampled from a 6 m mast that is 18 m above the sea surface and well forward of the ship's stack. Sampled aerosols then passed through a submicron impactor (1.1 μm cutoff) and into the HR-AMS then into the soot photometer AMS, the cavity ring down/photoacoustic, single particle soot photometer and the scanning mobility particle sizer. The relative humidity of the sampled air was maintained at 55% (Bates et al., 2012; Cappa et

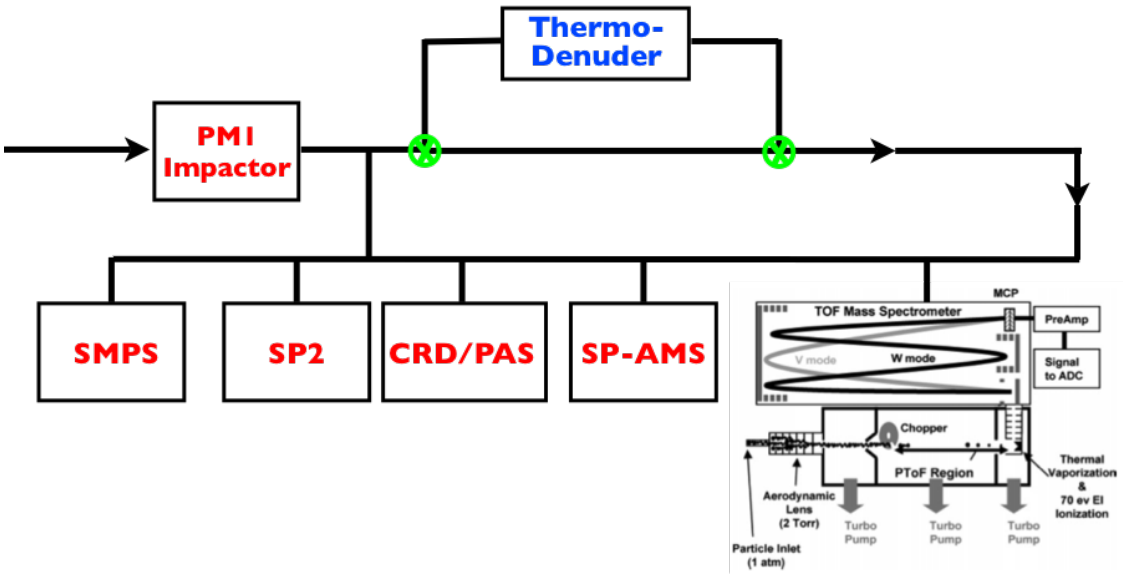

Figure 5.2: Instrumentation setup in the container aboard *Atlantis*.

al., 2012). The sampled air was either sampled directly in the bypass mode, or passed through a thermal denuder (made and installed by Aerodyne Inc.). The temperature in the thermal denuder was ramped from ambient to 240 °C. For most of the study, when sampling ambient air the HR-AMS was operated on a 2.5 min cycle, which alternated between the V-mode and W-mode. In the V-mode, the sampling was evenly split between the MS and PTOF modes. This sampling was adapted for the bypass and thermal denuder modes. During sea sweep experiments we only operated in bypass mode (Bates et al., 2012). For ship emissions we operated in FastMS mode, where an mass spectrum is obtained every second (Cappa et al., 2013; Lack et al., 2011). The data and subsequent analysis presented here are in bypass V-mode only.

Other measurements used in this chapter include air temperature and RH, which were measured by Eric Williams of NOAA. Photolysis rates were measured and quan-

tified by Brian Lerner of NOAA. A University of Washington chemical ionization mass spectrometer (UW-CIMS) was used to measure $ClNO_2$ (Riedel et al., 2012). Aerosol filter measurements were performed by Tim Bates and Patricia Quinn of NOAA. Using this technique aerosols were sampled using one and two-stage multijet cascade impactors (Berner et al., 1979). The concentrations of several cations and anions on the filter were determined using ion chromatography (IC) (Quinn et al., 1998; Bates et al., 2012).

5.2 HR-AMS calibrations

The HR-AMS was calibrated twice with ammonium nitrate to establish the instrument's ionization efficiency, which is an essential parameter in establishing mass concentrations as discussed previously in the experimental section. In this calibration, an aerosol Atomizer containing a solution of NH_4NO_3 was used to generate NH_4NO_3 aerosols. The aerosols were then size selected at 300 nm by an SMPS and a largely monodispersed aerosol beam is produced with concentrations of a few hundred particle/cm^3. This aerosol beam is connected to the HR-AMS by $\sim$ 1.5 m copper tubing line.

The HR-AMS was operated in the brute-force single-particle (BFSP) mode for the calibration. The BFSP mode is a version of the PTOF mode where signals for each chopper cycle is captured and saved to the computer without the typical averaging of many chopper cycles, which in this study was more than 11000 cycles per 70 s sampling average. For the HR-AMS, the BFSP mode can only be operated in the V-mode, since

the number of ions detected in the W-mode are much lower due to the longer path length and are too low for a BFSP (Jimenez Research Group, 2014). The IE values for the V-mode data used in this analysis was determined to be 1.03×10^{-7}. Recall that this value is required to accurately establish aerosol mass concentrations. The HR-AMS data shown here are 10 min averages unless otherwise specified.

5.3 Collection efficiency

In order to accurately determine the concentrations of measured aerosol species by the HR-AMS a collection efficiency (CE) parameter was applied. The CE for the HR-AMS was determined through a comparison of the ambient SO_4 concentrations measured by the HR-AMS to the submicron ($D_a < 1.1$) ambient concentrations of SO_4 measured using filters and analyzed by ion chromatography (IC), this comparison is shown in Figure 5.3.

The measurements from both methods were well correlated with R^2 of 0.97 and the CE established from Figure 5.3 is 0.468. A CE of 0.5 is commonly observed and used for the AMS (Canagaratna et al., 2007), which in line with the collection efficiency observed in this study. Given the CE determined, a correction factor of 2.14 was applied to the data set (1/CE). This correction factor corrects for loss of particles that bounce off the vaporizer upon impact. The CE correction also accounts for transmission losses of aerosols with sampling off the aerosol mast. The aerosol transmission losses are caused by aerosol impact with the tubing walls due to beam spreading.

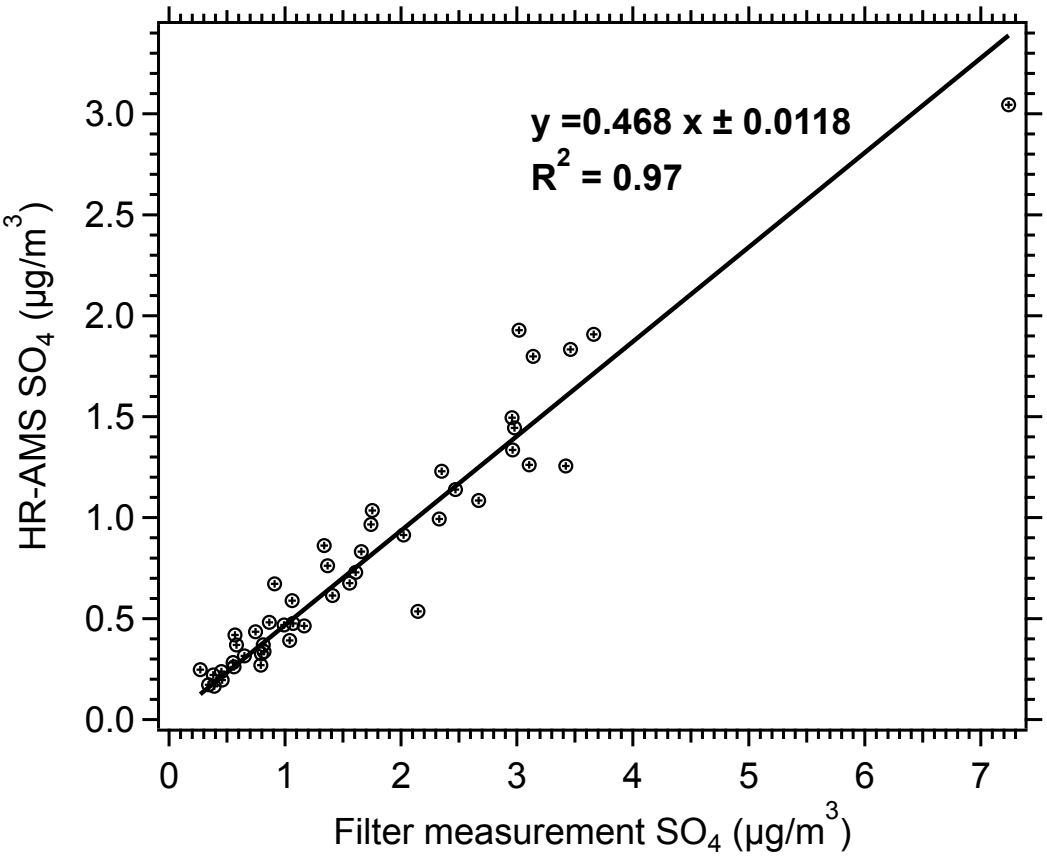

Figure 5.3: Determination of the CE of the HR-AMS through a comparison with filter measurements.

5.4 Sea sweep experiments by NOAA

During CalNex, ambient aerosols were sampled by the HR-AMS for the determination of aerosol concentrations and composition. In addition, seawater aerosols were also probed through in situ bubbling of seawater in sea sweep experiments. Figure 5.4[5] shows the schematic of the sea sweep.

[5]Reprinted with permission from Bates et al (2012), licence number:3594960141303. Figure5.4 was published as Figure 1 in Bates.

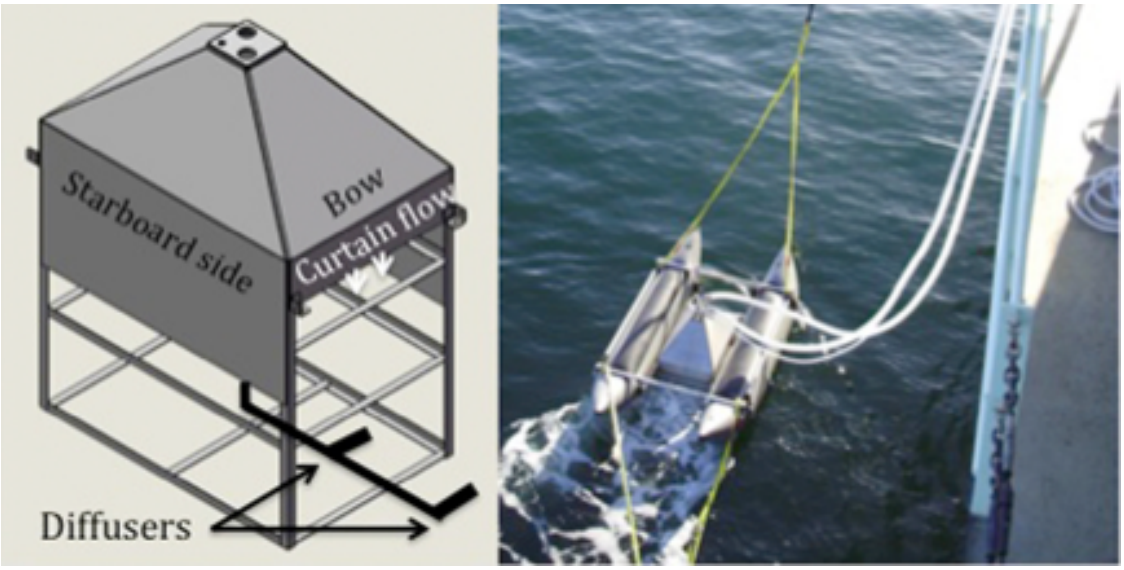

Figure 5.4: a) Sea sweep schematic designed by NOAA b) Sea sweep deployed off R/V *Atlantis*. Adapted from Bates et al., 2012, reprinted with permission.

The sea sweep frame is 0.61 m wide, 0.91 m long and 0.91 m high and is made of stainless steel flat bars. Stainless steel sheet metal covers the upper 0.15 m and 0.46 m of the frame. Stainless steel in a cone shape that is 0.3 m above the frame enclosed the top. Two inflatable pontoon floats that are 3 m long and attached to aluminium tubing support the sea sweep frame. An adjustment of the frame in the pontoons was made such that the opening was 1.0 cm above the water under calm conditions. As shown in Figure 5.4 three hoses were attached to the sea sweep cone top. One hose provides compressed air at 50 L min^{-1} to two diffusion stones that are horizontally mounted at the bottom of the frame, 0.75 m below the sea surface. A second hose provides a particle free air curtain at 2 m^3 min^{-1} to prevent entrainments of ambient air and dilute the aerosols generated. A third hose brings 1 m^3 min^{-1} of sea sweep aerosol sample

into the aerosol sampling mast used for ambient air that was mentioned earlier.

The deployment of the sea sweep was off the bow of R/V *Atlantis* with the ship position such that the wind is off the starboard bow. The sea sweep was steamed along slowly at 0.2 cm sec^{-1} to ensure continued sampling from fresh ocean surface water with the true wind blocked by the ship. While moving, most bubbles generated were captured in the enclosure while some were kept trailing behind the sea sweep. The sea sweep was deployed 11 times, 2 were contaminated with ambient air and the data obtained were discarded. One was aborted due to high winds and another was not sampled by the HR-AMS.

5.5 Overview of aerosol concentrations and composition

Figure 5.5 is a mass concentration time series of submicron aerosol species typically measured by the HR-AMS. Note that the dates shown here are in cooridnated universal time (UTC) with the local pacific daylight saving time being 7 hours behind UTC (i.e. UTC-7). UTC time will be used in all the analyses henceforth in this chapter. Aerosol levels were elevated with continental outflow events (land breezes) from populated regions. Outflow events from Santa Monica Bay (SMB), Los Angeles (L.A.), Sacramento (SAC), San Francisco area (S.F.) and Oakland (OAK) are shown in Figure 5.5. Recall that the time used here is UTC time and these land breezes took place at night and during early morning hours.

Figure 5.6 is a flexpart model by Jerome Brioude of NOAA, which shows a land

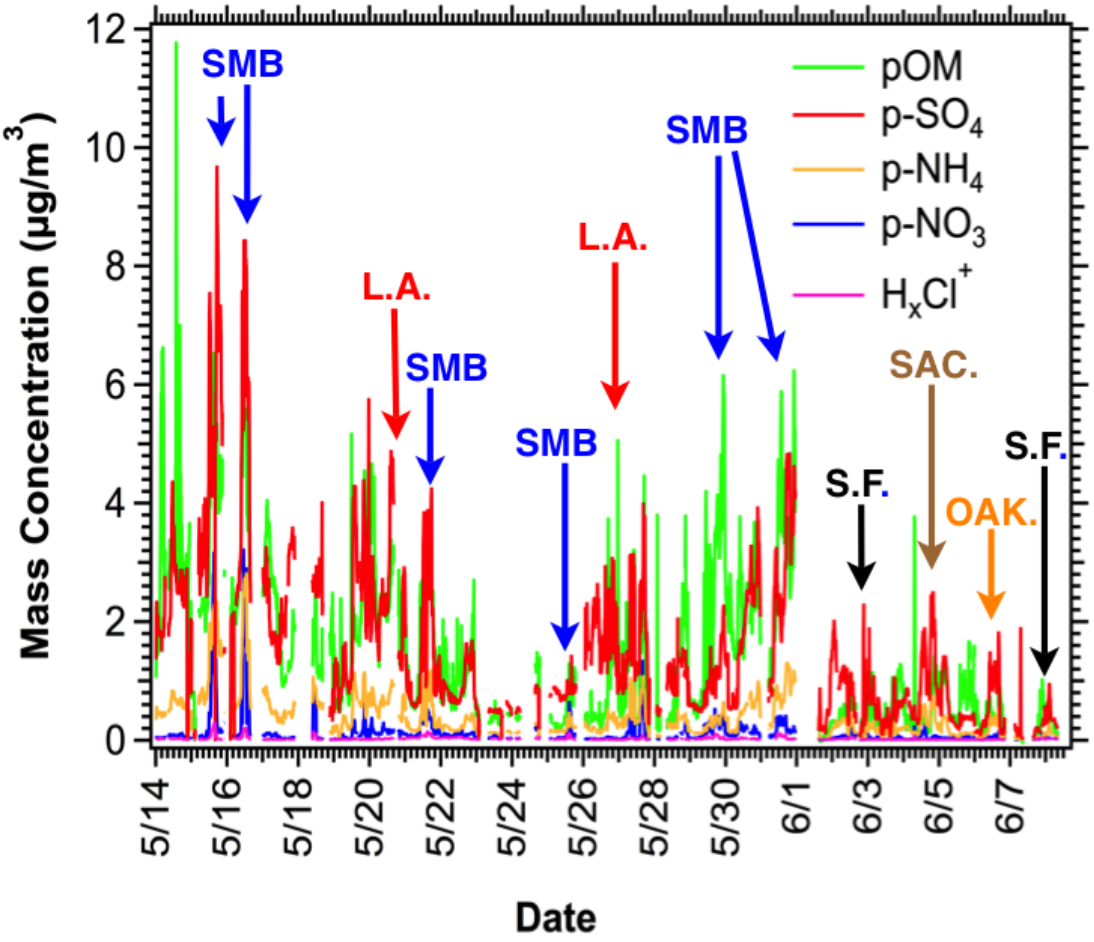

Figure 5.5: Time series of submicron aerosol concentrations measured by an HR-AMS during CalNex. Continental outflow events from Santa Monica Bay (SMB), Los Angeles (L.A.) Harbours, San Francisco (S.F.), Sacramento (SAC.) and Oakland (OAK.) are highlighted

.

breeze (continental outflow) event from Santa Monica Bay on May 21st. This outflow event is representative of other events encountered during the study in terms of sea-land air circulation and pollutant transport in Southern California. For this model CO was

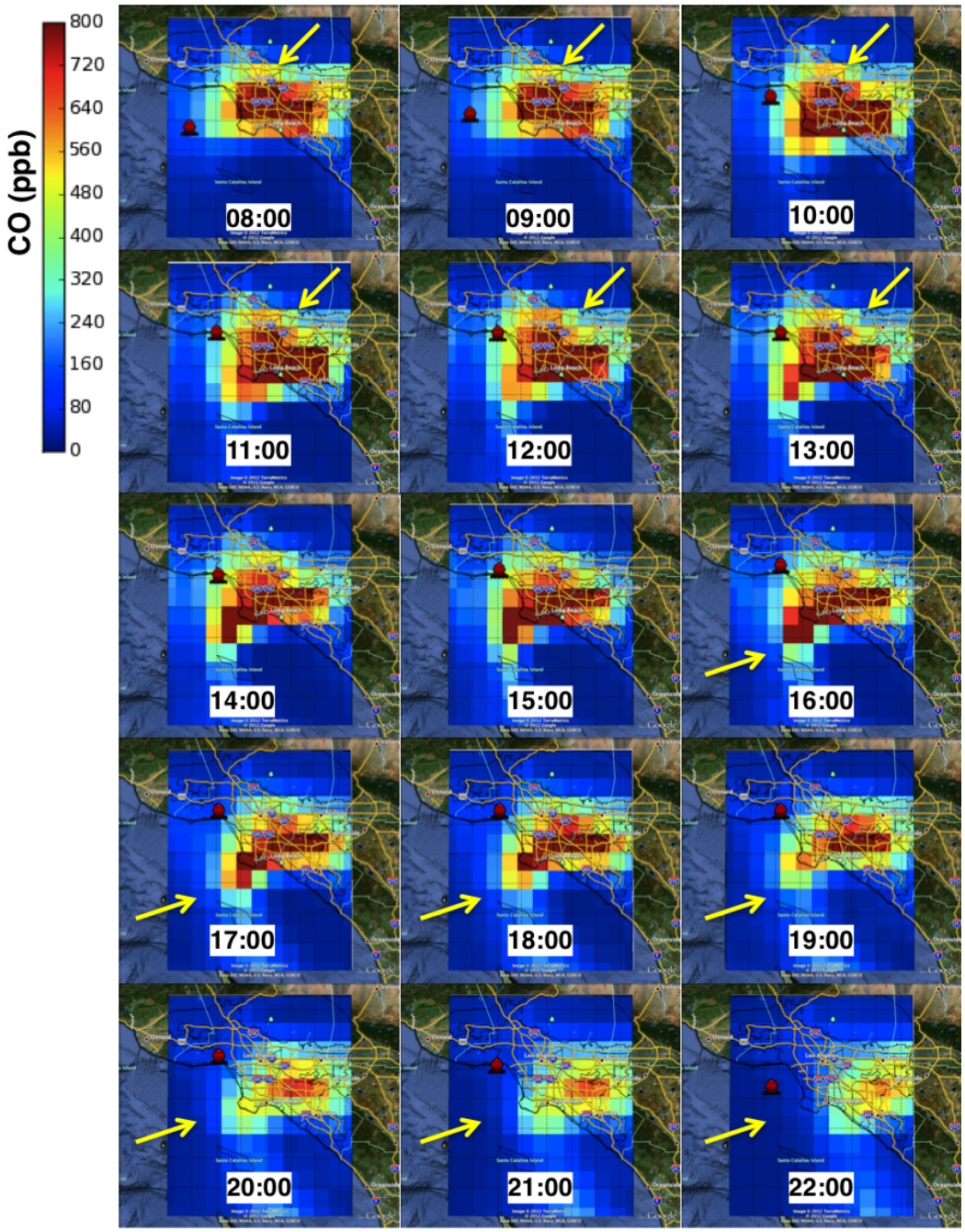

Figure 5.6: Flexpart model by Jerome Brioude of NOAA shows continental outflow when *Atlantis* approached SMB on May 21st. CO was used as a tracer for pollution. Ship position is shown in red and arrows show general wind direction.

.

used as a tracer for pollution. Also shown in Figure 5.6 is the relative ship position in red and general wind directions represented by arrows (the absence of arrows indicates variable wind direction). In this case a land breeze transported polluted air into the pacific (evening and overnight) and a sea breeze pushed a clean marine airmass back inland (morning and afternoon).

On May 21st, *Atlantis* moved into the polluted airmass around 09:30 and stayed roughly in the same position until about 21:00. The wind direction was N-NE from 09:30 to 13:32 and was variable from 13:32 to 15:22 (hence no arrows). The wind direction changed to SW transporting the polluted airmass towards the land from 15:22 until about 21:00. At about 18:00 the polluted airmass was mostly transported inland and a clean marine airmass was sampled on the ship, as observed from the flexpart model. As expected an increase in aerosol concentrations was concurrent with *Atlantis* moving into the polluted air mass. Note that *Atlantis* was not in a position of highest transported pollution at any point during the event and this was generally true for other outflow events.

Figure 5.7 shows the fractional composition of the measured aerosol species during CalNex using median concentrations. Also shown in Figure 5.7 are the O/C and H/C molar ratios for the total organic mass measured (Aiken et al., 2007; 2008). These molar ratios are indicative of the degree of oxidation of the organic mass fraction. Higher H/C ratio suggests a fresher and less oxidized air mass while a higher O/C ratio suggests a more aged and oxidized air mass. The measured aerosols were dominated by pOM and p-SO_4 with study-wide median contributions of 41% and 45% respectively.

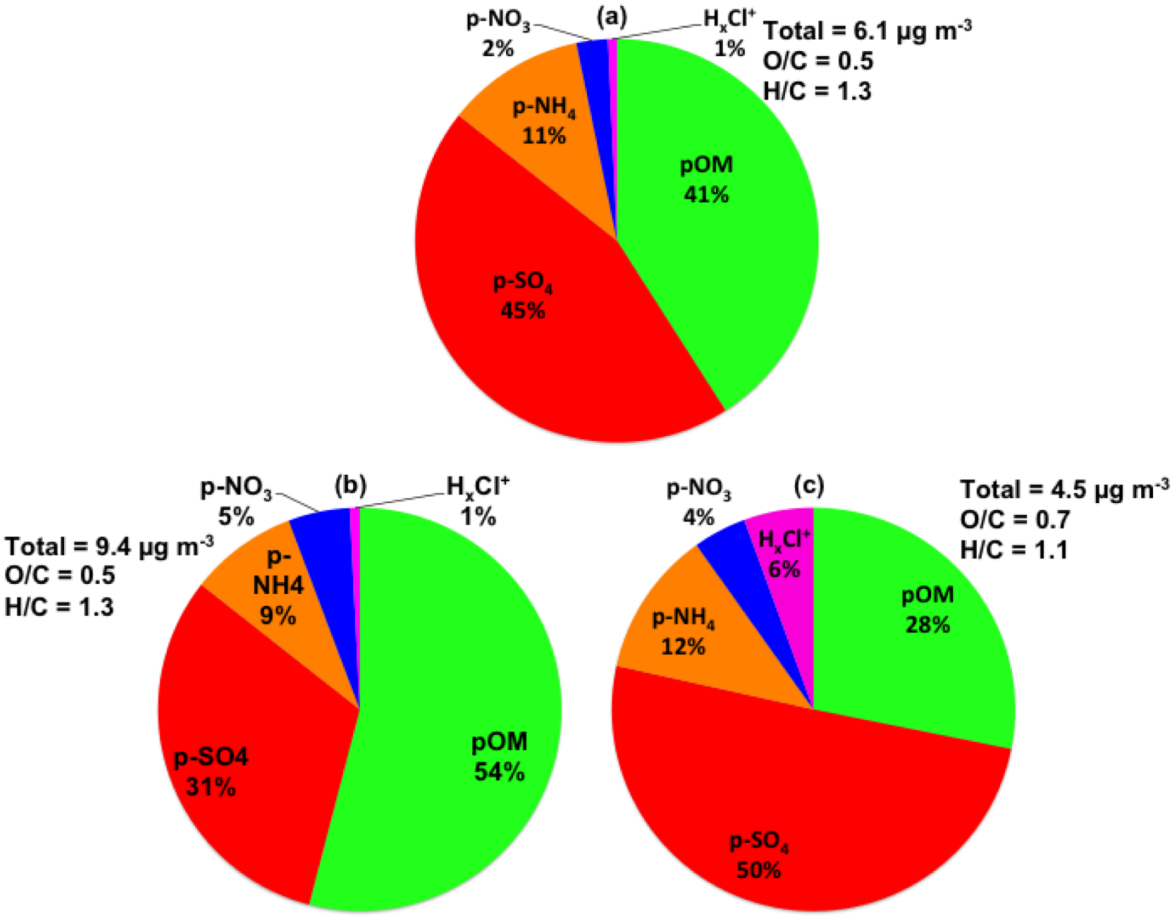

Figure 5.7: Fractional composition of submicron aerosol species measured using an HR-AMS during CalNex a) Study-wide b) Outflow events off SMB c) Background/Clean marine.

.

The median contributions of p-NH_4, p-NO_3 and H_xCl^+ were much lower at 11%, 2% and 1% respectively (Figure 5.7a).

This study-wide fractional composition is neither reflective of polluted nor of clean-marine air masses and is a mixture of both. It is therefore worthwhile to examine

Table 5.1: Periods and sampling locations of continental outflow events used in Figure 5.7b.

Start Time	End Time	Location
15 May/1140	15 May/1800	Santa Monica Bay 1-5 nm offshore
16 May/0940	16 May/1530	Santa Monica Bay 1-5 nm offshore
21 May/1000	21 May/1930	Santa Monica Bay 1-5 nm offshore
29 May/0920	29 May/1600	On station west of Palos Verdes Pt
29 May/1600	30 May/0400	Transit Santa Monica Bay coastline
30 May/0800	30 May/1300	Santa Monica Bay near Palos Verdes
30 May/1830	30 May/2130	Transit Santa Monica Bay coastline

the aerosol composition of these two distinct air masses separately. Figure 5.7b shows the fractional composition for polluted air masses. For this analysis, we used periods of continental outflow (land breezes) from the Los Angeles area when *Atlantis* approached Santa Monica Bay (Table 5.1). Note that data from May 25th were not included as the aerosol concentrations were not highly elevated (Figure 5.7). pOM was the most dominant species in continental outflow events (land breezes) with a median contribution of 54%. p-SO_4 and p-NH_4 were the 2nd and 3nd most dominant with median contributions of 31% and 9% respectively. The median contributions of p-NO_3 and H_xCl^+ were the least dominant at 5% and 1% respectively.

Figure 5.7c shows the fractional composition of aerosols in clean-marine/background air masses (sea breezes). Ryerson et al. (2013) identified these periods and further investigation revealed that some of the identified periods might be impacted by regional emissions and are not true background concentrations. As such, periods with elevated

Table 5.2: Periods and locations of clean marine/background air sampling used in Figure 5.7c.

Start Time	End Time	Location
23 May/0000	23 May/0800	Catalina Island
23 May/1530	23 May/2000	Catalina Island
27 May/1000	28 May/0130	Sea lanes south of Pt. Fermin
06 Jun/1900	07 Jun/1900	Farallon Islands

aerosol concentrations were excluded from the analysis of clean-marine/background air. Within this context, elevated aerosol levels were defined to be those that are greater than or equal to 0.6 or 0.5 μg m^{-3} for p-SO_4 and pOM respectively. Table 5.2 shows the locations and time periods used for the clean-marine analysis. Results from the analysis shows p-SO_4 to be the most dominant species at 50% followed by pOM, p-NH_4, H_xCl^+ and p-NO_3 with median contributions of 28%, 12%, 6% and 4% respectively.

A comparison between Figures 5.7b and 5.7c shows that aerosol levels are more than a factor of two higher in polluted air masses associated with land breezes when compared to clean marine cases which are associated with sea breezes. Furthermore the contribution of p-SO_4 and H_xCl^+ are significantly higher for clean-marine air masses, while that of pOM is significantly lower. The prominence of p-SO_4 in clean-marine air could be indicative of a more oxidized air mass and/or sea salt sulfate and/or the oxidation of DMS. A more oxidized airmass is consistent with a higher median O/C ratio and a lower median H/C ratio observed for clean-marine air when compared to polluted air (Figure 5.7). Note that the O/C and H/C ratio are elemental molar

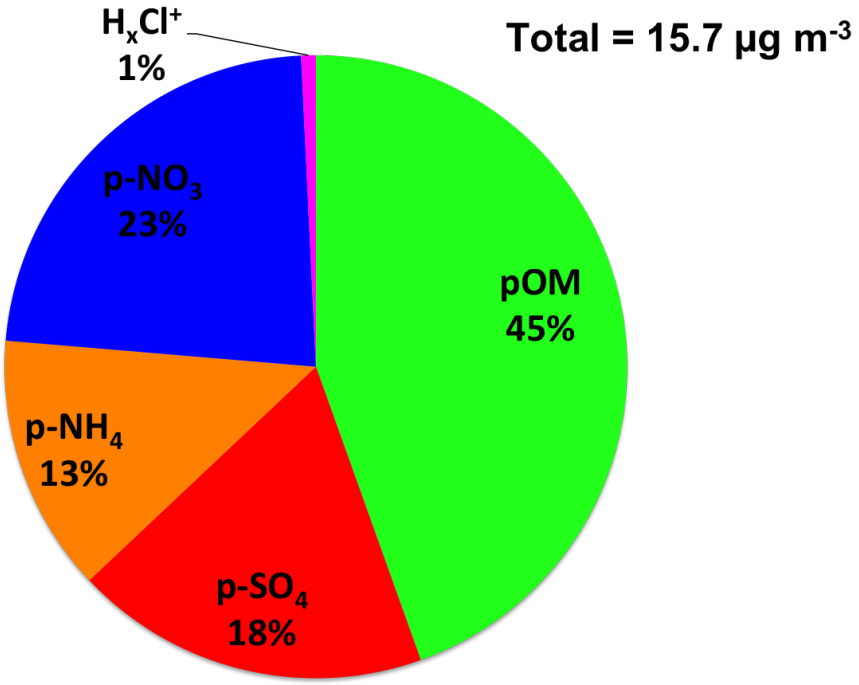

Figure 5.8: Fractional composition of submicron aerosol species measured by an HR-AMS in Pasadena. Values from Hayes et al., 2013; used with permission

.

ratios determined using only organic (Aiken et al., 2007); a higher O/C signifies a more oxidized airmass while a higher H/C signifies a less oxidized airmass. The higher contribution of H_xCl^+ in background marine air is expected to be a result of higher NaCl and a detailed analysis of chloride will follow. From these two results the contribution of pOM seems to increase with fresher air masses originating from emission sources in urban cities.

A study by Hayes et al (2013) reported aerosol mass concentrations and fractional composition that were measured by an HR-AMS in the Pasadena ground site during

CalNex. The location of this ground site was 18 km northeast of downtown Los Angeles (Hayes et al., 2013). Figure 5.8[6] is the fractional composition plot of submicron aerosols measured by the HR-AMS in Pasadena (Hayes et al., 2013). In this plot average levels were used as opposed to the median levels used in Figure 5.7. The levels reported in this study were higher than the ones observed aboard *Atlantis*, even when compared to periods of continental outflow events (Figure 5.7b). This could be due to the local and regional emissions in Pasadena. The lower aerosol levels observed on *Atlantis* along the Pacific coast could be a result of dilution and the position of the ship relative to the pollution event (Figure 5.6). Pollutants, including aerosols, are diluted with increased distance from the source. In Pasadena, the pOM was the most dominant species with a 45% followed by p-NO_3, p-SO_4, p-NH_4 and H_xCl^+ (reported as p-Cl) with average contributions of 23%, 18%, 13% and 1% respectively.

The fractional composition during continental outflow events aboard textitAtlantis (Figure 5.7b) and Pasadena (Figure 5.8) both show pOM to be the most dominant species, although the relative contribution of pOM is higher in the former. The contribution of p-NO_3 is much higher in Pasadena and seems to increase with fresher air masses that are closer to the source. This can be supported by the results from Figure 5.7b for continental airmasses, which shows a higher p-NO_3 contribution when compared to clean marine air shown in Figure 5.7c. For p-SO_4, the relative contribution is much lower in Pasadena than continental outflow events sampled aboard *Atlantis*. This

[6]The values used in this plot are from Hayes et al. (2013); used with permission (license number: 3594960458412).

is consistent with a fresher air mass in Pasadena as discussed previously. Finally, the relative contributions of H_xCl^+ at Pasadena is close to that observed during continental outflow events aboard *Atlantis*; both constitute 1%, which is much lower than the 6% observed for clean marine analysis (Figure 5.7c).

5.6 Mass spectrum of seawater aerosols

[7] An average aerosol mass spectrum obtained using the AMS for the sea sweep experiments is shown in Figure 5.9. The signals reported in 5.9 are in the form of NECs (recall that NEC is nitrate equivalent concentration as outlined in chapter 4), but for the discussion of the ion signals in Figure 5.9 the NEC symbol will be omitted for clarity. The mass spectrum includes the ions for aerosol species typically measured and reported by the AMS including particulate organics (OM), sulfate (p-SO_4), ammonium (p-NH_4) and nitrate (p-NO_3). The H_xCl^+ ion group is also shown in Figure 5.9, which is typically utilized to establish chloride concentration using an AMS as established previously. Also included in the mass spectrum are ions observed that are typical of sea salt aerosol components namely, Na^+, $NaCl^+$, Mg^+, $MgCl^+$, K^+, and KCl^+. Other ion signals (such as metal ions) were grouped under the Other category, while air and

[7]Disclaimer: The following sections from 5.6 to 5.11 inclusive were published as part of a journal article entitled "Separating refractory and non-refractory particulate chloride and estimating chloride depletion by aerosol mass spectrometry in a marine environment" by Ibraheem Nuaaman et al (2015). This journal article was published in Atmospheric Chemistry and Physics Discussions Journal in January of 2015. Copernicus Publications is the publisher of this work, which is licensed under the Creative Commons Attribution 3.0 License. Under this license, an explicit permission from Copernicus Publications to reproduce, reuse and reprint this published work is not required. For more details, the reader can visit the publisher's copyright webpage at http : //www.atmospheric − chemistry − and − physics.net, accessed on January 23rd, 2015.

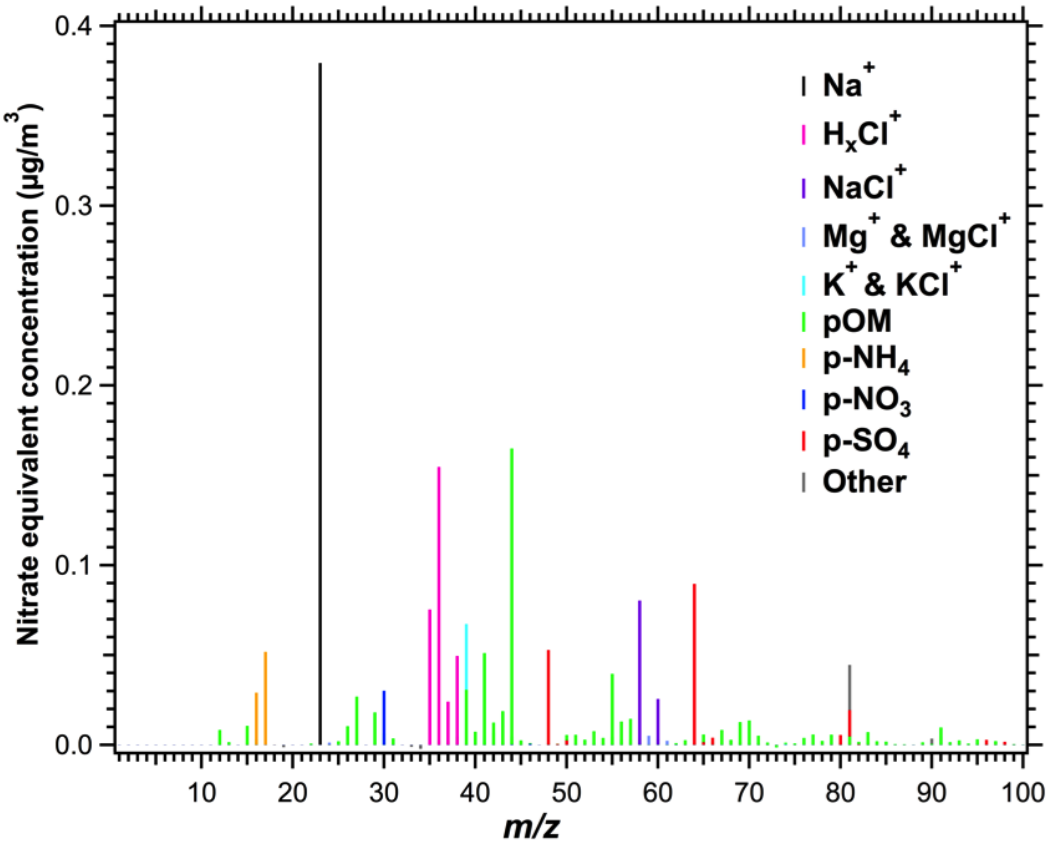

Figure 5.9: Average aerosol mass spectrum of the sea sweep experiments. Air and water peaks were omitted for clarity.

.

water signals were not included for clarity.

The most dominant ion signals in the spectrum, in order of intensity are: Na^+ at m/z 22.99, pOM components such as m/z 43.99 (CO_2^+) and 41.04 ($C_3H_5^+$), H_xCl^+ components at m/z 34.97 ($^{35}Cl^+$), 35.97 ($H^{35}Cl^+$), 36.97 ($^{37}Cl^+$) and 37.97 ($H^{37}Cl^+$), p-SO_4 components such as m/z 47.97 (SO^+) and 63.96 (SO_2^+), as well as, $Na^{35}Cl^+$ at m/z 57.96 and $Na^{37}Cl^+$ at m/z 59.96. The observed $Na^{37}Cl^+$ to $Na^{35}Cl^+$ ratio is 0.32:1, which is typical for chloride clusters given chlorine's isotopic abundance ratios (Numata

et al., 2001). The organic signals in sea spray aerosols during sea sweep experiments will be covered in Section 5.14.

The dominance of ion signals associated with sodium chloride (i.e., Na^+, H_xCl^+ components and $NaCl^+$ ions) in the sea salt aerosols during the sea sweeps was similarly observed by Ovadnevaite et al. (2012) despite the fact that sodium chloride is not typically considered to be detectable by the AMS, since it is a refractory (RF) aerosol component with a melting point of 800.7 °C and a boiling point of 1465 °C (Haynes, 2012), much higher than the vaporizer temperature of 600 °C. However, large ion signals are apparent given the large amounts of sea salt sampled into the AMS during these experiments. Even if only a small fraction of NaCl was vaporized, ionized and then detected by the AMS, this fraction appears dominant in the mass spectrum for the sea sweep experiments.

It is worth noting that the software based reporting of NR p-Cl usually includes the H_xCl^+ mass fragments outlined above, but does not include the NaCl ions. It should be obvious from the sea sweep signals in Figure 5.9 that any report of non-refractory chloride mass in areas that contain sea salt aerosols will be compromised. This is especially true if the AMS samples significant amounts of sea salt aerosols such as might be true in coastal and marine areas.

5.7 Observation of sea salt chloride (ss p-Cl) in ambient air

In non-sea sweep collections of ambient aerosol during the CalNex study, the Na^+, $Na^{35}Cl^+$ and $Na^{37}Cl^+$ signals were low but detectable with well-resolved peaks. The $Na^{37}Cl^+$ peak at 59.956, however, has significant overlaps with potential interfering ions, CSO^+ (59.967) and $SiO_2{}^+$ (59.967), even at the high resolution of this AMS, and is thus not used as a quantitative indicator of sea salt.

Figure 5.10 shows a time series of H_xCl^+, Na^+ and $Na^{35}Cl^+$ signals throughout CalNex including ambient air measurements and sea sweep experiments. All three signals are given as chloride equivalent concentrations (CECs), which was explained in chapter 4. The highest H_xCl^+ signals were observed during sea sweep experiments at more than 2 μg m^{-3}, which assumes a non-refractory collection efficiency of 0.468. This chloride is largely due to the sampling of NaCl in sea salt during these experiments. The coincident Na^+ and $Na^{35}Cl^+$ signals correlate strongly with the H_xCl^+ signal during these experiments, peaking at 1.8 and 0.41 μg m^{-3} respectively. Note that these levels should only be treated as relative signals and not true concentrations.

It was found in this study that refractory NaCl suffered from slow evaporation in the AMS after high sea salt aerosol sampling such as that during sea sweep experiments. This slow evaporation led to high background signal for certain ions, which was apparent from the chopper-closed signal. During this study, the background signals for Na^+, H_xCl^+ and Na^+ were much higher than the "open - closed" measurement signal after sea sweep experiments. This trend was least prominent for the $Na^{35}Cl^+$ signal. Similar

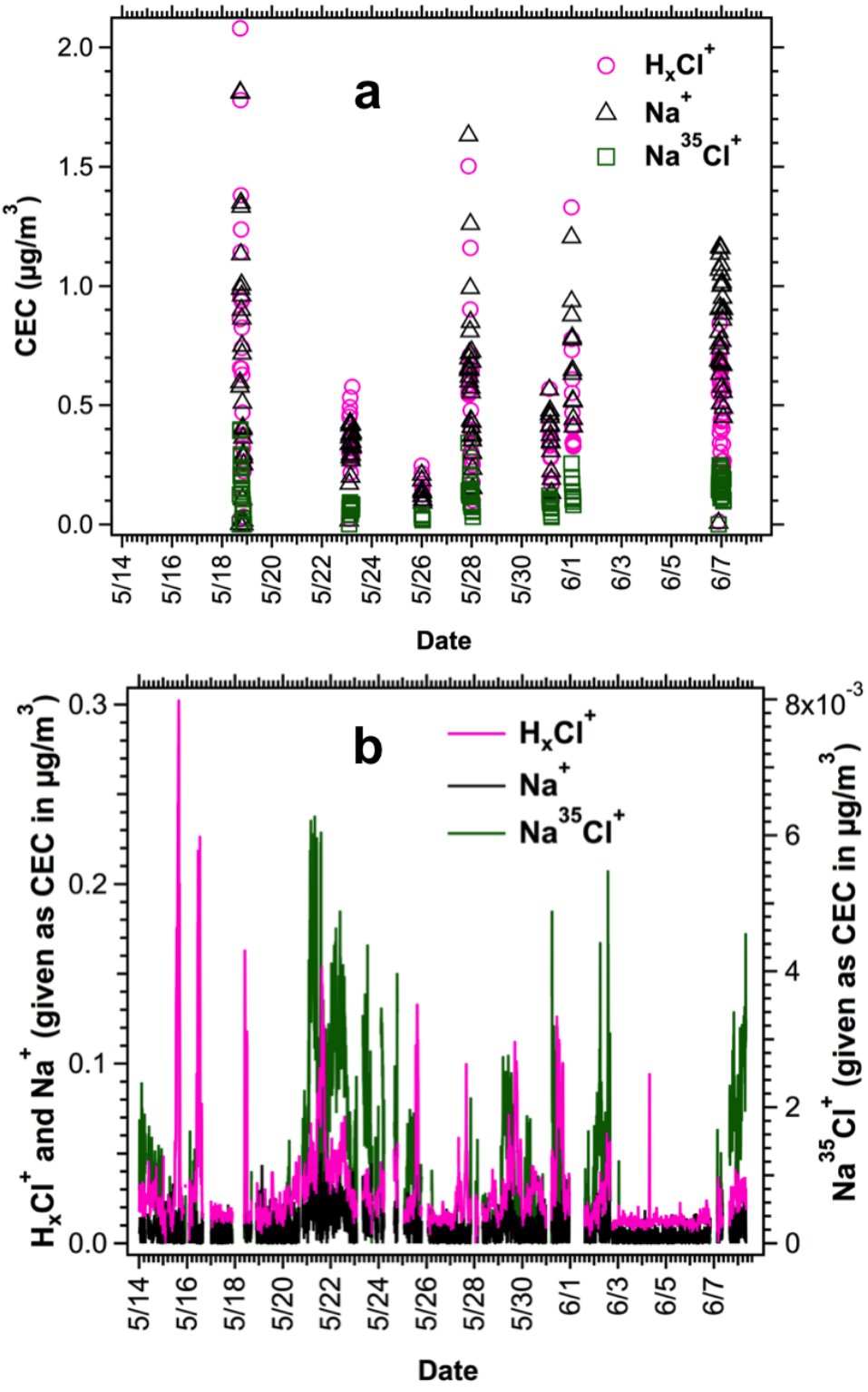

Figure 5.10: Time series of H_xCl^+, Na^+ and $Na^{35}Cl^+$ signals measured using an HR-AMS: a) sea sweep experiments b) ambient air.

trends of the slow evaporation have been observed in other studies for sodium and lead signals when using an AMS for sampling refractory aerosols (Ovadnevaite et al., 2012; Salcedo et al., 2010). In this study, we found that the time it takes for complete disappearance of refractory sea salt signals was directly proportional to the amount of sea salt injected and ranged from 5 to 28 hr for Na^+, 2.2 to 6.8 h for H_xCl^+ and 0.07 to 5.2 h for $Na^{35}Cl^+$. Ovadnevaite et al. (2012) reported the time for complete refractory signal disappearance to be about 12 h for Na^+, 2 h for H_xCl^+ and <0.083 h for $Na^{35}Cl^+$, all of which are in the ranges observed here. This high background signal resulted in a low signal to noise ratio for the ambient measurements that followed the sea sweep experiments; and so we have eliminated these time periods from further analysis. The difference in background signal recovery times for the different ion components of the same parent compound is not fully understood.

The observation of Na^+ and $Na^{35}Cl^+$ signals in ambient aerosol measurements confirms the detection of refractory (RF) sodium chloride by the AMS in ambient samples. Thus, refractory chloride is contributing to the H_xCl^+ signals, which are typically used to calculate non-refractory chloride (i.e., NR p-Cl in the form of NH_4Cl or other volatile chlorinated species) concentrations using the AMS. We therefore confirm that the contributions of this RF signal to the H_xCl^+ signal needs to be corrected before reporting mass concentrations of NR p-Cl. To do this, it is necessary to isolate the NR p-Cl signal from the H_xCl^+ signal. In the following section, we present a method to establish NR p-Cl concentration from H_xCl^+ and $Na^{35}Cl^+$ signals. Note that NR p-Cl can also be defined as nss p-Cl (non-sea salt p-Cl), but here we use the former term in accordance

with common terminology used with AMS measurements (Canagaratna et al., 2007).

5.8 A method to establish [NR p-Cl] in marine coastal environments with sea salt chloride interferences

In order to establish [NR p-Cl] we need to estimate the RF H_xCl^+, which we define to be the chloride portion of the H_xCl^+ signal that is in the form of NaCl. For this estimate, we need to use an ion (I) that is not a part of the H_xCl^+ group but results exclusively from the fragmentation and ionization of NaCl. In addition, we need to establish the H_xCl^+/I ratio for NaCl in sea salt aerosol using an AMS. For I, one can consider using Na^+ or $Na^{35}Cl^+$, but while $Na^{35}Cl^+$ is expected to result exclusively from the ionization and fragmentation of NaCl, Na^+ could also arise from $NaNO_3$ and/or Na_2SO_4 in sea salt aerosol. This is especially true with aged sea salt aerosols, where acid displacement can remove chloride (see Finlayson-Pitts and Pitts, 1999, and references therein). It is therefore advantageous to use the $Na^{35}Cl^+$ signal to correct for the refractory component of H_xCl^+, since this signal only arises from NaCl in sea salt aerosols. The ratio $H_xCl^+/Na^{35}Cl^+$ for sea salt chloride from NaCl can be established using sea sweep experiments.

In order to prove the validity of using the $Na^{35}Cl^+$ signal as an indicator of sea salt, the ambient $Na^{35}Cl^+$ signal (given as a CEC) measured using the HR-AMS was compared to the submicron Na and total sea salt aerosol concentrations determined from filter measurements (Figure 5.11). In Figure 5.11, the $Na^{35}Cl^+$ signal was averaged to

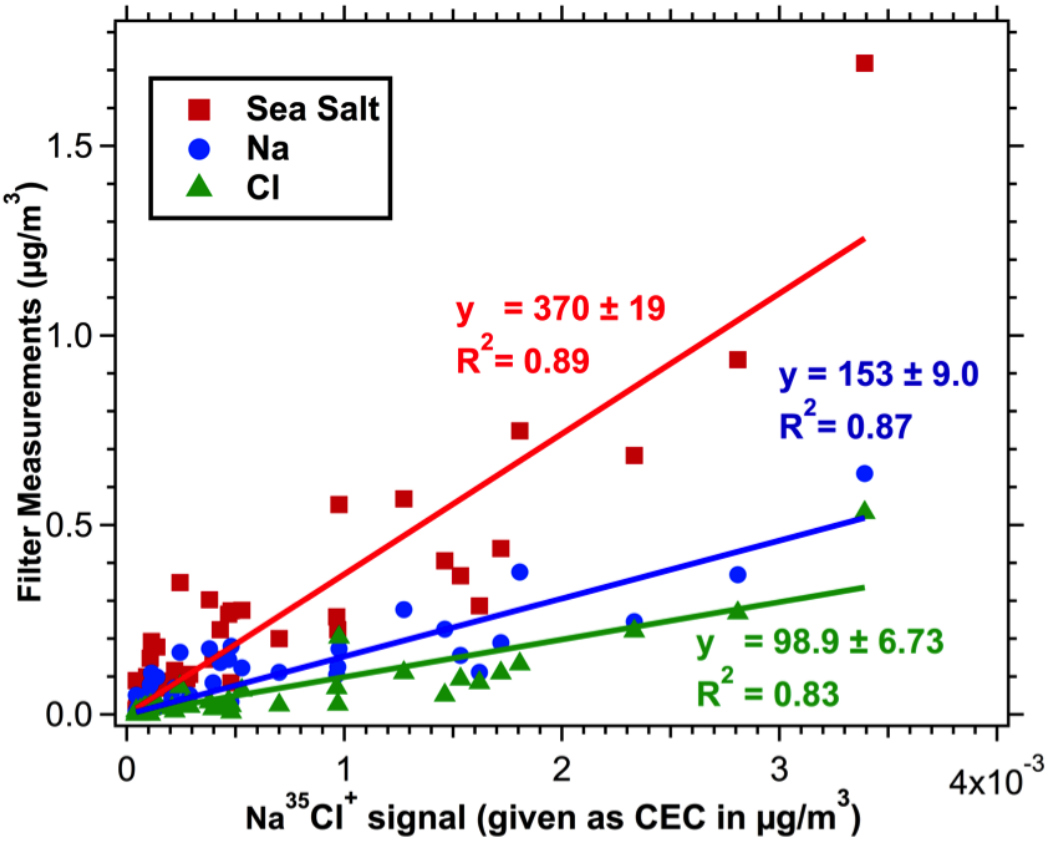

Figure 5.11: Comparison of the AMS measured $Na^{35}Cl^{+}$ signal to filter measurements of submicron sea salt and Na concentrations.

.

the collection time of the filters. The total sea salt concentration in Figure 5.11 was calculated from the filter measurements using the following equation (Bates et al., 2012, and references therein):

$$Sea\ Salt\ (\mu gm^{-3}) = [Cl^{-}] + 1.47\ \times\ [Na^{+}] \tag{5.1}$$

where $[Cl^{-}]$ and $[Na^{+}]$ are the ambient concentrations of Cl^{-} and Na^{+} determined from filters, respectively, and the coefficient 1.47 factor is the mass ratio of major non-

chloride ions (Na^+, K^+, Mg^{+2}, Ca^{+2}, ${SO_4}^{-2}$, ${HCO_3}^{-2}$) to Na^+ ions present in sea salt. From Figure 5.11, the AMS-derived $Na^{35}Cl^+$ signal shows positive correlations with submicron sea salt, Na and Cl concentrations determined using filter measurements. The Pearson correlation coefficients, R^2 are 0.89, 0.87 and 0.83 for the sea salt, Na and Cl traces respectively (Figure 5.11). The observed slopes for filter measurements versus $Na^{35}Cl^+$ are of 370, 153 and 98.9 for the sea salt, Na and Cl traces respectively. The observed correlations suggest that the $Na^{35}Cl^+$ signal from the AMS can indeed be reasonably used as a tracer for sea salt aerosol in ambient air. The source of scatter in the graph may be a result of the low time resolution of the filter measurements with sampling frequency of 1-3 per day and sampling duration of 2 - 16 hours and the different particle size cutoff for both measurements. Note that the slopes are higher limits as the aerosols sampled on filters had a cutoff of $D_a < 1.1$ μm, while the AMS cutoff size is $D_a < 700$ nm and thus the AMS only sampled a fraction of the sea salt aerosols that were collected on filters.

Figure 5.12 is a plot of H_xCl^+ versus $Na^{35}Cl^+$ for sea sweep experiments and ambient data. The sea sweep line shows the observed ratio of H_xCl^+ to $Na^{35}Cl^+$ from the fragmentation and ionization of NaCl in sea salt aerosol. The H_xCl^+ and $Na^{35}Cl^+$ signals are highly correlated during sea sweep experiments with a H_xCl^+ versus $Na^{35}Cl^+$ slope of 3.91 ± 0.156 and R^2 of 0.83. The 95% confidence intervals about the regression line are also shown in Figure 5.12. These were calculated using the standard errors of the slope and intercept, as well as the critical t value at probability (p) of 0.05 and 130 degrees of freedom (n-2). Thus, all ambient air data with a H_xCl^+ to $Na^{35}Cl^+$ ratio

higher than the confidence interval line in Figure 5.12 are expected to have significant contributions from chloride sources other than NaCl, which could be in the form of NH_4Cl and other chlorinated species.

Also observed from Figure 5.12 are ambient data with H_xCl^+ to $Na^{35}Cl^+$ ratios similar to that observed in sea sweep experiments that lie well within the 95% confidence lines around the sea sweep linear regression line. For these ambient data points, the RF chloride component significantly contributes to the H_xCl^+ signal measured by the AMS. In order to establish the concentration of NR p-Cl ([NR p-Cl]), the following equation can be used, which utilizes the H_xCl^+ to $Na^{35}Cl^+$ ratio established from sea sweep experiments with the AMS H_xCl^+ and $Na^{35}Cl^+$ ionic signals:

$$NR\,H_xCl^+ = H_xCl^+ - (3.90 \times Na^{35}Cl^+) \tag{5.2}$$

The H_xCl^+ signal is equivalent to NR p-Cl mass concentration:

$$NR\,H_xCl^+ \equiv NR\,p-Cl\,(\mu gm^{-3}) \tag{5.3}$$

Equation 5.3 is true given that the H_xCl^+ signal has been expressed as a chloride equivalent concentration (CEC) throughout this analysis. As a CEC signal, an RIE of 1.3 has already been applied (Chapter 4). Recall from Chapter 4 that an RIE of 1.3 is used for the determination of NR p-Cl when using the AMS.

The term in parentheses in Eq 5.3 refers to the RF Cl component of the ambient H_xCl^+ signal. Note that for Eq 5.3, the intercept was forced to zero and only the H_xCl^+

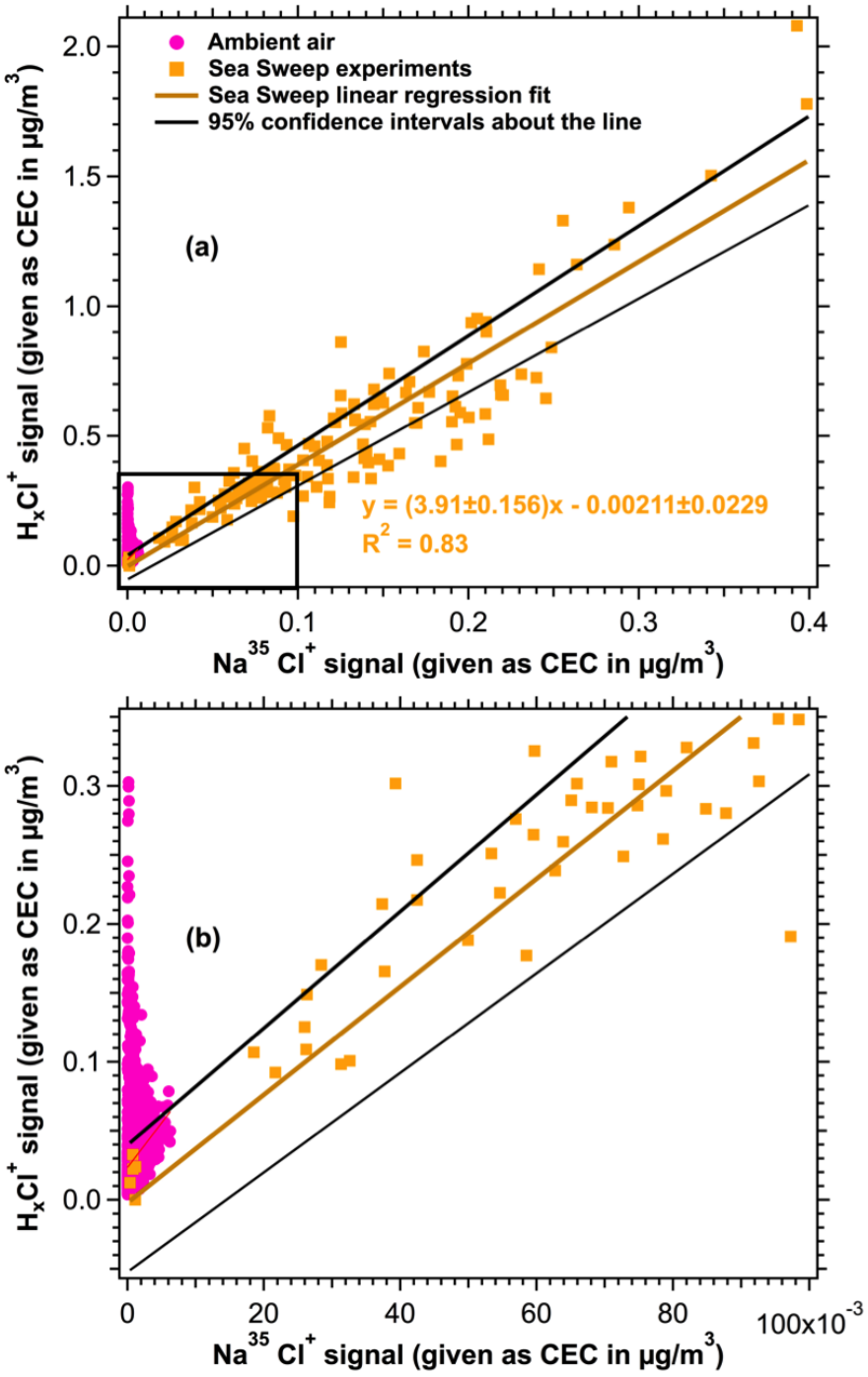

Figure 5.12: A plot of H_xCl^+ signal vs $Na^{35}Cl^+$ in ambient air and sea sweep experiments. (b) is a blow up of the area indicated by the box in (a).

.

to $Na^{35}Cl^+$ ratio was used. A zero intercept was used since the 0.00211 intercept (Figure 5.12) is zero given the 0.0229 standard error of the intercept. In addition, both the H_xCl^+ and $Na^{35}Cl^+$ signals are from the same source in sea sweep experiments (correlation is improved with a forced zero intercept, R^2= 0.95). Using the last term in Eq 5.3, we can quantify the contribution of refractory H_xCl to the total H_xCl signal, i.e. how much of the H_xCl signal can be attributed to NaCl. This contribution is simply estimated by (3.90 x $Na^{35}Cl^+$) / H_xCl^+ x 100%, and the result of this estimation is shown in Figure 5.13. Also shown in Figure 5.13 is the submicron chloride concentration from filter measurements, which primarily detects NaCl, not NR p-Cl, due to evaporation issues of volatile chlorinated compounds (such as NH_4Cl) from the filters (Bates, oral communication). The contribution of refractory H_xCl^+ to the total H_xCl^+ signal is reasonably correlated with sea salt chloride concentrations measured with filters. Given this correlation, high contributions of refractory H_xCl to total H_xCl signal where observed during periods of elevated sea salt chloride concentrations.

Using the $Na^{35}Cl^+$ ion fragment and a factor of 3.90, the RF H_xCl^+ signal, detected by the AMS, was low in ambient air during this study. However, the contribution of refractory H_xCl^+ to the total H_xCl^+ signal was significant with a maximum contribution of 89% and an average contribution of 10%. In this study, periods with high contribution from RF H_xCl^+ to the H_xCl^+ signal were also periods of relatively low H_xCl^+ signals and were not enriched with NR p-Cl. The contribution of RF H_xCl^+ to the total H_xCl^+ signal would be high in marine regions with elevated sea salt chloride concentration, especially when levels of NR p-Cl are low.

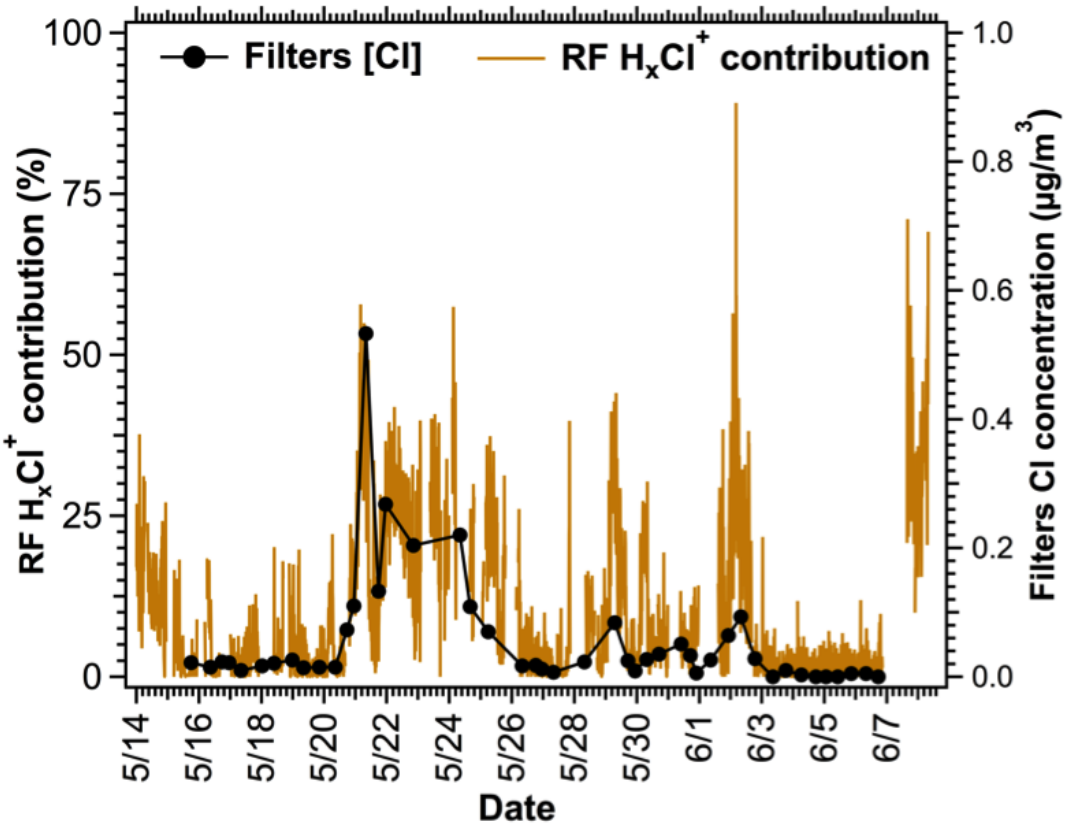

Figure 5.13: Contribution of RF H_xCl^+ signal to the total H_xCl^+ signal in ambient air. Chloride concentrations determined using filters measurements (by NOAA) are shown for comparison.

.

5.9 A method to establish [ss p-Cl] and [p-Cl] from AMS measurements

In this section we will propose an empirical formula to estimate the air concentrations of submicron sea salt chloride [ss p-Cl] and total submicron ambient chloride [p-Cl]. Note that ss p-Cl is not the same as RF H_xCl^+ and must be distinguished. ss

p-Cl refers to submicron sea salt concentration in ambient air while RF H_xCl^+ refers to the portion of the H_xCl^+ signal measured by the AMS that is in the form of sea salt chloride. In order to estimate [ss p-Cl], we use $Na^{35}Cl^+$ and a scaling factor established using [Cl] concentrations from filter measurements. The ratio of submicron [Cl] from filters to $Na^{35}Cl^+$ was observed to be 98.9±6.73 (Figure 5.11). Sea salt chloride concentration is therefore estimated as follows:

$$[ssp - Cl]\,(\mu gm^{-3}) \;=\; Na^{35}Cl^+ \;\times 98.9 \tag{5.4}$$

Note that the factor of 98.9 assumes that all of the chloride measured on the filters is in the form of NaCl and not NR p-Cl. This assumption is reasonable, since the filter measurements employed here does not detect volatile chlorinated species as mentioned previously. Now that we have a measure of [NR p-Cl] and [ssCl], [pCl] can be estimated using the following equation :

$$p - Cl\,(\mu gm^{-3}) = [NR\,p - Cl] \;+ [ss\,p - Cl] \tag{5.5}$$

Figure 5.14 shows the time series of p-Cl, NR p-Cl and ss p-Cl concentrations measured by the AMS, as well as the submicron Cl concentration measured by filters. The lack of sensitivity of the filter measurements to NR p-Cl is apparent from Figure 5.14 as an increase in NR p-Cl concentrations does not seem to impact the [Cl^-] measured by filters. In this study, the median levels observed for [p-Cl], [NR p-Cl] and [ss p-Cl] were 0.052, 0.017 and 0.024 μg m^{-3} respectively and the 5th to 95th percentile ranges were

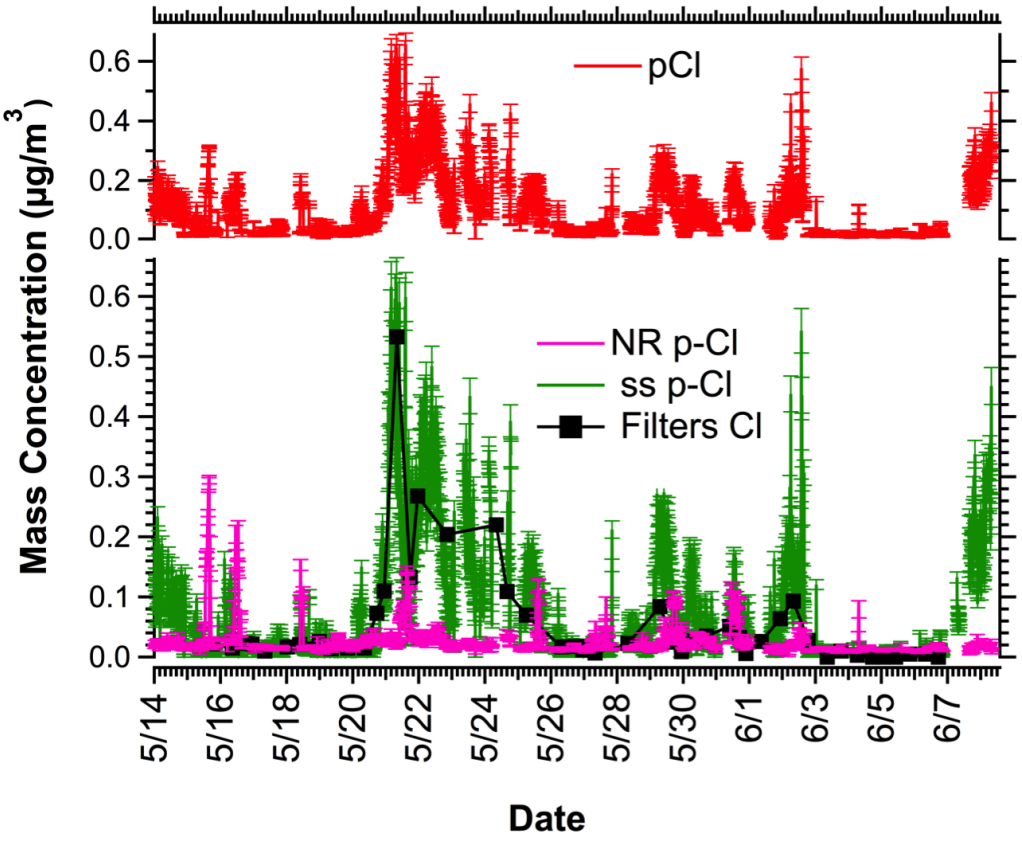

Figure 5.14: Time series of HR-AMS measurements for p-Cl, NR p-Cl and ss p-Cl. Filter measurements of submicron p-Cl by NOAA is also shown.

.

0.012-0.33, 0.0096-0.077 and 0-0.30 μg m^{-3} respectively. The average contributions of NR p-Cl and ss p-Cl to p-Cl were 48% and 52% respectively. NR p-Cl was dominant during periods of continental outflow, while ss p-Cl was dominant during periods of high wind speeds, which enhances wave action. The determination of ambient chloride concentrations using AMS measurements and Eq 5.5 proposed here is advantageous over filter measurements, since filter measurements have significant positive and nega-

tive artefacts. These include evaporation of high volatile species, such as NH_4Cl, from the surface of the filters, which results in a negative bias. A positive bias includes the adsorption of gases onto the filter surface. The filters, however are not limited to non-refractory species and to the 70-700 nm size range as the AMS done. Given the limitations of the filter measurements, it is advantageous to use the AMS especially sice the time resolution of the AMS is higher than that of the filter measurements.

5.10 Estimating total sea salt concentrations from the $Na^{35}Cl^+$ signal

As discussed in section 5.8, total submicron sea salt aerosol concentrations [sea salt] can be established from filter measurements and Eq 5.1 above. The ratio of [sea salt] from filter measurements to $Na^{35}Cl^+$ observed in this study was 370 ± 19.3 (Figure 5.11). Ovadnevaite et al (2012) used nitrate equivalent $Na^{35}Cl^+$ concentration (NEC with RIE of 1) and a scaling factor of 51 to establish submicron sea salt concentration. The scaling factor proposed by Ovadnevaite (2012) would be equal to 66, when using CEC as is this case in this study (recall that chloride RIE is 1.3). The scaling factor proposed by Ovadnevaite (2012) is $\sim$ 5-6 times lower than the scaling factor reported here. This difference could be partially attributed to the higher vaporizer temperature utilized by Ovadnevaite et al (2012) of 650 °C, which is 50 °C higher than the vaporizer temperature employed in this study.

Figure 5.15 shows the [sea salt] determined from the AMS using the $Na^{35}Cl^+$ signal

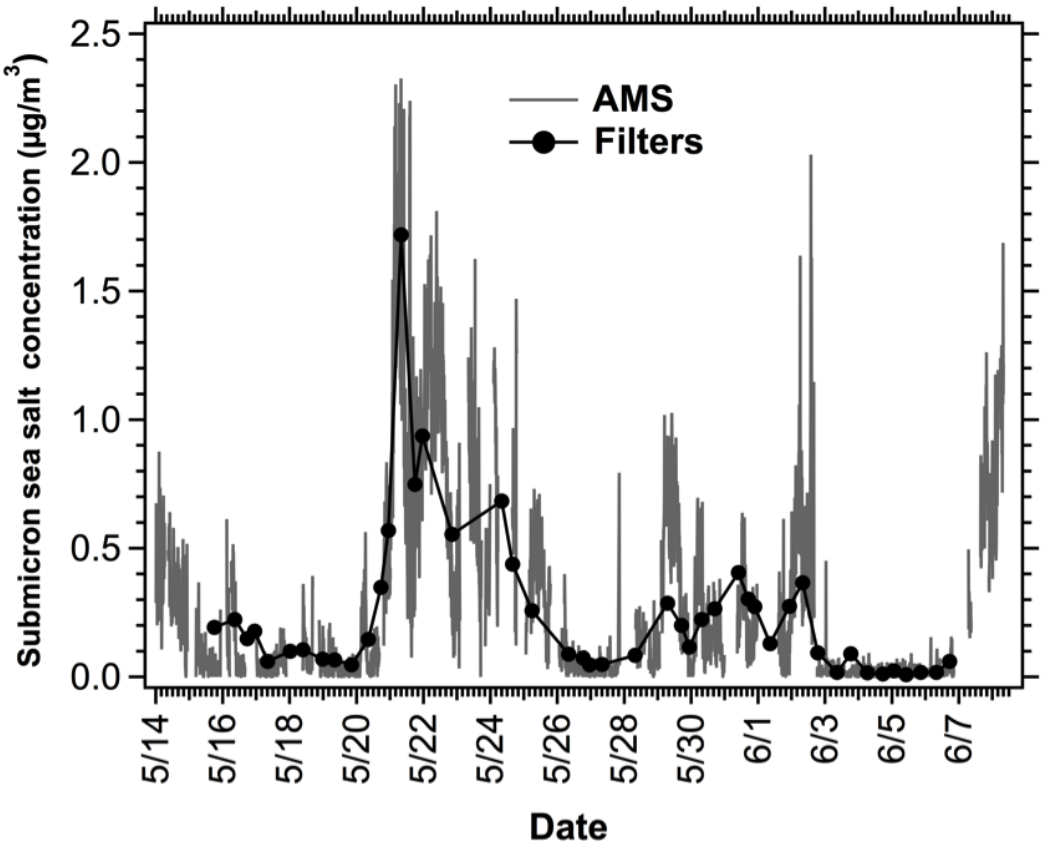

Figure 5.15: Submicron sea salt concentrations observed during CalNex determined using AMS and filter measurements.

.

and the scaling factor of 370. Figure 5.15 also shows [sea salt] determined using filter measurements and Eq.5.1. Using $Na^{35}Cl^{+}$ measurements, significant levels of [sea salt] were observed peaking at 2.3 μg m^{-3} with a study wide average of 0.28 μg m^{-3}. In comparison, the peak value in the study by Ovadnevaite et al (2012) was higher at 4.5 μg m^{-3}, although the running mean peaks were 2.2 to 2.4 μg m^{-3}. Overall the levels were lower in the current study, although they are likely attributable to the lower wind

speeds experienced during CalNex.

5.11 Determining chloride depletion in sea salt using AMS data

We present a method to establish the percentage of chloride depleted from sea salt chloride in ambient air using AMS measurements. Chloride depletion is an important indicator of sea salt aerosol ageing and leads to the formation of activated chloride in the form of HCl. Chloride depletion is typically calculated using the difference between the expected ssCl and observed ssCl (Zhao and Gao, 2008) as follows:

$$\%Cl\ depletion = \frac{Expected\ ss\ p-Cl\ -\ Observed\ ss\ p-Cl}{Expected\ ss\ p-Cl} \times\ 100\% \tag{5.6}$$

The expected ss p-Cl in Eq 5.6 is estimated from the sodium concentration and mass ratio of Cl to Na in seawater, which is 1.81 μg m^{-3}/μg m^{-3} (Haynes, 2012). The estimation assumes that while ss p-Cl is volatilized by acid displacement reactions, Na is not volatilized and stays in the aerosol phase. Equation 5.6 becomes:

$$\%Cl\ depletion = \frac{1.81\,[Na]\ -\ [Cl]}{1.81\,[Na]} \times\ 100\% \tag{5.7}$$

The method proposed here strictly uses ion signal measurements from the AMS. The expected chloride signal (Eq 5.6) from NaCl fragmentation can be estimated using ambient Na^+ and the H_xCl^+/Na^+ ratio in sea salt aerosols derived from the sea sweep

experiments. Figure 5.16 is a plot of H_xCl^+ signal versus Na^+ signal for sea sweep experiments. Na^+ is well correlated with H_xCl^+ with $R^2 = 0.94$ and a H_xCl^+/Na^+ ratio of 0.827 $\pm$ 0.0175. Note that this ratio should be viewed as a signal to signal ratio, since ion signals are utilized in this study. As such, the 0.827 ratio observed for H_xCl^+ to Na^+ can not be directly compared to the true [Cl] to [Na] ratio of 1.81. The difference between these two ratios is due to different ionization efficiencies in the AMS for chloride and sodium.

Using AMS measurements, the observed chloride signal (Eq 5.6) from NaCl fragmentation is estimated to be 3.90 x Na^+ as discussed in section 5.8. Using the aforementioned estimates for expected and observed chloride, Eq 5.6 becomes:

$$\%\, Cl\ depletion = \frac{0.827\ \times\ Na^+\ -\ 3.90\ \times\ NaCl^+}{0.827\ \times\ Na^+} \tag{5.8}$$

Figure 5.17 shows a time series for the percentage chloride depletion in ambient air and sea sweep experiments. For ambient air, the percentage chloride depletion was calculated using two methods. The first is method A, which uses Eq 5.8 and AMS measurements. The second is Method B, which uses filter measurements and Eq 5.6. Method A was exclusively used to establish percentage chloride depletion in sea sweep experiments, since filter measurements were not available for these experiments. For method A, hourly averages of the AMS data were utilized to reduce noise in the Na^+ signals in the original 10-min averages. From Figure 5.17 the percentage chloride depletions for sea sweep experiments are very close to zero, which is expected since the

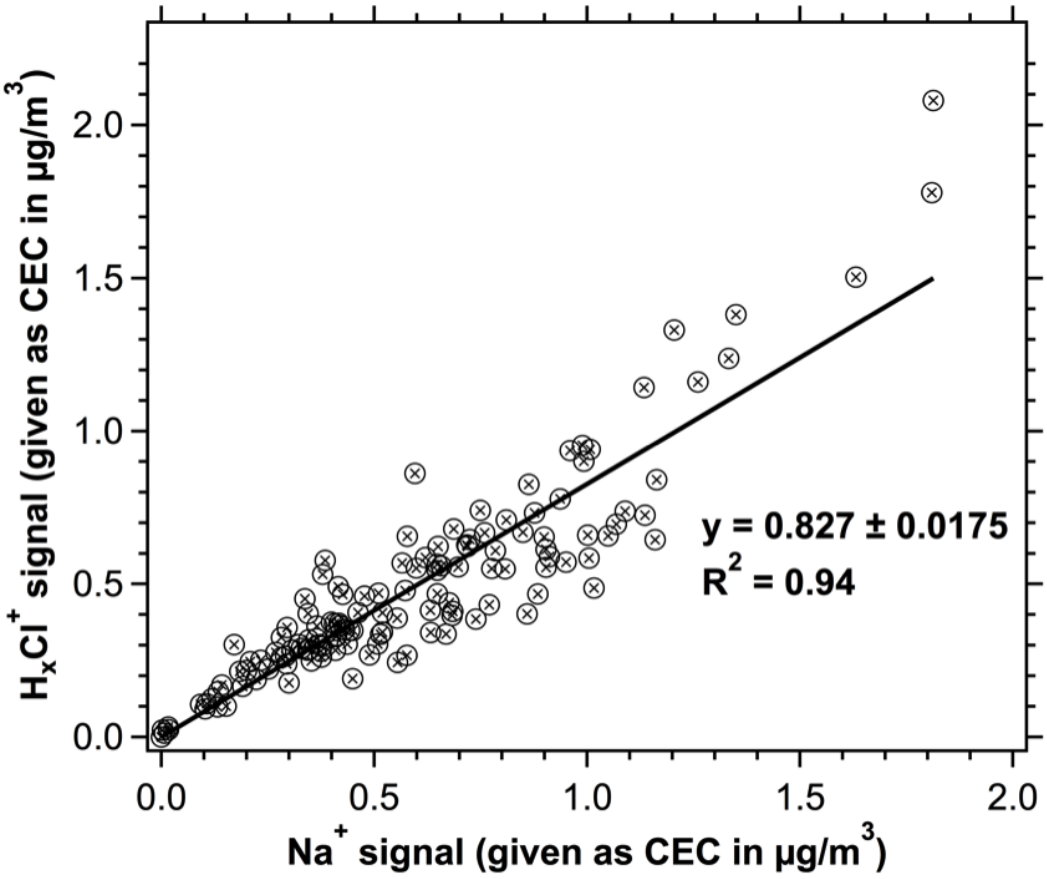

Figure 5.16: Establishing the H_xCl^+ to Na^+ ratio in sea sweep experiments.

.

aerosols sampled during these experiments were assumed to be fresh sea salt aerosols and the ratios used in equation 5.8 were derived from these experiments. For ambient data, Method A gives reasonable results with ∼95% of the data in the 0-100% range,∼5% are less than 0 and are attributed to the noise associated with the HR-AMS measurements. Results from Method A and Method B show similar trends and are positively correlated, which gives confidence to Method A proposed here. Note that Method A captures more variations due to the higher time resolution of the HR-AMS measurements. Using the

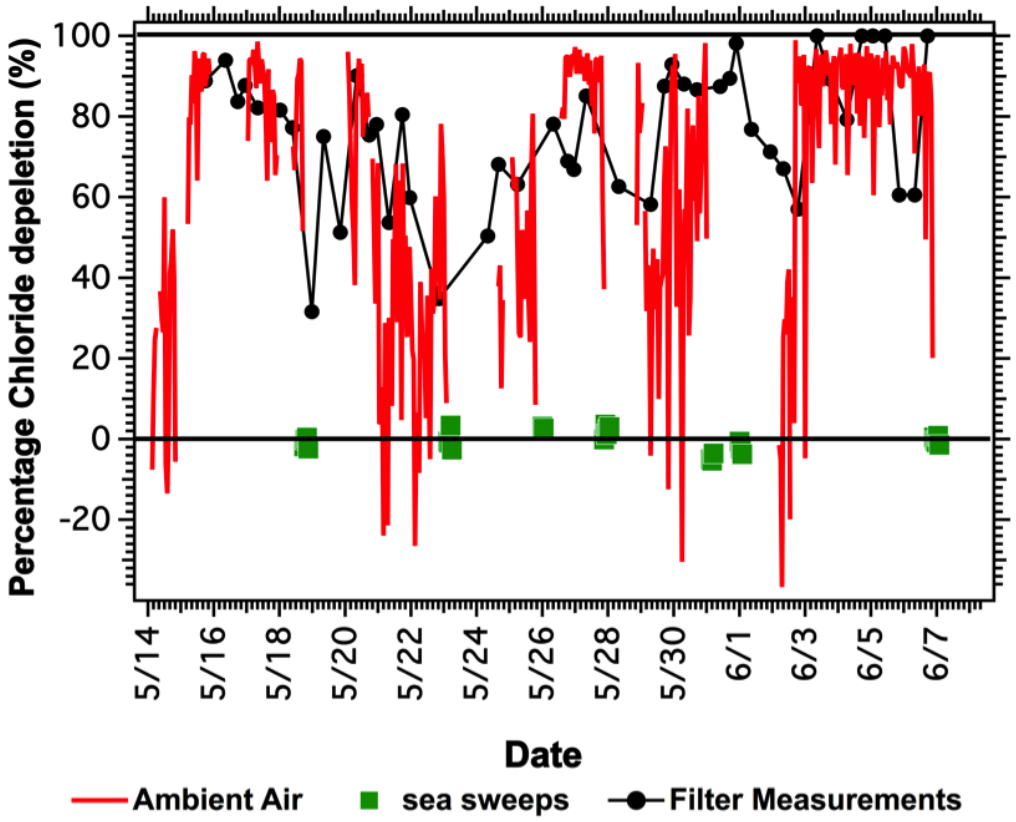

Figure 5.17: Time series for percentage chloride depletion calculated from HR-AMS measurements and Eq 5.8 (Method A) for ambient air and sea sweep experiments. Also shown for comparison is chloride depletion calculated using filter measurements (by NOAA) and Eq 5.6 (Method B).

.

HR-AMS data, the median percentage chloride depletion observed in this study was 78% with a 5^{th} to 95^{th} percentile range of 0 to 96%. Finally, it is important to note that the method proposed here only considers chloride depletion from NaCl and does not take into account other chlorinated species in sampled aerosols.

5.12 The effect of temperature and relative humidity on NR p-Cl

In the aerosol phase, NR p-Cl is expected to be in the form of NH_4Cl as opposed to HCl as mentioned previously. The formation of NH_4Cl (s, aq) is favourable under conditions of low temperatures and high relative humidity (RH) (Ianniello et al., 2011; Matsumoto & Tanaka, 1996; Pio & Harrison, 1987; Trebs et al., 2005). In this section, we will establish the effect of temperature and RH on the formation of NR p-Cl. Figure 5.18 is a time series of NR p-Cl, temperature and RH established using the methodology outlined above. Eight case studies with elevated levels are shown in Figure 5.18, which were associated with continental outflow events. Table 5.3 summarizes the time periods and ship locations for these case studies. Also shown in Figure 5.18 are temperature and relative humidity (RH) measurements in ambient air. Temperatures ranged from 10.4 to 29.2 °C with a study-wide median temperature of 13.9 °C, whereas RH, had a study-wide range of 22.8 to 100.6% with an 88% median. The highest RH was observed at night while the lowest was observed during the day as expected.

Figure 5.19 is a plot of NR p-Cl as a function of air temperature (a) and RH (b) for the case studies listed in Table 5.3. In these case studies the temperatures observed were from 11.6 to 16.8 °C and the RH observed were from 56.0% to 99.7%. From Figure 5.19, a general decrease in NR p-Cl concentration is observed with an increase in temperature likely due to the evaporation of NH_4Cl from the submicron aerosol phase to the gas phase. In contrast, an increase in NR p-Cl concurrent with an increase in

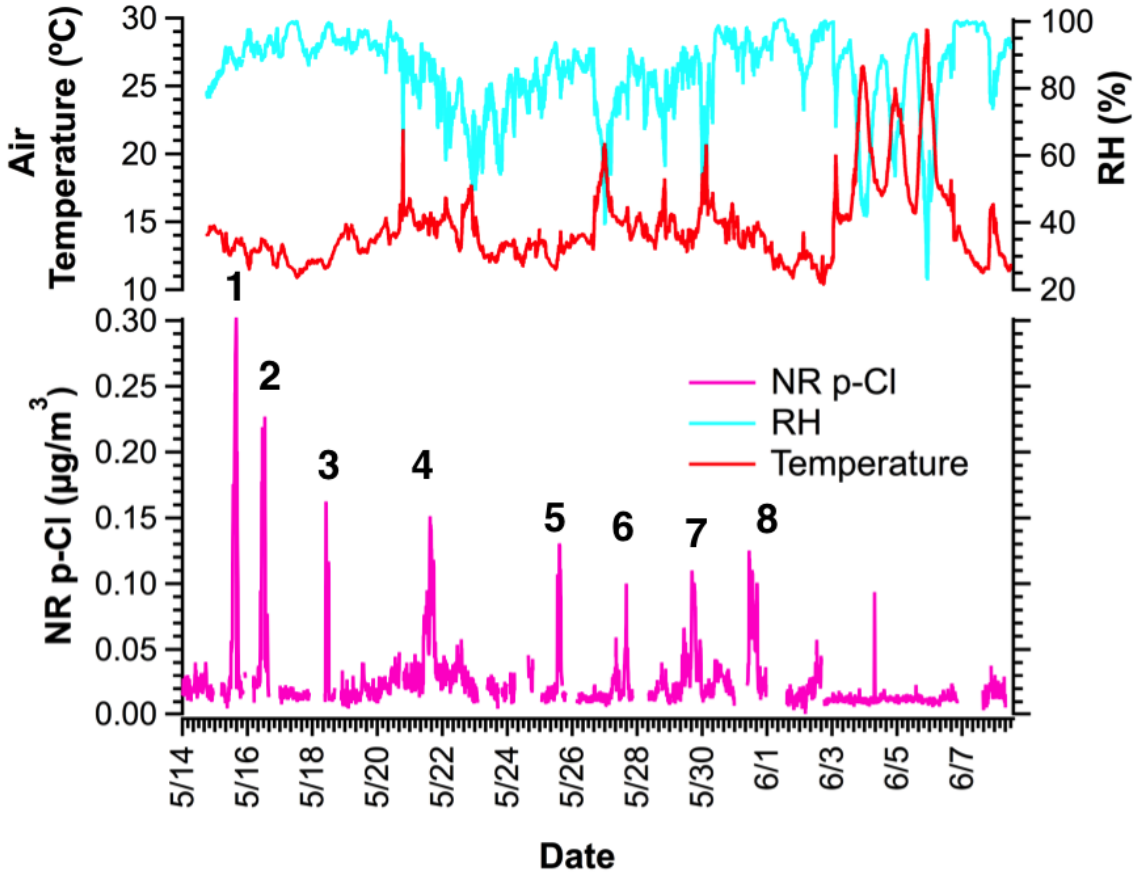

Figure 5.18: Time series of NR p-Cl, air temperature and RH. Case studies of elevated chloride levels are highlighted.

.

RH is observed as expected. It is worthwhile to note that temperature and RH are not independent of each other as higher RH is typically associated with lower temperatures and vice versa and this was observed for the case studies studied presented here. The decoupling of temperature and RH effects on NR p-Cl is beyond the scope of this study but it is more likely that both temperature and RH have separate effects on NR p-Cl concentrations. In Figure 5.19 the data show significant variance around the regression

Table 5.3: Time periods and locations summary of the case studies with elevated chloride concentrations that are highlighted in Figure 5.18.

No.	Start Time	End Time	Location
1	15 May/1140	15 May/1720	Santa Monica Bay 1-5 nm offshore
2	16 May/0940	16 May/1440	Santa Monica Bay 1-5 nm offshore
3	18 May/1000	18 May/1220	Off Port Hueneme
4	21 May/1000	21 May/1920	Santa Monica Bay 1-5 nm offshore
5	25 May/1300	25 May/1630	Santa Monica Bay 1-5 nm offshore
6	27 May/0440	27 May/1600	LA harbor; west basin
6	27 May/1600	27 May/1840	Transit through Long Beach harbor to San Pedro Bay
7	29 May/0920	29 May/1600	On station west of Palos Verdes Pt
7	29 May/1600	30 May/2320	Transit Santa Monica Bay coastline
8	31 May/0920	30 May/1920	Off Ventura

fit presented. Despite this variance, there appears to be two distinct periods with much higher NR-Cl concentrations as indicated by arrows in Figure 5.19. These periods will be discussed separately below.

Figure 5.20 is the same as Figure 5.19 but the data points are coloured by ion signal of $C_2H_4O_2$. The importance of the $C_2H_4O_2$ signal is that this ion is known to be a biomass burning tracer (Alfarra et al., 2007; Aiken et al.,2009). Biomass burning is a primary source of particulate chloride (Keene et al., 1999).Figure 5.20 shows the highest levels of $C_2H_4O_2$ coincident with the NR p-Cl peak indicated by the arrows. The enhancement of NR p-Cl (Figure 5.20) corresponds to the periods from 13:10 to 16:30 (UTC) on May 15^{th} and 10:50 to 13:30 (UTC) on May 16^{th}. In these two periods

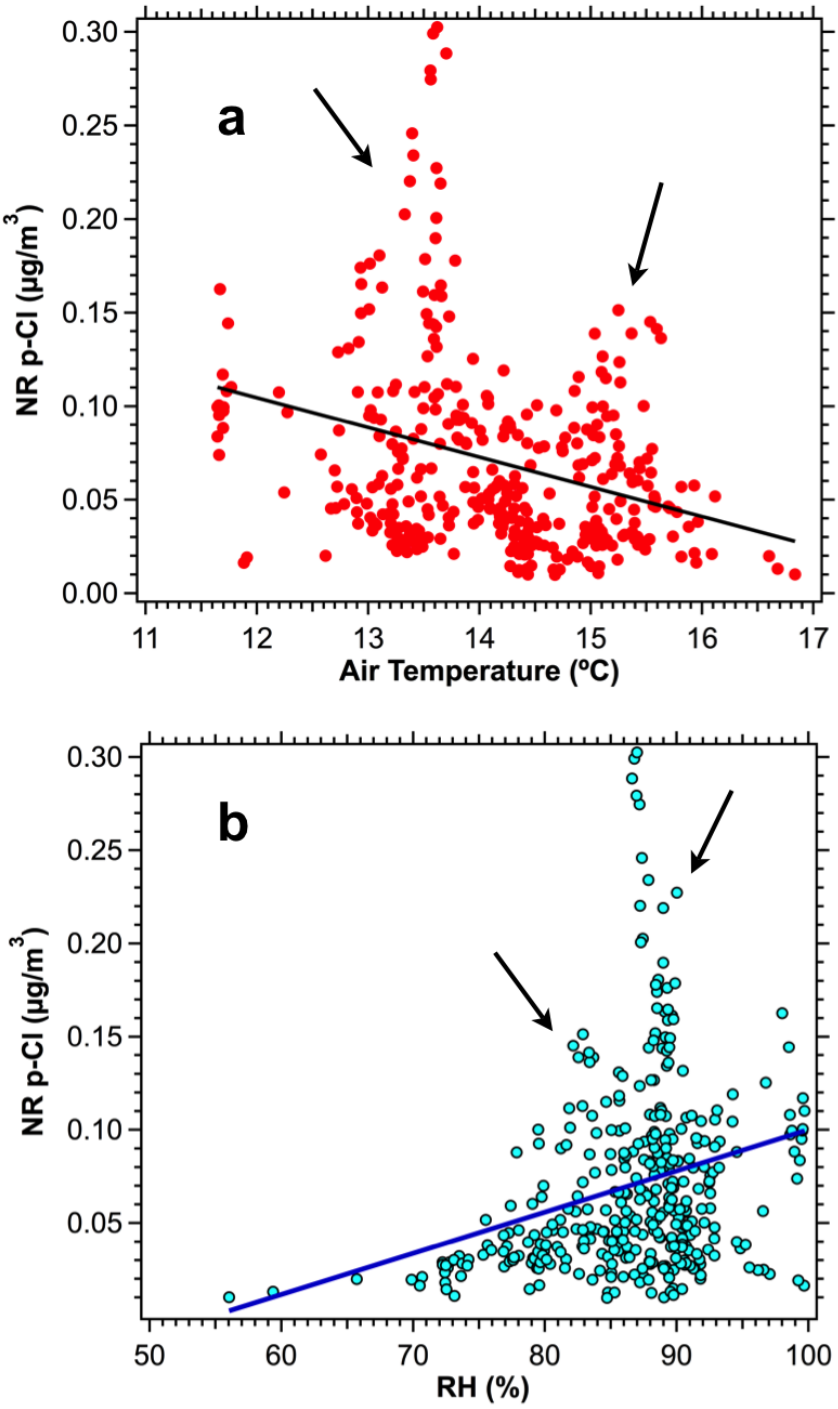

Figure 5.19: A plot of NR p-Cl as a function of temperature (a) and RH (b) for the case studies in Table 5.3 to establish the effect of temperature and RH on NR p-Cl. Arrows show two periods of deviation from the general trend.

NR p-Cl and $C_2H_4O_2$ are highly correlated with Pearson's correlation coefficient R^2 of 0.94. This suggests that biomass burning may have contributed to the enhancement of NR p-Cl during these periods and may account for the deviation of these peaks from the general decreasing trend of NR p-Cl with temperature and the increasing trend with RH (Figure 5.20).

Figure 5.21 is the same as Figure 5.19 but the data points are colour coded by the rate of chlorine atom production from the photolysis of $ClNO_2$ i.e. $jClNO_2 \times ClNO_2$. High levels of chlorine atom formation were observed coincident with the enhancement of NR p-Cl indicated by an arrow in Figure 5.21. During this period on May 21st from 14:40 to 16:40 (UTC), significant levels of chlorine atom were produced that may have given rise to the enhancement in NR p-Cl. The mechanism of NR p-Cl formation from chlorine atoms is shown in Figure 5.22, where photolysis of $ClNO_2$ and Cl_2 form Cl atoms upon photolysis. These Cl atoms oxidize organic species by hydrogen abstraction to form HCl. HCl and NH_3 are in a reversible equilibrium with NH_4Cl (s, aq). A study by Riedel et al (2012), aboard RV *Atlantis*, showed that the photolysis of $ClNO_2$ was the largest source of chlorine atom formation at 14:40 to 16:40 UTC (corresponds to 07:40-9:40 local time) when compared to the photolysis of Cl_2 and the oxidation of HCl by OH radicals.

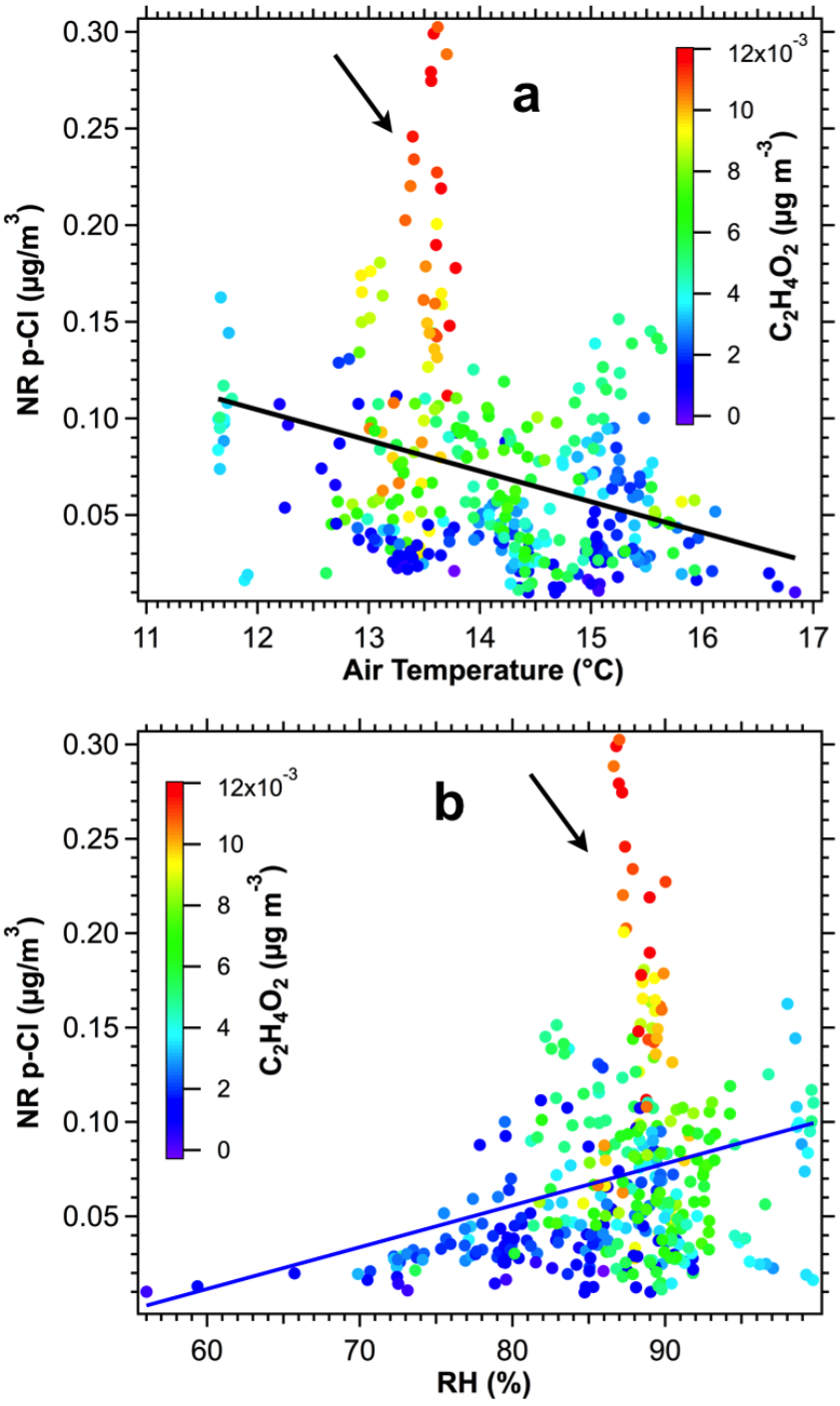

Figure 5.20: Same as Figure 5.19 but the points are colour coded by biomass burning marker $C_2H_4O_2$. a) Air temperature b) RH. Arrow shows an apparent enhancement of NR p-Cl and $C_2H_4O_2^+$ for a deviation period.

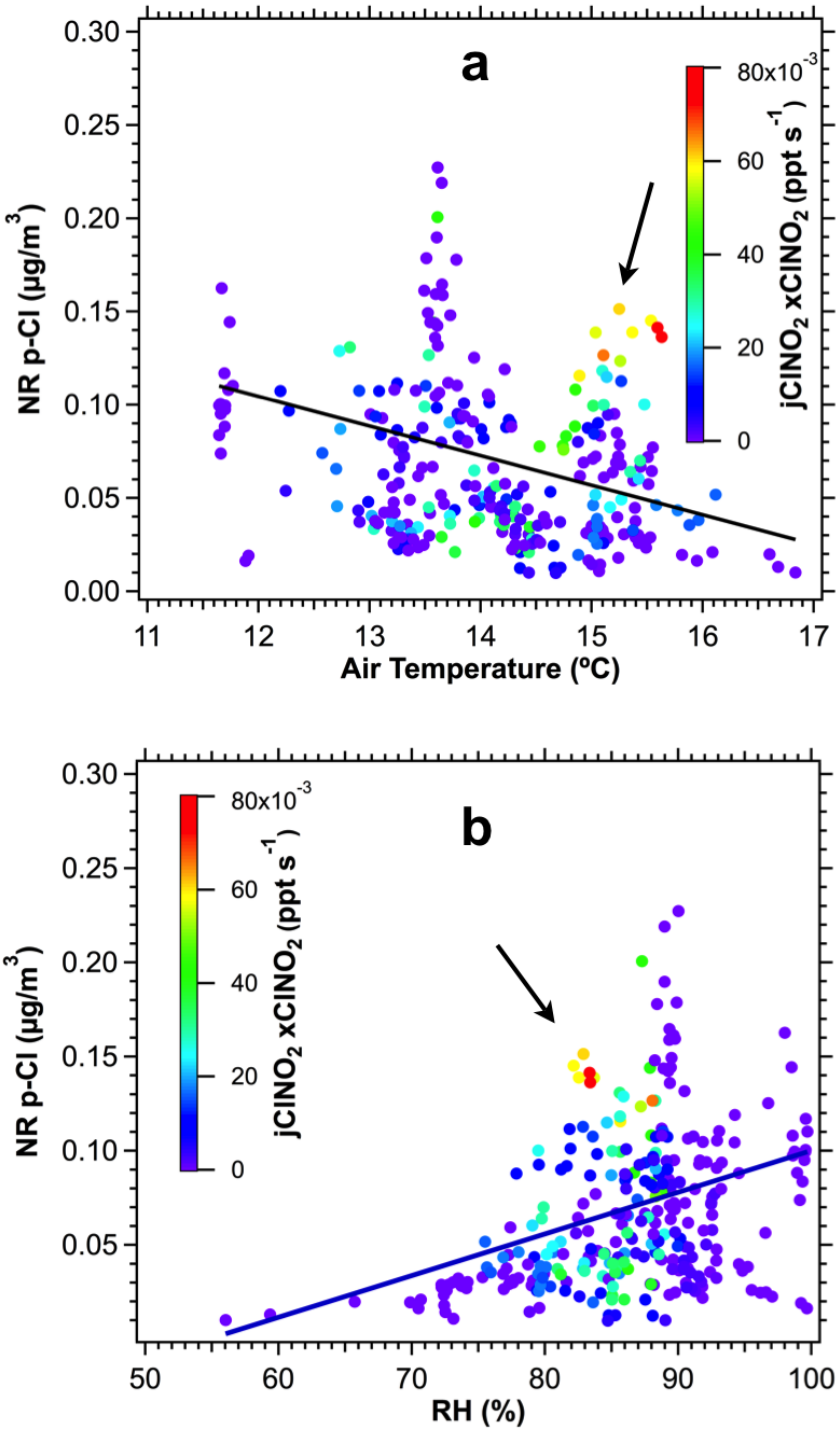

Figure 5.21: Same as Figure 5.19 but the points are colour coded by the rate of Cl atom formation from the photolysis of $ClNO_2$. a) Air temperature b) RH. Arrow shows an apparent enhancement of NR p-Cl and $jClNO_2 \times ClNO_2$ for a deviation period.

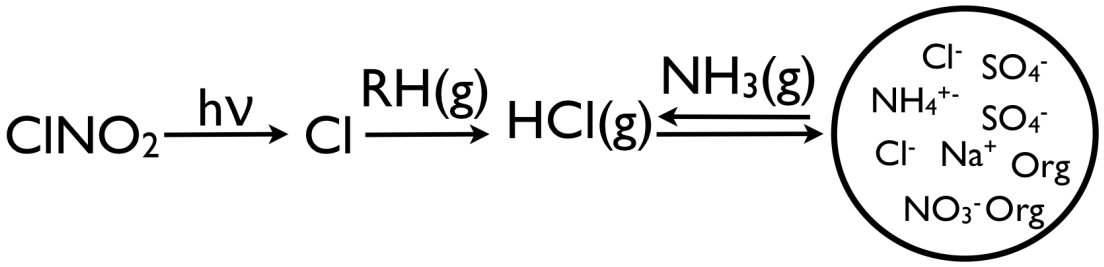

Figure 5.22: A possible mechanism of NR p-Cl formation from the photolysis of gaseous $ClNO_2$ and Cl_2.

.

5.13 The effect of aerosol pH on NR p-Cl formation

The formation of NH_4Cl is dependent on the availability of NH_3 after its neutralization with sulfuric acid (Ianniello et al., 2011; Trebs et al., 2005). This is due to the higher affinity of NH_3 for H_2SO_4 than HCl. Du et al (2010) found a linear correlation between non-sulfate ammonium and secondary particulate chloride formation. Furthermore, HCl can partition into the aerosol through the mechanism in Figure 5.22 discussed in the previous section. It is therefore expected that an increase in aerosol pH results in increased aerosol NR p-Cl formation given that other contributing factors remain constant.

Figure 5.23 is a plot of NH_4 molar concentration versus SO_4 molar concentration for the case studies listed in Table 5.3. The data points in are colour coded to reflect NR p-Cl concentrations. In this plot, a higher NH_4 to SO_4 molar ratio indicates a more basic aerosol. The position of H_2SO_4 and ammonium sulfate salts within the plot are shown in Figure 5.23. As expected an increased NR p-Cl concentration is

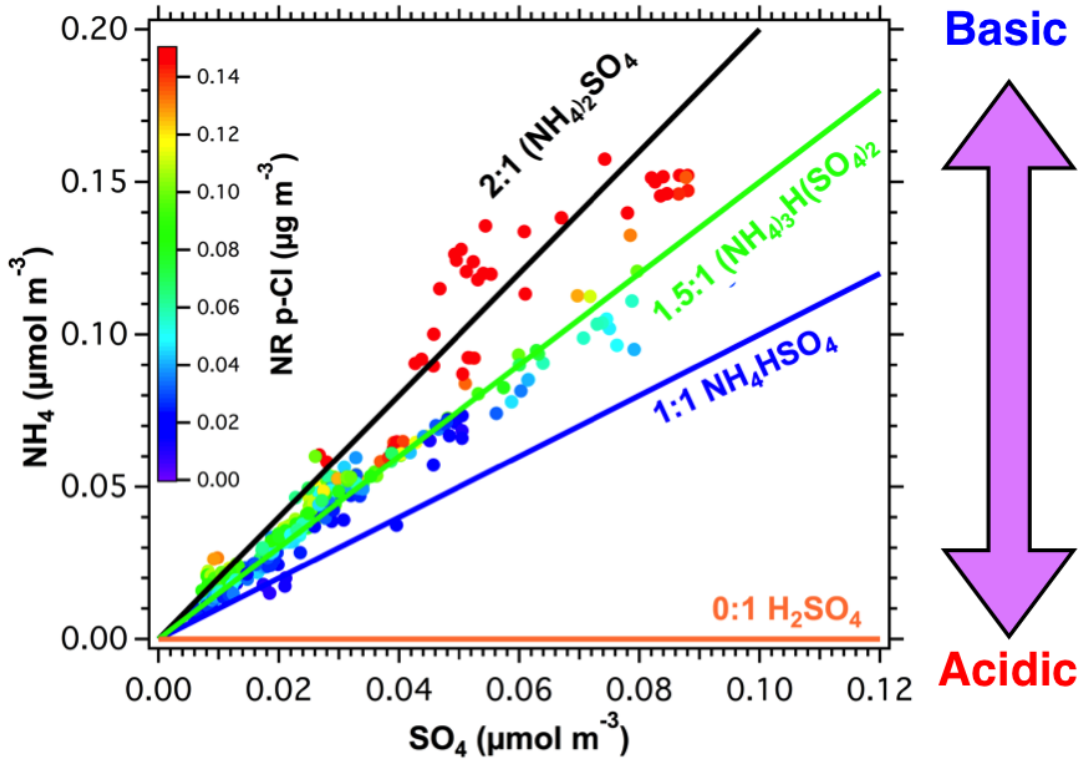

Figure 5.23: A plot of NH_4 VS SO4 for the case studies listed in Table 5.3. The data points are coloured to reflect NR p-Cl concentrations.

.

associated with more basic aerosols. Another way to show the dependence is shown in Figure 5.24, which is a box plot that shows the 5^{th}, 25^{th}, 75^{th} and 95^{th} percentiles of NR p-Cl concentrations as a function of NH_4/SO_4 molar concentrations for the case studies. A clear trend of increasing NR p-Cl concentrations with increasing NH_4 to SO_4 ratio is observed. This indicates that the particle acidity and the availability of excess ammonium is a determining factor in the formation of secondary aerosol chloride. Note that NR p-Cl measurements with associated NH_4 to SO_4 ratio < 1 were not included as they constituted only 1% of the case study measurements.

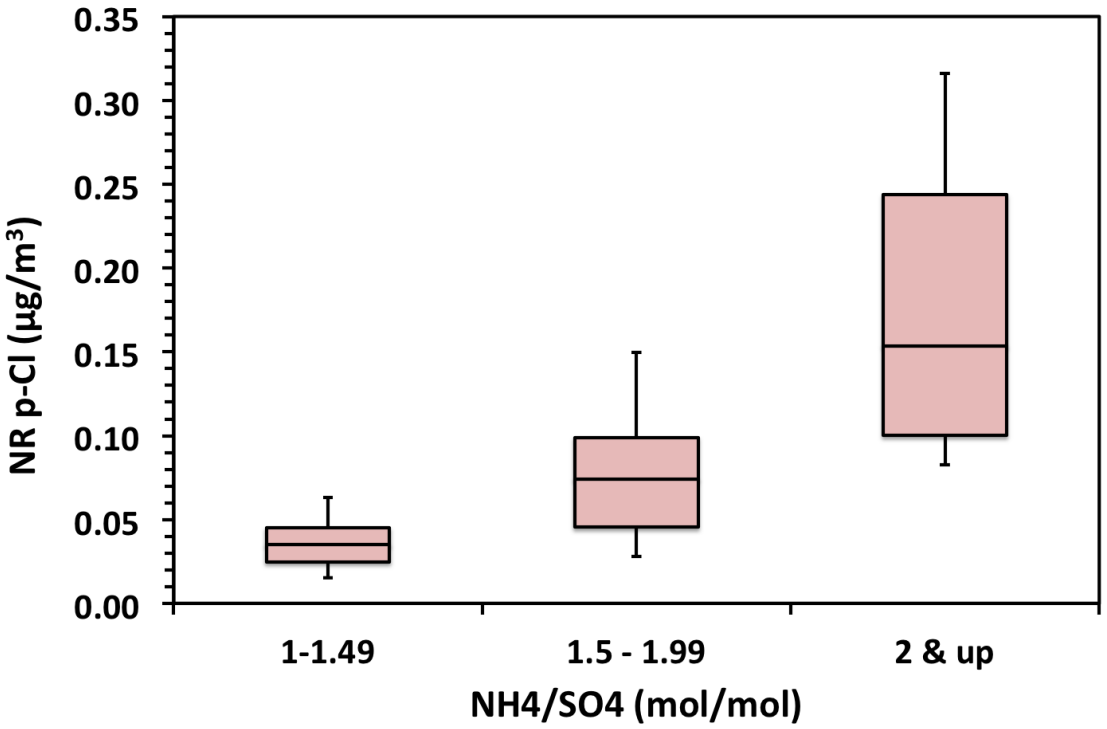

Figure 5.24: Box plot of 5^{th}, 25^{th}, 75^{th} and 95^{th} percentiles of NR p-Cl concentrations as a function of NH_4/SO_4 molar concentrations for the case studies.

.

Similar to NR p-Cl, p-NO_3 is reported to form via the formation of NH_4NO_3 from the reaction of non-sulfate ammonium with nitric acid (Ianniello et al., 2011; Trebs et al., 2005). Therefore, the dependence of p-NO_3 on pH is expected to be similar to that of NR p-Cl. Figures 5.25 and 5.26 are similar to Figure 5.23 and 5.24 above, but with p-NO_3 instead of NR p-Cl. As expected, p-NO_3 shows a pH dependence similar to that of NR p-Cl, with higher observed p-NO_3 concentrations observed with higher p-NH_4 to p-SO_4 ratios. Indeed, the highest correlations observed between NR p-Cl and p-NO_3 in these case studies were in periods with p-NH_4/p-SO_4 ratio ≥ 2. The pearson's

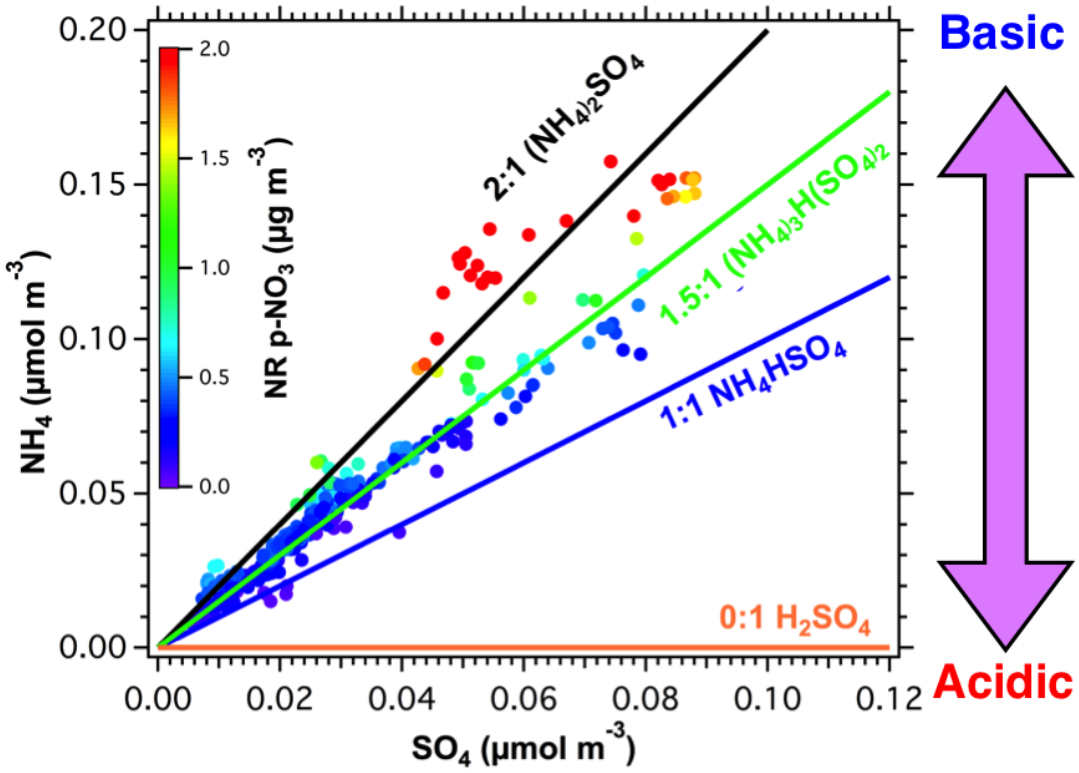

Figure 5.25: A plot of NH_4 VS SO4 for the case studies listed in Table 5.3. The data points are coloured to reflect p-NO_3 concentrations.

.

correlation coefficient, R^2 for these periods was 0.92. This is in comparison to an R^2 of 0.80 for the other periods, where $1 \leq$ p-NH_4/p-$SO_4 \leq 1.99$.

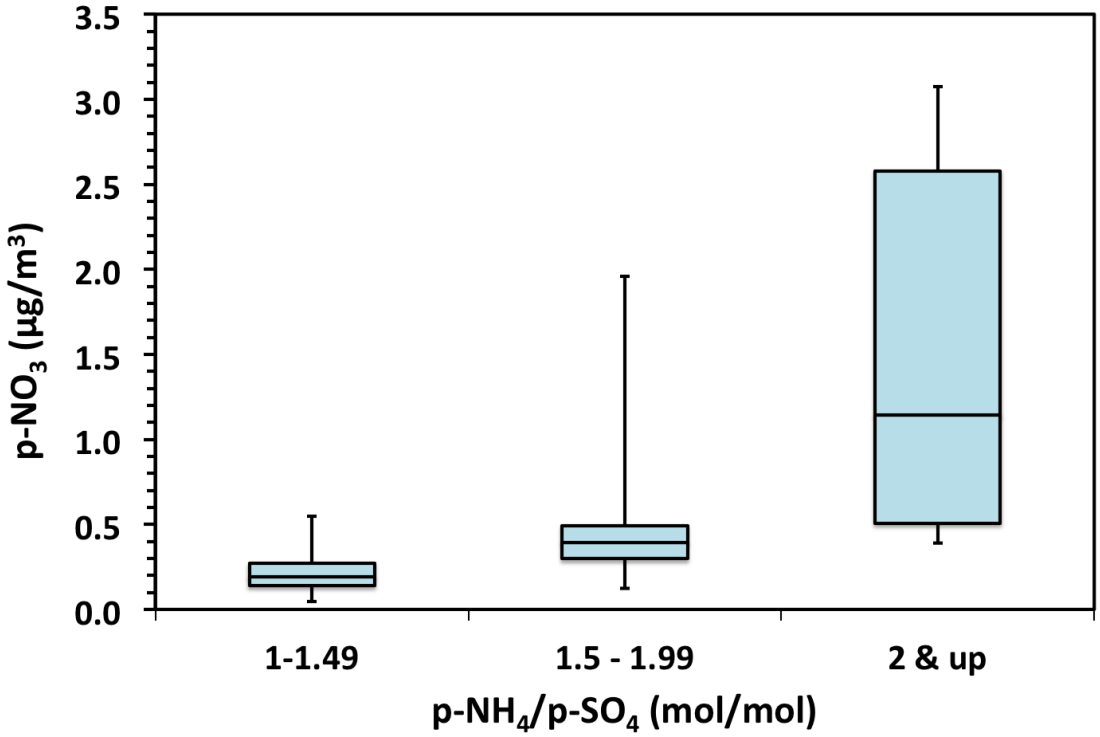

Figure 5.26: Box plot of 5^{th}, 25^{th}, 75^{th} and 95^{th} percentiles of p-NO_3 concentrations as a function of NH_4/SO_4 molar concentrations for the case studies.

.

5.14 Organic fractionation of sea spray aerosols

[8] In this section we examine the organic fractionation of Pacific sea spray aerosols sampled during sea sweep experiments. The design and deployment of the sea sweeps was by Bates and Quinn from NOAA (Section 5.4). My work involved the determination

[8]The results in this section were published in Bates, T. S., Quinn, P. K., Frossard, A. A., Russell, L. M., Hakala, J., T., P., Kulmala, M., Covert, D. S., Cappa, C. D., Li, S.-M., Hayden, K. L., Nuaaman, I., McLaren, R., Massoli, P., Canagaratna, M. R., Onasch, T. B., Sueper, D., Worsnop, D. R., and Keene, W. C. (2012). Measurements of ocean derived aerosol off the coast of California. J. Geophys. Res. Atmos. 117, D00V15. The permission to reuse and reproduce our work illustrated in Figures and written as text from this publication were granted by John Wiley and Sons; license numbers: 3594960141303 and 3594950485556.

of the fractionation of pOM in sea spray aerosols generated from sea sweeps using the HR-AMS. We have contributed to Bates et al (2012) through the work presented here.

Figure 5.27 is the mass spectrum of the non-refractory pOM in seawater during sea sweep experiments. This mass spectrum is the average of the 7 successful sea sweep experiments. The mass spectrum was divided into hydrocarbon, oxygenated hydrocarbon and nitrogen hydrocarbon classes. The hydrocarbon class was further deconvolved into saturated hydrocarbons and unsaturated hydrocarbons. Saturated hydrocarbons are shown as C_nH_{2n+1} ions and represent alkanes. Unsaturated hydrocarbons are indicated by C_nH_{2n-1} and C_nH_{2n-3} ions. The former unsaturated group represents alkenes and cycloalkanes, while the latter represents dienes, alkynes and cycloalkenes. Oxygenated hydrocarbons were separated into C_nH_mO and $C_nH_mO_{w>1}$ classes. Nitrogen hydrocarbons were separated into C_nH_mN, C_nH_mNO and $C_nH_mNO_{w\geq1}$.

For hydrocarbon non-oxygenated signal, the most dominant ions in order of prominence were m/z 41 ($C_3H_5^+$; C_nH_{2n-1}), 55 ($C_4H_7^+$; C_nH_{2n-1}), 39 ($C_3H_3^+$; C_nH_{2n-3}) and 27 ($C_2H_3^+$; C_nH_{2n-1}). Other significant contributions to the hydrocarbon spectra fragments were 29 ($C_2H_5^+$; C_nH_{2n+1}), 43 ($C_3H_7^+$; C_nH_{2n+1}) and 57 ($C_4H_9^+$; C_nH_{2n+1}). A study by Ovadnevaite (2011) at Mace Head, Ireland investigated the organic composition of marine aerosols originating from the N. E. Atlantic. Similar to this study, Ovadnevaite et al (2011) also reported a dominance of the signals at m/z 41, 39 and 27.

The most dominant ions in the mass spectrum were for oxygenated hydrocarbons at m/z 28 (CO^+; C_nH_mO) and 44 (CO_2^+; $C_nH_mO_{w>1}$). Note that, by default the

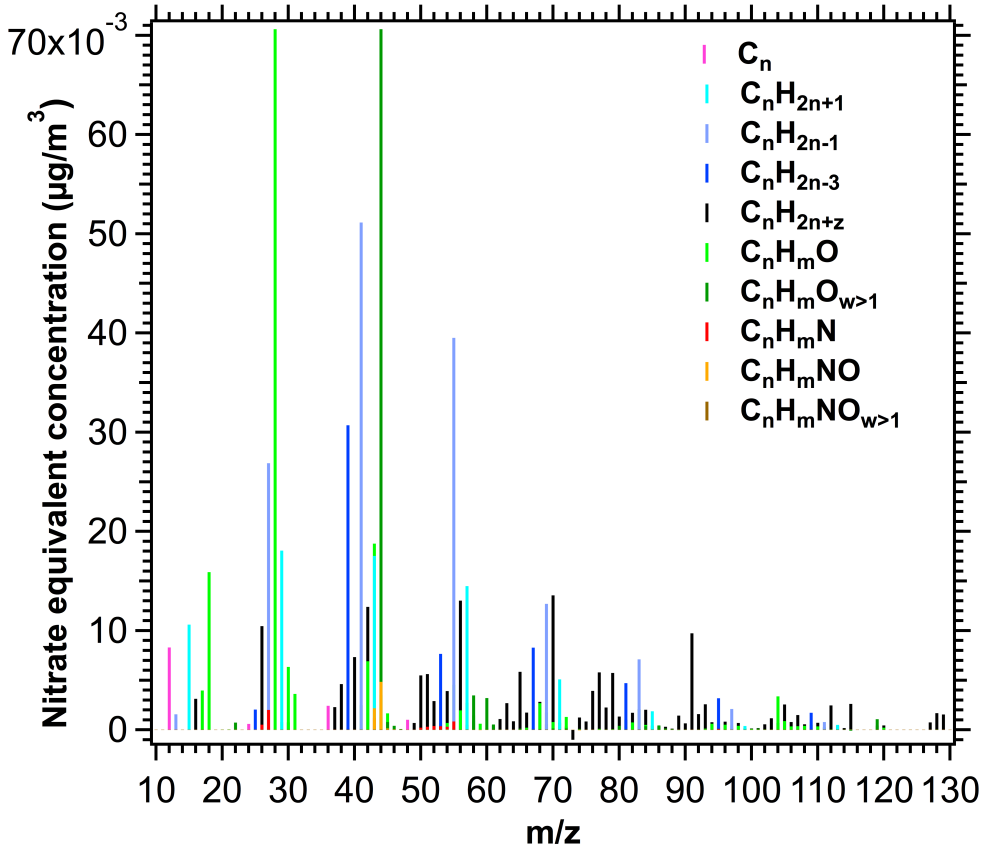

Figure 5.27: Mass spectrum of non-refractory pOM in seawater measured by an HR-AMS during sea sweep experiments. This mass spectrum is the average of 7 successful sea sweep experiments.

.

CO^+ signal at m/z 28 was set to be equal to the CO_2^+ signal at m/z 44. This is since the signal of CO^+ at m/z 28 is difficult to determine using an HR-AMS, due to an overwhelming contribution of the N_2 signal (Aiken et al., 2008). In ambient air, Takegawa et al (2007) and Aiken et al (2007) (for instance) used pTOF data and determined the ratio of CO^+ to CO_2^+ to be 1, which is similar to the default value.

Also using pTOF data, other studies report this ratio to be as low 0.85 and as high as 1.55 in ambient air (Zhang et al., 2005; Takegawa 2009). Therefore, the CO^+ signal is observed to be dominant but the signal reported can be off by 15 - 55 %. Another significant ion was $C_2H_3O^+$ at m/z 43, although its relative contribution was much less than the ion signals at m/z 28 and 44. For this oxygenated class, Ovadnevaite et al (2011) also reported dominant signals at m/z 44 and 43 and although not discussed a clear signal at m/z 28 equal to that at m/z 44 is observed from the mass spectrum by Ovadnevaite et al (2011). The lack of discussion of the signal at m/z 28 by Ovadnevaite could be due to the uncertainty outlined here.

For nitrogen hydrocarbons, the highest signals observed were for the spectral fragments at m/z 44 (CH_2NO^+) and 43 (CHNO) both of which are from the C_nH_mNO class. These fragments are typical of organonitrates and are associated with secondary organic aerosols (SOAs) in ambient air (Farmer et al., 2010). The observation of these fragments could be due to the deposition of ambient aerosols on the ocean surface. Also noteworthy are the absence of amino acid marker fragments at m/z 30 and 42 that are associated with biological aerosols (Schneider et al., 2011).

Figure 5.28 shows the contribution of the identified organic classes to the total pOM signal of sea sweep aerosols. Hydrocarbon classes dominated the pOM mass, accounting for 38-66% of the total pOM with an average of 55%. Unsaturated hydrocarbons accounted for about half of the hydrocarbon class. The contribution of oxygenated hydrocarbons to total pOM was 28-66% with an average of 37%. Nitrogen hydrocarbons had the lowest contributions accounting for only 1-4% with a 2% average.

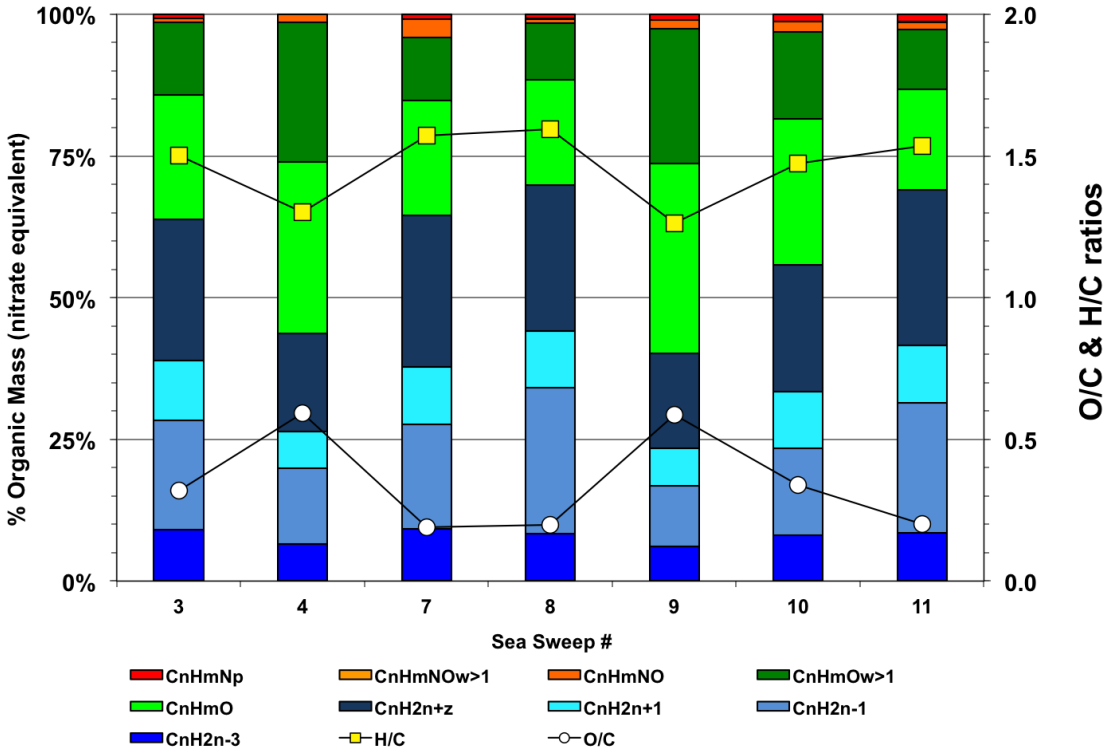

Figure 5.28: Contribution of the organic classes to the pOM signal in Sea Sweep experiments. O/C and H/C molar ratios are also shown. Hydrocarbons are in blue, oxygenates are in green and nitrogen hydrocarbons are in red.

.

The average observed O/C and H/C molar ratios for the sea spray aerosols were 0.35±0.18 and 1.5±0.13 respectively. The observed O/C ratio was lower than the 0.6 O/C reported by Ovadnevaite et al (2011). Since measurements by Ovadnevaite et al (2011) were taken at Mace Head, the higher O/C ratio could be due to the oxidation of marine aerosols during transport.

The concentrations of seawater aerosols (including pOM) were variable during sea sweep experiments increasing with higher aerosol injection into the HR-AMS. In order

to compare the observed pOM concentrations with seawater chlorophyll, the concentrations of pOM were normalized to chloride (H_XCl^+). In this analysis, no correlation was observed between normalized pOM and seawater chlorophyll. In contrast to chlorophyll, chloride normalized pOM showed a significant correlation ($R^2 = 0.57$) with seawater dimethylsulfide (Figure 5.29). DMS is produced from phytoplankton and macrophytes, diffusing through biological membranes and into cells where it acts as an antioxidant against OH radical in any cellular compartment (Lesser, 2006). Furthermore, DMS and other cellular components maybe released upon membrane rupture and cellular death.

Phytoplankton (algal) biomass contributes to pOM sea surface pool. Chlorophyll a is typically used as an indicator of phytoplankton (Quinn et al., 2014). A study by Quinn et al. (2014) reported that the organic mass fraction for nascent sea salt aerosol was independent of chlorophyll levels, which could explain the results observed in this study with regards to the correlation of pOM with chlorophyll a. The study by Quinn et al (2014), sampled coastal California and North Atlantic seawaters during CalNex and WACS campaigns utilizing sea sweep experiments.

Quinn et al (2014) concluded that the enrichment of sea salt by organics is associated with a large organic reservoir in the sea surface. The influence of this reservoir is much larger than any influence by biological activity as indicated by Chlorophyll a. This large reservoir is composed of dissolved organic carbon, which is produced from direct algal release, cell lysis and senescence by viruses and bacteria, as well as sloppy feeding of marine heterotrophs that ingest oceanic pOM (Quinn et al., 2014, and the references therein).

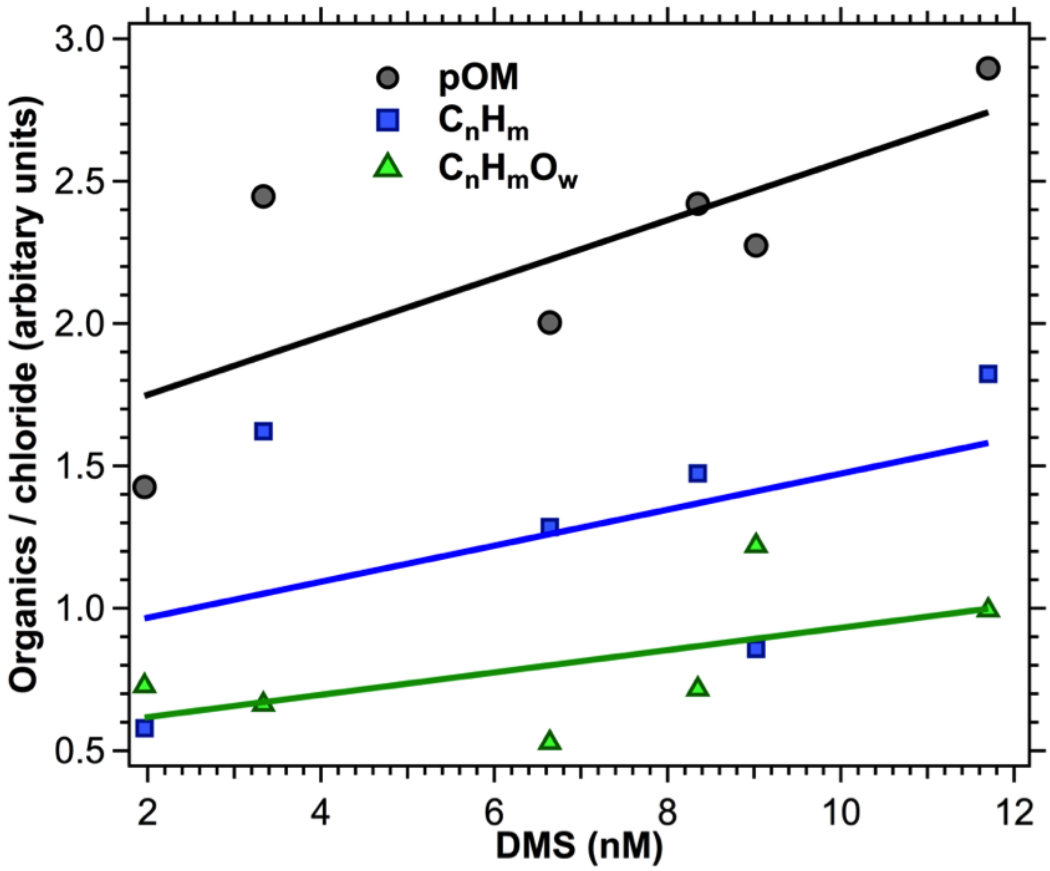

Figure 5.29: Observed correlation of chloride normalized organics measured during sea sweep experiments with seawater DMS. Linear equation for pOM: y = 0.10x + 1.54, $R^2 = 0.57$.

.

6 Conclusions and Future Work

6.1 Carbonyls measurements in southwestern Ontario during BAQS-Met

Six C1-C4 gaseous carbonyls were measured and quantified in the rural area of Ridgetown using an AT-DNPH-HPLC system. Median mixing ratios for formaldehyde, acetaldehyde, acetone, propanal, MEK and butanal were 1.5, 0.67, 1.9, 0.072, 0.22 and 0.41 ppb respectively. Measured carbonyls were dominated by formaldehyde, acetaldehyde and acetone, which accounted for 92% of the total on average. In this study, carbonyl contribution towards the NMHC carbon (ppbC) distribution was 22%, which was the second largest contribution after alkanes. Carbonyls had significant contributions towards the reactivity of the air masses, which was probed using the k_{OH} rate constant for the VOCs. Using only carbonyls reactivity towards OH oxidation and not photolysis, aldehydes were the second largest contributors towards air mass OH reactivity after alkenes accounting for 37% of the total reactivity.

Daytime photochemical formation sources and sinks for formaldehyde, acetaldehyde and acetone were established from the reactions of VOCs with OH and O_3 radicals.

Formaldehyde rate of formation was dominated by the reaction of OH with isoprene, methane and acetaldehyde respectively accounting for 84% of formaldehyde's total formation of 0.89 ppb/hr (assuming OH concentration of 5x10^6 molec/cm^{-3}). Sinks of formaldehyde were largely driven by OH oxidation and photolysis, which accounted for 62 and 34% (boundary layer height of 1000 m)of the 0.75 ppb/hr removal rate respectively.

The photochemical formation of acetaldehyde was dominated by the reactions of alkenes with OH, which accounted for 66% of the 0.21 ppb/hr total rate of formation. Sinks of acetaldehyde were largely dominated by the oxidation by OH radicals which accounted for 94% of the 0.19 ppb/hr rate of acetaldehyde removal. For acetone, the rate of formation was dominated by the reactions of isobutene, propane, isopentane and 2-methyl-2-butene with OH radical, which accounted for 82% of the total 0.070 ppb/hr rate of formation. Oxidation by OH and photolysis accounted for 62 and 38% acetone's 0.010 ppb/hr removal rate of 0.010 ppb/hr respectively. The net photochemical formation for acetone was estimated to be 0.060 ppb/hr.

Carbonyl diurnal profiles peaked in the afternoon and exhibited a similar trend as O_3, which confirms a photochemical origin for carbonyls. The diurnal profiles were more pronounced for aldehydes when compared to ketones, which is attributed to the longer lifetime of ketones. The CO diurnal profile was sigificantly different than that of carbonyls, could suggest that primary sources of carbonyls might not be significant contributors to their observed concentrations in this study.

The HCHO to CH_3CHO ratio was used as an indicator to establish whether car-

bonyls precursors are anthropogenic or biogenic in nature. The median ratio was observed to be 2.2, which suggests anthropogenic VOCs are the main precursors of carbonyl compounds. For a significant portion of the study (48% of the points), the HCHO to CH_3CHO ratio was in the 2-3 range, which suggests carbonyl formation results from the photo-oxidation of both anthropogenic and biogenic VOCs. The contribution of biogenic VOCs is in-line with modelled HCHO photochemical formation, which showed that isoprene oxidation by OH radical accounted for 32% of HCHO daytime photochemical formation.

The effect of trans-boundary transport on carbonyl was probed using back trajectory analysis, which showed that the highest carbonyl concentrations were associated with airmasses that passed over the U.S. states of Michigan and Illinois and could have originated from the Ohio Valley. This is the only analysis, to our knowledge, that links high carbonyl concentrations to trans-boundary transport in Canada.

Local ozone sensitivity was evaluated using the $HCHO/NO_2$ ratio (Tonnesen and Dennis., 2000), which established that ozone was largely sensitive to both VOC and NO_x. This is not a typical of rural areas and could be related to the impact of trans-boundary transport on this region. The contribution of carbonyls to O_3 formation was evaluated using the MIR scale (Carter 1994; 2010). The contribution of carbonyls to O_3 formation was estimated to be 35% during this study. Finally, the effects of lake breezes on carbonyl concentrations were investigated. For the duration of this study, no significant effect of lake breezes on carbonyl mixing ratio was observed. This also held true for O_3 and CO. This insiginificant impact could be explained by the type of lake

breezes encountered, which were the HD circulation type. With HD type lake breezes, the recirculation of pollutants and their subsequent enhancements are reduced.

Future work could include improvements of the AT-DNPH-HPLC system including the utilization of two DNPH cartridges. In this system, the contents of one DNPH cartridge can be flushed out and analyzed by the HPLC, while the other cartridge is simultaneously sampling ambient air. This could effectively decrease the time resolution by half from 2 hrs to 1 hr. The HPLC mobile phase and VWD programs can also be optimized for the measurement and quantification of dicarbonyls including methylglyoxal, glyoxal and diacetyl. The optimum detections of dicarbonyls is at wavelength $\sim$ 440 nm (Aiello and McLaren, 2009).

In addition, further carbonyl measurements in Canada in areas close to the border and impacted by lake/sea breeze circulations. Some areas of interest include Vancouver, British Columbia and Saint John, New Brunsiwck. These carbonyl measurements can include dicarbonyls (methylglyoxal, glyoxal and diacetyl), which could be measured and quantified using the AT-DNPH-HPLC system, through the optimization of the mobile phase and VWD programs, the latter for optimum detection at 440 nm. These measurements could further our understanding on the effects of trans-boudary transport and lake breeze events on carbonyl concentrations. It would also be interesting to investigate the sources and sinks of mono and dicarbonyls in these areas.

Other areas of scientific interest could be the investigation of wet precipitation as a sink of carbonyls. This could be through an investigation of carbonyl levels during the winter months at York University, where significant amounts of snow is expected and

samples could potentially be collected and analyzed for carbonyl compounds. Finally, the study of heterogeneous reaction of carbonyls, which might include the partitioning of low volatility gas phase diccarbonyls into particulate matter.

6.2 Aerosol measurements along the the coast of California during CalNex

Aerosol concentrations and composition were established along the coast of California using an HR-AMS during the CalNex study in 2010. The HR-AMS typically measures non-refractory submicron aerosols. The highest submicron (70-700 nm) aerosol concentrations were observed with land breeze events (continental outflows) from polluted cities in southern California. In contrast, the lowest concentrations were associated with clean marine sea breeze events. Using study-wide median concentrations, measured aerosols were dominated by p-SO_4 and pOM during, which accounted for 45% and 41% of the total aerosol measured during the study respectively. This is in contrast to p-NH_4, p-NO_3 and H_xCl^+ ion signal which accounted for 11%, 2% amd 1% respectively. Higher pOM contributions (54%) were observed with land breezes and were associated with relatively fresh emissions. The contributions of p-SO_4 and H_xCl^+ were significantly higher with clean marine events at 50% and 6% respectively, which are consistent with aged air masses in the case of p-SO_4 and the detection of sea salt chloride for H_xCl^+.

The highest chloride signal was observed during sea sweep experiments (Bates et

al., 2012), where artificially generated sea spray aerosols were sampled. During these experiments, high ions signals where detected for Na^+ at m/z 22.99 and $Na^{35}Cl^+$ at m/z 57.96. In these experiments, the source of chloride is primarily NaCl and a high signal was detected although the HR-AMS has a low sensitivity towards this refractory species. The latter two signals were also detected when sampling ambient air, which indicates that the RF H_xCl^+ signal in the form of NaCl is contributing towards the total H_xCl^+ signal. Sampling ambient air, the RF H_xCl^+ signal contribution reached a maximum of 89% in ambient but the study-wide average was 10%. A method was proposed for the first time to establish NR p-Cl in ambient air through a subtraction of RF H_xCl^+. The RF H_xCl^+ signal was estimated using the H_xCl^+ to $Na^{35}Cl^+$ ratio in sea sweep experiments. Sea salt (ss) p-Cl was established using the $Na^{35}Cl^+$ signal and a scaling factor of 98.9 derived from a comparison of Cl^- present in submicron aerosol collected on filters and the $Na^{35}Cl^+$ signal during the study. It then follows, that the ambient p-Cl concentration is the sum of ss p-Cl and NR p-Cl. The median concentrations for p-Cl, NR p-Cl and SS p-Cl were 0.052, 0.017 and 0.024 μg m^{-3} respectively and the average contributions of NR p-Cl and ss p-Cl to p-Cl were 48% and 52% respectively. NR p-Cl was dominant during periods of continental outflow, while ss p-Cl was dominant during periods of high wind speeds, which enhances wave action. Total submicron sea salt concentrations were established from $Na^{35}Cl^+$ and a scaling factor of 370, which was established through a comparison between filter measurements and $Na^{35}Cl^+$ similar to ss p-Cl. Ambient sea salt concentrations were observed to peak at 2.3 μg m^{-3} with a study wide average of 0.28 μg m^{-3}. A method that determined

percentage chloride depletion from ambient aerosol was proposed, which strictly uses HR-AMS measurements of Na^+ and $Na^{35}Cl^+$. This is the first time such a method was proposed. In this study, the median chloride depletion in submicron aerosols was established to be 78%.

The effects of temperature and RH on NR p-Cl were also investigated. A decrease in NR p-Cl concentrations with an increase in temperature was observed, whereas NR p-Cl concentrations increased with increasing RH. There were two periods of apparent deviations from this general trend. The first showed an enhancement of NR p-Cl with a biomass burning indicator $C_2H_2O_4$, which suggests that biomass burning may have contributed to the enhancement of NR p-Cl during this period. The second period showed an enhancement of NR p-Cl with an enhancement of chlorine atom formation. The reaction of Cl atoms with VOCs forms HCl which could deposit directly on basic aerosols and/or react with NH_3 to form NH_4Cl in the gaseous phase and subsequently in the aqueous or solid phases.

The effect of aerosol pH on NR p-Cl and p-NO_3 concentrations was investigated in this study. Aerosol p-NH_4 to p-SO_4 ratio was used as a surrogate for aerosol pH. Increasing concentrations of NR p-Cl and p-NO_3 was observed with increasing pH during this study. This was linked to the formation of NH_4Cl and NH_4NO_3, which is dependent on the availability of NH_3 after its preferential neutralization with sulfuric acid. Finally, organic fractionation of sea spray aerosols was established using sea sweep experiments. pOM mass was dominated by hydrocarbon classes accounting for an average of 55% (range from 38 to 66%) of the total pOM. Unsaturated hydrocarbons

accounted for about half of the hydrocarbon class. The second largest contribution was that of oxygenated hydrocarbons, which accounted for an average of 37% (range from 28 to 66%), whereas nitrogen hydrocarbons had the lowest average contribution of 2% (range from 1 to 2%). Seawater pOM was correlated with seawater DMS but not with chlorophyll. DMS is produced from phytoplankton and macrophytes and can be released upon membrane rupture and cellular death.

Future work could include a flow tube study laboratory study to investigate the impact of chlorine atom formation on p-Cl and pOM. Ambient air that contains both ambient particles and VOCs can be sampled through a flow tube. A flow tube with ambient air is advantageous over a chamber study, as the latter typically only utilizes few VOCs. Chlorine atoms can be introduced into the flow tube through an injection of Cl_2 gas followed by photolysis with a UV lamp. Ammonia gas can also be introduced to facilitate the formation of p-Cl from HCl formed from chlorine atom oxidation of VOCs. The fraction of chlorine atoms that partition into the aerosol as NH_4Cl can then be quantified. For pOM, the oxidation of ambient VOCs by chlorine atoms is expected to form SOA. This experiment will allow for the quantification of total SOA formed from chlorine oxidation. Aerosol concentrations, composition and size distribution can be obtained using an HR-AMS.

In addition, laboratory experiments can be performed to investigate and quantify the separate effects of RH and temperature on NR p-Cl formation. In these experiments, chlorine atoms, VOCs, NH_3 and seed aerosols could introduced into a chamber with the objective of forming NH_4Cl(s, aq). The chamber RH can then be varied at a

constant temperature for different experiments to investigate the effect of RH. Similarly, the chamber temperature can be varied at a constant RH to investigate the effect of temperature.

References

Abbatt, J. P., Lee, A. K., and Thornton, J. A. (2012). Quantifying trace gas uptake to tropospheric aerosol: recent advances and remaining challenges. Chem. Soc. Rev. 41, 6555-6581.

Agilent Technologies (2002). Agilent 1100 Series Variable Wavelength Detector: Reference Manual (Waldbronn, Germany: Agilent Technologies).

Aiello, M., and McLaren, R. (2009). Measurement of airborne carbonyls using an automated sampling and analysis system. Environ. Sci. Technol. 43, 8901-8907.

Aiello, M. An automated instrument for the quatitation of atmospheric carbonyls: Measurements and interpretation in Southern Ontario. Toronto: York University; 2003. p. Dissertation.

Aiken, A. C., DeCarlo, P. F., and Jimenez, J. L. (2007). Elemental analysis of organic species with electron ionization high-resolution mass spectrometry. Anal. Chem. 79, 8350-8358.

Aiken, A. C., Salcedo, D., Cubison, M. J., Huffman, J. A., DeCarlo, P. F., Ulbrich, I. M., Docherty, K. S., Sueper, D., Kimmel, J. R., Worsnop, D. R., and others (2009). Mexico City aerosol analysis during MILAGRO using high resolution aerosol mass spectrometry at the urban supersite (T0)–Part 1: Fine particle composition and organic source apportionment. Atmos. Chem. Phys. 9, 6633-6653.

Aiken, A. C., DeCarlo, P. F., Kroll, J. H., Worsnop, D. R., Huffman, J. A., Docherty, K. S., Ulbrich, I. M., Mohr, C., Kimmel, J. R., Sueper, D., Sun, Y., Zhang, Q., Trimborn, A., Northway, M., Ziemann, P. J., Canagaratna, M. R., Onasch, T. B., Alfarra,

M. R., Prevot, A. S. H., Dommen, J., Duplissy, J., Metzger, A., Baltensperger, U., and Jimenez, J. L. (2008). O/C and OM/OC Ratios of primary, secondary, and ambient organic aerosols with High-Resolution Time-of-Flight Aerosol Mass Spectrometry. Environ. Sci. Technol. 42, 4478-4485.

Alfarra, M. R., Prevot, A. S. H., Szidat, S., Sandradewi, J., Weimer, S., Lanz, V. A., Schreiber, D., Mohr, M., and Baltensperger, U. (2007). Identification of the mass spectral signature of organic aerosols from wood burning emissions. Environ. Sci. Technol. 41, 5770-5777.

Alfarra, M. R. Insights into atmospheric organic aerosols using an aerosol mass spectrometer. University of Manchester; 2004. p. Dissertation.

Alfarra, M. R., Coe, H., Allan, J. D., Bower, K. N., Boudries, H., Canagaratna, M. R., Jimenez, J. L., Jayne, J. T., Garforth, A. A., Li, S.-M., and Worsnop, D. R. (2004). Characterization of urban and rural organic particulate in the Lower Fraser Valley using two Aerodyne Aerosol Mass Spectrometers. Atmos. Environ. 38, 5745-5758.

Allan, J. D., Delia, A. E., Coe, H., Bower, K. N., Alfarra, M. R., Jimenez, J. L., Middlebrook, A. M., Drewnick, F., Onasch, T. B., Canagaratna, M. R., Jayne, J. T., and Worsnop, D. R. (2004). A generalised method for the extraction of chemically resolved mass spectra from Aerodyne aerosol mass spectrometer data. J. Aer. Sci. 35, 909-922.

Allan, J. D. (2004). Submicron aerosol composition at Trinidad Head, California, during ITCT 2K2: Its relationship with gas phase volatile organic carbon and assessment of instrument performance. J. Geophys. Res. 109, D23S24.

Allan, J. D., Jimenez, J. L., Williams, P. I., Alfarra, M. R., Bower, K. N., Jayne, J. T., Coe, H., and Worsnop, D. R. (2003). Quantitative sampling using an Aerodyne aerosol mass spectrometer 1. Techniques of data interpretation and error analysis. J. Geophys. Res. 108, 4090.

Altshuller, A. P. (1991a). Chemical reactions and transport of alkanes and their products in the troposphere. J. Atmos. Chem. 12, 19-61.

Altshuller, A. P. (1991b). Estimating product yields of carbon-containing products

from the atmospheric photooxidation of ambient air alkenes. J. atmos. chem. 13, 131-154.

Altshuller, A. P. (1993). Production of aldehydes as primary emissions and from secondary atmospheric reactions of alkenes and alkanes during the night and early morning hours. Atmos. Environ. 27, 21-32.

Anderson, L. G., Lanning, J. A., Barrell, R., Miyagishima, J., Jones, R. H., and Wolfe, P. (1996). Sources and sinks of formaldehyde and acetaldehyde: An analysis of Denvers ambient concentration data. Atmos. Environ. 30, 2113-2123.

Andino, J. M., Smith, J. N., Flagan, R. C., Goddard, W. A., and Seinfeld, J. H. (1996). Mechanism of atmospheric photooxidation of aromatics: A theoretical study. J. of Phys. Chem. 100, 10967-10980.

Andreae, M. O. (1982). Marine Aerosol Chemistry at Cape Grim, Tasmania, and Townsville, Queensland. J. Geophys. Res. 87, 8875-8885.

Andreae, M. O., Atlas, E., Harris, G. W., Helas, G., De, K., A, Koppmann, R., Maenhaut, W., Man, S., Pollock, W. H., Rudolph, J., and others (1996). Methyl halide emissions from savanna fires in southern Africa. J. Geophys. Res. 101, 23603-23623.

Atkinson, R. (1997). Gas-Phase tropospheric chemistry of volatile organic compounds: 1. Alkanes and alkenes. J. Phys. Chem. Ref. Data 26, 215.

Atkinson, R., Baulch, D. L., Cox, R. A., Crowley, J. N., Hampson, R. F., Hynes, R. G., Jenkin, M. E., Rossi, M. J., Troe, J., and IUPAC, S. (2006). Evaluated kinetic and photochemical data for atmospheric chemistry: Volume II-gas phase reactions of organic species. Atmos. Chem. Phys. 6, 3625-4055.

Atkinson, R. (1990). Gas-phase tropospheric chemistry of organic compounds: A review. Atmos. Environ. 24, 1-41.

Atkinson, R. (2000). Atmospheric chemistry of VOCs and NO_x. Atmos. Environ. 34, 2063-2101.

Atkinson, R., and Lloyd, A. C. (1984). Evaluation of kinetic and mechanistic data for modelling of photochemical smog. Journal of physical and chemical reference data 13, 315-444.

Atkinson, R., Tuazon, E. C., and Aschmann, S. M. (1995a). Products of the gas-phase reactions of a series of 1-alkenes and 1-methylcyclohexene with the OH radical in the presence of NO. Environ. Sci. Technol. 29, 1674-1680.

Atkinson, R., Tuazon, E. C., and Aschmann, S. M. (1995b). Products of the gas-phase reactions of O_3 with alkenes. Environ. Sci Technol. 29, 1860-1866.

Avzianova, E. V., and Ariya, P. A. (2002). Temperature-dependent kinetic study for ozonolysis of selected tropospheric alkenes. Int. J. Chem. Kinet. 34, 678-684.

Bates, T. S., Quinn, P. K., Frossard, A. A., Russell, L. M., Hakala, J., T., P., Kulmala, M., Covert, D. S., Cappa, C. D., Li, S.-M., Hayden, K. L., Nuaaman, I., McLaren, R., Massoli, P., Canagaratna, M. R., Onasch, T. B., Sueper, D., Worsnop, D. R., and Keene, W. C. (2012). Measurements of ocean derived aerosol off the coast of California. J. Geophys. Res. Atmos. 117, D00V15.

Baumgardner, D., Raga, G. B., Grutter, M., and Lammel, G. (2006a). Evolution of anthropogenic aerosols in the coastal town of Salina Cruz, Mexico: part I particle dynamics and land-sea interactions. Sci. Total Environ. 367, 288-301.

Baumgardner, D., Raga, G. B., Grutter, M., Lammel, G., and Moya, M. (2006b). Evolution of anthropogenic aerosols in the coastal town of Salina Cruz, Mexico: part II particulate phase chemistry. Sci. Total Environ. 372, 287-298.

Berner, A., Lurzer, C., Pohl, F., Preining, O., and Wagner, P. (1979). The size distribution of the urban aerosol in Vienna. Sci. Total Environ. 13, 245-261.

Bicking, M. K. L. (2006). Integration errors in chromatographic analysis, part II: Large peak size ratios.

Blanchard, D. C., and Woodcock, A. H. (1980). The production, concentration and vertical distribution of the sea-salt aerosol. Annals of the New York Academy of Sciences 338, 330-347.

Blanchard, D. C. (1985). The oceanic production of atmospheric sea salt. J. Geophys. Res. 90, 961-963.

Blumenthal, D. L., White, W. H., and Smith, T. B. (1978). Anatomy of a Los Angeles smog episode: Pollutant transport in the daytime sea breeze regime. Atmos.

Environ. 12, 893-907.

Brankov, E., Henry, R. F., Civerolo, K. L., Hao, W., Rao, S. T., Misra, P. K., Bloxam, R., and Reid, N. (2003). Assessing the effects of transboundary ozone pollution between Ontario, Canada and New York, USA. Environmental Pollution 123, 403-411.

Brook, J. R., Makar, P. A., Sills, D. M. L., Hayden, K. L., and McLaren, R. (2013). Exploring the nature of air quality over southwestern Ontario: main findings from the Border Air Quality and Meteorology Study. Atmos. Chem. Phys. 13, 10461-10482.

Brook, J. R., Strawbridge, K. B., Snyder, B. J., Boudries, H., Worsnop, D., Sharma, S., Anlauf, K., Lu, G., and Hayden, K. (2004). Towards an understanding of the fine particle variations in the LFV: integration of chemical, physical and meteorological observations. Atmos. Environ. 38, 5775-5788.

Brown, S. S., and Stutz, J. (2012). Nighttime radical observations and chemistry. Chem. Soc. Rev. 41, 6405-6447.

Buffaloe, G. M., Lack, D. A., Williams, E. J., Coffman, D., Hayden, K. L., Lerner, B. M., Li, S.-M., Nuaaman, I., Massoli, P., Onasch, T. B., Quinn, P. K., and Cappa, C. D. (2014). Black carbon emissions from in-use ships: a California regional assessment. Atmos. Chem. Phys. 14, 1881-1896.

Cai, X., and Griffin, R. J. (2006). Secondary aerosol formation from the oxidation of biogenic hydrocarbons by chlorine atoms. J. Geophys. Res. 111, D14206.

Cai, X., Ziemba, L. D., and Griffin, R. J. (2008). Secondary aerosol formation from the oxidation of toluene by chlorine atoms. Atmos. Environ. 42, 7348-7359.

Canagaratna, M. R., Jayne, J. T., Jimenez, J. L., Allan, J. D., Alfarra, M. R., Zhang, Q., Onasch, T. B., Drewnick, F., Coe, H., Middlebrook, A., Delia, A., Williams, L. R., Trimborn, A. M., Northway, M. J., DeCarlo, P. F., Kolb, C. E., Davidovits, P., and Worsnop, D. R. (2007). Chemical and microphysical characterization of ambient aerosols with the aerodyne aerosol mass spectrometer. Mass Spectrom. Rev. 26, 185-222.

Cantrell, C. A., Stockwell, W. R., Anderson, L. G., Busarow, K. L., Perner, D., Schmeltekopf, A., Calvert, J. G., and Johnston, H. S. (1985). Kinetic study of the

nitrate free radical (NO3)-formaldehyde reaction and its possible role in nighttime tropospheric chemistry. J. Phys. Chem. 89, 139-146.

Cappa, C. D., Onasch, T. B., Massoli, P., Worsnop, D. R., Bates, T. S., Cross, E. S., Davidovits, P., Hakala, J., Hayden, K. L., Jobson, B. T., Kolesar, K. R., Lack, D. A., Lerner, B. M., Li, S.-M., Mellon, D., Nuaaman, I., Olfert, J. S., Petaja, T., Quinn, P. K., Song, C., Subramanian, R., Williams, E. J., and Zaveri, R. A. (2013). Response to Comment on Radiative absorption enhancements due to the mixing state of atmospheric black carbon. Science 339, 393-393.

Cappa, C. D., Williams, E. J., Lack, D. A., Buffaloe, G. M., Coffman, D., Hayden, K. L., Herndon, S. C., Lerner, B. M., Li, S.-M., Massoli, P., McLaren, R., Nuaaman, I., Onasch, T. B., and Quinn, P. K. (2014). A case study into the measurement of ship emissions from plume intercepts of the NOAA ship Miller Freeman. Atmos. Chem. Phys. 14, 1337-1352.

Cappa, C. D., Onasch, T. B., Massoli, P., Worsnop, D. R., Bates, T. S., Cross, E. S., Davidovits, P., Hakala, J., Hayden, K. L., Jobson, B. T., Kolesar, K. R., Lack, D. A., Lerner, B. M., Li, S. M., Mellon, D., Nuaaman, I., Olfert, J. S., Petaja, T., Quinn, P. K., Song, C., Subramanian, R., Williams, E. J., and Zaveri, R. A. (2012). Radiative absorption enhancements due to the mixing state of atmospheric black carbon. Science 337, 1078-1081.

Carlier, P., Hannachi, H., and Mouvier, G. (1986). The chemistry of carbonyl compounds in the atmosphere–A review. Atmos. Environ. 20, 2079-2099.

Carter, W. P. L. (1994). Development of ozone reactivity scales for volatile organic compounds. Air and waste 44, 881-899.

Carter, W. P. L. (1996). Condensed atmospheric photooxidation mechanisms for isoprene. Atmos. Environ. 30, 4275-4290.

Carter, W. P. L. (2010). Updated maximum incremental reactivity scale and hydrocarbon bin reactivities for regulatory applications. California Air Resources Board Contract 07-339 1-25.

Carter, W. P. L., and Atkinson, R. (1996). Development and evaluation of a detailed

mechanism for the atmospheric reactions of isoprene and NO_x. Int. J. Chem. Kinet. 28, 497-530.

Cavalli, F., Facchini, M. C., Decesari, S., Mircea, M., Emblico, L., Fuzzi, S., Ceburnis, D., Yoon, Y. J., ODowd, C. D., Putaud, J.-P., and others (2004). Advances in characterization of size-resolved organic matter in marine aerosol over the North Atlantic. J. Geophys. Res. 109, D24215.

Cern, R. M., Cern, J. G., and Muriel, M. (2007). Diurnal and seasonal trends in carbonyl levels in a semi-urban coastal site in the Gulf of Campeche, Mexico. Atmos. Environ. 41, 63-71.

Cerqueira, M. A., Pio, C. A., Gomes, P. A., Matos, J. S., and Nunes, T. V. (2003). Volatile organic compounds in rural atmospheres of central Portugal. Sci. Tot. Environ. 313, 49-60.

Cheng, W.-L. (2002). Ozone distribution in coastal central Taiwan under sea-breeze conditions. Atmos. Environ. 36, 3445-3459.

Chin, M., and Jacob, D. J. (1996). Anthropogenic and natural contributions to tropospheric sulfate: A global model analysis. J. Geophys. Res. Atmos. 101, 18691-18699.

Christensen, C. S., Skov, H., Nielsen, T., and Lohse, C. (2000). Temporal variation of carbonyl compound concentrations at a semi-rural site in Denmark. Atmos. Environ. 34, 287-296.

Cox, R. A., Derwent, R. G., and Williams, M. R. (1980). Atmospheric photooxidation reactions. Rates, reactivity, and mechanism for reaction of organic compounds with hydroxyl radicals. Environ. Sci. Technol. 14, 57-61.

Dai, W. T., Ho, S. S. H., Ho, K. F., Liu, W. D., Cao, J. J., and Lee, S. C. (2012). Seasonal and diurnal variations of mono- and di-carbonyls in Xian, China. Atmos. Res. 113, 102-112.

Dasgupta, P. K., Campbell, S. W., Al-Horr, R. S., Ullah, S. M. R., Li, J., Amalfitano, C., and Poor, N. D. (2007). Conversion of sea salt aerosol to NaNO3 and the production of HCl: Analysis of temporal behavior of aerosol chloride/nitrate and

gaseous HCl/HNO3 concentrations with AIM. Atmos. Environ. 41, 4242-4257.

Dasgupta, P. K., Li, J., Zhang, G., Luke, W. T., McClenny, W. A., Stutz, J., and Fried, A. (2005). Summertime ambient formaldehyde in five U.S. metropolitan areas: Nashville, Atlanta, Houston, Philadelphia, and Tampa. Environ. Sci. Technol. 39, 4767-4783.

Davidson, C. I., Phalen, R. F., and Solomon, P. A. (2005). Airborne particulate matter and human health: A review. Aerosol Sci. Technol. 39, 737-749.

DeCarlo, P. F., Dunlea, E. J., Kimmel, J. R., Aiken, A. C., Sueper, D., Crounse, J., Wennberg, P. O., Emmons, L., Shinozuka, Y., Clarke, A., Zhou, J., Tomlinson, J., Collins, D. R., Knapp, D., Weinheimer, A. J., Montzka, D. D., Campos, T., and Jimenez, J. L. (2008). Fast airborne aerosol size and chemistry measurements above Mexico City and Central Mexico during the MILAGRO campaign. Atmos. Chem. Phys. 8, 4027-4048.

DeCarlo, P. F., Kimmel, J. R., Trimborn, A., Northway, M. J., Jayne, J. T., Aiken, A. C., Gonin, M., Fuhrer, K., Horvath, T., Docherty, K. S., Worsnop, D. R., and Jimenez, J. L. (2006). Field-Deployable, High-Resolution, Time-of-Flight Aerosol Mass Spectrometer. Anal. Chem. 78, 8281-8289.

Docherty, K. S., Stone, E. A., Ulbrich, I. M., DeCarlo, P. F., Snyder, D. C., Schauer, J. J., Peltier, R. E., Weber, R. J., Murphy, S. M., Seinfeld, J. H., Grover, B. D., Eatough, D. J., and Jimenez, J. L. (2008). Apportionment of primary and secondary organic aerosols in Southern California during the 2005 Study of Organic Aerosols in Riverside (SOAR-1). Environ. Sci. Technol. 42, 7655-7662.

Dockery, D. W., Pope, C. A., Xu, X., Spengler, J. D., Ware, J. H., Fay, M. E., Ferris, J., Benjamin G, and Speizer, F. E. (1993). An association between air pollution and mortality in six US cities. New England journal of medicine 329, 1753-1759.

Draxler, R. R., and Rolph, G. D. (2014). HYbrid Single-Particle Lagrangian Integrated Trajetory. Model access via NOAA ARL READY Website <http://ready.arl.noaa.gov/HYSPLIT.php>. [8 December 2014]

Du, H. (2010). Insights into ammonium particle-to-gas conversion: Non-sulfate

ammonium coupling with nitrate and chloride. Aerosol Air Qual. Res. 589-595.

Dunlea, E. J., Herndon, S. C., Nelson, D. D., Volkamer, R. M., San, M., F, Sheehy, P. M., Zahniser, M. S., Shorter, J. H., Wormhoudt, J. C., Lamb, B. K., Allwine, E. J., Gaffney, J. S., Marley, N. A., Grutter, M., Marquez, C., Blanco, S., Cardenas, B., Retama, A., Ramos Villegas, C. R., Kolb, C. E., Molina, L. T., and Molina, M. J. (2007). Evaluation of nitrogen dioxide chemiluminescence monitors in a polluted urban environment. Atmos. Chem. Phys. 7, 2691-2704.

EC CGGMP: Environment Canada Canadian Greenhouse Gas Measurement Program. (2011). Canadian Greenhouse Gas Measurement Program <http://www.ec.gc.ca/mges-ghgm/>.

Ensberg, J. J., Craven, J. S., Metcalf, A. R., Allan, J. D., Angevine, W. M., Bahreini, R., Brioude, J., Cai, C., Coe, H., de, G., J. A., Ellis, R. A., Flynn, J. H., Haman, C. L., Hayes, P. L., Jimenez, J. L., Lefer, B. L., Middlebrook, A. M., Murphy, J. G., Neuman, J. A., Nowak, J. B., Roberts, J. M., Stutz, J., Taylor, J. W., Veres, P. R., Walker, J. M., and Seinfeld, J. H. (2013). Inorganic and black carbon aerosols in the Los Angeles Basin during CalNex. J. Geophys. Res. Atmos. 118, 1777-1803.

EC: Environment Canada (2013). 10 Years of Data From the National Pollution Surveillance (NAPS) Network <http://www.ec.gc.ca/rnspa-naps/77FECF05-E241-4BED-8375-5A NAPS_Annual_Report_August2013_E.pdf>. [20 November 2014]

EC: Environment Canada (2014). Volatile Organic Compounds Emissions for Ontario <http://www.ec.gc.ca/inrp-npri/donnees-data/ap/index.cfm?do=ap_query&lang=en>. [15 October 2014]

EC: Environment Canada (2015). Pollution Issues <http://www.ec.gc.ca/inrp-npri/donnees-data/ap/index.cfm?do=ap_query&lang=en>. [6 February 2015]

EPA: Environmental Protection Agency (2015). Pollutants and Sources <http://www.epa.gov/airquality/aqmportal/management/control_strategies.htm>.[January 13, 2015]

Erickson, D. J., III, Seuzaret, C., Keene, W. C., and Gong, S. L. (1999). A general circulation model based calculation of HCl and ClNO2 production from sea salt dechlo-

rination: Reactive chlorine emissions inventory. J. Geophys. Res. 104, 8347-8372.

Evtyugina, M. G., Nunes, T., Pio, C., and Costa, C. S. (2006). Photochemical pollution under sea breeze conditions, during summer, at the Portuguese West Coast. Atmos. Environ. 40, 6277-6293.

Facchini, M. C., Rinaldi, M., Decesari, S., Carbone, C., Finessi, E., Mircea, M., Fuzzi, S., Ceburnis, D., Flanagan, R., Nilsson, E. D., de, L., Gerrit, Martino, M., Woeltjen, J., and ODowd, C. D. (2008). Primary submicron marine aerosol dominated by insoluble organic colloids and aggregates. Geophys. Res. Lett. 35, 17.

Farmer, D. K., Matsunaga, A., Docherty, K. S., Surratt, J. D., Seinfeld, J. H., Ziemann, P. J., and Jimenez, J. L. (2010). Response of an aerosol mass spectrometer to organonitrates and organosulfates and implications for atmospheric chemistry. Proc. Natl. Acad. Sci. U.S.A. 107, 6670-6675.

Feng, Y., Wen, S., Wang, X., Sheng, G., He, Q., Tang, J., and Fu, J. (2004). Indoor and outdoor carbonyl compounds in the hotel ballrooms in Guangzhou, China. Atmos. Environ. 38, 103-112.

Finalyson-Pitts, and Pitts. (1999). Chemistry of the Upper and Lower Atmosphere: Theory, Experiments and Applications (San Diego: Academic Press).

Finley, B. D., and Saltzman, E. S. (2006). Measurement of Cl in coastal urban air. Geophys. Res. Lett. 33, L11809.

Finley, B. D., and Saltzman, E. S. (2008). Observations of Cl, Br, and I in coastal marine air. J. Geophys. Res. 113, D21301.

Fosco, T., and Schmeling, M. (2006). Aerosol ion concentration dependence on atmospheric conditions in Chicago. Atmos. Environ. 40, 6638-6649.

Frankenberg, C., Aben, I., Bergamaschi, P., Dlugokencky, E. J., van, H., R., Houweling, S., van, D. M., P., Snel, R., and Tol, P. (2011). Global column-averaged methane mixing ratios from 2003 to 2009 as derived from SCIAMACHY: Trends and variability. J. Geophys. Res. 116, D04302.

Fridlind, A. M., and Jacobson, M. Z. (2000). A study of gas-aerosol equilibrium and aerosol pH in the remote marine boundary layer during the First Aerosol Charac-

terization Experiment (ACE 1). J. Geophys. Res. Atmos. 105, 17325-17340.

Friedfeld, S., Fraser, M., Ensor, K., Tribble, S., Rehle, D., Leleux, D., and Tittel, F. (2002). Statistical analysis of primary and secondary atmospheric formaldehyde. Atmos. Environ. 36, 4767-4775.

Goldan, P. D., Kuster, W. C., Fehsenfeld, F. C., and Montzka, S. A. (1995). Hydrocarbon measurements in the southeastern United States: the Rural Oxidants in the Southern Environment (ROSE) program 1990. J. Geophys. Res. Atmos. 100, 25945-25963.

Goldstein, A. H., and Schade, G. W. (2000). Quantifying biogenic and anthropogenic contributions to acetone mixing ratios in a rural environment. Atmos. Environ. 34, 4997-5006.

Graedel, T. E., and Keene, W. C. (1995). Tropospheric budget of reactive chlorine. Global Biogeochem. Cycles 9, 47-77.

Greenspan, L. (1977). Humidity fixed points of binary saturated aqueous solutions. Journal of research of the national Bureau of Standards, A. Physics and Chemistry A 21, 2711-2715.

Grosjean, D. (1982). Formaldehyde and other carbonyls in Los Angeles ambient air. Environ. Sci. Technol. 16, 254-262.

Grosjean, Daniel and Barbara Wright (1983). Carbonyls in urban fog, ice fog, cloudwater and rainwater. Atmos. Environ. 17(10), 2093-2096.

Grosjean, D. (1997). Atmospheric chemistry of alcohols. J. Brazilian Chem. Soc. 8, 433-442.

Grosjean, D. (1992). Atmospheric concentrations and temporal variations of C1-C3 carbonyl compounds at two rural sites in central Ontario. Atmos. Environ. 26, 349 - 351.

Grosjean, D., Grosjean, E., and Gertler, A. W. (2001). On-Road emissions of carbonyls from light-duty and heavy-duty vehicles. Environ. Sci. Technol. 35, 45-53.

Grosjean, D., Williams, E. L., and Grosjean, E. (1993). Atmospheric chemistry of isoprene and of its carbonyl products. Enviro. Sci. Technol. 27, 830-840.

Grosjean, D., and Williams, I. I., Edwin L (1992). Environmental persistence of organic compounds estimated from structure-reactivity and linear free-energy relationships. Unsaturated aliphatics. Atmos. Environ. 26, 1395-1405.

Grosjean, E., Green, P. G., and Grosjean, D. (1999). Liquid Chromatography Analysis of Carbonyl (2,4-Dinitrophenyl)hydrazones with detection by Diode Array Ultraviolet Spectroscopy and by Atmospheric Pressure Negative Chemical Ionization Mass Spectrometry. Anal. Chem. 71, 1851-1861.

Grosjean, E., de Andrade, J. B., and Grosjean, D. (1996a). Carbonyl products of the gas-phase reaction of ozone with simple alkenes. Environ. Sci. Technol. 30, 975-983.

Grosjean, E., Grosjean, D., Fraser, M. P., and Cass, G. R. (1996b). Air quality model evaluation data for organics. 2. C1-C14 carbonyls in Los Angeles air. Environ. Sci. Technol. 30, 2687-2703.

Grosjean, E., Rasmussen, R. A., and Grosjean, D. (1998). Ambient levels of gas phase pollutants in Porto Alegre, Brazil. Atmos. Environ. 32, 3371-3379.

Halla, J. D., Wagner, T., Beirle, S., Brook, J. R., Hayden, K. L., OBrien, J. M., Ng, A., Majonis, D., Wenig, M. O., and McLaren, R. (2011). Determination of tropospheric vertical columns of NO_2 and aerosol optical properties in a rural setting using MAX-DOAS. Atmos. Chem. Phys. 11, 12475-12498.

Harley, R. A., and Kean, A. J. (2004). Chemical composition of vehicle-related volatile organic compound emissions in Central California. Prepared for: San Joaquin Valleywide Air Pollution Study Agency and California Air Resources Board. Contract 00-14CCOS

Harris, G. W., Mackay, G. I., Iguchi, T., Mayne, L. K., and Schiff, H. I. (1989). Measurements of formaldehyde in the troposphere by tunable diode laser absorption spectroscopy. J. Atmos. Chem. 8, 119-137.

Hastie, D. R., Narayan, J., Schiller, C., Niki, H., Shepson, P. B., Sills, D. M. L., Taylor, P. A., Moroz, J., Drummond, J. W., Reid, N., Taylor, R., Roussel, P. B. and Melos, O. T. (1999). Observational evidence for the impact of the lake breeze circulation

on ozone concentrations in Southern Ontario. Atmos. Environ.

Hayden, K. L., Sills, D. M. L., Brook J. R., Li S-M., Makar P. A., Markovic, M. Z., Liu, P., Anlauf K. G., O'Brien J. M., Li, Q. and McLaren R. (2011). Aircraft study of the impact of lake-breeze circulations on trace gases and particles during BAQS-Met 2007. Atmos, Chem. Phys 11, 10173-10192.

Hayes, P. L., Ortega, A. M., Cubison, M. J., Froyd, K. D., Zhao, Y., Cliff, S. S., Hu, W. W., Toohey, D. W., Flynn, J. H., Lefer, B. L., Grossberg, N., Alvarez, S., Rappenglck, B., Taylor, J. W., Allan, J. D., Holloway, J. S., Gilman, J. B., Kuster, W. C., de, G., J. A., Massoli, P., Zhang, X., Liu, J., Weber, R. J., Corrigan, A. L., Russell, L. M., Isaacman, G., Worton, D. R., Kreisberg, N. M., Goldstein, A. H., Thalman, R., Waxman, E. M., Volkamer, R., Lin, Y. H., Surratt, J. D., Kleindienst, T. E., Offenberg, J. H., Dusanter, S., Griffith, S., Stevens, P. S., Brioude, J., Angevine, W. M., and Jimenez, J. L. (2013). Organic aerosol composition and sources in Pasadena, California, during the 2010 CalNex campaign. J. Geophys. Res. Atmos. 9233-9257.

Haynes, W. M. (2012). CRC Handbook of Chemistry and Physics (Boca Raton, Florida: CRC press).

Healy, R. M., Sciare, J., Poulain, L., Crippa, M., Wiedensohler, A., Prvt, A. S. H., Baltensperger, U., Sarda-Estve, R., McGuire, M. L., Jeong, C.-H., McGillicuddy, E., OConnor, I. P., Sodeau, J. R., Evans, G. J., and Wenger, J. C. (2013). Quantitative determination of carbonaceous particle mixing state in Paris using single-particle mass spectrometer and aerosol mass spectrometer measurements. Atmos. Chem. Phys. 13, 9479-9496.

Heck, R. M. (1999). Catalytic abatement of nitrogen oxides–stationary applications. Catal. Today 53, 519-523.

Hellen, H., Hakola, H., Reissell, A., and Ruuskanen, T. M. (2004). Carbonyl compounds in boreal coniferous forest air in Hyyti, Southern Finland. Atmos. Chem. Phys. 4, 1771-1780.

Herrington, J. S., and Hays, M. D. (2012). Concerns regarding 24-h sampling for formaldehyde, acetaldehyde, and acrolein using 2,4-dinitrophenylhydrazine (DNPH)-

coated solid sorbents. Atmos. Environ. 55, 179-184.

Hersey, S. P., Craven, J. S., Metcalf, A. R., Lin, J., Lathem, T., Suski, K. J., Cahill, J. F., Duong, H. T., Sorooshian, A., Jonsson, H. H., Shiraiwa, M., Zuend, A., Nenes, A., Prather, K. A., Flagan, R. C., and Seinfeld, J. H. (2013). Composition and hygroscopicity of the Los Angeles Aerosol: CalNex. J. Geophys. Res. Atmos. 118, 3016-3036.

Hewitt, C. N., and Harrison, R. M. (1985). Tropospheric concentrations of the hydroxyl radical-A review. Atmos. Environ. 19, 545-554.

Ho, S. S. H. H. (2013). Technical Note: Concerns on the Use of Ozone Scrubbers for Gaseous Carbonyl Measurement by DNPH-Coated Silica Gel Cartridge. Aerosol Air Qual. Res. 13, 1151-1160.

Holloway, A. M., and Wayne, R. P. (2010). Atmospheric Chemistry. Royal Society of Chemistry.

Hottle, J. R., Huisman, A. J., DiGangi, J. P., Kammrath, A., Galloway, M. M., Coens, K. L., and Keutsch, F. N. (2009). A Laser Induced Fluorescence-Based Instrument for In-Situ measurements of atmospheric formaldehyde. Environ. Sci. Technol. 43, 790-795.

Hu, D., Chen, J., Ye, X., Li, L., and Yang, X. (2011). Hygroscopicity and evaporation of ammonium chloride and ammonium nitrate: Relative humidity and size effects on the growth factor. Atmos. Environ. 45, 2349-2355.

Huffman, J. A., Ziemann, P. J., Jayne, J. T., Worsnop, D. R., and Jimenez, J. L. (2008). Development and characterization of a Fast-Stepping/Scanning Thermodenuder for chemically-Resolved Aerosol volatility measurements. Aerosol Sci. Tech. 42, 395-407.

Ianniello, A., Spataro, F., Esposito, G., Allegrini, I., Hu, M., and Zhu, T. (2011). Chemical characteristics of inorganic ammonium salts in PM2.5 in the atmosphere of Beijing (China). Atmos. Chem. Phys. 11, 10803-10822.

IPCC: Intergovernmental Panel on Climate Change. (2013): The physical science basis. Cambridge University Press.

IPCC: Intergovernmental Panel on Climate Change. (2014). Climate change 2014 synthesis report. Cambridge University Press.

Jacob, D. J., Field, B. D., Jin, E. M., Bey, I., Li, Q., Logan, J. A., Yantosca, R. M., and Singh, H. B. (2002). Atmospheric budget of acetone. J. Geophys. Res. 107, ACH-AC5.

James, D. A., Alice, E. D., Hugh, C., Keith, N. B., M.Rami, A., Jose, L. J., Ann, M. M., Frank, D., Timothy, B. O., Manjula, R. C., John, T. J., and Douglas, R. W. (2004). A generalised method for the extraction of chemically resolved mass spectra from Aerodyne aerosol mass spectrometer data. J. Aerosol Sci. 35, 909 - 922.

Jayne, J. T., Leard, D. C., Zhang, X., Davidovits, P., Smith, K. A., Kolb, C. E., and Worsnop, D. R. (2000). Development of an Aerosol Mass Spectrometer for size and composition analysis of submicron particles. Aerosol Sci. Tech. 33, 49-70.

Jenkin, M. E., Saunders, S. M., and Pilling, M. J. (1997). The tropospheric degradation of volatile organic compounds: a protocol for mechanism development. Atmos. Environ. 31, 81 - 104.

Jimenez-Research-Group (2014). Field ToF-AMS Operation <http://cires.colorado.edu/jimenez-group/wiki/index.php/Field_ToF-AMS_Operation>.[5 May 2014]

Jimenez, J. L., Canagaratna, M. R., Donahue, N. M., Prevot, A. S., Zhang, Q., Kroll, J. H., DeCarlo, P. F., Allan, J. D., Coe, H., Ng, N. L., Aiken, A. C., Docherty, K. S., Ulbrich, I. M., Grieshop, A. P., Robinson, A. L., Duplissy, J., Smith, J. D., Wilson, K. R., Lanz, V. A., Hueglin, C., Sun, Y. L., Tian, J., Laaksonen, A., Raatikainen, T., Rautiainen, J., Vaattovaara, P., Ehn, M., Kulmala, M., Tomlinson, J. M., Collins, D. R., Cubison, M. J., Dunlea, E. J., Huffman, J. A., Onasch, T. B., Alfarra, M. R., Williams, P. I., Bower, K., Kondo, Y., Schneider, J., Drewnick, F., Borrmann, S., Weimer, S., Demerjian, K., Salcedo, D., Cottrell, L., Griffin, R., Takami, A., Miyoshi, T., Hatakeyama, S., Shimono, A., Sun, J. Y., Zhang, Y. M., Dzepina, K., Kimmel, J. R., Sueper, D., Jayne, J. T., Herndon, S. C., Trimborn, A. M., Williams, L. R., Wood, E. C., Middlebrook, A. M., Kolb, C. E., Baltensperger, U., and Worsnop, D. R. (2009). Evolution of organic aerosols in the atmosphere. Science 326, 1525-1529.

Jimenez, J. L., Jayne, J. T., Shi, Q., Kolb, C. E., Worsnop, D. R., Yourshaw, I., Seinfeld, J. H., Flagan, R. C., Zhang, X., Smith, K. A., Morris, J. W., and Davidovits, P. (2003). Ambient aerosol sampling using the Aerodyne Aerosol Mass Spectrometer. J. Geophys. Res. 108, 8425.

Jobson, B. T., Niki, H., Yokouchi, Y., Bottenheim, J., Hopper, F., and Leaitch, R. (1994). Measurements of C2-C6 hydrocarbons during the Polar Sunrise1992 Experiment: Evidence for Cl atom and Br atom chemistry. J. Geophys. Res. 99, 25355-25368.

Jobson, B. T., Berkowitz, C. M., Kuster, W. C., Goldan, P. D., Williams, E. J., Fesenfeld, F. C., Apel, E. C., Karl, T., Lonneman, W. A., and Riemer, D. (2004). Hydrocarbon source signatures in Houston, Texas: Influence of the petrochemical industry. J. Geophys. Res. 109, D24305.

Johnson, K. S., Laskin, A., Jimenez, J. L., Shutthanandan, V., Molina, L. T., Salcedo, D., Dzepina, K., and Molina, M. J. (2008). Comparative Analysis of Urban Atmospheric Aerosol by Particle-Induced X-ray Emission (PIXE), Proton Elastic Scattering Analysis (PESA), and Aerosol Mass Spectrometry (AMS). Environ. Sci. Technol. 42, 6619-6624.

Kambezidis, H. D., Weidauer, D., Melas, D., and Ulbricht, M. (1998). Air quality in the Athens basin during sea breeze and non-sea breeze days using laser-remote-sensing technique. Atmos. Environ. 32, 2173-2182.

Kanakidou, M., Seinfeld, J. H., Pandis, S. N., Barnes, I., Dentener, F. J., Facchini, M. C., Van Dingenen, R., Ervens, B., Nenes, A. N. C. J. S. E., and Nielsen, C. J. (2005). Organic aerosol and global climate modelling: a review. Atmos. Chem. Phys. 5, 1053-1123.

Kawamura, K., Steinberg, S., Ng, L., and Kaplan, I. R. (2001). Wet deposition of low molecular weight mono-and dicarboxylic acids, aldehydes and inorganic species in Los Angeles. Atmos. Environ. 35(23), 3917-3926.

Kean, A. J., Grosjean, E., Grosjean, D., and Harley, R. A. (2001). On-Road Measurement of Carbonyls in California Light-Duty Vehicle Emissions. Environ. Sci. Technol. 35, 4198-4204.

Keene, W. C., Khalil, M. A. K., Erickson, D. J., McCulloch, A., Graedel, T. E., Lobert, J. M., Aucott, M. L., Gong, S. L., Harper, D. B., Kleiman, G., Midgley, P., Moore, R. M., Seuzaret, C., Sturges, W. T., Benkovitz, C. M., Koropalov, V., Barrie, L. A., and Li, Y. F. (1999). Composite global emissions of reactive chlorine from anthropogenic and natural sources: Reactive Chlorine Emissions Inventory. J. Geophys. Res. 104, 8429-8440.

Keene, W. C., Maring, H., Maben, J. R., Kieber, D. J., Pszenny, A. A. P., Dahl, E. E., Izaguirre, M. A., Davis, A. J., Long, M. S., Zhou, X., Smoydzin, L., and Sander, R. (2007a). Chemical and physical characteristics of nascent aerosols produced by bursting bubbles at a model air-sea interface. J. Geophys. Res. 112, D21202.

Keene, W. C., Stutz, J., Pszenny, A. A. P., Maben, J. R., Fischer, E. V., Smith, A. M., von, G., Roland, Pechtl, S., Sive, B. C., and Varner, R. K. (2007b). Inorganic chlorine and bromine in coastal New England air during summer. J. Geophys. Res. 112, D10S12.

Kelly, T. J., and Fortune, C. R. (1994). Continuous monitoring of gaseous formaldehyde using an improved fluorescence approach. Int. J. Environ. Anal. Chem. 54, 249-263.

Kesselmeier, J., and Staudt, M. (1999). Biogenic volatile organic compounds (VOC): an overview on emission, physiology and ecology. J. Atmos. Chem. 33, 23-88.

Khwaja, H. A., and Narang, A. (2008). Carbonyls and non-methane hydrocarbons at a rural mountain site in northeastern United States. Chemosphere 71, 2030-2043.

Kieber, R. J., Zhou, X., and Mopper, K. (1990). Formation of carbonyl compounds from UV-induced photodegradation of humic substances in natural waters: fate of riverine carbon in the sea. Limnol. Oceano. 35, 1503-1515.

Kim, S., Huey, L. G., Stickel, R. E., Pierce, R. B., Chen, G., Avery, M. A., Dibb, J. E., Diskin, G. S., Sachse, G. W., McNaughton, C. S., Clarke, A. D., Anderson, B. E., and Blake, D. R. (2008). Airborne measurements of HCl from the marine boundary layer to the lower stratosphere over the North Pacific Ocean during INTEX-B. Atmos. Chem. Phys. Discuss. 8, 3563-3595.

Kleinman, L. I. (2003). Photochemical age determinations in the Phoenix metropolitan area. J. Geophys. Res. 108, 4096.

Kornilova, A., McLaren, R., Moukhtar. S., Nuaaman, I., and Rudolph, J. (2011). Photochemical age of air masses observed during the Border Air Qualiy Study (BAQS-Met 2007). Unpublished report

Kroll, J. H., and Seinfeld, J. H. (2008). Chemistry of secondary organic aerosol: Formation and evolution of low-volatility organics in the atmosphere. Atmos. Environ. 42, 3593-3624.

Lack, D. A., Cappa, C. D., Langridge, J., Bahreini, R., Buffaloe, G., Brock, C., Cerully, K., Coffman, D., Hayden, K., Holloway, J., Lerner, B., Massoli, P., Li, S. M., McLaren, R., Middlebrook, A. M., Moore, R., Nenes, A., Nuaaman, I., Onasch, T. B., Peischl, J., Perring, A., Quinn, P. K., Ryerson, T., Schwartz, J. P., Spackman, R., Wofsy, S. C., Worsnop, D., Xiang, B., and Williams, E. (2011). Impact of fuel quality regulation and speed reductions on shipping emissions: implications for climate and air quality. Environ. Sci. Technol. 45, 9052-9060.

Laskin, A., Moffet, R. C., Gilles, M. K., Fast, J. D., Zaveri, R. A., Wang, B., Nigge, P., and Shutthanandan, J. (2012). Tropospheric chemistry of internally mixed sea salt and organic particles: Surprising reactivity of NaCl with weak organic acids. J. Geophys. Res. 117, D15302.

Lee, A., Goldstein, A. H., Kroll, J. H., Ng, N. L., Varutbangkul, V., Flagan, R. C., and Seinfeld, J. H. (2006). Gas-phase products and secondary aerosol yields from the photooxidation of 16 different terpenes. J. Geophys. Res. 111, D17305.

Lee, B. P., Li, Y. J., Yu, J. Z., Louie, P. K. K., and Chan, C. K. (2013). Physical and chemical characterization of ambient aerosol by HR-ToF-AMS at a suburban site in Hong Kong during springtime 2011. J. Geophys. Res. Atmos. 118, 8625-8639.

Lesser, M. P. (2006). Oxidative stress in marine environments: biochemistry and physiological ecology. Annu. Rev. Physiol. 68, 253-278.

Levy, I., Makar, P. A., Sills, D., Zhang, J., Hayden, K. L., Mihele, C., Narayan, J., Moran, M. D., Sjostedt, S., and Brook, J. (2010). Unraveling the complex local-scale

flows influencing ozone patterns in the southern Great Lakes of North America. Atmos. Chem. Phys. 10, 10895-10915.

Lewis, A. C., Hopkins, J. R., Carpenter, L. J., Stanton, J., Read, K. A., and Pilling, M. J. (2005). Sources and sinks of acetone, methanol, and acetaldehyde in North Atlantic marine air. Atmos. Chem. Phys. 5, 1963-1974.

Liggio, J. Uptake of carbonyls to atmospheric particulate matter: Ambient measurements and laboratory studies. Toronto: York University; 2004. Dissertation.

Liggio, J., Li, S.-M., and McLaren, R. (2005). Reactive uptake of glyoxal by particulate matter. J. Geophys. Res. Atmos. 110, D10304.

Lindinger, W., Hansel, A., and Jordan, A. (1998). On-line monitoring of volatile organic compounds at pptv levels by means of proton-transfer-reaction mass spectrometry (PTR-MS) medical applications, food control and environmental research. Int. J. Mass Spec. Ion Proc. 173, 191-241.

Linstrom, P. J., and Mallard, W. G. (2001). The NIST Chemistry WebBook: A Chemical Data Resource on the Internet. J. Chem. Eng. Data 46, 1059-1063.

Lippmann, M., Ito, K., Nadas, A., and Burnett, R. T. (2000). Association of particulate matter components with daily mortality and morbidity in urban populations. Res. Rep. Health Effects Inst.

Liu, P. S. K., Deng, R., Smith, K. A., Williams, L. R., Jayne, J. T., Canagaratna, M. R., Moore, K., Onasch, T. B., Worsnop, D. R., and Deshler, T. (2007). Transmission Efficiency of an Aerodynamic Focusing Lens System: Comparison of Model Calculations and Laboratory Measurements for the Aerodyne Aerosol Mass Spectrometer. Aerosol Sci. Technol. 41, 721-733.

Liu, S. C., Trainer, M., Fehsenfeld, F. C., Parrish, D. D., Williams, E. J., Fahey, D. W., Hubler, G., and Murphy, P. C. (1987). Ozone production in the rural troposphere and the implications for regional and global ozone distributions. J. Geophys. Res. 92, 4191-4207.

Livingston, C., Rieger, P., and Winer, A. (2009). Ammonia emissions from a representative in-use fleet of light and medium-duty vehicles in the California South Coast

Air Basin. Atmos. Environ. 43, 3326-3333.

MacDonald, S. M., Oetjen, H., Mahajan, A. S., Whalley, L. K., Edwards, P. M., Heard, D. E., Jones, C. E., and Plane, J. M. C. (2012). DOAS measurements of formaldehyde and glyoxal above a south-east Asian tropical rainforest. Atmos. Chem. Phys. 12, 5949-5962.

Makar, P. A., Zhang, J., Gong, W., Stroud, C., Sills, D., Hayden, K. L., Brook, J., Levy, I., Mihele, C., Moran, M. D., Tarasick, D. W., He, H., and Plummer, D. (2010). Mass tracking for chemical analysis: the causes of ozone formation in southern Ontario during BAQS-Met 2007. Atmos. Chem. Phys. 10, 11151-11173.

Martin, R. S., Villanueva, I., Zhang, J., and Popp, C. J. (1999). Nonmethane hydrocarbon, monocarboxylic acid, and low molecular weight aldehyde and ketone emissions from vegetation in central New Mexico. Enviro. Sci. Technol. 33, 2186-2192.

Matsumoto, K., and Tanaka, H. (1996). Formation and dissociation of atmospheric particulate nitrate and chloride: an approach based on phase equilibrium. Atmos. Environ. 30, 639-648.

McCulloch, A., Aucott, M. L., Benkovitz, C. M., Graedel, T. E., Kleiman, G., Midgley, P. M., and Li, Y.-F. (1999). Global emissions of hydrogen chloride and chloromethane from coal combustion, incineration and industrial activities: Reactive Chlorine Emissions Inventory. J. Geophys. Res. Atmos. 104, 8391-8403.

McGuire, M. L., Chang, R. Y.-W., Slowik, J. G., Jeong, C.-H., Healy, R. M., Lu, G., Mihele, C., Abbatt, J. P. D., Brook, J. R., and Evans, G. J. (2014). Enhancing non-refractory aerosol apportionment from an urban industrial site through receptor modelling of complete high time-resolution aerosol mass spectra. Atmos. Chem. Phys. Discuss. 14, 5081-5145.

McLaren, R., Wojtal, P., Majonis, D., McCourt, J., Halla, J. D., and Brook, J. (2010). NO_3 radical measurements in a polluted marine environment: links to ozone formation. Atmos. Chem. Phys. 10, 4187-4206.

McLaren, R., Salmon, R. A., Liggio, J., Hayden, K. L., Anlauf, K. G., and Leaitch, W. R. (2004). Nighttime chemistry at a rural site in the Lower Fraser Valley. Atmos.

Environ. 38, 5837-5848.

Mielke, L. H., Furgeson, A., and Osthoff, H. D. (2011). Observation of $ClNO_2$ in a mid-continental urban environment. Environ. Sci. Technol. 45, 8889-8896.

Millet, D. B., Guenther, A., Siegel, D. A., Nelson, N. B., Singh, H. B., de, G., J. A., Warneke, C., Williams, J., Eerdekens, G., Sinha, V., Karl, T., Flocke, F., Apel, E., Riemer, D. D., Palmer, P. I., and Barkley, M. (2010). Global atmospheric budget of acetaldehyde: 3-D model analysis and constraints from in-situ and satellite observations. Atmos. Chem. Phys. 10, 3405-3425.

Miyoshi, A., Hatakeyama, S., and Washida, N. (1994). OH radical-initiated photooxidation of isoprene: An estimate of global CO production. J. Geophys. Res. Atmos. 99, 18779-18787.

Mller, D. (1990). The Na/Cl ratio in rainwater and the seasalt chloride cycle. Tellus B 42, 254-262.

Mopper, K., and Stahovec, W. L. (1986). Sources and sinks of low molecular weight organic carbonyl compounds in seawater. Marine Chem. 19, 305-321.

Moya, M., Pandis, S. N., and Jacobson, M. Z. (2002). Is the size distribution of urban aerosols determined by thermodynamic equilibrium?: An application to Southern California. Atmos. Environ. 36, 2349-2365.

Mller, K., Haferkorn, S., Grabmer, W., Wisthaler, A., Hansel, A., Kreuzwieser, J., Cojocariu, C., Rennenberg, H., and Herrmann, H. (2006). Biogenic carbonyl compounds within and above a coniferous forest in Germany. Atmos. Environ. 40, 81-91.

Nash, T. (1953). The colorimetric estimation of formaldehyde by means of the Hantzsch reaction. Biochem. J. 55, 416.

Neuman, J. A. (2003). Variability in ammonium nitrate formation and nitric acid depletion with altitude and location over California. J. Geophys. Res. 108, 4557.

Nowak, J. B., Neuman, J. A., Bahreini, R., Middlebrook, A. M., Holloway, J. S., McKeen, S. A., Parrish, D. D., Ryerson, T. B., and Trainer, M. (2012). Ammonia sources in the California South Coast Air Basin and their impact on ammonium nitrate formation. Geophys. Res. Lett. 39, L07804.

Nuaaman, I., Li, S.-M., Hayden, K. L., Onasch, T. B., Massoli, P., Sueper, D., Worsnop, D. R., Bates, T. S., Quinn, P. K., and McLaren, R. (2015). Separating refractory and non-refractory particulate chloride and estimating chloride depletion by aerosol mass spectrometry in a marine environment. Atmos. Chem. Phys. Discuss. 15, 2085-2118.

Numata, M., Nakamura, N., and Gamo, T. (2001). Precise measurement of chlorine stable isotopic ratios by thermal ionization mass spectrometry. Geochem. J. 35, 89-100.

OBrien, J. M., Shepson, P. B., Wu, Q., Biesenthal, T., Bottenheim, J. W., Wiebe, H. A., Anlauf, K. G., and Brickell, P. (1997). Production and distribution of organic nitrates, and their relationship to carbonyl compounds in an urban environment. Atmos. Environ. 31, 2059-2069.

O'Dowd, C. D., Facchini, M. C., Cavalli, F., Ceburnis, D., Mircea, M., Decesari, S., Fuzzi, S., Yoon, Y. J., and Putaud, J.-P. (2004). Biogenically driven organic contribution to marine aerosol. Nature 431, 6760-6680.

OME: Ontario Ministry of the Environment.(2003). Air Quality in Ontario 2003. Report.

OME: Ontario Ministry of the Environment. (2006). Air Quality in Ontario 2006, Report.

Osthoff, H. D., Roberts, J. M., Ravishankara, A. R., Williams, E. J., Lerner, B. M., Sommariva, R., Bates, T. S., Coffman, D., Quinn, P. K., Dibb, J. E., Stark, H., Burkholder, J. B., Talukdar, R. K., Meagher, J., Fehsenfeld, F. C., and Brown, S. S. (2008). High levels of nitryl chloride in the polluted subtropical marine boundary layer. Nature Geosci. 1, 324-328.

Ovadnevaite, J., Ceburnis, D., Canagaratna, M., Berresheim, H., Bialek, J., Martucci, G., Worsnop, D. R., and ODowd, C. (2012). On the effect of wind speed on submicron sea salt mass concentrations and source fluxes. J. Geophys. Res. 117, D16201.

Ovadnevaite, J., ODowd, C., DallOsto, M., Ceburnis, D., Worsnop, D. R., and Berresheim, H. (2011). Detecting high contributions of primary organic matter to

marine aerosol: A case study. Geophys. Res. Lett. 38, L02807.

Owega, S., Khan, B.-U.-Z., Evans, G. J., Jervis, R. E., and Fila, M. (2006). Identification of long-range aerosol transport patterns to Toronto via classification of back trajectories by cluster analysis and neural network techniques. Chemometrics and Intelligent Laboratory Systems 83, 26-33.

Pal, R., and Kim, K. H. (2007). Experimental choices for the determination of carbonyl compounds in air. J. Sep. Sci. 30, 2708-2718.

Pal, R., and Kim, K. H. (2008). Influences of sampling volume and sample concentration on the analysis of atmospheric carbonyls by 2,4-dinitrophenylhydrazine cartridge. Anal. Chim. Acta 610, 289-296.

Pio, C. A., and Harrison, R. M. (1987). Vapour pressure of ammonium chloride aerosol: Effect of temperature and humidity. Atmos. Environ. (1967) 21, 2711 - 2715.

Platt, U., and Honninger, G. (2003). The role of halogen species in the troposphere. Chemosphere 52, 325-338.

Pope, C. A., Burnett, R. T., Thun, M. J., Calle, E. E., Krewski, D., Ito, K., and Thurston, G. D. (2002). Lung cancer, cardiopulmonary mortality, and long-term exposure to fine particulate air pollution. JAMA: the journal of the American Medical Association 287, 1132-1141.

Possanzini, M., Di, P., V, Petricca, M., Fratarcangeli, R., and Brocco, D. (1996). Measurements of lower carbonyls in Rome ambient air. Atmos. Environ. 30, 37573764.

Possanzini, M., Di, P., Vincenzo, Brancaleoni, E., Frattoni, M., and Ciccioli, P. (2000). A train of carbon and DNPH-coated cartridges for the determination of carbonyls from C 1 to C 12 in air and emission samples. Atmos. Environ. 34, 5311-5318.

Possanzini, M., Palo, V. D., and Cecinato, A. (2002). Sources and photodecomposition of formaldehyde and acetaldehyde in Rome ambient air. Atmos. Environ. 36, 3195-3201.

Possanzini, M., Tagliacozzo, G., and Cecinato, A. (2007). Ambient Levels and Sources of Lower Carbonyls at Montelibretti, Rome (Italy). Water Air Soil Pollut. 183, 447-454.

Pszenny, A. A. P., Fischer, E. V., Russo, R. S., Sive, B. C., and Varner, R. K. (2007). Estimates of Cl atom concentrations and hydrocarbon kinetic reactivity in surface air at Appledore Island, Maine (USA), during International Consortium for Atmospheric Research on Transport and Transformation/Chemistry of Halogens at the Isles of Shoals. J. Geophys. Res. 112, D10S13.

Pugliese, S. C., Murphy, J. G., Geddes, J. A., and Wang, J. M. (2014). The impacts of precursor reduction and meteorology on ground-level ozone in the Greater Toronto Area. Atmos. Chem. Phys. 14, 8197-8207.

Quinn, P. K., Coffman, D. J., Kapustin, V. N., Bates, T. S., and Covert, D. S. (1998). Aerosol optical properties in the marine boundary layer during the First Aerosol Characterization Experiment (ACE 1) and the underlying chemical and physical aerosol properties. J. Geophys. Res. 103, 16547-16563.

Quinn, P. K., Bates, T. S., Schulz, K. S., Coffman, D. J., Frossard, A. A., Russell, L. M., Keene, W. C., and Kieber, D. J. (2014). Contribution of sea surface carbon pool to organic matter enrichment in sea spray aerosol. Nature Geosci. 7, 228-232.

Raul, A.-I. J., Mora-Diez, N., Boyd, R. J., and Vivier-Bunge, A. (2001). On the Importance of Prereactive Complexes in MoleculeRadical Reactions: Hydrogen Abstraction from Aldehydes by OH. J. Am. Chem. Soc. 123, 2018-2024.

Ravishankara, A. R. (2009). Are chlorine atoms significant tropospheric free radicals? Proccedings of the national academy of sciences of the United States of America. 106, 13639-13640.

Riedel, T. P., Bertram, T. H., Ryder, O. S., Liu, S., Day, D. A., Russell, L. M., Gaston, C. J., Prather, K. A., and Thornton, J. A. (2012a). Direct N_2O_5 reactivity measurements at a polluted coastal site. Atmos. Chem. Phys. 12, 2959-2968.

Riedel, T. P., Bertram, T. H., Crisp, T. A., Williams, E. J., Lerner, B. M., Vlasenko, A., Li, S. M., Gilman, J., de Gouw, J., Bon, D. M., Wagner, N. L., Brown, S. S., and Thornton, J. A. (2012b). Nitryl chloride and molecular chlorine in the coastal marine boundary layer. Environ. Sci. Technol. 46, 10463-10470.

Roberts, J. M., Osthoff, H. D., Brown, S. S., and Ravishankara, A. R. (2008). N_2O_5

oxidizes chloride to Cl_2 in acidic atmospheric aerosol. Science 321, 1059-1059.

Rolph, G. D. (2014). Real-time Environmental Applications and Display sYstem (READY) Website <http://ready.arl.noaa.gov>.[8 December 2014]

Roussel, P. B., Lin, X., Camacho, F., Laszlo, S., Taylor, R., Melo, O. T., Shepson, P. B., Hastie, D. R., and Niki, H. (1996). Observations of ozone and precursor levels at two sites around Toronto, Ontario, during SONTOS 92. Atmos. Environ. 30, 2145-2155.

Ryerson, T. B., Andrews, A. E., Angevine, W. M., Bates, T. S., Brock, C. A., Cairns, B., Cohen, R. C., Cooper, O. R., de, G., J.A., Fehsenfeld, F. C., Ferrare, R. A., Fischer, M. L., Flagan, R. C., Goldstein, A. H., Hair, J. W., Hardesty, R. M., Hostetler, C. A., Jimenez, J. L., Langford, A. O., McCauley, E., McKeen, S. A., Molina, L. T., Nenes, A., Oltmans, S. J., Parrish, D. D., Pederson, J. R., Pierce, R. B., Prather, K., Quinn, P. K., Seinfeld, J. H., Senff, C. J., Sorooshian, A., Stutz, J., Surratt, J. D., Trainer, M., Volkamer, R., Williams, E. J., and Wofsy, S. C. (2013). The 2010 California research at the Nexus of air quality and climate change (CalNex) field study. J. Geophys. Res. Atmos. 5830-5866.

Saha, S. K., Jo, S.-H., Song, H.-N., Brown, R. J. C., and Kim, K.-H. (2012). Contrasting recovery patterns of 2, 4-dinitrophenylhydrazones (DNPH) derivative of carbonyls between liquid and gas phase standards using HPLC-based analysis. Atmos. Environ. 62, 562-565.

Salcedo, D., Onasch, T. B., Aiken, A. C., Williams, L. R., de, F., B., Cubison, M. J., Worsnop, D. R., Molina, L. T., and Jimenez, J. L. (2010). Determination of particulate lead using aerosol mass spectrometry: MILAGRO/MCMA-2006 observations. Atmos. Chem. Phys. 10, 5371-5389.

Salcedo, D., Onasch, T. B., Dzepina, K., Canagaratna, M. R., Zhang, Q., Huffman, J. A., DeCarlo, P. F., Jayne, J. T., Mortimer, P., Worsnop, D. R., Kolb, C. E., Johnson, K. S., Zuberi, B., Marr, L. C., Volkamer, R., Molina, L. T., Molina, M. J., Cardenas, B., Bernab, R. M., Marquez, C., Gaffney, J. S., Marley, N. A., Laskin, A., Shutthanandan, V., Xie, Y., Brune, W., Lesher, R., Shirley, T., and Jimenez, J. L. (2006). Characterization of ambient aerosols in Mexico City during the MCMA-2003 campaign with

Aerosol Mass Spectrometry: results from the CENICA Supersite. Atmos. Chem. Phys. 6, 925-946.

San Martini, F. M. Decision support tools for urban air quality management. Massachusetts Institute of Technology; 2004. Dissertation.

Sander, S. P., Golden, D. M., Kurylo, M. J., Moortgat, G. K., Wine, P. H., Ravishankara, A. R., Kolb, C. E., Molina, M. J., Finlayson-Pitts, B. J., Huie, R. E., Orkin, V. L., Friedl, R. R., and Keller-Rudek, H. (2006). Chemical kinetics and photochemical data for use in atmospheric studies : evaluation number 15. JPL Publication 06-02

Sarwar, G., Simon, H., Bhave, P., and Yarwood, G. (2012). Examining the impact of heterogeneous nitryl chloride production on air quality across the United States. Atmos. Chem. Phys. 12, 6455-6473.

Satsumabayashi, H., Kurita, H., Chang, Y.-S., Carmichael, G. R., and Ueda, H. (1995). Photochemical formations of lower aldehydes and lower fatty acids under long-range transport in central Japan. Atmos. Environ. 29, 255-266.

Schneider, J., Freutel, F., Zorn, S. R., Chen, Q., Farmer, D. K., Jimenez, J. L., Martin, S. T., Artaxo, P., Wiedensohler, A., and Borrmann, S. (2011). Mass-spectrometric identification of primary biological particle markers and application to pristine submicron aerosol measurements in Amazonia. Atmos. Chem. Phys. 11, 11415-11429.

Seinfeld, J. H., and Pankow, J. F. (2003). Organic atmospheric particulate material. Annu. Rev. Phys. Chem. 54, 121-140.

Seinfeld, J. H., and Pandis, S. N. (2006). Atmospheric Chemistry and Physics: From Air Pollution to Climate Change John Wiley and Sons).

Shepson, P. B., Hastie, D. R., Schiff, H. I., Polizzi, M., Bottenheim, J. W., Anlauf, K., Mackay, G. I., and Karecki, D. R. (1991). Atmospheric concentrations and temporal variations of C1- C3 carbonyl compounds at two rural sites in central Ontario. Atmos. Environ. 25, 2001-2015.

Sillman, S. (1995). The use of NOy, H2O2, and HNO3 as indicators for ozone-NO x-hydrocarbon sensitivity in urban locations. J. Geophys. Res. Atmos. 100, 14175-14188.

Sillman, S. (1999). The relation between ozone, NOx and hydrocarbons in urban and polluted rural environments. Atmos. Environ. 33, 1821-1845.

Sills, D. M. L., Brook, J. R., Levy, I., Makar, P. A., Zhang, J., and Taylor, P. A. (2011). Lake breezes in the southern Great Lakes region and their influence during BAQS-Met 2007. Atmos. Chem. Phys. 11, 7955-7973.

Simon, H., Kimura, Y., McGaughey, G., Allen, D. T., Brown, S. S., Coffman, D., Dibb, J., Osthoff, H. D., Quinn, P., and Roberts, J. M. (2010). Modeling heterogeneous ClNO2 formation, chloride availability, and chlorine cycling in Southeast Texas. Atmos. Environ. 44, 5476-5488.

Simpson, W. R., von, G., R., Riedel, K., Anderson, P., Ariya, P., Bottenheim, J., Burrows, J., Carpenter, L. J., Frie, U., Goodsite, M. E., Heard, D., Hutterli, M., Jacobi, H.-W., Kaleschke, L., Neff, B., Plane, J., Platt, U., Richter, A., Roscoe, H., Sander, R., Shepson, P., Sodeau, J., Steffen, A., Wagner, T., and Wolff, E. (2007). Halogens and their role in polar boundary-layer ozone depletion. Atmos. Chem. Phys. 7, 4375-4418.

Singh, H. B., Ohara, D., Herlth, D., Sachse, W., Blake, D. R., Bradshaw, J. D., Kanakidou, M., and Crutzen, P. J. (1994). Acetone in the atmosphere: Distribution, sources, and sinks. J. Geophys. Res. Atmos. 99, 1805-1819.

Singh, H. B., Kanakidou, M., Crutzen, P. J., and Jacob, D. J. (1995). High concentrations and photochemical fate of oxygenated hydrocarbons in the global troposphere. Nature 378, 50-54.

Singh, H., Chen, Y., Staudt, A., Jacob, D., Blake, D., Heikes, B., and Snow, J. (2001). Evidence from the Pacific troposphere for large global sources of oxygenated organic compounds. Nature 410, 1078-1081.

Sinreich, R., Coburn, S., Dix, B., and Volkamer, R. (2010). Ship-based detection of glyoxal over the remote tropical Pacific Ocean. Atmos. Chem. Phys. 10, 11359-11371.

Sjostedt, S. J., Slowik, J. G., Brook, J. R., Chang, R. Y.-W., Mihele, C., Stroud, C. A., Vlasenko, A., and Abbatt, J. P. D. (2011). Diurnally resolved particulate and VOC measurements at a rural site: indication of significant biogenic secondary organic aerosol formation. Atmos. Chem. Phys. 11, 5745-5760.

Solomon, S., Qin, D., Manning, M., Chen, Z., Marquis, M., Averyt, K. B., Tignor, M., and Miller, H. L. (2007). Climate Change 2007: The Physical Science Basis. Contribution of Working Group I to the Fourth Assessment Report of the Intergovernmental Panel on Climate Change Cambridge University Press, Cambridge, United Kingdom and New York, NY, USA.

Sommariva, R., de, G., J. A., Trainer, M., Atlas, E., Goldan, P. D., Kuster, W. C., Warneke, C., and Fehsenfeld, F. C. (2011). Emissions and photochemistry of oxygenated VOCs in urban plumes in the Northeastern United States. Atmos. Chem. Phys. 11, 7081-7096.

Spicer, C. W., Chapman, E. G., Finlayson-Pitts, B. J., Plastridge, R. A., Hubbe, J. M., Fast, J. D., and Berkowitz, C. M. (1998). Unexpectedly high concentrations of molecular chlorine in coastal air. Nature 394, 353-356.

Steinbacher, M., Zellweger, C., Schwarzenbach, B., Bugmann, S., Buchmann, B., Ordez, C., Prevot, A. S. H., and Hueglin, C. (2007). Nitrogen oxide measurements at rural sites in Switzerland: Bias of conventional measurement techniques. J. Geophys. Res. 112, D113-D117.

Stone, D., Whalley, L. K., and Heard, D. E. (2012). Tropospheric OH and HO_2 radicals: field measurements and model comparisons. Chem. Soc. Rev. 41, 6348-6404.

Sueper, D. (2010). ToF-AMS software downloads, <http://cires.colorado.edu/jimenez-group/ToFAMSResources/ToFSoftware/index.html>. [26 April 2010]

Sumner, A. L., Shepson, P. B., Couch, T. L., Thornberry, T., Carroll, M. A., Sillman, S., Pippin, M., Bertman, S., Tan, D., Faloona, I., Brune, W., Young, V., Cooper, O., Moody, J., and Stockwell, W. (2001). A study of formaldehyde chemistry above a forest canopy. J. Geophys. Res. Atmos. 106, 24387-24405.

Takegawa, N., Miyakawa, T., Kawamura, K., and Kondo, Y. (2007). Contribution of selected dicarboxylic and ω–Oxocarboxylic Acids in Ambient Aerosol to the 44 Signal of an Aerodyne Aerosol Mass Spectrometer. Aerosol Sci. Technol. 41, 418-437.

Takegawa, N., Miyakawa, T., Kondo, Y., Jimenez, J. L., Zhang, Q., Worsnop, D. R., and Fukuda, M. (2006). Seasonal and diurnal variations of submicron organic aerosol

in Tokyo observed using the Aerodyne aerosol mass spectrometer. J. Geophys. Res. 111, D11206.

Takegawa, N., Miyakawa, T., Watanabe, M., Kondo, Y., Miyazaki, Y., Han, S., Zhao, Y., van, P., D., Bruggemann, E., Gnauk, T., Herrmann, H., Xiao, R., Deng, Z., Hu, M., Zhu, T., and Zhang, Y. (2009). Performance of an Aerodyne Aerosol Mass Spectrometer (AMS) during Intensive Campaigns in China in the Summer of 2006. Aerosol Sci. Technol. 43, 189-204.

Talbot, R. W., Mosher, B. W., Heikes, B. G., Jacob, D. J., Munger, J. W., Daube, B. C., Keene, W. C., Maben, J. R., and Artz, R. S. (1995). Carboxylic acids in the rural continental atmosphere over the eastern United States during the Shenandoah Cloud and Photochemistry Experiment. J. Geophys. Res. 100, 9335-9343.

Tanaka, P. L., Oldfield, S., Neece, J. D., Mullins, C. B., and Allen, D. T. (2000). Anthropogenic sources of chlorine and ozone formation in urban atmospheres. Environ. Sci. Technol. 34, 4470-4473.

Tanaka, P. L., Riemer, D. D., Chang, S., Yarwood, G., McDonald-Buller, E. C., Apel, E. C., Orlando, J. J., Silva, P. J., Jimenez, J. L., Canagaratna, M. R., Neece, J. D., Mullins, C. B., and Allen, D. T. (2003a). Direct evidence for chlorine-enhanced urban ozone formation in Houston, Texas. Atmos. Environ. 37, 1393-1400.

Tanaka, P. L., Allen, D. T., and Mullins, C. B. (2003b). An environmental chamber investigation of chlorine-enhanced ozone formation in Houston, Texas. J. Geophys. Res. 108, 4576.

Thornton, J. A., Kercher, J. P., Riedel, T. P., Wagner, N. L., Cozic, J., Holloway, J. S., Dube, W. P., Wolfe, G. M., Quinn, P. K., Middlebrook, A. M., Alexander, B., and Brown, S. S. (2010). A large atomic chlorine source inferred from mid-continental reactive nitrogen chemistry. Nature 464, 271-274.

Tiwari, V., Hanai, Y., and Masunaga, S. (2010). Ambient levels of volatile organic compounds in the vicinity of petrochemical industrial area of Yokohama, Japan. Air Qual. Atmos. Health 3, 65-75.

Tonnesen, G. S., and Dennis, R. L. (2000). Analysis of radical propagation effi-

ciency to assess ozone sensitivity to hydrocarbons and NO x: 2. Long-lived species as indicators of ozone concentration sensitivity. J. Geophys. Res. Atmos. 105, 9227-9241.

Trebs, I., Metzger, S., Meixner, F. X., Helas, G., Hoffer, A., Rudich, Y., Falkovich, A. H., Moura, M. A. L., da, S., Rosiberto S., Artaxo, P., Slanina, J., and Andreae, M. O. (2005). The $NH4^{+}$-$NO3^{-}$-Cl^{-}-$SO4^{2-}$-H2O aerosol system and its gas phase precursors at a pasture site in the Amazon Basin: How relevant are mineral cations and soluble organic acids? J. Geophys. Res. 110, D07303.

Tuazon, E. C., Graham, R. A., Winer, A. M., Easton, R. R., Pitts, J. N., and Hanst, P. L. (1978). A kilometer pathlength Fourier-transform infrared system for the study of trace pollutants in ambient and synthetic atmospheres. Atmos. Environ. 12, 865-875.

Tuazon, E. C., Aschmann, S. M., Arey, J., and Atkinson, R. (1998). Products of the gas-phase reactions of a series of methyl-substituted ethenes with the OH radical. Environ. Sci. Technol. 32, 2106-2112.

Uchiyama, S., Inaba, Y., and Kunugita, N. (2011). Derivatization of carbonyl compounds with 2,4-dinitrophenylhydrazine and their subsequent determination by high-performance liquid chromatography. J. Chromatography B. 879, 1282-1289.

Veguilla, R. Temperature Dependence on the Deliquescence Relative Humidity of Inorganic Aerosol Particles. Report

Villanueva-Fierro, I., Popp, C. J., and Martin, R. S. (2004). Biogenic emissions and ambient concentrations of hydrocarbons, carbonyl compounds and organic acids from ponderosa pine and cottonwood trees at rural and forested sites in Central New Mexico. Atmos. Environ. 38, 249-260.

Villanueva, F., Tapia, A., Notario, A., Albaladejo, J., and Martnez, E. (2014). Ambient levels and temporal trends of VOCs, including carbonyl compounds, and ozone at Cabaeros National Park border, Spain. Atmos. Environ. 85, 256-265.

Vlasenko, A., Macdonald, A. M., Sjostedt, S. J., and Abbatt, J. P. D. (2010). Formaldehyde measurements by Proton transfer reaction Mass Spectrometry (PTR-MS): correction for humidity effects. Atmos. Meas. Tech. 3, 1055-1062.

Vogt, R., Crutzen, P. J., and Sander, R. (1996). A mechanism for halogen release

from sea-salt aerosol in the remote marine boundary layer. Nature 383, 327-330.

Wade, L. G. (2002). Organic Chemistry (Upper Saddle River, New Jersey: Prentice Hall).

Wang, P. Optimization of an automated DNPH cartridge system for continous measurement of ambient gaseous carbonyls. York University; 2007. MSc. Thesis.

Warneke, C., Veres, P., Holloway, J. S., Stutz, J., Tsai, C., Alvarez, S., Rappenglueck, B., Fehsenfeld, F. C., Graus, M., Gilman, J. B., and de, G., J. A. (2011). Airborne formaldehyde measurements using PTR-MS: calibration, humidity dependence, inter-comparison and initial results. Atmos. Meas. Tech. 4, 2345-2358.

Warneke, C., de, G., Joost A., Edwards, P. M., Holloway, J. S., Gilman, J. B., Kuster, W. C., Graus, M., Atlas, E., Blake, D., Gentner, D. R., Goldstein, A. H., Harley, R. A., Alvarez, S., Rappenglueck, B., Trainer, M., and Parrish, D. D. (2013). Photochemical aging of volatile organic compounds in the Los Angeles basin: Weekday-weekend effect. J. Geophys. Res. Atmos. 118, 5018-5028.

Warneke, C., de, G., Joost A., Holloway, J. S., Peischl, J., Ryerson, T. B., Atlas, E., Blake, D., Trainer, M., and Parrish, D. D. (2012). Multiyear trends in volatile organic compounds in Los Angeles, California: Five decades of decreasing emissions. J. Geophys. Res. 117, D21305.

Watson, J. G. (2002). Visibility: Science and Regulation. J. Air Waste Manage. 52, 628-713.

Wayne, R. P., Barnes, I., Biggs, P., Burrows, J. P., Canosa-Mas, C. E., Hjorth, J., Le, B., G, Moortgat, G. K., Perner, D., Poulet, G., and others (1991). The nitrate radical: physics, chemistry, and the atmosphere. Atmos. Environ. 25, 1-203.

Wentworth, G. R., Murphy, J. G., and Sills, D. M. L. (2015). Impact of lake breezes on ozone and nitrogen oxides in the Greater Toronto Area. Atmos. Environ. 109, 52-60.

Wexler, A. S., and Seinfeld, J. H. (1990). The distribution of ammonium salts among a size and composition dispersed aerosol. Atmospheric Environment. Part A. General Topics 24, 1231-1246.

WHO: World Health Organization (2000). Air Quality Guidelines for Europe WHO Regional Publications).

WHO: World Health Organization (2002). Concise International Chemical Assessment Document 43: Acrolein (Geneva: World Health Organization).

WHO: World Health Organization (2006). Air Quality Guidelines: Global Update 2005: Particulate Matter, Ozone, Nitrogen Dioxide and Sulfur Dioxide World Health Organization).

WHO: World Health Organization (2015). Air Pollution <http://www.who.int/topics/air_pollution/en/>.[19 January 2015]

Wittrock, F., Richter, A., Oetjen, H., Burrows, J. P., Kanakidou, M., Myriokefalitakis, S., Volkamer, R., Beirle, S., Platt, U., and Wagner, T. (2006). Simultaneous global observations of glyoxal and formaldehyde from space. Geophys. Res. Lett. 33, L16804.

Xia, L., and Gao, Y. (2010). Chemical composition and size distributions of coastal aerosols observed on the US East Coast. Mar. Chem. 119, 77-90.

Yao, X., Lau, N. T., Chan, C. K., and Fang, M. (2005). The use of tunnel concentration profile data to determine the ratio of NO_2/NO_x directly emitted from vehicles. Atmos. Chem. Phys. Dis. 5, 12723-12740.

Yao, X., and Zhang, L. (2012). Chemical processes in sea-salt chloride depletion observed at a Canadian rural coastal site. Atmos. Environ. 46, 189-194.

Yap, D., Reid, N., De Brou, G., Bloxam, R., Piche, E., Chan, W., Cheng, C., Bitzos, M., and Wong, S. (2005). Transboundary Air Pollution in Ontario. Report.

Zhang, L., Moran, M. D., Makar, P. A., Brook, J. R., and Gong, S. (2002). Modelling gaseous dry deposition in AURAMS: a unified regional air-quality modelling system. Atmos. Environ. 36, 537-560.

Zhang, Q., Jimenez, J. L., Canagaratna, M. R., Allan, J. D., Coe, H., Ulbrich, I., Alfarra, M. R., Takami, A., Middlebrook, A. M., Sun, Y. L., Dzepina, K., Dunlea, E., Docherty, K., DeCarlo, P. F., Salcedo, D., Onasch, T., Jayne, J. T., Miyoshi, T., Shimono, A., Hatakeyama, S., Takegawa, N., Kondo, Y., Schneider, J., Drewnick,

F., Borrmann, S., Weimer, S., Demerjian, K., Williams, P., Bower, K., Bahreini, R., Cottrell, L., Griffin, R. J., Rautiainen, J., Sun, J. Y., Zhang, Y. M., and Worsnop, D. R. (2007). Ubiquity and dominance of oxygenated species in organic aerosols in anthropogenically-influenced Northern Hemisphere midlatitudes. Geophys. Res. Lett. 34, L13801.

Zhang, Q., Alfarra, M. R., Worsnop, D. R., Allan, J. D., Coe, H., Canagaratna, M. R., and Jimenez, J. L. (2005). Deconvolution and Quantification of Hydrocarbon-like and Oxygenated Organic Aerosols Based on Aerosol Mass Spectrometry. Environ. Sci. Technol. 39, 4938-4952.

Zhao, Y., and Gao, Y. (2008). Acidic species and chloride depletion in coarse aerosol particles in the US east coast. Sci. Total Environ. 407, 541-547.

Zhou, J., and R., M. (1999). Oxygenated hydrocarbons in ambient air: Methods and measurements using solid-phase microextraction. Proceedings of the 92nd Annual Meeting of the Air and Waste Management Association, refereed CD Publication. 99-316, P1-P18.

Zorn, S. R., Drewnick, F., Schott, M., Hoffmann, T., and Borrmann, S. (2008). Characterization of the South Atlantic marine boundary layer aerosol using an aerodyne aerosol mass spectrometer. Atmos. Chem. Phys. 8, 4711-4728.